‘SMART’ MAGNETIC NANOCOMPOSITE HYDROGELS FOR DRUG DELIVERY

‘SMART’, INJECTABLE MAGNETIC NANOCOMPOSITE HYDROGELS FOR BIOMEDICAL APPLICATIONS WITH A FOCUS ON EXTERNALLY-MEDIATED RELEASE

By SCOTT BRICE CAMPBELL, B.Sc.

A Thesis Submitted to the School of Graduate Studies in Partial Fulfilment of the Requirements for the Degree Ph.D. of Chemical Engineering

McMaster University Ph.D. OF ENGINEERING (2016) Hamilton, Ontario (Chemical Engineering)

TITLE: ’Smart’, injectable, magnetic nanocomposite hydrogel materials for biomedical applications with a focus on externally-mediated drug release

AUTHOR: Scott Brice Campbell, B.Sc. (Queen’s University)

SUPERVISOR: Professor Todd R. Hoare

NUMBER OF PAGES: xxxii, 263

Lay Abstract

This thesis focuses on the development of nanocomposite materials that can be injected into a specific location in the body and deliver therapeutic drugs by a remote-controlled process. These nanocomposites are composed of magnetic particles and polymers that respond to changes in temperature. The combination of these materials results in nanocomposites that can change their properties in response to specific magnetic fields to switch from releasing drug slowly (or not at all) to releasing drug quickly on demand. The changes are fully reversible and solely depend on whether the external magnetic field is switched on or off. These novel systems offer an alternative to therapies that require frequent injections, such as insulin for diabetes, or therapies that need the drug to be released in very precise locations, such as cancer treatments, and could improve the safety, reduce the risk of side effects, and lower the cost of many medical treatments.

Abstract

The capability of precisely controlling the kinetics of therapeutic delivery at the optimal location and rate for a given patient would have great potential to improve health and well-being in a range of current drug therapies (insulin, chemotherapeutics, vaccines, etc.). Indeed, if successfully developed, locally administered injectable drug delivery vehicles capable of remotely-triggered release would be the gold standard for many treatments.

Multiple injectable nanocomposites have been investigated for this purpose that are generally comprised of a thermosensitive polymeric material and superparamagnetic iron oxide nanoparticles (SPIONs). SPIONs generate heat when exposed remote alternating magnetic fields (AMFs), and the transfer of this heat to thermosensitive polymers can be used to control the release of therapeutics. Ideally, these systems would be capable of returning to their original state and basal release rate when the external AMF trigger is removed.

Several novel injectable nanocomposite materials that explore interactions between SPIONs and thermosensitive polymers to mediate drug release, from the macroscale to the nanoscale, were developed and demonstrated to be capable of remotely-triggered, AMF-mediated enhanced release. The macroscale magnetic nanocomposites have thermosensitive hydrogel and/or microgel components that regulate release based on the heat produced from SPIONs in response to an external AMF. On the millimeter-scale, a microinjection system capable of producing thermosensitive hydrogel beads that could potentially incorporate SPIONs is described. On the nanoscale, nanoparticles with

a glass transition temperature and thermosensitive microgels are combined with SPIONs and investigated for their remote, AMF-mediated release characteristics. The engineered macroscale and nanoscale systems are capable of up to ~4:1 and ~7:1 enhancements in release due to an AMF application, respectively, compared to the basal release rate.

Collectively, these nanocomposites represent a promising stride towards improved remote-actuation of drug release and a stepping stone for future attempts at precisely controlling the site and kinetics of drug release.

Acknowledgements

This dissertation could not have been completed without a wide array of my friends and colleagues, both within and outside of academia. First and foremost, I'd like to thank my supervisor, Dr. Todd Hoare. Your guidance, intellect, and generosity over the last 6 years as a supervisor have been immeasurable in the ultimate development of this document and myself as a researcher. This work is indebted to your ability to come up with innovative project ideas with great potential and that are so good that I can't say 'no' to taking on yet another project. I still hope to think of a way to get that main project done one day! What I particularly appreciate is the freedom that you have given me to work through my projects independently, including through their hurdles, and the multitude of opportunities that you've given me to attend a ton of conferences (which I always really enjoy) to get new ideas, be a part of the CC-CRS to see how scientific societies work, supervise a whole bunch of undergraduate students, and much, much more. I also really appreciate your uncanny ability to write fantastic reference letters that help us get scholarships that we may not otherwise deserve! Overall, it was really neat to see the lab grow from its near-beginnings when I started to where it is today, and I wish the lab the best of luck in going forward to new heights.

I'd also like to thank my supervisory committee members Dr. Carlos Filipe and Dr. Ravi Selvaganapathy for providing vital advise during committee meetings to solve many of the issues I've had with these and many more projects over the years. I really appreciated the light-hearted banter before and after the committee meetings, which definitely made the whole process less stressful on my part. Also, thank you for your constant attempts to try and keep me on track so I could eventually tone down my curiosity to try out new project ideas and finally get a document like this done!

I'd also like to thank the other professors in the Department of Chemical Engineering here at McMaster, who always provided good insight, guidance, and are a pleasure to be around. I'd particularly like to thank Drs. Emily Cranston and Thomas Adams for many great conversations outside of school (and often during sports), Dr. Chris Swartz for always helping out whenever I asked for help with scholarship applications, and Dr. David Latulippe for being great to work for as a TA, for providing guidance on how to start out as a professor, and for allowing me to be a part of his manuscript and conference presentation describing how to improve the way fluid mechanics is taught.

The Chemical Engineering staff has also been incredibly helpful. I definitely couldn't have finished this work off without the help of Dan, Paul, Lynn, Michelle, and Justina for helping me out with getting the lab and my experiments in good working order (which was a constant challenge) and guiding me through all of the administrative accoutrements that go along with being in grad school. I'd particularly like to thank Melissa Vasil for letting me know about the Vanier scholarship program, which I had no idea about before and really did change my life in a very cool way. On that note, I'd like to thank both Vanier scholarship program and NSERC USRA and CGS programs, without which I probably wouldn't have made the decision I did to go to grad school in the first place.

And grad school would not have been a fun experience at all without fantastic lab mates along the way. I've met some of my best friends during my time at McMaster and many of you were proud members of the Hoare lab. I remember meeting Daryl even before I officially started in a lab and his friendliness and inclusiveness was clearly contagious within our lab during those early golden years. You were always great to work with, and thank you so much for including me in your sports teams and extracurricular fun times – you really made me feel at home in the Hammer early on. Mat and Rabia will forever be

a part of my very exclusive crew of best buds. I've had so many awesome, unforgettable little powwows, g-chat convos, and experiences both in and out of the lab with you and it was truly a pleasure working with you two. I'm just glad that I didn't turn out to be the super conservative ultra-nerd that you thought I was when I started! I can't wait until I can book my first appointment with Dr. Dr. Patenaude so I can schedule in more hang out times with him and to convocate alongside Rabia after all these years. Trevor has always been there to help out whenever I or anyone in the lab needs him and you're confidence and party hosting skillz has grown in leaps and bounds since we first met, which is awesome. Trevor's truly one of the nicest people I've ever met and I wish you the best of luck in finishing up that PhD in a time filled with the dankest of memes. Niels, it was great working with you once again and thanks for all the good times at Sinterklaas parties, the Phoenix, science chats, and much more. I'll let you know where I go next when I find out so you can follow me there too! The unparalleled sarcastic wit of Danielle was always able to lighten up our lab and an oppressive darkness has spread ever since you left. It was great working on those magnetic release projects and I'm glad that we could help each other graduate the way that we did. Also, I think we all collectively just realized that you were, in fact, a fully-fledged graduate student at one point or another!

This work really could not have been completed without the help of the many undergraduate students that I've proudly supervised and worked over the years as well, including Stuart Young, Elysia Jellema, Jared Gour, Leo Mak, Dennis Kinio, Jenny Chen, and Angus Lam. I'd especially like to thank Jenny and Angus, who have volunteered their time to help me finish a few my final projects. I really appreciate it! I wish you guys all the best of luck in the future and definitely hit me up anytime if you'd ever need a glowing reference letter! I'd like to thank all of the other graduate students and undergraduate students that were involved in our lab over the years. Without you

fine folks, the experience would not have been the same (partly because y'all graciously allowed me to blast my tunes pretty much all the time!). I also wish the current Hoare lab members good luck in the future! I'm sure you'll be in good hands with Maddi seizing full control of everyday lab organizing operations with her sparkling personality and supreme baking skills!

I'd definitely like to acknowledge all the other grad students that I've worked and hung out with over the years. While not all of our projects worked out in the end, I really enjoyed and learned a lot about microfluidics from Siawash, Wen, and Jun over the years. And I certainly will not forget all the good times I've had with all of the JHE 256 officemates over the years, including Rahul, Pedram, Amanda, Stefan, Si Pan, Mat, and SeungMi, who is one of the nicest and smartest people I've had the privilege of meeting. I'd also like to thank Jen too for putting up with me while I write this massive thing! It was also a fantastic opportunity to serve on the Chem Eng Grad Club with fantastic people over the years, including, but not limited to, Brian, Patty, Leffy, Jaffer, and Jake (basically MACC). I had a ton of fun organizing events to get the grad students out and an even better time going to events that I didn't have to organize!

I remember my first day here when Daryl took me to see Kyla to get me to join what would become the Sax Panthers softball team, with Fitzy, Ryan Love and Mark Machado. Ever since then it almost feels like I took a dual degree in gym when I think of all the good times I've had playing sports with great teammates in the last 6 years! I've had just the best time playing with and captaining and co-captaining squads filled with my best friends in intramurals, Jake and Brandon's amazing GSA curling league, HUC, and the GSA softball league and, almost especially, hanging out with everyone after at the Phoenix. All those championships are nothing to sniff at either! But, honestly, these were the moments that kept me more or less (depending on who you're asking) sane as

I took on way too many projects and responsibilities at work. The Phoenix Cups, along with Jake's cottage gatherings, will forever be a highlight of the summers in Hamilton and I will certainly never forget both the championship and non-championship years, filled with Jake's clutch dingers, Patty's defense, rowdy pre-tourney team bonding sessions, Leffy's loud mouth, Danielle's oppo poppos, Kat's near lady-dinger, and just the best people.

I'd also like to thank Jenny for convincing me to try out for the McMaster Ultimate team! My time with the team over the last few years has just been amazing, and the welcoming nature and friendliness of the Mac Ulti fam, especially Linc, Molly, Nico, Myf, Roy, Jenny, Breezy, and Sean, has made me a much way ultimate player and a much better person. Playing frizz in all the other leagues with you all is always the highlight of my week! It was awesome to have the chance to represent McMaster with all you fine folks!

Lastly, I'd like to thank my actual, for-realzies family for supporting me and always being there throughout this long, long process. My sisters Erin and Meghan, were always fun to hang out and catch up with during my vacation downtime, even if you were normally only there one at a time whenever I was able to come back home! That just made all those times where we could all make it back during vacations and where I could poke fun of Meghan with Erin laughing in the background extra special! My Dad kind of set me up for me to pursue this PhD by reading technical papers and his Master's thesis to put me to sleep as a kid and he was there for me from the start (including when the Civic finally broke down), so I guess this end result isn't all that unexpected. And my mom was always there to ask me when I was going to be finished, provide multitudes of family gossip, and make me completely question my future with every phone conversation; all while supporting me the whole way. I think that you finally understand what I actually did during my PhD though! But seriously, I love you all and thank you for everything.

Table of Contents

List of Figures

List of Tables

List of all Abbreviations and Symbols

AA	Acrylic acid
AAEM	Acetoacetoxyethyl methacrylate
ADH	Adipic acid dihydrazide
AIBME	2,2-azobisisobutyric acid dimethyl ester
Ald	Aldehyde
Am/AAm	Acrylamide
AMF	Alternating magnetic field
ANOVA	Analysis of variance
API	Active pharmaceutical ingredient
APS	Ammonium persulfate
AuNP	Gold nanoparticles
BMA	Butyl methacrylate
BPO	Benzoyl peroxide
CMC	Carboxymethyl cellulose
CNT	Carbon nanotube
DEX/Dex	Dextran
DIW	Deionized water
DLS	Dynamic light scattering
DMAEMAm/DMAEMA	*N*-(2,2-dimethylaminoethyl)methacrylamide
DMEM	Dulbecco's modified Eagle's medium-high glucose
DMSO	Dimethyl sulfoxide
EDC	N-3-dimethylaminopropyl-N-ethyl carbodiimide hydrochloride

FBS	Fetal bovine serum
FeNW	Iron nanowire
FITC	Fluorescein isothiocyanate
G’	Storage modulus
G’’	Loss modulus
GelMA	Gelatin methacrylate
GPC	Gel permeation chromatography
HEMA	2-hydroxyethyl methacrylate
Hzd	Hydrazide
HCl	Hydrochloric acid
HPLC	High performance liquid chromatography
IOP	Intraocular pressure
IR	Infrared
LCST	Lower critical solution temperature
MAA	Mercaptoacetic acid
MBA	N,N-methylenebisacrylamide
MIC	Minimal inhibitory concentration
MITCH	Mixing induced two-component hydrogel
MMA	Methyl methacrylate
MRI	Magnetic resonance imaging
MHT	Magnetic hyperthermia treatment
MTA	Magnetic thermal ablation
MTT	Thiazolyl blue tetrazolium bromide
NaCl	Sodium chloride

NaOH	Sodium hydroxide
NHS	*N*-hydroxysuccinimide
NIR	Near-infrared
NIPAM	N-isopropylacrylamide
NIPMAM	N-isopropyl methacrylamide
NP	Nanoparticle
OEGMA	Oligoethylene glycol methacrylate
OMF	Oscillating magnetic field (see AMF)
PBS	Phosphate buffered saline
PDMS	poly(dimethylsiloxane)
PDI	Polydispersity index
PEG	poly(ethylene glycol)
PLGA	poly(lactic-co-glycolic acid)
PNIPAM	poly(N-isopropylacrylamide)
PNIPMAM	poly(N-isopropyl methacrylamide)
POEGMA	poly(oligoethylene glycol methacrylate)
PPA	polyethylene polyamine
PS	Penicillin streptomycin
PVA	polyvinyl alcohol
RES	Reticuloendothelial system
RF	Radiofrequency
SDS	Sodium dodecyl sulfate
SEM	Scanning electron microscopy
SQUID	Superconducting Quantum Interference Device

SPION	Superparamagnetic iron oxide nanoparticle
TEM	Transmission electron microscopy
T_g	Glass transition temperature
TGA	Thermogravimetric analysis or Thioglycolic acid
T_m	Melting point (temperature)
UV	Ultraviolet
VPTT	Volume Phase Transition Temperature

Declaration of Academic Achievement

The majority of the written work described herein was conceived, conducted, analysed, and written by the author of this thesis, in consultation from Dr. Todd Hoare, with the exception of the following:

Chapter 2: Dr. Mathew Patenaude and I performed the animal experiments together. Dr. Patenaude performed the histology from these studies, created Figure 2.8 on this histology, along with providing a brief description of these results in the results and discussion section. Dennis Kinio aided in polymer synthesis. TGA experiments were performed by Frank Gibbs in the Brockhouse Institute for materials research at McMaster University. Dr. Paul Dube performed the SQUID experiments for this work.

Chapter 3: Danielle Maitland performed the majority of the experiments and a portion of the data analysis that led to Figures 3.3 and 3.4. Danielle also made Figures S3.1, S3.5a, and S3.9. A good portion of the writing describing these figures was an adaptation between my analysis for committee reports and Danielle's Master's thesis. Dr. Paul Dube performed the SQUID experiments for this work.

Chapter 4: Danielle Maitland was a co-first author on this work, as she performed quite a few of the experiments for her Master's thesis. These experiments led resulted in a good proportion or all of the data from Figures 4.3, 4.6, 4.7, 4.8, and S4.4 and Tables 4.1, 4.2, S4.1, S4.2, S4.3, and S4.4.

Chapter 5: Jun Yang performed the nearly all of the work in developing the microinjector design and he solely performed the experiments that resulted in Figure 5.3 and 5.5. Jun

and I jointly developed Figure 5.2 and performed the experiment that is shown in Figure 5.6. Ben Muirhead and I performed the *in vivo* intraocular injection experiments using the microinjector together, as it is a two man operation. Ben took the images of the eyes in this process that are shown in Figure 5.7. Ben also excised the eyes and encased them in wax on his own and we both sliced sections and imaged them to result in the images in Figure 5.8.

Chapter 6: Jenny Chen was integral in developing a suitable protocol for the synthesis of the cationic, thermosensitive microgels, and the associated DLS and Zeta potential measurements. Angus Lam aided in the development of a method to centrifuge these materials down, both before and after SPIONs were incorporated into the matrix. Angus also assisted with the DLS and *in vitro* cytocompatibility studies for these materials. TGA experiments were performed by Frank Gibbs in the Brockhouse Institute for materials research at McMaster University. Dr. Paul Dube performed the SQUID experiments for this work as well.

Chapter 7: Dr. Niels Smeets and I came up with the concept for this project, or a variation of it before it evolved into what it is today. Jared Gour played an important role in tuning the T_g of our materials by altering the BMA/MMA ratios and was able to develop a method to produce magnetic latex nanoparticles, although these were not ultimately chosen for further studies. Angus Lam once again developed a method to centrifuge these materials down to purify them and was very helpful in the thermally-triggered rhodamine B release study (Figure 7.3). TGA experiments were performed by Frank Gibbs in the Brockhouse Institute for materials research at McMaster University. Dr. Paul Dube performed the SQUID experiments for this work as well.

Chapter 1: Introduction

1.1 Generating materials for externally-controlled drug release

This work centers on the development of 'smart' materials that can be used to regulate drug release in the body via an external source. This is achieved by using polymeric hydrogels that experience fully reversible, significant volume changes as their temperature alters around a specific volume phase transition temperature (VPTT).[1] Increasing the temperature of a given thermosensitive hydrogel above its VPTT will cause its volume to dramatically decrease, forcing it to expel some of its water content, and lowering its temperature below this VPTT will increase the volume of this hydrogel back to its original state. These volume changes can be exploited to control the release of therapeutic drugs.

The body is an excellent at regulating its temperature, so other components must be added to induce temperature changes to hydrogel systems *in vivo*. One of the commonly used components for this purpose are superparamagnetic iron oxide nanoparticles (SPIONs), which generate heat in response to alternating magnetic fields (AMFs).[2] Thus, combining SPIONs into thermosensitive hydrogels can be useful in preparing 'smart', magnetic drug-releasing systems that are capable of externally-mediated drug release using AMFs. Furthermore, if such hydrogel-based systems are engineered to be injectable in nature, the materials can be injected directly into the site of interest for the therapeutic treatment. Localized drug release such as this are highly preferred over forms of systemic release for a wide array of treatments.[3]

The aim of this work is to develop a set of injectable materials that could be used to controllably release therapeutics via external means. These materials all utilize a combination of SPIONs and hydrogels with a VPTT just above physiological temperatures (~40°C) or analogous thermosensitive polymers such that release from these systems can be triggered by an external AMF. The array of 'smart', injectable, magnetic systems that are explored range in scale from macroscale hydrogels nanocomposites to the nanoscale materials, which is the general theme of this work.

This introduction first covers different strategies for the development of externally-actuated hydrogel nanocomposites in a review article that was written in 2014. A brief update in the externally-addressable technologies developed in the two years since follows this. The introduction concludes with a summary of the reasoning behind using the materials and approach that we did to develop our materials and a brief overlay of the outline of the thesis as a whole.

1.1.1 References

1 Hoare, T. R.; Kohane, D. S. *Polymer* **2008**, *49*, 1993–2007.

2 S. Laurent, S. Dutz, U. O. Häfeli and M. Mahmoudi, *Adv. Colloid Interface Sci.*, 2011, **166**, 8–23.

3 Y. Brudno and D. J. Mooney, *J. Control. Release*, 2015, **219**, 8–17.

1.2 Externally-addressable hydrogel nanocomposites for biomedical applications

Campbell, S.B., and Hoare, T. *Curr. Opin. Chem. Eng.* **2014**, *4*, 1-10.

1.2.1 Abstract

Hydrogels are widely applied in a variety of biomedical applications given their biologically-relevant mechanical, interfacial, and chemical properties. By combining (soft) hydrogels with (hard) nanoparticles, the attractive electromagnetic properties of many nanoparticles can be applied *in vivo* while maintaining biocompatibility. Herein, we outline recent progress in the design of hydrogel nanocomposites coupling carbon nanotubes, gold nanoparticles, and superparamagnetic iron oxide nanoparticles (SPIONs) with hydrogels, including both conventional hydrogels as well as "smart", stimuli-responsive hydrogels whose properties can be remotely changed "on-demand" using the nanoparticle as a transducer to convert highly penetrative near-infrared radiation or alternating magnetic fields into a physically-relevant phase transition stimulus. The applications of such materials for on-demand drug delivery, hyperthermia therapies, and tissue adhesives are described.

Keywords: hydrogel nanocomposites, carbon nanotubes, magnetic nanoparticles, gold nanoparticles, on-demand drug delivery, tissue engineering, remote-control biomedical devices.

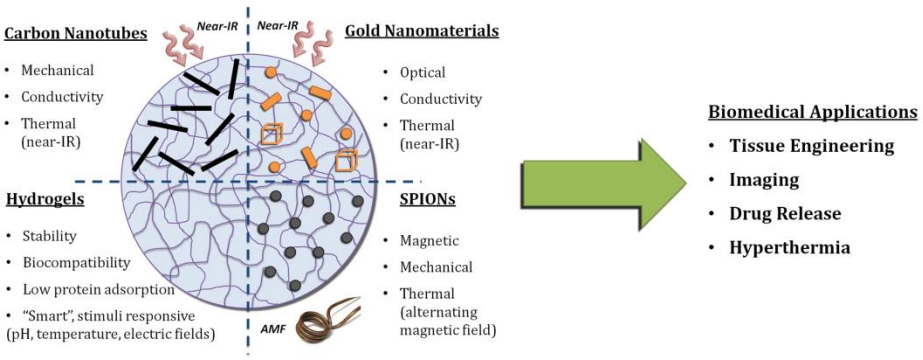

1.2.2 Introduction

The use of hydrogels as biomaterials has been steadily increasing ever since crosslinked 2-hydroxyethyl methacrylate (HEMA) hydrogels were first reported by Wichterle and Lim in 1960 [1]. Hydrogels are three-dimensional (3D) crosslinked networks of hydrophilic polymer chains that can be swollen up to thousands of times their dry weight with water. Hydrogels can be designed to have high void fractions (i.e. tunable diffusivities) and are mechanically and physically similar to the extracellular matrix of soft tissues [2]. The high water content of hydrogels results in a low interfacial tension that suppresses protein adsorption [2–4]; minimizing protein adsorption is essential to reduce inflammatory responses to biomaterials, imperative for cell encapsulation or tissue engineering applications. `Smart`, stimuli-responsive hydrogels that are able to swell and deswell in response to external stimuli such as environmental pH [5], ionic strength [6], temperature [7], or electric fields [8] offer further advantages in terms of facilitating switchable drug release kinetics, reversible cell adhesion/release and/or dynamic modification of pore sizes. Due to these properties, both bulk hydrogels and their nano/microscale counterparts, microgels (ranging in size from 50 nm – 5 μm) [9], have received a great deal of recent attention as potential materials for tissue

engineering [10–12], adhesives and wound-healing [13,14], catalysis [15], biosensors [16], and drug delivery [17–19].

However, despite these favorable properties, the biomedical use of hydrogels also faces several limitations. Most conventional synthetic hydrogels are not degradable, and the inherent elasticity of hydrogels renders them difficult to inject (typically requiring surgical implantation). These issues can be largely addressed by adjusting the chemistry by which the crosslinking structure of the hydrogel is formed, exploiting shear-disrupted physical interactions [20], supramolecular interactions which can self-heal [21], or rapidly reactive and reversible covalent bond-forming chemistries by which gelation can occur following simple mixing [3,7]. As an example of the latter approach, our lab utilizes *in situ* gelling hydrogels by which the crosslinks are formed via the rapid condensation of aldehyde and hydrazide groups functionalized on two respective polymers to form hydrolytically degradable hydrazone crosslinked hydrogels upon co-injection of the polymers [22,23]. More difficult to address are limitations associated with the relatively weak mechanical properties of hydrogels (particularly injectable hydrogels) [24] and challenges associated with safely and practically applying the “smart” stimulus required to exploit the properties of responsive hydrogels within the highly regulated physiochemical environment of the body.

These latter two challenges can be addressed by adding nanoparticles to hydrogels. Nanoparticles can be physically entrapped within the hydrogel matrix or cross-linked via interfacial chemistry into the network structure of hydrogels to develop nanocomposite materials with improved mechanical strength as well as well-defined optical, thermal, electronic, and magnetic properties [25]. Specifically, the incorporation of nanoparticles

that can transduce specific external stimuli to generate heat (in particular, alternating magnetic fields and near-infrared light, both of which are highly penetrative and thus can transmit through biological tissues) offers particular promise when coupled with thermosensitive hydrogels such as those based on poly(N-isopropylacrylamide) (PNIPAM), effectively providing non-invasive and remote control over hydrogel swelling [26,27]. Furthermore, nanoparticles with electrically-conductive properties can be applied to remotely switch cell behavior, in particular muscle cells programmed to contract or (in the case of cardiac cells) beat upon electrical stimulation or neural cells transmitting electrical signals. In turn, relative to the use of these nanoparticles alone in the body, the hydrogel can provide benefits such as generally enhanced biocompatibility, tunable cell interactions, and improved control over drug release with higher loading capacities and better release characteristics [28]. The hydrogel network also effectively localizes the nanoparticles of interest at the desired biological site, facilitating (for example) more effective local drug delivery with fewer systemic side-effects and hyperthermia treatments better targeting lysis of temperature-sensitive cancer cells via externally controlled heating [28].

This mini-review will highlight recent research in the development of hydrogel nanocomposites that permit these hydrogels to be externally addressable in the context of biomedical applications, with a particular focus on papers published within the last 2-3 years. Specifically, we review the use of hydrogel nanocomposites containing carbon nanotubes, gold nano-objects, and/or superparamagnetic iron oxide nanoparticles (SPIONs) in the context of designing “on-demand”, switchable biomaterials able to either themselves respond to a stimulus via swelling, shrinking, shape changes, hydrophobicity changes etc. or to mediate a cellular response to a stimulus (Figure 1.1).

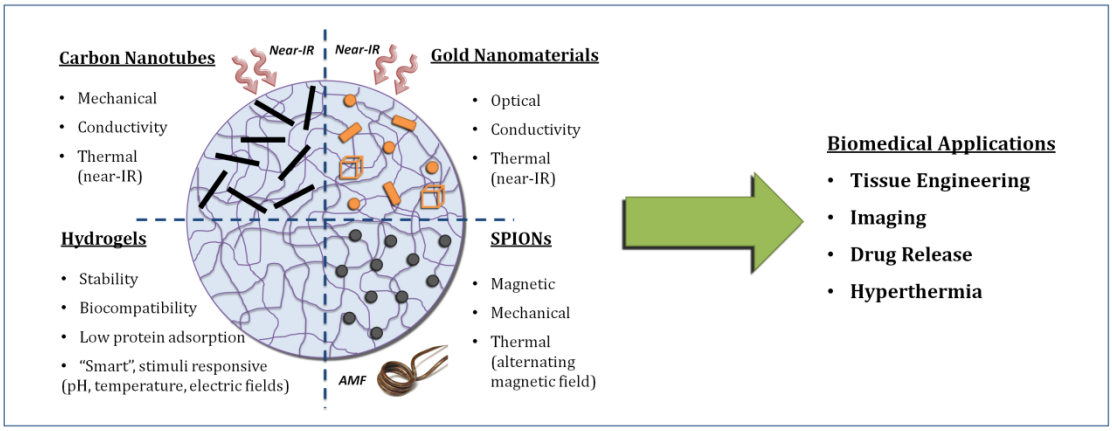

Figure 1.1: Properties and typical compositions of externally-addressable hydrogel-nanoparticle nanocomposite materials for biomedical applications**.**

1.2.3 Carbon Nanotube-Hydrogel Nanocomposites

Carbon nanotubes (CNTs) are seamless cylinders of one or more layers of graphene and have long been recognized to possess superior mechanical, thermal, and electric properties useful to augment hydrogel structures [29,30]. Indeed, a great number of CNT-hydrogel hybrids have been developed that take advantage of these properties for the purposes of tissue engineering (particularly for neural and cardiac tissues where electrical conductivity is crucial) [31,32] and drug delivery [33–35].

CNT-gel hybrids were initially made primarily to improve the mechanical properties of hydrogels and hydrogel scaffolds. Low concentrations of CNTs, and graphene oxide (unrolled CNTs), have been shown to mechanically reinforce hydrogels to allow them to better mimic stiffer soft tissues [36–38]. CNTs can also significantly influence cell-biomaterial interactions. For example, Chen et al. demonstrated that incorporation of only 0.067 wt% of CNTs in a PNIPAM hydrogel drastically improved both cell attachment

and proliferation at physiological temperature while still maintaining the potential to harvest the resulting cell sheet by lowering the temperature to 20°C [37].

More recently, the other, more unique properties of CNTs have attracted significant interest in biomedical applications. In particular, the electrical conductivity of CNTs can be exploited in both tissue engineering and drug delivery applications. Ramón-Azcón et al. [31] demonstrated that CNT-containing hydrogels can be used to direct cell orientation inside a hydrogel in the presence of an electrical current. Dielectrophoresis followed by UV polymerization effectively aligned carbon nanotubes in a gelatin methacrylate (GelMA) hydrogel, resulting in significantly more conductive and stronger hybrid materials that improved the differentiation of C2C12 myoblast cells into contractile myotubes relative to non-aligned CNT hydrogels [31]. Analogously, Shin et al. [30] fabricated CNT-GelMA hydrogel films that were structurally similar to that of heart muscle networks with purkinje fibres. Cardiac cells exhibited improved adhesion, spreading, retention, and viability on CNT-GelMA hydrogels relative to GelMA hydrogels alone; furthermore, the conductive nature of the CNT-GelMA composite promoted the propagation of electrical signals between the cardiac cells, facilitating strong spontaneous beating even in the presence of cardio-toxins and cardio-inhibitors [30]. Servant et al. [35] also demonstrated the use of electric fields to initiate triggerable pulsatile drug release with a CNT-methyl methacrylate hydrogel material that deswells in the presence of an electric field.

In terms of designing externally-addressable hydrogels, the thermal properties of CNTs have also attracted significant recent interest. In the context of drug delivery, by combining “smart” thermosensitive gels with CNTs that can heat in response to a remote

deep-penetrating near-IR source, thermal phase transitions can been remotely triggered via near-IR irradiation [39]. Such activity could be applied to facilitate pulsatile release of therapeutics, although this specific application has yet to be explored. However, graphene oxide has been combined with a thermosensitive hydrogel to show promising CNT-mediated drug release [40]. In the context of tissue adhesives, Du et al. [41] reported a self-healing and temperature, pH and near-IR responsive supramolecular CNT-polyethylene polyamine (PPA) hydrogel that exhibited excellent mechanical strength and remarkable adhesion properties changeable externally using near-IR irradiation (Figure 1.2); such a material is attractive for use as a switchable tissue adhesive.

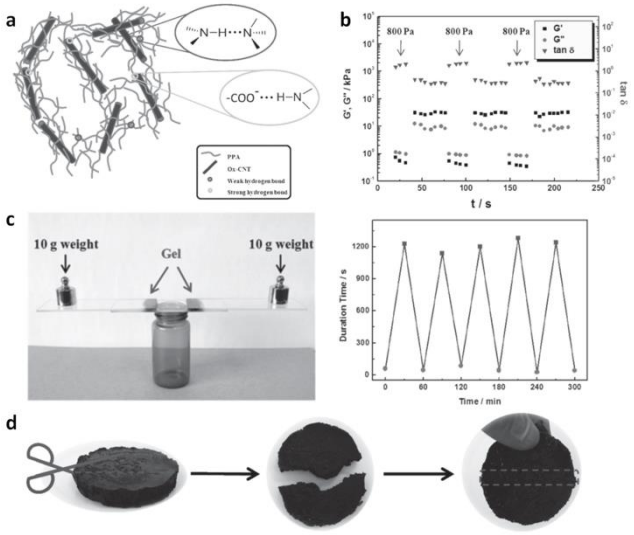

Figure 1.2: Supramolecular CNT-PPA hydrogel composites. a) The proposed gelation mechanism involving relatively strong and weak hydrogen bond formation. b) Response of hydrogels to a repeated deformation stress of 800 Pa. The gels break completely but immediately recover their elasticity, making these gels easily injectable. c) The hydrogel nanocomposites adhere to glass substrates (left) and experience temperature-sensitive adhesion characteristics, with the graph on the right showing the duration of time the weight could be loaded on the glass slide at 40°C (circles) and 5°C (squares) d) Macroscopic self-healing of CNT-PPA nanocomposites, with healing observed in two minutes after the gel was cut in half [Adapted with permission from [41].]

The practical use of CNT-loaded hydrogels as biomaterials is currently somewhat limited because of the great deal of controversy regarding the toxicity of CNTs, with much debate on either side of this issue [42–44]. It should be noted that CNTs used in biomedical applications are typically shorter than CNTs that originally provoked toxicity concerns (i.e. CNTs with lengths > 20 μm, analogous to asbestos fibres) [45]. However, even for the shorter CNTs, toxicity has been attributed to CNTs eliciting oxidative stresses and inflammation on cells in vivo and in vitro [46]. Both the surface chemistry and the geometry of CNTs have been demonstrated to positively influence biocompatibility [45]; nonetheless, given the diversity of opinion on the definition of biocompatibility and how the term is used and evaluated in the literature, it remains unclear as to whether CNT-based materials are ultimately translatable to the clinic and, if so, for what specific applications or in which particular biological environments. Regardless, the application of nanomaterials with more well-demonstrated inertness or the potential for biological processing/clearance is preferable to the use of CNTs in biomedical applications if such substitutions can maintain the desired hydrogel properties.

1.2.4 Gold Nanoparticle-Hydrogel Nanocomposites

Gold nanoparticles (AuNPs) can be fabricated as spherical nanoparticles, cylindrical nanorods, or hollow nanocages. AuNPs can be physically entrapped inside a forming hydrogel, loaded into a pre-formed hydrogel via electrostatic interactions [47], or grown *in situ* inside a hydrogel via the precipitation of gold salts [48], offering more flexibility in terms of how the nanocomposites are formed relative to CNTs. Analogous to CNTs, Au

nanorods can also generate heat when exposed to a near-IR source by tuning the aspect ratio, and therefore anisotropy, such that the absorption maximum of the nanorods lies within the near-IR range [49]. Spherical AuNPs exhibit absorption maxima in the visible range, depending on particle size (~520 – 550 nm); as the aspect ratio of the particles is increased, the wavelength can be increased to the near-IR range (800-1200 nm), which is more intriguing from a biomedical perspective due to the deep-penetrating nature of light at these wavelengths [47, 50]. Furthermore, Au nanorods are electrically conductive, leading to applications in terms of hyperthermia, drug release, and tissue engineering [48,51].

The majority of gold nanoparticle hydrogel nanocomposites reported have been developed for combined therapies involving near-IR induced drug release, imaging, and hyperthermia, with most therapies targeted to cancer treatment [52–54]. Such therapies exploit the both the near-IR absorption capacity as well as the surface plasmon resonance properties of gold nanoparticles. For example, Wu et al. [54] fabricated “smart” biomaterials consisting of AuNP encapsulated in hydrogel shells that could internalize into specific cancer cells and subsequently allow for both imaging and *in situ* drug release triggered by the lower pH of local areas within the cell. Other therapeutic targets have also been pursued. For example, Kojic et al. [55] used the heating properties of AuNPs to create injectable AuNP-silk hydrogels that successfully used thermotherapy to treat bacterial infections in hard-to-reach areas as an alternative to conventional antibiotic treatments.

Analogous to CNTs, the electrical conductivity of AuNPs makes AuNP-hydrogel scaffolds of potential use for cardiac, neuronal, and muscle tissue engineering [48]. Dvir

et al. [56] first reported 3D hydrogel-inorganic nanoparticle scaffolds that enhanced the structure, phenotype, and function of seeded heart cells using gold nanorods inside an alginate gel (Figure 1.3). The nanorods within the hydrogel formed star-like structures that were thicker than the walls between the hydrogel pores, resulting in enhanced electrical signal transmission throughout the scaffold. Heart cells grown in the presence of an electrical pulse were better aligned and displayed phenotypes associated with improved electrical and contractile properties, with synchronous contraction upon electrical stimulation demonstrated following 8 days of culture [56].

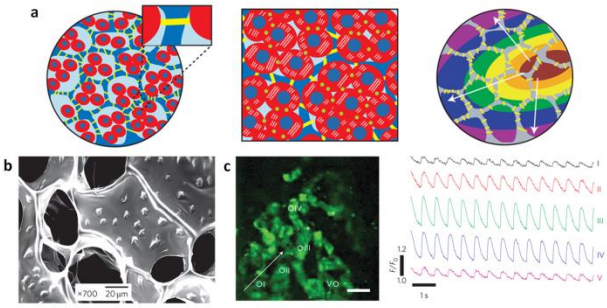

Figure 1.3: Growth of cardiomyocytes in an electrically conductive alginate-Au nanowire scaffold for cardiac patches. a) Mechanism of synchronization of cardiomyocytes (red) across walls of a porous alginate hydrogel scaffold (blue) impregnated with Au nanowires (yellow). b) SEM image of star-shaped Au nanowires embedded in scaffold walls. c) Calcium transients (which indicate muscle cell contractions) at various points 2-3 mm from a local electric stimulus indicate that cardiomyocytes grown in the nanocomposite scaffold contract synchronously in response to electric stimuli, analogous to natural cardiac tissue. [Adapted with permission from [56].]

Gold has a long-standing record of biocompatibility in multiple biological applications [57], with its use in the body dating back centuries. As such, there are quite appropriately many more examples of nanoscale AuNP-gel systems than CNT-gel systems. AuNPs are also simpler to generate and easier to functionalize than CNTs while offering many of the same properties of near-IR absorption and electrical

conductivity. As such, at least in the short term, gold nanocomposite hydrogels have significantly higher probabilities of being translated to the clinic, with some clinical trials involving polymer-coated AuNPs now underway [58]. However, while evidence suggests that gold is biologically quite inert, it cannot be biologically cleared, offering a potential drawback for longer-term chronic therapeutic targets.

1.2.5 SPION-Hydrogel Nanocomposites

The use of magnetic nanoparticles, and in particular superparamagnetic iron oxide nanoparticles (SPIONs), as biomaterials has grown increasingly popular in recent years due to their facile and inexpensive bulk preparation, simple separation and detection, and good record of biocompatibility *in vivo* [59]. In addition, unlike other inorganic nanoparticles, iron-based magnetic nanoparticles can be degraded *in vivo*, exploiting a biotransformation mechanism whereby SPIONs are converted into nontoxic iron species within acidic intracellular lysosomes [60,61]. The superparamagnetic characteristics of SPIONs allow for both site-specific focusing *in vivo* using permanent magnetic fields and the potential to generate heat in the presence of an alternating magnetic field (AMF) via hysteresis losses associated with the relaxation characteristics of SPIONs in response to AMFs (the exact mechanism of this heating is discussed in detail elsewhere [62,63]). These properties have propelled research investigating the use of polymer coated SPIONs for drug delivery, generating contrast in magnetic resonance imaging (MRI), and hyperthermia therapy [64].

SPIONs can be incorporated into hydrogel matrices to form magnetic hydrogels, often termed ferrogels, that can also be used as hyperthermia agents and/or drug delivery devices [65]. SPIONs can be physically entrapped into a hydrogel network, generated *in situ* via precipitation of iron salts, or (as described by Ilg [66]), used as a crosslinker to drive gel formation [67]. When a ferrogel is placed in an AMF, drug release can be enhanced by the physical motion of the SPIONs (typically triggered using lower frequency AMFs); if the hydrogel is thermosensitive, drug release can be driven by this same physical motion mechanism or heat generation by SPIONs (typically using higher frequency AMFs) that drives a phase transition within the hydrogel and, by extension, drug release [68,69].

In most reported SPION-hydrogel composites, SPIONs are physically entrapped within the ferrogel network, limiting their capacity to provide significant mechanical enhancement. Furthermore, most ferrogels are not injectable and would require undesirable surgical implantation for *in vivo* use. We have recently developed an injectable, degradable, highly elastic SPION-hydrogel composite that addresses these limitations (Figure 1.4) [69]. This hydrogel is formed upon injection via a condensation reaction between aldehyde-functionalized dextran and SPIONs functionalized with hydrazide-functionalized PNIPAM. The resulting hydrogel is highly elastic (with elastic moduli > 60 kPa and bulk properties more akin to an elastomer than a hydrogel despite the high water content (> 80%)), both thermally and magnetically responsive, and (via slow hydrolysis of the hydrazone crosslinks) degradable in physiological conditions. The composite was also demonstrated to be biocompatible both *in vitro* and *in vivo* and facilitated pulsatile, “on-demand” release of drugs using an external AMF.

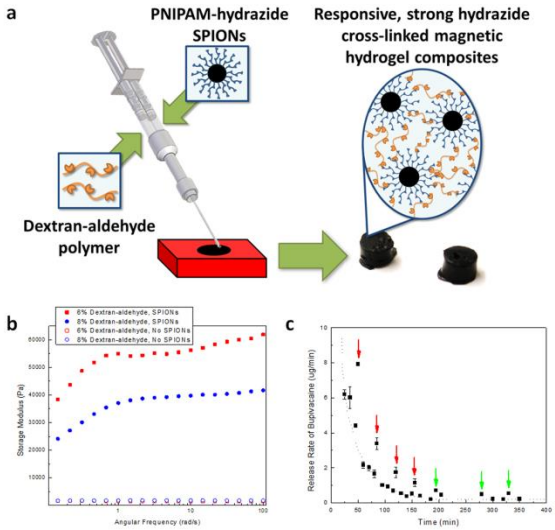

Figure 1.4: Injectable, magnetic, thermosensitive superparamagnetic hydrogels with exceptionally elastic properties. a) Preparation of the SPION-PNIPAM hydrogels via the formation of hydrazone crosslinks between aldehyde-functionalized dextran and hydrazide-functionalized SPION-PNIPAM upon injection. b) Mechanical strengthening effect of SPION incorporation into the hydrogel matrix, showing the elastic modulus with (filled points) and without (hollow points) SPION incorporation. c) Pulsatile release of bupivacaine (a local anaesthetic) from superparamagnetic nanocomposites at 37°C controlled externally via AMF. Enhanced release is seen immediately after both 5 minute AMF pulses and 10 minute AMF pulses (increasing the temperature to 43°C). [Adapted with permission from [69].]

Although mechanically weaker, the macroporous ferrogel reported by Zhao et al. [70] is also of significant interest from a drug delivery perspective; a 70% volume change was observed upon magnetic heating, facilitating excellent triggerable control over drug and cell release over multiple cycles.

The majority of research on ferrogels for biomedical applications involves sub-micron scale nanocomposites, with SPIONs being incorporated into (often thermosensitive) microgel structures or used to create nanoscale composites by forming gels around individual SPIONs or SPION clusters [71,72]. In fact, Paquet et al. [71] showed that

encapsulating clusters of SPIONs in microgel networks enhances the relaxation rate of SPIONs for magnetic resonance imaging (MRI) due to the lower diffusivity of water inside hydrogels. Magnetic microgels can circulate in the bloodstream *in vivo* and can be precisely targeted using magnetic fields, similar to SPIONs themselves. The microgel matrix facilitates improved biocompatibility, prolonged blood circulation times, and improved drug loading and release characteristics relative to SPIONs alone [73]. Of particular interest are the hollow superparamagnetic microgels fabricated via supramolecular assembly by Chiang et al. [74]. The hollow core could be loaded with drug and magnetically guided to tumor cells before being internalized. Drug release is induced at acidic pHs (present in intracellular endosomes and lysosomes [74]) and could be enhanced ~12-fold by AMF application. The particles were cytotoxic against tumor cells via drug release and hyperthermia individually, with further enhanced efficacy in combination. Tissue engineering applications have also been reported exploiting the externally-addressable properties of SPION-microgel composites. For example, Xu et al. [75] encapsulated cells within SPION-microgels and used their magnetism to assemble these microgels into various 3D constructs.

1.2.6 Future Outlook/Challenges

In our view, there are four major materials-related themes for future research in this field that are both scientifically interesting and practically necessary to facilitate translation of hydrogel nanocomposites to clinical applications. First, the development of injectable, degradable, and mechanically strong biocomposites, of which there are still very few reports, is essential to utilize such materials without requiring surgical implantation and

transition the applications of these materials to more biological environments, including applications requiring at least limited load bearing. Second, ongoing advances in engineering inorganic nanoparticles with more complex core-shell morphologies, in many cases facilitating multi-functional responses to applied stimuli, are expected to lead to the generation of novel hydrogel or microgel nanocomposites with “all-in-one” imaging and therapeutic functionality. Third, the production of nanoparticles with novel stimuli responses will permit the generation of new functional biomaterials. For example, recent research on the incorporation of lanthanide-based up-conversion nanoparticles into hydrogels that can absorb near-IR irradiation and release either visible light (useful for imaging) or UV irradiation (useful for *in situ* crosslinking for drug release applications or *in situ* cell killing) represent an attractive new class of materials with largely unexplored biomedical applications [76,77]. Fourth, for pulsatile drug delivery applications, increased enhancements in drug release upon triggering and decreases in baseline (non-triggered) release are required to apply such materials in most practical on-demand drug delivery applications.

However, in our view, the biggest challenge facing this field involves understanding the biological responses to the nanoparticles themselves. This issue of biocompatibility has been the source of a great deal of controversy for many of these nanoparticles due to conflicting toxicity results. Concerns that particles can be released from hydrogels *in vivo*, endocytosed by native cells, and damage local tissues and/or concentrate in organs associated with the lymphatic system (e.g. kidneys, spleen) to cause greater local damage are certainly warranted and have been supported by the work of Pan et al. [78] and Shvedova et al. [79], among others. However, at the same time, many studies have also shown promising *in vitro* and *in vivo* results, particularly as methods for

fabricating, stabilizing, and functionalizing the nanoparticles continue to improve. This has been particularly true for bulk hydrogels, which largely restrict the diffusion of the nanoparticles within in the body prior to gel degradation. Understanding how the particle toxicity is related to the specific properties of the individual nanoparticles (e.g. size, shape, surface chemistry, etc.), coupled with a thorough physicochemical characterization of those particles such that issues with toxicity can be accurately traced back to specific properties, are essential to mitigate these concerns [80]. Furthermore, the development of improved and more systematic methods to synthesize nanoparticles with reproducible and well-defined dimensions, purify those nanoparticles, and subsequently evaluate nanoparticle toxicity based on defined standards is imperative to accurately assess toxicity, understand the reasons for toxicity, and then engineer nanoparticles that mitigate these issues.

1.2.7 Conclusions

Combining nanoparticles with hydrogels on various length scales results in the generation of nanocomposites with several unique and useful physicochemical, mechanical, and biological properties, with interactions between the nanoparticles and hydrogels in some cases generating completely new properties. In particular, the use of nanoparticles to externally address either materials or cells remotely and on-demand *in vivo* offers the potential for higher resolution and longer term cell imaging, temporally-controllable tissue engineering matrix formation, on-demand pulsatile drug delivery, and switchable tissue adhesives, among other applications. We expect future work in developing more stable or multi-functional nanoparticles, coupled with an improved

understanding of the biological responses to those nanoparticles, will lead to future clinical applications of these materials.

1.2.8 Acknowledgements

The authors thank the J.P. Bickell Foundation (Medical Research Grant Program), the Natural Sciences and Engineering Research Council of Canada (NSERC), and the Vanier Canada Graduate Scholarships (CGS) program for funding.

1.2.9 References

[1] Wichterle O, Lim D: **Hydrophilic gels for biological use**. *Nature* 1960, **185**:117–118.

[2] Hoare TR, Kohane DS: **Hydrogels in drug delivery: Progress and challenges.** *Polymer* 2008, **49**:1993–2007.

[3] Fu Y, Kao WJ: **In situ forming poly(ethylene glycol)-based hydrogels via thiol-maleimide Michael-type addition.** *J Biomed Mater Res A* 2011, **98**:201–211.

[4] Park JH, Bae YH: **Hydrogels based on poly(ethylene oxide) and poly(tetramethylene oxide) or poly(dimethyl siloxane): synthesis, characterization, in vitro protein adsorption and platelet adhesion.** *Biomaterials* 2002 **23**:1797–1808.

[5] Gordijo CR, Koulajian K, Shuhendler AJ, Bonifacio LD, Huang HY, Chiang S, Ozin GA, Giacca AA, Wu XY: **Nanotechnology-enabled closed loop insulin delivery device: In vitro and in vivo evaluation of glucose-regulated insulin release for diabetes control.** *Adv Funct Mater* 2011 **21**:73–82.

[6] Verdejo B, Rodríguez-Llansola F, Escuder B, Miravet JF, Ballester P: **Sodium and pH responsive hydrogel formation by the supramolecular system calix[4]pyrrole derivative/tetramethylammonium cation.** *Chem Commun* 2011 **47**:2017–2019.

[7] Patenaude M, Hoare T: **Injectable, degradable thermoresponsive poly(N -isopropylacrylamide) hydrogels.** *ACS Macro Lett* 2012 **1**:409–413.

[8] Tanaka T, Nishio I, Sun S-T, Ueno-Nishio S: **Collapse of gels in an electric field.** *Science* 1982 **218**:467–469.

[9] Pelton R: **Temperature-sensitive aqueous microgels.** *Adv Colloid Interface Sci* 2000 **85**:1–33.

[10] Seliktar D: **Designing cell-compatible hydrogels for biomedical applications.** *Science* 2012 **336**:1124–1128.

[11] Mannoor MS, Jiang Z, James T, Kong YL, Malatesta KA, Soboyejo WO, Verma N, Gracias DH, McAlpine MC: **3D printed bionic ears.** *Nano Lett* 2013 **13**:2634–2639.

[12] Malda J, Visser J, Melchels FP, Jüngst T, Hennink WE, Dhert WJA, Groll J, Hutmacher DW: **25th anniversary article: Engineering hydrogels for biofabrication.** *Adv Mater* 2013 DOI: 10.1002/adma.201302042.

[13] Li H, Yang J, Hu X, Liang J, Fan Y, Zhang X: **Superabsorbent polysaccharide hydrogels based on pullulan derivate as antibacterial release wound dressing.** *J Biomed Mater Res A* 2011 **98**:31–39.

[14] Heilmann S, Küchler S, Wischke C, Lendlein A, Stein C, Schäfer-Korting M: **A thermosensitive morphine-containing hydrogel for the treatment of large-scale skin wounds.** *Int J Pharm* 2013 **444**:96–102.

[15] Zhu C-H, Hai Z-B, Cui C-H, Li H-H, Chen J-F, Yu S-H: **In situ controlled synthesis of thermosensitive poly(N-isopropylacrylamide)/Au nanocomposite hydrogels by gamma radiation for catalytic application.** *Small* 2012 **8**:930–936.

[16] Reddy SM, Phan QT, El-Sharif H, Govada L, Stevenson D, Chayen NE: **Protein crystallization and biosensor applications of hydrogel-based molecularly imprinted polymers.** *Biomacromolecules* 2012 **13**:3959–3965.

[17] Kesselman LRB, Shinwary S, Selvaganapathy PR, Hoare T: **Synthesis of monodisperse, covalently cross-linked, degradable "smart" microgels using microfluidics.** *Small* 2012 **8**:1092–1098.

[18] Chen H, Dai LL: **Adsorption and Release of Active Species into and from Multifunctional Ionic Microgel Particles.** *Langmuir* 2013 **29**:11227–11235.

[19] Hoare T, Pelton R: **Impact of microgel morphology on functionalized microgel-drug interactions.** *Langmuir* 2008 **24**:1005–1012.

[20] Hunt JN, Feldman KE, Lynd NA, Deek J, Campos LM, Spruell JM, Hernandez BM, Kramer EJ, Hawker CJ: **Tunable, high modulus hydrogels driven by ionic coacervation.** *Adv Mater* 2011 **23**:2327–2331.

[21] Krogsgaard M, Behrens MA, Pedersen JS, Birkedal H: **Self-healing mussel-inspired multi-pH-responsive hydrogels.** *Biomacromolecules* 2013 **14**:297–301.

[22] Patenaude M, Hoare T: **Injectable, Mixed Natural-Synthetic Polymer Hydrogels with Modular Properties**. *Biomacromolecules* 2012 **13**:369–378.

[23] Sivakumaran D, Maitland D, Hoare T: **Injectable microgel-hydrogel composites for prolonged small-molecule drug delivery.** *Biomacromolecules* 2011 **12**:4112–4120.

[24] Overstreet DJ, Dutta D, Stabenfeldt SE, Vernon BL: **Injectable hydrogels** *J Polym Sci Part B Polym Phys* 2012 **50**:881–903.

[25] Schexnailder P, Schmidt G: **Nanocomposite polymer hydrogels**. *Colloid Polym Sci* 2008 **287**:1–11.

[26] Hoare T, Santamaria J, Goya GF, Irusta S, Lin D, Lau S, Padera R, Langer R, Kohane DS: **A magnetically triggered composite membrane for on-demand drug delivery.** *Nano Lett* 2009 **9**:3651–3657.

[27] Satarkar NS, Biswal D, Hilt JZ: **Hydrogel nanocomposites: a review of applications as remote controlled biomaterials**. *Soft Matter* 2010 **6**:2364–2371.

[28] Meenach SA, Anderson AA, Suthar M, Anderson KW, Hilt JZ: **Biocompatibility analysis of magnetic hydrogel nanocomposites based on poly(N-isopropylacrylamide) and iron oxide.** *J Biomed Mater Res A* 2009 **91**:903–909.

[29] Liu L, Ma W, Zhang Z: **Macroscopic carbon nanotube assemblies: preparation, properties, and potential applications.** *Small* 2011 **7**:1504–1520.

[30] Cha C, Shin SR, Annabi N, Dokmeci MR, Khademhosseini A: **Carbon-based nanomaterials: Multifunctional materials for biomedical engineering.** *ACS Nano* 2013 **7**:2891–2897.

[31] **Ramón-Azcón J, Ahadian S, Estili M, Liang X, Ostrovidov S, Kaji H, Shiku H, Ramalingam M, Nakajima K, Sakka Y, Khademhosseini A, Matsue T: **Dielectrophoretically aligned carbon nanotubes to control electrical and mechanical properties of hydrogels to fabricate contractile muscle myofibers.** *Adv Mater* 2013 **25**:4028–4034.

- Used dielectrophoresis and UV polymerization to align carbon nanotubes in a gelatin methacrylate hydrogel. The higher conductivity of these hydrogels provided for improved maturation and contractility of myofibres grown on these materials when the cells were electrically stimulated.

[32] Dvir T, Timko BP, Kohane DS, Langer R: **Nanotechnological strategies for engineering complex tissues.** *Nat Nanotechnol* 2011 **6**:13–22.

[33] Yun J, Im JS, Lee Y-S, Kim H-I: **Electro-responsive transdermal drug delivery behavior of PVA/PAA/MWCNT nanofibers**. *Eur Polym J* 2011 **47**:1893–1902.

[34] Im JS, Bai BC, Lee Y-S: **The effect of carbon nanotubes on drug delivery in an electro-sensitive transdermal drug delivery system.** *Biomaterials* 2010 **31**:1414–1419.

[35] *Servant A, Bussy C, Al-Jamal K, Kostarelos K: **Design, engineering and structural integrity of electro-responsive carbon nanotube- based hydrogels for pulsatile drug release.** *J Mater Chem B* 2013 **1**:4593–4600.

- Recently fabricated electrically responsive carbon nanotube-poly(methacrylic acid) hydrogels that showed improved pulsatile release characteristics over blank gels in the presence of an electric field.

[36] Homenick CM, Sheardown H, Adronov A: **Reinforcement of collagen with covalently-functionalized single-walled carbon nanotube crosslinkers.** *J Mater Chem* 2010 **20**:2887–2894.

[37] Chen Y-S, Tsou P-C, Lo J-M, Tsai H-C, Wang Y-Z, Hsiue G-H: **Poly(N-isopropylacrylamide) hydrogels with interpenetrating multiwalled carbon nanotubes for cell sheet engineering.** *Biomaterials* 2013 **34**:7328–7334.

[38] Shin SR, Aghaei-Ghareh-Bolagh B, Dang TT, Topkaya SN, Gao X, Yang SY, Jung SM, Oh JH, Dokmeci MR, Tang XS, Khademhosseini A: **Cell-laden microengineered and mechanically tunable hybrid hydrogels of gelatin and graphene oxide**. *Adv Mater* 2013 DOI: 10.1002/adma.201301082.

[39] Fujigaya T, Morimoto T, Niidome Y, Nakashima N: **NIR laser-driven reversible volume phase transition of single-walled carbon nanotube/poly(N-isopropylacrylamide) composite gels.** *Adv Mater* 2008 **20**:3610–3614.

[40] Wang C, Mallela J, Garapati US, Ravi S, Chinnasamy V, Girard Y, Howell M, Mohapatra S: **A chitosan-modified graphene nanogel for noninvasive controlled drug release.** *Nanomedicine* 2013 **9**:903–911.

[41] **Du R, Wu J, Chen L, Huang H, Zhang X, Zhang J: **Hierarchical hydrogen bonds directed multi-functional carbon nanotube-based supramolecular hydrogels.** *Small* 2013 DOI: 10.1002/smll.201302649.

- Generated thermal, pH, and near-IR-responsive injectable supramolecular carbon nanotube-polyethylene polyamine hydrogels formed by a combination of relatively strong and relatively weak hydrogen bonds. The resulting composites exhibit exceptional (and multiresponsive) self-healing and adhesive characteristics, which could have potential for a variety of biomedical applications.

[42] Poland CA, Duffin R, Kinloch I, Maynard A, Wallace WAH, Seaton A, Stone V, Brown S, MacNee W, Donaldson K: **Carbon nanotubes introduced into the**

abdominal cavity of mice show asbestos-like pathogenicity in a pilot study. *Nat Nanotechnol* 2008 **3**:423–428.

[43] Mutlu GM, Budinger GRS, Green AA, Urich D, Soberanes S, Chiarella SE, Alheid GF, McCrimmon DR, Szleifer I, Hersam MC: **Biocompatible nanoscale dispersion of single-walled carbon nanotubes minimizes in vivo pulmonary toxicity.** *Nano Lett* 2010 **10**:1664–1670.

[44] De Volder MFL, Tawfick SH, Baughman RH, Hart AJ: **Carbon nanotubes: present and future commercial applications.** *Science* 2013 **339**:535–539.

[45] Bianco A, Kostarelos K, Prato M: **Making carbon nanotubes biocompatible and biodegradable.** *Chem Commun* 2011 **47**:10182–10188.

[46] Johnston HJ, Hutchison GR, Christensen FM, Peters S, Hankin S, Aschberger K, Stone V: **A critical review of the biological mechanisms underlying the in vivo and in vitro toxicity of carbon nanotubes: The contribution of physico-chemical characteristics.** *Nanotoxicology* 2010 **4**:207-246.

[47] Gorelikov I, Field LM, Kumacheva E: **Hybrid microgels photoresponsive in the near-infrared spectral range.** *J Am Chem Soc* 2004 **126**:15938–15939.

[48] You J-O, Rafat M, Ye GJC, Auguste DT: **Nanoengineering the heart: conductive scaffolds enhance connexin 43 expression.** *Nano Lett* 2011 **11**:3643–3648.

[49] Timko BP, Dvir T, Kohane DS: **Remotely triggerable drug delivery systems.** *Adv Mater* 2010 **22**:4925–4943.

[50] Jain PK, Lee KS, El-Sayed IH, El-Sayed MA: **Calculated absorption and scattering properties of gold nanoparticles of different size, shape, and composition: Applications in biological imaging and biomedicine.** *J Phys Chem B* 2006 **110**:7238-7248.

[51] Shiotani A, Mori T, Niidome T, Niidome Y, Katayama Y: **Stable incorporation of gold nanorods into N-isopropylacrylamide hydrogels and their rapid shrinkage induced by near-infrared laser irradiation.** *Langmuir* 2007 **23**:4012–4018.

[52] Zhao X, Wang T, Liu W, Wang C, Wang D, Shang T, Shen L-H, Ren L: **Multifunctional Au@IPN-pNIPAAm nanogels for cancer cell imaging and combined chemo-photothermal treatment.** *J Mater Chem* 2011 **21**:7240–7247.

[53] Das M, Sanson N, Fava D, Kumacheva E: **Microgels loaded with gold nanorods: photothermally triggered volume transitions under physiological conditions.** *Langmuir* 2007 **23**:196–201.

[54] Wu W, Zhou T, Berliner A, Banerjee P, Zhou S: **Smart core−shell hybrid nanogels with Ag nanoparticle core for cancer cell imaging and gel shell for pH-regulated drug delivery.** *Chem Mater* 2010 **22**:1966–1976.

[55] *Kojic N, Pritchard EM, Tao H, Brenckle MA, Mondia JP, Panilaitis B, Omenetto F, Kaplan DL: **Focal Infection Treatment using Laser-Mediated Heating of**

Injectable Silk Hydrogels with Gold Nanoparticles. *Adv Funct Mater* 2012 **22**:3793–3798.

- Incorporated gold nanoparticles into a silk hydrogel to produce materials that showed promising bactericidal effects with laser exposure for the treatment of focal infections.

[56] **Dvir T, Timko BP, Brigham MD, Naik SR, Karajanagi SS, Levy O, Jin H, Parker KK, Langer R, Kohane DS: **Nanowired three-dimensional cardiac patches.** *Nat Nanotechnol* 2011 **6**:720–725.

- Bridged the pores of alginate hydrogels with gold nanorods to improve the conductivity and electrical communication between cells during the engineered growth of cardiomyocytes in the development of cardiac patches. Cardiomyocytes grown in these nanocomposites to form engineered cardiac tissue under electrical stimulation showed improved structure, phenotype and function relative to conventional hydrogels.

[57] Khlebtsov N, Dykman L: **Biodistribution and toxicity of engineered gold nanoparticles: a review of in vitro and in vivo studies.** *Chem Soc Rev* 2011 **40**:1647–1671.

[58] Etheridge ML, Campbell SA, Erdman AG, Haynes CL, Wolf SM, McCullough J: **The big picture on nanomedicine: the state of investigational and approved nanomedicine products.** *Nanomedicine* 2013 **9**:1–14.

[59] Mok H, Zhang M: **Superparamagnetic iron oxide nanoparticle-based delivery systems for biotherapeutics.** *Expert Opin Drug Deliv* 2013 **10**:73–87.

[60] Gu J, Xu H, Han Y, Dai W, Hao W, Wang C, Gu N, Xu HY, Cao JM: **The internalization pathway, metabolic fate and biological effect of superparamagnetic iron oxide nanoparticles in the macrophage-like RAW264.7 cell.** *Sci China Life Sci* 2011 **54**:793–805.

[61] Levy M, Luciani N, Alloyeau D, Elgrabli D, Deveaux V, Pechoux C, Chat S, Wang G, Vats N, Gendron F, Factor C, Lotersztajn S, Luciani A, Wilhelm C, Gazeau F: **Long term in vivo biotransformation of iron oxide nanoparticles.** *Biomaterials* 2011 **32**:3988–3999.

[62] Laurent S, Dutz S, Häfeli UO, Mahmoudi M: **Magnetic fluid hyperthermia: Focus on superparamagnetic iron oxide nanoparticles.** *Adv Colloid Interface Sci* 2011 **166**:8–23.

[63] Huber DL: **Synthesis, properties, and applications of iron nanoparticles.** *Small* 2005 **1**:482–501.

[64] Mahmoudi M, Sant S, Wang B, Laurent S, Sen T: S**uperparamagnetic iron oxide nanoparticles (SPIONs): development, surface modification and applications in chemotherapy.** *Adv Drug Deliv Rev* 2011 **63**:24–46.

[65] Meenach SA, Otu CG, Anderson KW, Hilt JZ: **Controlled synergistic delivery of paclitaxel and heat from poly(β-amino ester)/iron oxide-based hydrogel nanocomposites.** *Int J Pharm* 2012 **427**:177–184.

[66] Ilg P: **Stimuli-responsive hydrogels cross-linked by magnetic nanoparticles**. *Soft Matter* 2013 **9**:3465–3468.

[67] Oh JK, Park JM: **Iron oxide-based superparamagnetic polymeric nanomaterials: Design, preparation, and biomedical application.** *Prog Polym Sci* 2011 **36**:168–189.

[68] Brazel CS: **Magnetothermally-responsive nanomaterials: combining magnetic nanostructures and thermally-sensitive polymers for triggered drug release.** *Pharm Res* 2009 ***26*** :644–656.

[69] **Campbell SB, Patenaude M, Hoare T. **Injectable superparamagnets: Highly elastic and degradable poly(N-isopropylacrylamide)-superparamagnetic iron oxide nanoparticle (SPION) composite hydrogels.** *Biomacromolecules* 2013 **14**:644–653.

- Fabricated injectable, magnetic, thermosensitive superparamagnetic hydrogels using hydrolytically degradable hydrazone crosslinks between between aldehyde-functionalized dextran and hydrazide-functionalized SPION-PNIPAM. The magnetic hydrogels are highly versatile for a range of biomedical applications, showing exceptional elastic properties ($G' > 60$ kPa) despite their high water content, no significant cytotoxic nor adverse effects *in vivo*, and are capable of facilitating pulsatile, “on-demand” changes in drug release controlled by an alternating magnetic field.

[70] Zhao X, Kim J, Cezar CA, Huebsch N, Lee K, Bouhadir K, Mooney DJ: **Active scaffolds for on-demand drug and cell delivery.** *Proc Natl Acad Sci U.S.A.* 2011 **108**:67–72.

[71] Paquet C, de Haan HW, Leek DM, Lin H-Y, Xiang B, Tian G, Kell A, Simard B: **Clusters of superparamagnetic iron oxide nanoparticles encapsulated in a hydrogel: a particle architecture generating a synergistic enhancement of the T2 relaxation.** *ACS Nano* 2011 **5**:3104–3112.

[72] Key J, Aryal S, Gentile F, Ananta JS, Zhong M, Landis MD, Decuzzi P: **Engineering discoidal polymeric nanoconstructs with enhanced magneto-optical properties for tumor imaging.** *Biomaterials* 2013 **34**:5402–10.

[73] Karmali PP, Chao Y, Park J-H, Sailor MJ, Ruoslahti E, Esener SC, Simberg D: **Different effect of hydrogelation on antifouling and circulation properties of dextran-iron oxide nanoparticles.** *Mol Pharm* 2012 **9**:539–545.

[74] **Chiang W-H, Ho VT, Chen H-H, Huang W-C, Huang Y-F, Lin S-C, Chern C-S, Chiu H-C: **Superparamagnetic hollow hybrid nanogels as a potential guidable vehicle system of stimuli-mediated MR imaging and multiple cancer therapeutics.** *Langmuir* 2013 **29**:6434–6443.

- Produced intricate hollow, magnetically guidable nanogels of SPIONs in a pH-responsive polyacrylic acid/poly(N-isopropyl acrylamide) shell stabilized by monomethoxy-PEG segments. These nanoparticles that could be used for hyperthermia, controlled drug release, cellular uptake,

and as MRI contrast agents, with drug release and hyperthermia shown to synergistically improve *in vivo k*illing of cancerous HeLa cells.

[75] Xu F, Wu C-AM, Rengarajan V, Finley TD, Keles HO, Sung Y, Li B, Gurkan UA, Demirci U: **Three-dimensional magnetic assembly of microscale hydrogels.** *Adv Mater* 2011 **23**:4254–4260.

[76] *Dai Y, Ma P, Cheng X, Kang X, Zhang X, Hou Z, Li C, Yang D, Zhai X, Lin J: **Up-conversion cell imaging and pH-induced thermally controlled drug release from $NaYF_4$:Yb^{3+}/Er^{3+}@Hydrogel core-shell hybrid microspheres.** *ACS Nano* 2012 **6**:3327–3338.

- Developed hybrid microspheres of up-conversion nanoparticles coated in a poly(N-isopropyl acrylamide-co-N-hydroxymethyl acrylamide) shell that could be used for cellular imaging and IR-laser-induced and pH-induced drug release. This work represents an example of an emerging trend in hydrogel-based nanocomposite materials in terms of using novel, complex nanoparticles with unique, well defined properties to fabricate new classes of materials with largely unexplored biomedical applications.

[77] Yan B, Boyer J-C, Habault D, Branda NR, Zhao Y: **Near infrared light triggered release of biomacromolecules from hydrogels loaded with upconversion nanoparticles.** *J Am Chem Soc* 2012 **134**:16558–16561.

[78] Pan Y, Leifert A, Ruau D, Neuss S, Bornemann J, Schmid G, Brandau W, Simon U, Jahnen-Dechent W: **Gold nanoparticles of diameter 1.4 nm trigger**

necrosis by oxidative stress and mitochondrial damage. *Small* 2009 **5**:2067–2076.

[79] Shvedova AA, Kagan VE, Fadeel B: **Close encounters of the small kind: adverse effects of man-made materials interfacing with the nano-cosmos of biological systems.** *Annu Rev Pharmacol Toxicol* 2010 **50**:63–88.

[80] D.B. Warheit: **How meaningful are the Results of nanotoxicity studies in the absence of adequate material characterization?** *Toxicol Sci* 2008 **101**:183–185.

1.3 Update on current trends in SPION-hydrogel nanocomposites for drug delivery

Ever since pulsatile release from hydrogel nanocomposites was first demonstrated in the mid-1980s, the field of externally-mediated drug delivery has slowly but steadily grown as the understanding of polymer and materials science advanced to where they are today.[1] These advancements have afforded ample tools that have led to a burst of activity in the development of novel triggerable drug releasing systems, a field still very much in its infancy, in recent years. This can also be attributed to the realization that the periodic delivery of therapeutics, termed chronopharmaceutical drug delivery, can be highly beneficial for a multitude of treatments.[2] For example, improved biological responses have been shown to be observed for the pulsatile delivery of hormones, allergen treatments, chemotherapeutics, and vaccines, as well as for nitroglycerin and opiates, which lose efficacy if delivered passively.[2–5] Despite this knowledge, these treatments are still clinically performed via passive drug delivery systems that have predetermined release rates that are independent of changing physiological circumstances or patient needs.[6] Once such systems are implanted/injected into the body they are completely beyond the control of health professionals and the patient. This gap between what is known to be a worthier treatment method and the current state of clinical therapies presents as a significant market opportunity in the development of triggerable release systems. Consequently, there has been a plethora of research investigating triggerable release systems, as evidenced by the number of review articles in the area since my own previous review,[1,7–11] including a couple excellent publications by Merino et al. and Hauser et al.[1,7]

In these last few years, the amount of research regarding the use of carbon nanotubes within remotely triggerable nanomaterials has waned as the health concerns associated with these materials have grown over time. Many of the research groups formerly investigating these materials seem to have transitioned to graphene oxide sheets, which also respond to remote NIR sources.[12,13] In fact, the majority of the research associated with externally-triggered release revolves around NIR-thermally actuated systems with a focus on gold nanomaterials, as shown in a splendid reviews by and Timko et al. and Tong and Kohane.[5,14,15] For example, Timko et al. have recently developed a system analogous to that of Hoare et al.,[16] except the triggerable membrane containing microgels also contained gold nanoshells instead of superparamagnetic iron oxide nanoparticles (SPIONs).[6] The resulting systems possessed dramatic changes in release in response to a 570 mW/cm^2 near-infrared (NIR) light source with 30 minute dosing cycles, with a ratio of release rates between the on- and off- states of NIR-actuated release of 30 with good reproducibility.[6]

An alternative NIR-triggerable material to gold nanoparticles was recently reported by Wang et al.[17] This involves a degradable supramolecular hydrogel nanocomposite made from an alpha-cyclodextrin and poly(ethylene glycol) (PEG)-modified dendrimer hydrogel encapsulating platinum nanoparticles. The platinum nanoparticles acted as a photothermal agent that encouraged the degradation of the hydrogel upon NIR exposure and allowed for enhanced drug release with NIR exposure.[17] Light has also been used in non-traditional activation strategies to affect controlled release. For example, in a switch of common approaches for SPION-associated triggered release, PNIPAM hydrogel beads that are intended to work within transdermal patches were embedded with SPIONs were shown to be heated by visible light.[18] SPIONs are routinely actuated

by AMF, but in this case visible light was absorbed by the SPIONs, which, in turn, generated heat that was used to control dexamethasone release remotely and the rate of release could be facilely controlled by altering the intensity of light.

Magnetism is the next most common actuation method of release. Both static and alternating magnetic fields can be used to improve the efficacy of drug release from hydrogel nanocomposites. Both strategies primarily utilize superparamagnetic iron oxide nanoparticles (SPIONs), which are 5-20 nm nanoparticles that have enhanced magnetic properties that provide biomaterials with targeting, imaging and tracking properties, and the capacity to be used as triggers for drug release.[19] These particles are also generally considered more biocompatible than alternative inorganic nanoparticles and can be degraded to nontoxic iron species *in vivo* (indeed, they have been FDA-approved for iron deficiency treatment[1]).[20,21] Static magnetic fields are typically used to target magnetic particles to specific locations in vivo, however they can be utilized to control drug release as well. Static fields have been used to localize a chitosan/β-glycerophosphate hydrogel composite with 0.6 w/v% SPIONs to specific locations in the bladder to effectively treat bladder cancer.[22] Cezar et al. recently developed biphasic magnetic hydrogels that greatly deform due to a static magnetic field (a 1 Hz field for 2 minutes), and this deformation was shown to effectively release significant bursts of mitoxantrone and even cells.[23]

Several SPION-loaded hydrogel nanocomposites have been fabricated in the past couple years with varying degrees of success in terms of their capacity for remotely-actuated drug release, both on the macroscale and in bead form.[1,24–26] However, one of the more interesting and promising materials are SPION-loaded, degradable

poly(organophosphazene) microgels that are coated in PEG and $_{L}$-isoleucine ethyl ester. These microgels, developed by Zhang and Song, form a bulk hydrogel upon injection, similar to the sol-gel transition of thermogelling polymers.[27] The concentration of SPIONs throughout the gel is known, allowing for effective, consistent remotely-actuated hyperthermia and potential concurrent drug release. The injected materials were shown to be effective at reducing tumour volume via hyperthermia alone, as shown in Figure 1.5, so adding localized chemotherapeutic delivery to this treatment (which is their stated next step towards clinical trials) should prove even more intriguing.[27]

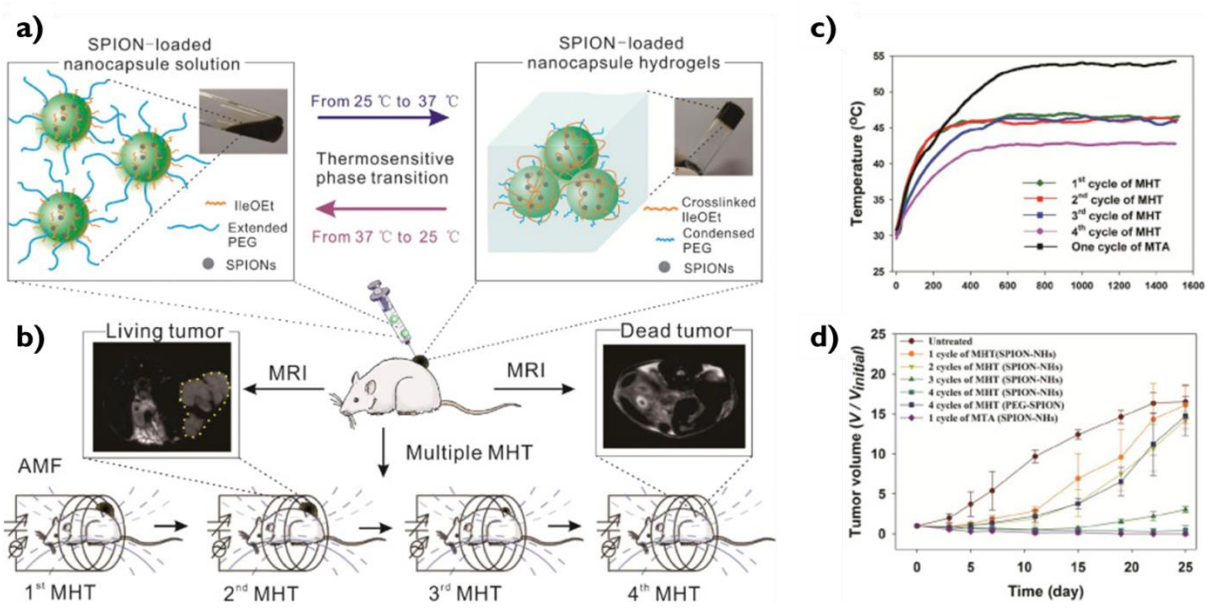

Figure 1.5: (a) Schematic of the composition of the SPION-loaded microgel particles and their thermosensitive sol-gel transition as the extended PEG chains collapse at higher temperatures and the $_{L}$-isoleucine ethyl ester components form physical junctions that result in a hydrogel that is localized in the region of injection. (b) The use of SPIONs *in vivo*, both acting as MRI contrast agents and the agents responsible for heating during single, or multiple magnetic hyperthermia treatments (MHTs). (c) Heating of the SPION-microgels for multiple MTHs (heating to 39-45°C) and magnetic thermal ablation (MTA, heating >45°C) with an AMF. (d) Therapeutic outcomes for *in vivo* studies on tumour xenografted mice with multiple MTHs or MTA via AMF. Adapted with permission from [27].

In what seems to be a new approach to the design of a remote actuation system, iron nanowires (FeNWs) have recently been combined with thermoresponsive materials to externally control drug release. Yassine et al. actually incorporated FeNWs (500 nm x 45 nm) into PNIPAM beads within a microfluidic chip and demonstrated enhanced release of Rhodamine B due to an AMF operating at 20 kHz, a much lower frequency than that required to activate SPIONs.[28] This lower frequency can produce similar amounts of heat as SPIONs in a AMF operating at 200 – 450 kHz, as the heat generated in response to the AMF is due to friction in the case of FeNWs instead of via magnetic losses (Néel and Brownian relaxation).[28] This difference in required operating frequencies relates to 5 times less power being used to generate the same amount of heat and means that simpler and inexpensive equipment can be used to generate the required amount of heat. FeNWs derived naturally from bacteria were loaded with doxorubicin and entrapped in hydrogels by Kumeria et al.[29] An AMF was applied to simulate concurrent hyperthermia/chemotherapy, with the doxorubicin release rate ~2 times larger upon to 30-45 minute pulses relative to the baseline release.

In an interesting twist to conventional uses of gold nanoparticles, gold nanoparticle films have also recently been embedded in PNIPAM hydrogels and used to generate heat to release doxorubicin using an AMF operating under normal conditions (similar to what would be used for thermogenesis with SPIONs).[30] This is the first example of thermogenesis of non-magnetic particles in an AMF, where the heat produced via eddy-current heating, which relies on the collective conductivity of the supra-structure of spherical gold nanoparticles arranged in a film. The justification for using this method was that gold nanoparticles are commonly shown good biocompatibility, the fabrication method was facile (using layer-by-layer techniques), and the penetration depth of near-

infrared systems needs to be improved to be effective on a large scale and be used in large animals; AMFs, which have unlimited penetration depth, are an obvious candidate in this regard.[14,30]

Other interesting strategies of externally-triggered, pulsatile delivery are also being investigated that do not involve hydrogels but could prove to ultimately be commercialized in the future. Nuxoll et al. have developed a membrane-based system based on alternating layers of drug depots and degradable polyvinyl alcohol (PVA) barriers, with the barriers designed to degrade and release a bolus of drug in the depot layers every 4 – 24 hours.[3] This system does, however, require surgical implantation, and the therapeutic release is predetermined and thus beyond the control of health professionals and the patient following implantation. In a method that utilizes the properties of inherently non-photoresponsive polymers, Viger et al. developed electrosprayed dense PLGA particles that contain drug and can be hydrated to contain water pockets that can release drug in response to laser light.[31] This laser light is specifically chosen to be resonant with the vibrational absorption of water in the near-IR region (980 nm) and is used so that the confined water pockets absorb the energy from the laser and generate heat that cannot be rapidly dissipated as they are tightly confined within the polymer matrix. Ultimately, this excitation energy is transferred to the polymer matrix, inducing a phase change as the temperature of the polymer matrix exceeds its glass transition temperature (T_g) and encouraging drug release. The ratio of the release rates of fluorescein from the polymer particles between the on- and off-states of the laser application up to a remarkable 25:1 in this case.[31] This type of work opens the door to release from heating thermoplastic polymers that reversibly transition (at a glass

transition temperature) from brittle states that oppose drug diffusion to a rubbery, amorphous state that promotes drug release.

There are only a couple of other examples of using the melting point (T_m) or T_g of polymers to remotely activate drug release. Müller et al. recently developed bio-based, hydrophobic dextran ester derivatives that had defined melting points. When magnetic nanoparticles were integrated into the polymer, the resulting composite showed well-defined drug release in response to an external AMF.[32] Rovers et al. have demonstrated the use of the glass transition to drive on-demand release[33], using an implantable polymer with a poly(methyl methacrylate) p(MMA)-co-SPION core and a poly(butyl methacrylate(BMA)-co-MMA) shell that can be tuned to have a specific T_g (Figure 1.6). The resulting cylindrical implant (10 mm L x 3 mm D) was shown to have significantly greater release rates of ibuprofen when exposed to an AMF for a brief period of time, as the shell can allow for much larger rates of diffusion in the rubbery, amorphous state.[33] However, given the tunable proximity of polymer T_g values to physiological temperatures coupled with the proven record of tissue compatibility of the pMMA/pBMA polymers such T_g-responsive materials can be based on, it seems clear that there is significant potential in further exploring the use of the T_g of polymers to initiate externally-mediated, on-demand release.

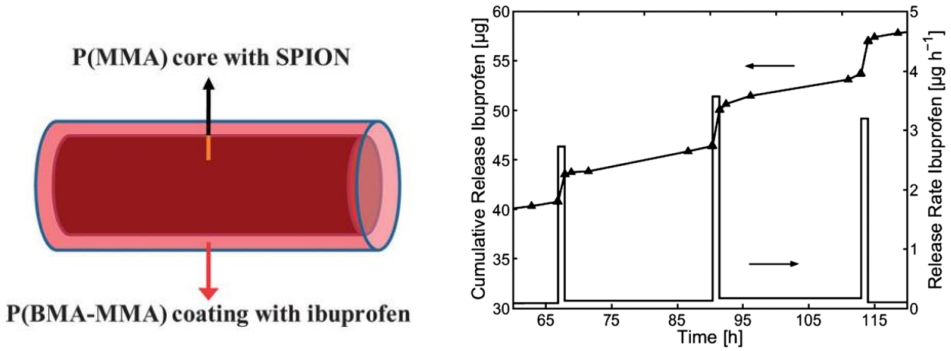

Figure 1.6: Schematic of the core-shell implant design (left) and the on-demand release from a composite with 5 wt% ibuprofen and 50% SPIONs in a bath at room temperature with periodic 1 hour AMF exposures (right). Adapted with permission from [33].

A common theme of the aforementioned release systems is that the majority of them are not injectable and have to be surgically implanted in the body. Improving the ease of administration would be highly important to minimize time and cost of treatment, as well as to improve patient compliance and well-being. Furthermore, the use of hydrogels, which currently have several biomedical applications[34] and are physiochemically similar to soft tissues (resulting typically in lower cytotoxicities and immune responses in comparison to many alternative biomaterials),[35] would also be a suitable material choice for the development of novel biomaterials.

Thus, using injectable hydrogel composites that contain a material that can undergo a phase transition and another material that can produce energy in response to an external stimulus and transfer that energy to the phase change material present as a plausible niche to explore to produce novel on-demand, externally triggerable 'smart' release systems.

1.3.1 References

1 A. K. Hauser, R. J. Wydra, N. A. Stocke, K. W. Anderson and J. Z. Hilt, *J. Control. Release*, 2015, **219**, 76–94.

2 B. C. Youan, *Adv. Drug Deliv. Rev.*, 2010, **62**, 898–903.

3 S. Gandhi, M. D. Gosse, Y. Nishii and E. Nuxoll, *J. Memb. Sci.*, 2015, **495**, 351–360.

4 R. Tong, H. D. Hemmati, R. Langer and D. S. Kohane, *J. Am. Chem. Soc.*, 2012, **134**, 8848–55.

5 B. P. Timko, T. Dvir and D. S. Kohane, *Adv. Mater.*, 2010, **22**, 4925–43.

6 B. P. Timko, M. Arruebo, S. Shankarappa, J. B. McAlvin, O. S. Okonkwo, B. Mizrahi, C. F. Stefanescu, L. Gomez, J. Zhu, A. Zhu, J. Santamaria, R. Langer and D. S. Kohane, *Proc. Natl. Acad. Sci.*, 2014, **111**, 1349–54.

7 S. Merino, C. Martin, K. Kostarelos, M. Prato and E. Vazquez, *ACS Nano*, 2015, 4686–4697.

8 Q. Vinh, D. Phu, J. Hyung and D. Sung, *Eur. Polym. J.*, 2015, **72**, 602–619.

9 J. Zhang, Q. Huang and J. Du, *Polym. Int.*, 2016, **65**, 1365-1372.

10 J. Liu, C. Detrembleur, C. Je and E. Duguet, *J. Mater. Chem. B*, 2015, **3**, 6117–6147.

11 Y. Brudno and D. J. Mooney, *J. Control. Release*, 2015, **219**, 8–17.

12 J. Wu, A. Chen, M. Qin, R. Huang, G. Zhang, B. Xue, J. Wei, Y. Li, Y. Cao and W. Wang, 2015, 1655–1660.

13 K. Yang, L. Feng and Z. Liu, *Adv. Drug Deliv. Rev.*, 2016, **105**, 228–241.

14 R. Tong and D. S. Kohane, *WIREs Nanomed Nanobiotechnol*, 2012, **4**, 638–662.

15 R. Tong and D. S. Kohane, *Annu. Rev. Pharmacol. Toxicol.*, 2016, **56**, 41–57.

16 T. Hoare, B. P. Timko, J. Santamaria, G. F. Goya, S. Irusta, S. Lau, C. F. Stefanescu, D. Lin, R. Langer and D. S. Kohane, *Nano Lett.*, 2011, **11**, 1395–400.

17 X. Wang, C. Wang, Q. Zhang and Y. Cheng, *Chem. Commun.*, 2015, **52**, 978–981.

18 H. Kim, H. Lee, K. Seong, E. Lee and S. Y. Yang, *Adv. Healthc. Mater.*, 2015, **4**, 2071–2077.

19 O. Veiseh, B. C. Tang, K. A. Whitehead, D. G. Anderson and R. Langer, *Nat. Rev. Drug Discov.*, 2014, **14**, 45–57.

20 J. Gu, H. Xu, Y. Han, W. Dai, W. Hao, C. Wang, N. Gu, H. Xu and J. Cao, *Sci. China. Life Sci.*, 2011, **54**, 793–805.

21 M. Levy, N. Luciani, D. Alloyeau, D. Elgrabli, V. Deveaux, C. Pechoux, S. Chat, G. Wang, N. Vats, F. Gendron, C. Factor, S. Lotersztajn, A. Luciani, C. Wilhelm and F. Gazeau, *Biomaterials*, 2011, **32**, 3988–99.

22 D. Zhang, P. Sun, P. Li, A. Xue, X. Zhang, H. Zhang and X. Jin, *Biomaterials*, 2013, **34**, 10258–10266.

23 C. A. Cezar, S. M. Kennedy, M. Mehta, J. C. Weaver, L. Gu, H. Vandenburgh and D. J. Mooney, *Adv. Healthc. Mater.*, 2014, **3**, 1869–1876.

24 A. Teleki, F. L. Haufe, A. M. Hirt, E. Pratsinis and G. A. Sotiriou, *RSC Adv.*, 2016, **6**, 21503–21510.

25 J. Lee, R. Ivkov and R. Blumenthal, *J. Nanomedine. Biotherapeutic Discov.*, 2014, **4**: 130. doi:10.4172/2155-983X.100013.

26 N. Rodkate and M. Rutnakornpituk, *Carbohydr. Polym.*, 2016, **151**, 251–259.

27 Z. Zhang and S. Song, *Biomaterials*, 2016, **106**, 13–23.

28 O. Yassine, A. Zah, E. Q. Li, A. Alfadhel and J. E. Perez, *Sci. Rep.*, 2016, **6**: 28539, doi:10.1038/srep28539.

29 T. Kumeria, S. Maher, Y. Wang, G. Kaur, L. Wang, M. Erkelens, P. Forward, M. F. Lambert, A. Evdokiou and D. Losic, *Biomacromolecules*, 2016, **17**, 2726–2736.

30 P. Wang, J. Sun, Z. Lou, F. Fan, K. Hu, Y. Sun and N. Gu, *Adv. Mater.*, 2016, doi: 10.1002/adma.201603632.

31 M. L. Viger, W. Sheng, K. Doré, A. H. Alhasan, C.-J. Carling, J. Lux, C. de Gracia Lux, M. Grossman, R. Malinow and A. Almutairi, *ACS Nano*, 2014, **8**, 4815–4826.

32 R. Müller, M. Zhou, A. Dellith, T. Liebert and T. Heinze, *J. Magn. Magn. Mater.*, 2016, http://dx.doi.org/10.1016/j.jmmm.2016.09.031.

33 S. A. Rovers, R. Hoogenboom, M. F. Kemmere and J. T. F. Keurentjes, *Soft Matter*, 2012, **8**, 1623–1627.

34 E. Caló and V. V Khutoryanskiy, *Eur. Polym. J.*, 2015, **65**, 252–267.

35 R. Pelton, *Adv. Colloid Interface Sci.*, 2000, **85**, 1–33.

1.4 Objectives

The successful development of devices capable of chronopharmaceutical delivery, where the rate of drug release is precisely controlled, could significantly improve a wide range of therapies.[1] It has recently come to light that tightly controlled chronopharmaceutical delivery could improve the treatment of not only diseases that are rather obvious candidates for improved therapies with precisely controlled release kinetics (such as insulin for diabetes, opiates for chronic pain treatments, and hormones), but also numerous others that are currently treated with passive release systems (such as allergens, vaccines, chemotherapeutic agents, etc.).[1,2] Such treatments could also be personalized to the patient and adaptable to their needs post-administration. Thus, the market potential of devices that could achieve chronopharmaceutical delivery of a broad variety of therapeutics is immense. Despite this knowledge, the vast majority of current therapies and current drug delivery research is focussed on passive-release systems that are beyond the control of health professionals and/or patients and are not adaptable to changing physiological circumstances and patient needs after their administration.[3]

The MicroCHIPS device initially developed in the Langer Lab is the currently the gold standard in the field of chronopharmaceutical delivery. These devices are undergoing clinical trials for the remotely triggered delivery of drugs to treat osteoporosis via wireless electrical signals sent to an implanted, localized MicroCHIPS device (roughly 5 cm x 3 cm x 1 cm in size).[4] While this type of system is extremely promising, these devices, along with several alternate promising devices,[5–7] are not injectable or degradable, and thus require both surgical implantation and removal. If similar control over release

kinetics could be achieved by a localized system that is both injectable and degradable, invasive surgical procedures could be avoided and patient compliance and quality of life could be further improved.

My approach focussed on developing injectable systems capable of the remotely triggerable release profiles associated with chronopharmaceutical release systems by utilizing the existing technologies and expertise of our lab and extending this knowledge to the area of externally-controlled, chronopharmaceutical drug release. The hydrogels that were developed by Mathew Patenaude were an obvious material to use, as they are injectable, degradable and highly adjustable properties.[8,9] These injectable hydrogels are generated from one polymer functionalized with hydrazide functionality interacting with another polymer with hydrazide functionality, resulting in a hydrogel with covalent, hydrolytically degradable hydrazone crosslinks. Heilshorn et al. coined the term 'mixing induced two-component hydrogel' (MITCH) for this type of hydrogel system.[10] These hydrazone MITCH-type hydrogels can be composed out of a variety of different polymers, including the thermosensitive polymer poly(N-isopropyl acrylamide) (PNIPAM), which can be used as the thermosensitive polymeric component to a nanocomposite drug-eluting system. Another potential thermosensitive polymeric component that can be used for smart, externally addressable systems are PNIPAM-based microgels, which were Todd Hoare's focus during his PhD and could be used for nanoscale externally controllable systems.[11,12] These materials also experience possess a VPTT that can be employed to mediate drug release. Another potential thermosensitive polymeric system is latexes that possess a glass transition temperature T_g, which I generated during my undergraduate thesis work.[13] The transition from a solid

and glassy state to a rubbery and amorphous state upon heating above the T_g of the material can be exploited to mediate drug release.

Any of these thermosensitive materials could be combined with an inorganic particle capable of generating heat in response to an external stimulus, which were discussed in depth in the previous section. SPIONS were chosen for our application not only because they were previously used by Todd Hoare in his post-doctorate work,[5] but also because, as previously mentioned, they are one of the least toxic thermogenerating inorganic nanoparticles and they produce heat in response to AMFs, which can penetrate into deep tissues.[14,15] Importantly these SPIONs can be facilely incorporated within thermosensitive latex particles, hydrogels, and microgels. Thus, this work revolves around the combination of SPIONs with thermosensitive polymeric components to development novel 'smart' materials that are capable of externally-triggered drug release, transitioning from macroscale hydrogel systems to nanoscale microgel and latex particle systems.

Chapter 2 is based on injectable superparamagnetic hydrogels fabricated by PNIPAM-ADH-functionalized SPIONs gelling with dextran-aldehyde that largely focussed on developing unique nanocomposite materials and analyzing their surprising mechanical and physical characteristics. These nanocomposites are also tested for their capacity for AMF-mediated drug release, along with their potential to be used as biomaterials in *in vitro* and *in vivo* experiments.

Chapter 3 involves injectable hydrogels with entrapped thermosensitive, PNIPAM-based microgels and SPIONs with them and focusses on the determination of the actual drug release mechanism from these systems due to AMF applications. These experiments

focus on the release characteristics from these systems with continuous and pulsed AMF applications to elucidate a probable release mechanism.

Chapter 4 explores our attempts to improve/further understand the degree of enhanced release from the same microgel-SPION-hydrogel nanocomposite systems. Various characteristics of the nanocomposites and AMF application process, such as the microgel volume phase transition temperature (VPTT), microgel content, hydrogel swelling characteristics and the duration of the AMF pulse, were altered to observe their effect on the ratio in release rate between having the AMF in the on- versus off-state.

Chapter 5 can be seen as the transition from micro- to nano-scale materials. This chapter involves the development of the microinjection device for ophthalmic delivery of our *in-situ* gelling MITCH-type hydrogel materials. The hydrogels injected from these devices are essentially large microgels (in the millimeter size range), and could ultimately be used to deliver magnetic, SPION-containing gels to the eye or other regions of the body for magnetic targeting or magnetically-actuated release.

Chapter 6 investigates the potential of magnetic thermosensitive poly(N-isopropyl methacrylamide (PNIPMAM)-co-acetoacetoxyethyl methacrylate (AAEM)) microgels for AMF-actuated drug release. The microgels are initially prepared via precipitation polymerization and then the SPIONs are coprecipitated in the presence of the microgels, allowing the SPIONs to coordinate with the AAEM within the microgels. This project is the first to show any sort of enhanced release from microgels with an AMF application.

Chapter 7 presents latex particles where a T_g-controlled release mechanism is used to allow for AMF-triggered drug release. These particles are entrapped with the MITCH-

type hydrazone-crosslinked hydrogel systems along with SPIONs for remote controlled release experiments. This is the first example of nanoscale latex particles being used for T_g-mediated release.

Chapter 8 offers as a brief discussion on this work as a whole, including its potential future significance in the field of remotely controlled therapeutic delivery.

1.4.1 References

1 B. C. Youan, *Adv. Drug Deliv. Rev.*, 2010, **62**, 898–903.

2 J. Kost and R. Langer, *Adv. Drug Deliv. Rev.*, 2012, **64**, 327–341.

3 B. P. Timko, T. Dvir and D. S. Kohane, *Adv. Mater.*, 2010, **22**, 4925–43.

4 R. Farra, N. F. S. Jr, L. Mccabe, R. M. Neer, J. M. Anderson, J. T. S. Jr, M. J. Cima and R. Langer, *Sci. Transl. Med.*, 2012, **4**, 122ra121, doi:10.1126/scitranslmed.3003276.

5 T. Hoare, B. P. Timko, J. Santamaria, G. F. Goya, S. Irusta, S. Lau, C. F. Stefanescu, D. Lin, R. Langer and D. S. Kohane, *Nano Lett.*, 2011, **11**, 1395–400.

6 B. P. Timko, M. Arruebo, S. a Shankarappa, J. B. McAlvin, O. S. Okonkwo, B. Mizrahi, C. F. Stefanescu, L. Gomez, J. Zhu, A. Zhu, J. Santamaria, R. Langer and D. S. Kohane, *Proc. Natl. Acad. Sci.*, 2014, **111**, 1349–54.

7 S. A. Rovers, R. Hoogenboom, M. F. Kemmere and J. T. F. Keurentjes, *Soft Matter*, 2012, **8**, 1623–1627.

8 M. Patenaude and T. Hoare, *ACS Macro Lett.*, 2012, **1**, 409–413.

9 M. Patenaude and T. Hoare, *Biomacromolecules*, 2012, **13**, 369–378.

10 C. T. S. Wong, P. Foo, J. Seok, W. Mulyasasmita, A. Parisi-Amon and S. C. Heilshorn, *Proc. Natl. Acad. Sci.*, 2009, **106**, 22067–22072.

11 R. Pelton, *Adv. Colloid Interface Sci.*, 2000, **85**, 1–33.

12 T. Hoare and R. Pelton, *Langmuir*, 2008, **24**, 1005–12.

13 S. B. Campbell, T. Larson, N. M. B. Smeets, U. El-Jaby and T. F. L. McKenna, *Chem. Eng. J.*, 2012, **183**, 534–541.

14 J. Gu, H. Xu, Y. Han, W. Dai, W. Hao, C. Wang, N. Gu, H. Xu and J. Cao, *Sci. China. Life Sci.*, 2011, **54**, 793–805.

15 R. Tong and D. S. Kohane, *WIREs Nanomed Nanobiotechnol*, 2012, **4**, 638–662.

Chapter 2: Superparamagnetic Hydrogels

2.1 Preface

This paper describes injectable superparamagnetic hydrogels that we fabricated by functionalizing or coating SPIONs with hydrazide-functionalized PNIPAM and gelling these SPIONs with dextran-aldehyde to generate a hydrogel nanocomposite with SPIONs directly incorporated into the network structure. As a result, these nanocomposite materials had remarkable mechanical and physical characteristics (G' > 60 kPa), exhibited low toxicity *in vitro*, and actually appeared to act as tissue adhesives *in vivo*. These magnetic nanocomposites were also assessed for their capacity for AMF-mediated drug release, where the release rate was found to be ~2.6:1 when the AMF was in the on- versus off-state.

2.2 Injectable superparamagnets: Highly elastic and degradable poly(N-isopropylacrylamide)-superparamagnetic iron oxide nanoparticle (SPION) composite hydrogels

Campbell, S.B., Patenaude, M., and Hoare, T. *Biomacromolecules*, **2013**, *14*(3), 644-653.

2.2.1 Abstract

Injectable, *in situ*-gelling magnetic composite materials have been fabricated by using aldehyde-functionalized dextran to cross-link superparamagnetic nanoparticles surface-functionalized with hydrazide-functionalized poly(N-isopropylacrylamide) (pNIPAM). The resulting composites exhibit high water contents (82-88 wt.%) while also displaying significantly higher elasticities (G' >60 kPa) than other injectable hydrogels previously reported. The composites hydrolytically degrade *via* slow hydrolysis of the hydrazone cross-links at physiological temperature and pH into degradation products that show no significant cytotoxicity. Subcutaneous injections indicate only minor chronic inflammation associated with material degradation, with no fibrous capsule formation evident. Drug release experiments indicate the potential of these materials to facilitate pulsatile, "on-demand" changes in drug release upon the application of an external oscillating magnetic field. The injectability of these high-strength and externally-triggerable materials, coupled with their biological degradability and inertness, suggest potential biological applications in tissue engineering and drug delivery.

Keywords: superparamagnetic nanoparticles, hydrogels, *in situ* gelation, injectable materials, composite materials

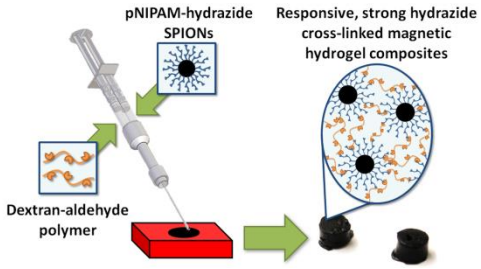

2.2.2 Introduction

Hydrogel-based composites have received a great deal of recent attention as potential materials for tissue engineering[1,2], wound-healing[3,4], catalysis[5,6], biosensors[7,8], and in drug delivery systems[9–12]. Such applications arise from the fact that hydrogels themselves are mechanically and physically similar to the extracellular matrix of soft tissues, have high void fractions for diffusion, and have highly tunable properties.[9] Hydrogels that are capable of swelling and deswelling in response to external stimuli, such as pH, ionic strength, temperature or electric field, offer additional advantages in the design of "on-demand" drug delivery systems that can be switched on and off based on their environment.[13–15] One of the most common polymers used to create "smart", stimuli responsive hydrogels is poly(N-isopropylacrylamide) (pNIPAM), which exhibits a volume phase transition temperature (VPTT) of approximately 33°C.[14,16,17] The VPTT may be altered by copolymerizing pNIPAM with monomers of different hydrophilicity to suit specific applications.[16]

Inorganic nanoparticle composites based on "smart", stimuli-responsive hydrogels have become a particular focus, both for mechanical reinforcement[18] as well as for introducing optical[7], electronic[19], anti-microbial[4], photothermal[20], and/or photocatalytic[6] properties to the hydrogel. Of particular interest, superparamagnetic iron oxide nanoparticles (SPIONs) not only generate heat when placed in an oscillating magnetic field (OMF) from hysteresis losses, but also have the additional capacity to provide site-specificity (*via* focusing with a permanent magnet).[20,21] Such composites could be used for externally-activated but locally-induced hyperthermia treatment (*i.e.* exposing cancerous regions to elevated temperatures (~43°C) that will lyse the more temperature sensitive cancer tissues while being safe for normal

tissues[23]) and/or as scaffolds for the delivery of therapeutic agents. Consequently, thermosensitive composite materials containing SPIONs have been widely pursued in recent years.[20,23–27] While several hydrogel-SPION composite materials have been fabricated, few are able to be directly injected to the desired site of interest while maintaining their mechanical integrity. The development of injectable materials with similar physical properties and drug release profiles to currently reported macroscale-systems[20,23] would be highly beneficial to expand the potential applications of such materials and improve patient convenience. Several mechanisms exist that could be used to facilitate *in situ* gelation of composite hydrogels, including physical triggers such as changes in pH or temperature or chemical reactions of complementary groups such as thiol-vinyl sulfone, thiol-maleimide, amine-acrylate, aldehyde-hydrazide, etc.[29–31] The further ability of many of these hydrogel crosslinks, and consequently the composite materials, to degrade *in vivo* would also allow for the clearance of their comprising components from the body over time.

Most currently reported SPION-hydrogel composite systems either physically entrap pre-fabricated SPIONs in a hydrogel matrix or form the SPIONs *in situ* following hydrogel synthesis.[32] These methods generally produce materials that exhibit weak interactions between the nanoparticles and polymer molecules, resulting in minimal enhancement of the mechanical properties of the composite material.[33] If the SPIONs are instead surface-functionalized (*via* physical adsorption of functional polymer[34] or some other method), the SPIONs can be directly crosslinked into the network. Such a morphology would be anticipated to significantly enhance the mechanical properties of the composite, transforming rather soft, brittle hydrogels[35] into

elastomeric materials, and thus lead to other potential applications of the composites (*e.g.* embolic or structural biomaterials).[31]

In this paper, we report the fabrication of novel composites involving a thermosensitive, injectable, covalently crosslinked, stimuli-responsive hydrogel in which one of the polymers used to form the hydrogel is physically adsorbed to SPIONs. Following the method of Patenaude and Hoare[35,36], the hydrogel is formed by crosslinking thermosensitive, hydrazide-functionalized pNIPAM with aldehyde-functionalized dextran to form hydrolytically degradable hydrazone crosslinks between the two polymer precursors. The *in situ*-forming composites can be injected using a double barrel syringe, with both components mixing just prior to being injected into the desired site.[12] A number of previous studies have examined composite materials combining pNIPAM and SPIONs, coupling the thermosensitive nature of pNIPAM with the externally-induced heating capability of SPIONs.[38–41] However, in this work the hydrazide-functionalized pNIPAM is directly peptized to the surface of the SPIONs, resulting in very strong interactions between the SPIONs and the covalently crosslinked hydrogel matrix. The resulting hydrogel composites show exceptional, elastomer-like mechanical properties while maintaing physiological degradability and high cytocompatibility.

2.2.3 Experimental

Materials: Acrylic acid (AA, 99%), ammonium hydroxide (NH_3 content 28-30%), bupivacaine hydrochloride (99%), dextran from *Leuconstroc spp*. [M_r = 500,000], ethylene glycol (99.8%), iron(III) chloride hexahydrate (97%), iron(II) chloride

tetrahydrate (99%), mercaptoacetic acid (MAA, 98%), N-3-dimethylaminopropyl-N-ethyl carbodiimide hydrochloride (EDC, commercial grade), sodium periodate (>99.8%), and thiazolyl blue tetrazolium bromide (MTT) were all purchased from Sigma Aldrich (Oakville, ON). Adipic acid dihydrazide (ADH, 97%) was purchased from Alfa Aesar (Ward Hill, MA). Dimethyl 2,2'-azobis(2-methylpropionate) (98.5%) was purchased from Waterstone Technologies (Carmel, IN). Dimethyl sulfoxide (DMSO, reagent grade) was purchased from Caledon Laboratory Chemicals (Georgetown, ON). Hydrochloric acid (1M) was received from LabChem Inc. (Pittsburgh, PA). NIPAM (99%), purchased from Thermo Fisher Scientific (New Jersey, NJ), was further purified by recrystallization with toluene/hexane. 3T3 *Mus musculus* mouse cells were obtained from ATCC: Cederlane Laboratories (Burlington, ON). Cell proliferation media, recovery media, and trypsin-EDTA were all acquired from Invitrogen (Burlington, ON). The proliferation medium components included Dulbecco's modified Eagle's medium-high glucose (DMEM), fetal bovine serum (FBS), and penicillin streptomycin (PS). All water used was of Milli-Q grade, purified with a Barnstead Nanopure ultrapure water system.

pNIPAM-hydrazide synthesis: In a similar procedure to Patenaude and Hoare[36], 4.00 g of NIPAM was copolymerized with 1.00g of acrylic acid in 20 mL of ethanol, using 87 µL of mercaptoacetic acid as a chain transfer agent and 0.0555 g of dimethyl 2,2'-azobis(2-methylpropionate) as an initiator. The polymerization was performed overnight at 56 °C under a nitrogen atmosphere, after which the ethanol was removed by evaporation and the polymer was dissolved in deionized water (DIW) and dialyzed over 6 cycles. The solution was then lyophilized to obtain dry poly(AA-NIPAM). Conductometric titration (ManTech Inc.) indicated the copolymer contained 16.1 $\pm$ 0.5 mol% acrylic acid residues. The resulting polymer was re-dissolved in DIW and

functionalized with hydrazide groups by adding a 10x molar excess of adipic acid dihydrazide, changing the pH of the solution to 4.75, and adding a 5x molar excess of EDC (dissolved in 5 mL of DIW). A pH of 4.75 was maintained for 4 hours *via* the addition of 0.1M HCl or NaOH, as required. The resulting hydrazide-functionalized pNIPAM polymer was then returned to neutral pH before being dialysed over 6 cycles and subsequently lyophilized. Conductometric titration indicated that 92 ± 3% of the carboxylic acid residues in the polymer were functionalized with hydrazide groups, resulting in a 14.8 ± 0.7 mol% functionalization of polymer with hydrazide groups. Aqueous gel permeation chromatography (GPC, Waters Corporation) indicated a number average molecular weight of 21.6 kDa (polydispersity 1.65).

Dextran-aldehyde synthesis: 1.50 g of dextran (MW: 500,000 Da) was dissolved in 150 mL of DIW in a 500 mL round bottom flask. 0.8 g of sodium periodate was dissolved in 5mL of DIW and added to the dextran solution dropwise under magnetic stirring. After two hours, 0.4 mL of ethylene glycol was added to the solution and stirred for one more hour to arrest the oxidation. The product was subjected to 6 cycles of dialysis for purification and lyophilized for storage.

The degree of aldehyde functionalization of periodate-oxidized dextran was determined by selectively oxidizing the polysaccharide-bound aldehyde groups to carboxylic acid groups using silver (I) oxide and quantifying the acid groups using conductometric titration.[42] Briefly, oxidized dextran (0.1g, 0.0002 mmol) was dissolved in 10 mL of DIW along with sodium hydroxide (0.248g, 6.2 mmol). After the dextran was completely dissolved, silver (I) oxide (0.3859g, 1.6 mmol) was added to the solution and the solution was allowed to stir overnight. 5 mL of reaction solution were then added to 45 mL of

deionized water, and the solution was titrated using 0.1M NaOH. Based on this assay, 17.4% of dextran residues underwent oxidative cleavage, yielding approximately 2400 aldehyde groups per chain of 500 kDa oxidized dextran.

pNIPAM-hydrazide-SPION synthesis: Iron (III) chloride hexahydrate and iron (II) chloride tetrahydrate were dissolved in a 2:1 molar ratio in 12.5 mL of deionized water. 6.5 mL of ammonium hydroxide was added dropwise under mixing over ten minutes. After ten additional minutes of mixing, 2 g of the pNIPAM-hydrazide polymer (dissolved in 15 mL water) was added and the mixture was heated to 70°C for 2 hours under vigorous stirring to peptize the ferrofluid surface. The ferrofluid was then cooled, washed using magnetic separation with 10 mM phosphate buffered saline (PBS) for 5 cycles, and concentrated using a permanent magnet. The magnetic particles were characterized in terms of their size using TEM and their magnetization properties using a Superconducting Quantum Interference Device (SQUID, Quantum Design MPMS SQUID Magnetometer). Thermogravimetric analysis indicated that 21-24 wt.% of the mass of the coated SPIONs is attributable to the polymer layer (see Supporting Information, Figure S2.1).

Composite formation: The composite hydrogels were fabricated *via* condensation of hydrazide-functionalized and aldehyde-functionalized copolymers dissolved in 10 mM PBS. The hydrazide functionalized polymer-SPION complex [12 wt.% (m/v)] and aldehyde functionalized polymer solution [2-10 wt.% (m/v)] were loaded into different barrels of a dual-barrel syringe, shown in Figure 2.1, capped with a static mixer so the two reactants are thoroughly mixed upon injection. The ratio of aldehyde:hydrazide functional groups for each composite material as the aldehyde polymer content of the

composites varies is shown in Table 2.1. Therapeutic agents, such as the local anaesthetic bupivacaine hydrochloride used here, can be dissolved in both reactive phases if desired. The components were injected into rubber cylindrical moulds (diameter 3/8" and height 1/8") and allowed to undergo gelation for 10 minutes to form composite magnetic disks.

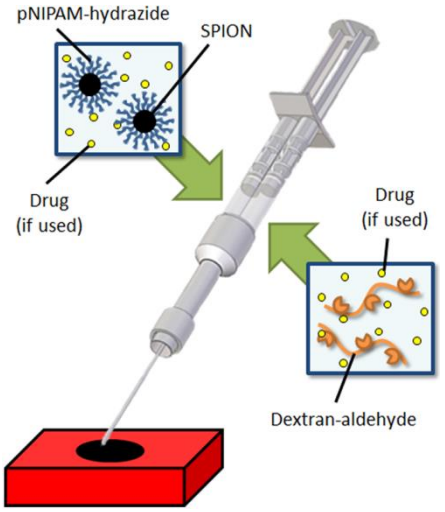

Figure 2.1: Hydrogel fabrication process. A double barrel syringe in which one barrel contains the pNIPAM-hydrazide-coated SPIONs and the other contains the dextran-aldehyde hydrogel precursor was used to prepare the composite disks for testing. Both materials are dissolved/suspended in PBS solutions, with a pharmaceutical agent of interest dissolved in both barrels if desired. Upon injection, the solutions are intimately mixed in a static mixing channel before being injected into a silicone mold through a needle tip for the formation of the test composite magnetic disks.

Table 2.1: Ratio of aldehyde:hydrazide functional groups in the composite magnetic disks.

Dextran-aldehyde content (wt.%)	Ratio of aldehyde:hydrazide functional groups
2	0.85
4	1.70
6	2.56
8	3.41
10	4.26

Thermogravimetric analysis (TGA): Prior to TGA, the water content of the composites was determined using gravimetric analysis by drying the samples overnight inside a 50°C oven. The magnetic nanoparticle concentration within the dried composites was subsequently determined by thermogravimetric analysis using a Luxx Netzsch STA-409 thermogravimetric analyzer. The composites were heated from 25°C to 900°C at a rate of 5°C per minute under an argon atmosphere.

Swelling measurements: The swelling of the composite materials was determined gravimetrically by comparing the mass of the composite disks directly after gelation (at 25°C) with the mass of those same disks following incubation in 10 mM PBS (total ionic strength 0.15M, pH 7.4) at physiological temperature. Composite disks were placed inside cell culture inserts (2.5 cm, 8μm pore size), removed at pre-defined intervals, lightly dabbed with a Kimwipe to remove surface water, and weighed, with changes in mass corresponding with changes in the water content of the composite disks. At least four replicates were performed for each sample, with the error bars representing the standard deviation of the percent mass change of the composite materials.

Composite degradation: Degradation assays were conducted by loading the composites (n = 4) inside the same cell culture inserts used for swelling assays and placing these samples into 2 mL of 0.01 M, 0.05 M, 0.1 M, 0.5 M, and 1 M hydrochloric acid (enhanced degradation) or 10 mM PBS (modelling physiological degradation). Changes in the gel mass were measured gravimetrically over time until the bulk material had completely degraded to soluble/suspended components.

Mechanical characterization: The storage and loss moduli (G' and G", respectively) were measured using an ARES parallel-plate rheometer (TA Instruments) using a

frequency sweep range of 0.1-100 rad/s at 25°C. The constant strain used for these frequency sweep tests was selected to lie within the linear viscoelastic region identified using a strain sweep test for every composite material tested. The parallel plates used were 7 mm in diameter and separated by a gap of 1 mm, with the composites carefully prepared to fill the entire void between the two plates. The compressive strength (the maximum stress a material can sustain under compressive loading) and compressive modulus (the ratio of stress to strain during compression) of the composites were determined using an Instron 3365 mechanical testing system based on methods previously described.[43] Composites 7 mm in diameter and 6 mm in height were compressed at a constant rate of 1 mm/min to a total of 2.5 mm of deformation at 25°C. The compressive stress-strain curve was measured using a 5 kN load cell, while the height and diameter of the composites were measured with digital calipers before and one minute after compression to determine how well the overall shape of the composite was retained after compression.

Pulsed-induction drug release experiments: Pulsed drug release tests were conducted by placing a composite disk in a vial with 3 mL of 10 mM PBS and mounting the vial inside a circulating water bath placed inside a magnetic coil. The circulating water bath maintained a constant temperature of 37°C in the sample in the absence of magnetic induction. Samples were collected before and after a 5 minute magnetic pulse (200 kHz, 30 A, 1.3 kW, with a 2 coil, 8 cm diameter solenoid), followed by 30 minutes (with three sample collections) during which no magnetic induction was applied. This cycle was repeated numerous times over the next 3-5 hours to evaluate the capacity of the materials to facilitate pulsatile release. Samples were analyzed for drug concentration using HPLC analysis (Waters Binary 1525 HPLC system, Atlantis 5 µm

4.6x100mm column, 35% phosphate buffer/65% acetonitrile continuous phase, Waters 2489 UV/Visible Detector, 263 nm wavelength).

***In vitro* cytocompatibility assay:** The cytocompatibility of the composite disks as well as both the polymeric and inorganic components of the composites were assessed using 3T3 *Mus musculus* mouse cells. 24-well polystyrene plates were cultured with 20,000 3T3 cells and 1 mL of proliferation media. After 24 hours, cells were exposed for an additional 24 hours to various concentrations of composite precursors (0.1, 0.4, 0.8, 1.2, 1.6, and 2 mg/mL) as well as the composites themselves, in which pre-cast composites were placed on top of the cell layer (assessment of leachate cytocompatibility). Cell viability was characterized *via* a modified MTT assay described by Pawlikowska *et al*.[44] The absorbance of the MTT solution was read using a Biorad microplate reader (model 550) at 540 nm against a 749 nm baseline and compared to that measured in cell-only wells in which no materials were added using the following equation:

$$cell\ viability\ (\%) = \frac{(absorbance_{polymer-exposed,540\ nm} - absorbance_{polymer-exposed,749\ nm})}{(absorbance_{blank,540\ nm} - absorbance_{blank,749\ nm})} \quad (1)$$

For all assays involving SPIONs, magnetic separation was used to separate SPIONs from the formazan dispersed in the DMSO, followed by centrifugation at 3,000 rpm for 10 minutes prior to measuring the sample absorbance to ensure no interference of SPION scattering in the assay. Each sample was tested four times, with error bars representing the standard deviation of the cell viability percentages measured.

***In vivo* tolerability assay:** The *in vivo* toxicity of the composite disks was assessed using a mouse subcutaneous injection model. A total of four BALB/c mice (22-24 g,

Charles River Laboratories) were injected with 0.35 mL of a 12 wt.% SPION-NIPAM-hydrazide / 8 wt.% dextran-aldehyde composite, using the previously described double-barrel syringe system. Four additional mice were injected with 10mM PBS to serve as controls for comparing the response of the mice to the composite disks. Animals were visually observed to identify any toxic response throughout, with two animals with composite disks and two PBS control animals sacrificed 3 days following injection (acute response) and another two animals with composite disks and two PBS control animals sacrificed 5 weeks after injection (chronic response). A tissue sample that includes skin, underlying tissue, and residual material was recovered from the animals and subjected to histological analysis using hematoxylin and eosin staining. Animals were cared for in compliance with protocols approved by the Animal Research Ethics Board at McMaster University and regulations of the Animals for Research Act of the Province of Ontario and the guidelines of the Canadian Council on Animal Care.

Statistical Analysis: The compression results are expressed as a mean ± standard deviation (n=3). Unless otherwise specified, error bars represent the standard deviation (n=4) from the mean. The determination of the statistical significance of differences was determined using a two-factor analysis of variance (ANOVA) with replication (n=4) at a confidence level of 95% ($p<0.05$).

2.2.4 Results and Discussion

Composite characterization: Thermosensitive magnetic composites were fabricated *via in situ* gelation of hydrazide-functionalized pNIPAM (peptized to the surface of SPIONs) and aldehyde-functionalized dextran. The pNIPAM-hydrazide-coated SPIONs

were concentrated to a total concentration of 12 wt.% in 10 mM PBS, while dextran-aldehyde was dissolved at different mass ratios in the same PBS buffer and co-extruded through a double-barreled syringe to form the composite. TGA of multiple batches of pNIPAM-hydrazide-coated SPIONs showed that their dry mass is 77-78% iron oxide (see Supporting Information, Figure S2.1), while TEM showed that the individual SPION particles were typically between 10-20 nm in diameter, with clusters from 30-200 nm in size (from Image J analysis), although some aggregation was observed typical of SPIONs produced via the coprecipitation method used herein[10,21,45–47] (see Supporting Information, Figure S2.2). Gravimetric analysis indicated that the composite materials have water contents of 88 ± 3, 86 ± 3 and 82 ± 5 wt.% for 2, 6, and 8 wt.% dextran aldehyde contents respectively, suggesting the composites have a primarily hydrogel character. Thermogravimetric analysis of the dry composite materials is shown in Figure 2.2.

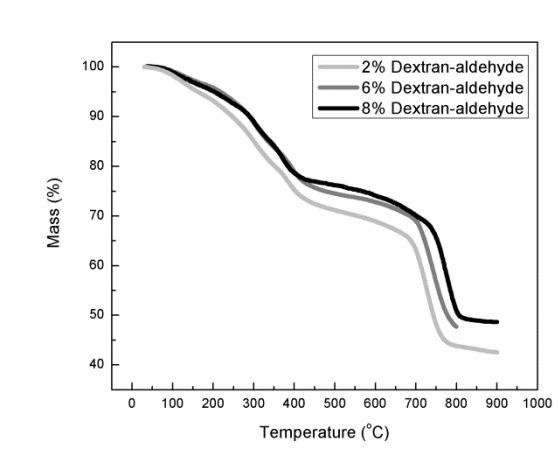

Figure 2.2: TGA curves of 2, 6, and 8 wt.% dextran-aldehyde composites.

The dry composites of varying dextran-aldehyde contents contain 68-76% iron oxide,

with composites containing a higher aldehyde polymer content exhibiting a slightly lower iron oxide fraction. Taking the gravimetric and TGA results together, the weight percent of magnetic nanoparticles in the water-swollen composites is approximately 5 wt.%. The TGA results in Figure 2.2 also indicate that the iron is fully oxidized within the composites; the mass loss between 600°C to 900°C, which corresponds to the temperature range where oxygen dissociates from iron directly corresponds with the amount of mass lost if the iron was fully oxidized for all samples.

SQUID measurements of the magnetization of the hydrazide-functionalized SPIONs are shown in Figure 2.3. Magnetic analysis indicated that the pNIPAM hydrazide-coated SPIONs are highly superparamagnetic, with a total magnetic saturation of approximately 42 emu/g (comparable to similarly produced SPIONs in the literature[23,48]). When the hydrazide-functionalized SPIONs are incorporated into the hydrogel, the total magnetic saturation was reduced to 30 emu/g, but the material still exhibited low coercivity and thus superparamagnetism. The pNIPAM hydrazide-coated SPIONs were shown to retain the heat generation capacity of SPIONs when in the presence of an oscillating magnetic field (OMF), where the heating rate depends on both the current (and therefore power) supplied through the OMF and the SPION concentration (see Supporting Information, Figure S2.3).

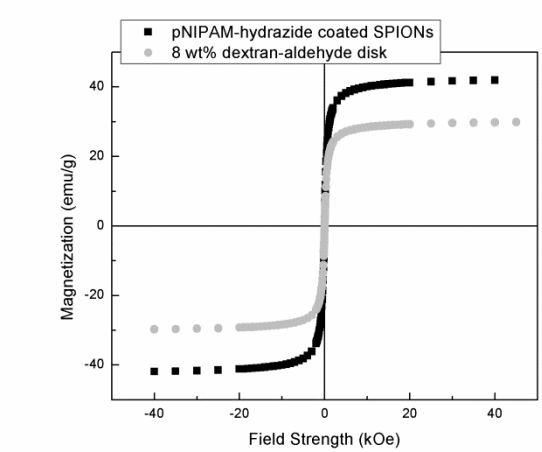

Figure 2.3: Magnetization curves for the pNIPAM-hydrazide SPION precursor and an 8 wt.% dextran-aldehyde composite disk measured at 303K.

Rheological properties: In these composite systems, the SPION particles function as both inorganic fillers as well as crosslinkers, suggesting that the incorporation of a small amount of SPIONs may have a large impact on the mechanical properties of the overall composite. The storage moduli for composites of varying dextran-aldehyde contents are shown in Figure 2.4a, as measured using parallel plate rheometry.

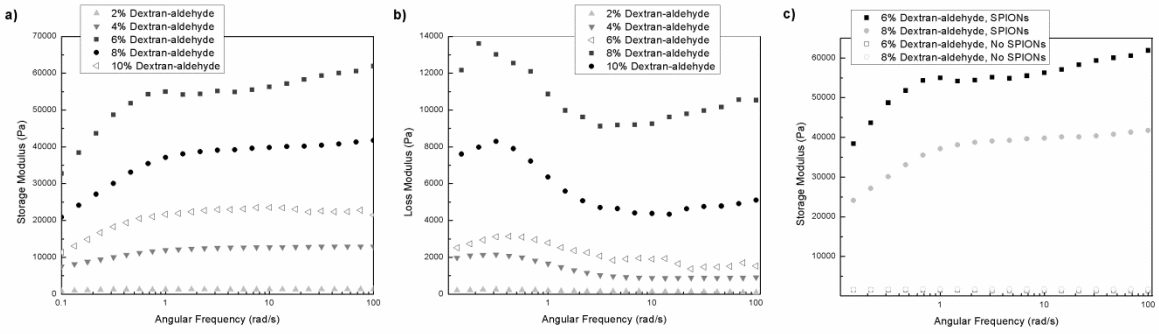

Figure 2.4: (a) Storage (G') moduli and (b) loss (G") moduli of composites with varying dextran-aldehyde content, and (c) the effect of adsorbing the pNIPAM precursor to the surface of SPIONs on the storage moduli of the composite disks with 6 and 8 wt.% dextran-aldehyde content. The concentration of the pNIPAM-hydrazide polymer used was identical in the comparison, where it was adsorbed to SPIONs in one case and dissolved in solution in the other.

The concentration of dextran-aldehyde has a dramatic effect on the mechanical properties of the composites. At low dextran-aldehyde contents, the storage modulus of the composite is low, corresponding to the low cross-linking density facilitated by the small number of aldehyde groups available for cross-linking. As the dextran-aldehyde concentration is increased (and thus the number of potential cross-linking pairs is increased), significant enhancements in G' are observed, with the 6 wt.% composite showing a 50-fold increase in G' compared to the 2 wt.% composite. However, as the dextran-aldehyde concentration is further increased, the G' of the composite decreases significantly. This observation may be attributable to the greater viscosity of the highly concentrated initial dextran-aldehyde solutions, inhibiting intimate mixing of the two reactive components upon injection, and/or the presence of excess, non-cross-linked dextran that served to plasticize the composites. The high ratio of aldehyde:hydrazide functionalities of the composite disks with greater dextran aldehyde content (as shown in Table 2.1) suggest that the presence of non-crosslinked dextran in higher dextran concentration composites is indeed a possibility. The ~2.5:1 aldehyde to hydrazide ratio of the 6 wt.% composites appears to strike an optimal balance in terms of crosslinking all of the hydrazide functional groups of the pNIPAM-hydrazide-coated SPIONs to the higher molecular weight dextran component while not leaving an excess of free, uncrosslinked dextran.

The magnitude of G' was much higher than G" in all cases (see Figure 2.4b and G'/G" plots, Supporting Information Figure S2.4), indicating that all of the composites are highly elastic. Indeed, the 6, 8 and 10 wt.% dextran-aldehyde composites in particular behave on a macroscopic scale more like elastomers than typical hydrogels, with storage moduli 12-20-fold higher than the corresponding hydrogel-only materials (Figure

2.4c). Similar to the findings of Meid *et al*.[35] for microgel incorporation in hydrogels, the SPIONs here behave analogously to hard carbon black fillers used to improve the mechanical stability of rubbers. This occurs at a greater extent in this case due to the enhanced interactions between the SPIONs and hydrogel matrix. Highly elastic bulk mechanical responses analogous to rubber "super balls" were observed, as composites dropped from a defined height bounced back to nearly their original height (see Supplementary Video). Compression testing confirmed the highly elastic nature of the composites, with the measured elastic recoveries and compressive moduli shown in Table 2.2.

Table 2.2: Compression properties of magnetic composites as a function of dextran-aldehyde content; 2.5 mm compression, compression rate 1 mm/min (n = 4).

Dextran-aldehyde content (%)	Compressive strength (kPa)	Compressive modulus (kPa)	Height recovered following deformation (%)
2	5.3 ± 0.8	61 ± 12	47 ± 11
6	190 ± 70	218 ± 68	53 ± 6
8	26 ± 5	213 ± 43	98 ± 6
10	23 ± 5	148 ± 16	94 ± 5

The compressive strength of the composites are in general agreement with the parallel plate rheometry results, with the 6 wt.% dextran-aldehyde composites clearly exhibiting the highest mechanical strength. Interestingly, the 6 and 8 wt.% composites had the same compressive moduli (p = 0.10) and the 10 wt.% composites exhibited only a slightly lower compressive modulus than the 8 wt.% composites (p = 0.02) and a comparable modulus to the 6 wt.% composites (p = 0.11); this result is likely attributable to the higher solids content of these (unswollen) composites that has a significantly higher impact on mechanical properties in compression as opposed to shear.

Composites with higher aldehyde-dextran contents (8-10 wt.%) elastically rebound to re-form their original shape over multiple compressive cycles (see Supporting Information Table S2.1 for an example of a 10 wt.% dextran-aldehyde composite undergoing multiple compressions), while composites with lower aldehyde-dextran contents (2-6 wt.%) remained significantly deformed after a single compression. This ability of a composite material to quickly return to its original shape upon the application of a stress is essential in potential applications in which the material would experience moderate compressive or shear forces.

Swelling characteristics: The inclusion of the thermoresponsive polymer pNIPAM as the surface coating imparts thermosensitive properties on the composite. The thermosensitive swelling characteristics of the composite materials were analyzed by comparing the mass of the gel directly after injection with the mass of the gel measured at various incubation times at 37°C in 10 mM PBS solutions. As shown in Figure 2.5, the 6 and 8 wt.% dextran-aldehyde composites deswelled to roughly -10% and -20% respectively of their original masses upon incubation at physiological pH and ionic strength. This swelling was compared to that of hydrogels fabricated with the same polymer concentration in the absence of SPIONs (3% pNIPAM hydrazide/6% dextran aldehyde and 3.6% pNIPAM hydrazide/8% dextran aldehyde, as respectively formulated based on the TGA findings). The hydrogels in the absence of SPIONs had deswelled to 95 ± 2% and 86 ± 4% of their initial weight for the 6 and 8wt.% composites respectively after 24 hours at 37°C, which is comparable to the findings shown in Figure 2.5. This relatively low degree of swelling compared to some other thermoresponsive systems[36] can be attributed to the fact that here the non-responsive dextran-aldehyde polymer

content is more concentrated in the disk than the responsive pNIPAM-hydrazide component.

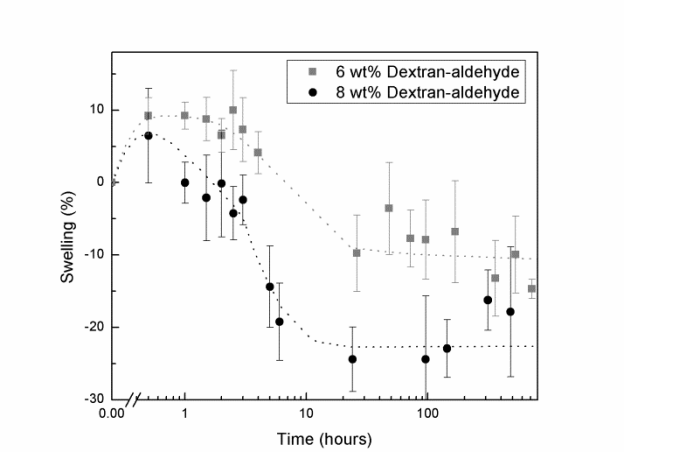

Figure 2.5: Swelling responses of the 6 and 8 wt.% dextran-aldehyde composites in 10 mM PBS solution at 37°C.

Where it was initially proposed that the strong interactions between the SPIONs and polymer may physically inhibit the deswelling of these gels, it was found that directly cross-linking SPIONs into a hydrogel network produced composites that are significantly stronger than similar hydrogels without significantly impacting the swelling capacity of the surrounding hydrogel. This is similar to the findings of Tong *et al*.[49], in which the entrapment of carbon nanotubes within a hydrogel network was shown to improve the mechanical strength of hydrogels while maintaining the hydrogel's ability to swell (*i.e.* mechanics can be tuned relatively independently of the degree of swelling as a function of the gel environment). These properties are important for biomaterials in muscle and tissue engineering, where materials with strong mechanical properties and well-defined swelling capabilities are desired.

Degradation: The hydrolytic lability of the hydrazone bond used to cross-link the composite material (together with the hydrolytic lability of the aldehyde-functionalized dextran[50]) facilitates the slow degradation of the composites over time. Figure 2.6a shows the degradation of a composite prepared with 8 wt.% dextran-aldehyde in both 10 mM PBS as well as accelerated conditions using varying concentrations of hydrochloric acid. Degradation was correlated with the residual mass of the macroscopic composites as a function of time.

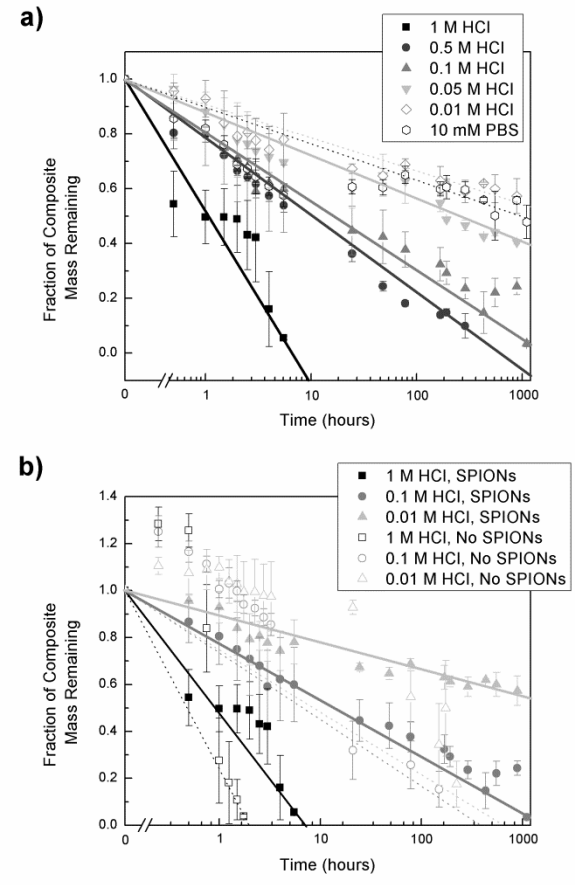

Figure 2.6: Composite degradation at 37°C from 8 wt.% dextran-aldehyde composites with (a) various concentrations of HCl and 10 mM PBS (pH 7.4) and (b) acid catalyzed degradation of disks with and without the pNIPAM precursor adsorbed to the surface of

SPIONs with 8 wt.% dextran-aldehyde. The concentration of the pNIPAM-hydrazide polymer used was identical in the comparison, where it was adsorbed to SPIONs in one case and dissolved in solution in the other.

The composites degrade over time in all conditions tested, with higher acid concentrations degrading the material faster (consistent with an acid-catalyzed degradation process known to apply to hydrazone bonds[51]). Notably, the rates at which these composites degrade is much slower than that of similar hydrogels without SPIONs, despite the fact that SPIONs are known to dissolve slowly in strong acids[52]; disks of similar composition without SPIONs degrade roughly three times more rapidly (see Figure 2.6b). This surprising increase in degradation time may be attributed to the mechanical strength of the composites, potentially slowing hydrolytic degradation due to the increased density of these materials, inhibiting the interaction of the hydrazide crosslinks with water; in addition, the immobilization of the reactive group on a solid nanoparticle introduces a heterogeneous aspect to the hydrolysis reaction which may further retard the kinetics. Importantly, the degradation of the composites as a whole still occurs at pH values at which the SPIONs are insoluble (10 mM PBS, 0.01 M HCl) such that degradation occurs *via* hydrolysis of the hydrazone bond instead of SPION dissolution. Notably, some of the initial composites (with 6 wt.% dextran-aldehyde content) solubilized completely when stored in a 0.15M NaCl solution over a period of ~8 months, confirming that degradation does indeed occur at physiologically-relevant conditions.

***In vitro* cytotoxicity:** The *in vitro* cytotoxicity of the gel components (and thus the degradation products) was screened using an MTT assay with 3T3 mouse fibroblasts, the results of which are shown in Figure 2.7.

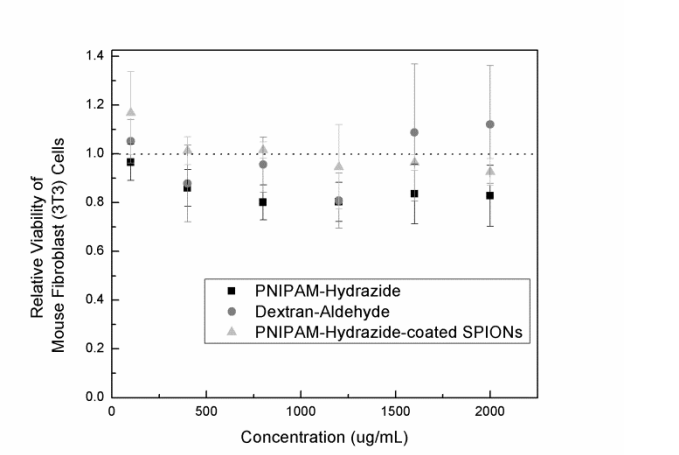

Figure 2.7: Relative viability (to cell-only control) of 3T3 mouse fibroblast cells for various concentrations of the composite precursors and potential degradation products.

All components of the composites exhibit no significant cytotoxicity over the full range of tested concentrations; while pNIPAM-hydrazide showed the lowest relative viabilities, these low viabilities (~80%) are generally considered to be associated with little to no cytotoxicity[53] and were evident at concentrations lower than the total polymer concentration in the composite; however the maximum concentration tested (2 mg/mL) is expected to be far in excess of the expected concentrations of free polymer that the body would be exposed to at any point given the very rapid gelation process and the slow degradation of the material.

The relative viability of 3T3 cells grown in the presence of 6 and 8 wt.% dextran-aldehyde composites for 24 hours are also not significantly different from the cell-only controls (0.85 ± 0.11 for 6 wt.% dextran-aldehyde composites and 1.06 ± 0.19 for 8 wt.% dextran-aldehyde composites). This result indicates that the composites, as well as any leachates from the composites, exhibit negligible cytotoxicity.

***In vivo* studies:** Acute (3 days) and chronic (5 weeks) histology following subcutaneous injections of the 6 wt% dextran composite gel are shown in Figure 2.8.

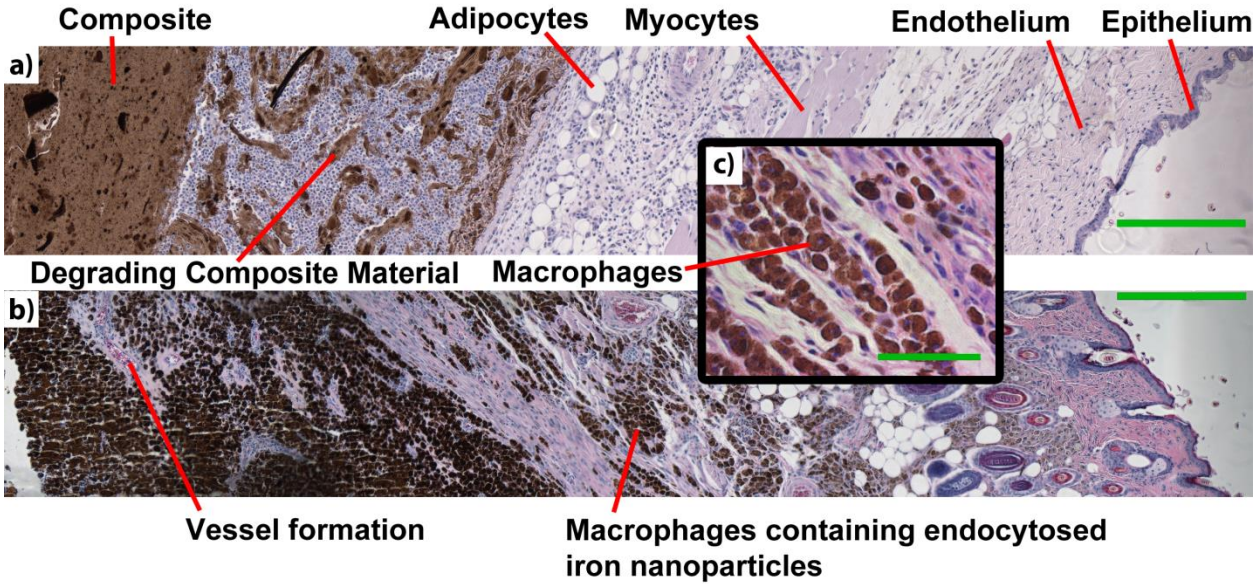

Figure 2.8: Host response toward 8 wt.% dextran-aldehyde composite hydrogels following subcutaneous injection after both a) acute and b) chronic time points. Inset c) depicts monocyte differentiation into macrophages and subsequent uptake of iron nanoparticles. The scale bars represent 0.5 mm in both a) and b) and 0.1 mm in c).

At the acute time point (Figure 2.8a), a significant inflammatory response is observed (compared to the control shown in the Supporting Information, Figure S2.5), with both monocytes and neutrophils present at the site of injection and particularly evident at the biomaterial interface (~4900 mm^{-2} at the interface). This response is typical of nanoparticle-impregnated materials in which a fraction of the nanoparticles can leach out over time.[47] An adhesion that could only be separated by blunt dissection was also observed between the material and the surrounding tissue. At the chronic time point (Figure 2.8b), a moderate chronic inflammation was observed, with granulation tissue and neovascularization observed both within and surrounding the gel. A significant

number of macrophages (~2800 mm^{-2} present within the bulk gel) are observed, which appear to be clearing the material from the site of implantation due to a distinct brown colour within their cytoplasm associated with SPION uptake. No foreign body giant cells are present at the site of injection at this chronic time point, demonstrating that macrophage sequestration appears to be the dominant method of gel/iron oxide removal. This is a significantly more mild response than that observed with, for example, membranes containing magnetic nanoparticles, which do promote fibrous capsule and foreign body giant cell formation[21]; this result suggests the advantage of using a highly hydrated hydrogel as the bulk structure for magnetic composite materials from a triggerable drug delivery perspective. However, macrophages appearing to be filled with magnetic nanoparticles (not observed in the PBS-only injection control, Supporting Information Figure S2.6) were still observed at the interface (Figure 2.8c), characteristic of a slow-degrading material response in which nanoparticles are slowly released from the degrading bulk gel over time. Evidence for neovascularization was also observed both near the composite surface and within the composite following chronic exposure (Figure 2.8b). The strong tissue adhesion also persisted at the chronic time point, suggestive of the potential utility of this material as a tissue adhesive; we speculate that the net excess of aldehyde groups at the tissue interface (from the continuous dextran-aldehyde phase of the composite) may form linkages with amine groups in native tissues to facilitate adhesion.

Pulsatile drug release: The high volumetric concentration of magnetic nanoparticles in these injectable composites makes these materials of particular interest for externally-mediated treatments *in vivo*, including hyperthermia, drug release, or combinations thereof.[46] In order to assess the potential of these materials for pulsatile drug delivery,

the release of bupivacaine hydrochloride (a cationic local anesthetic) was measured from an 8 wt.% dextran-aldehyde composite under the application of an external OMF, as shown in Figure 2.9. The OMF was applied in 5-10 minute pulses, increasing the temperature of the composites from 37°C to ~42°C to allow for OMF co-induced therapeutic delivery and hyperthermia treatment.

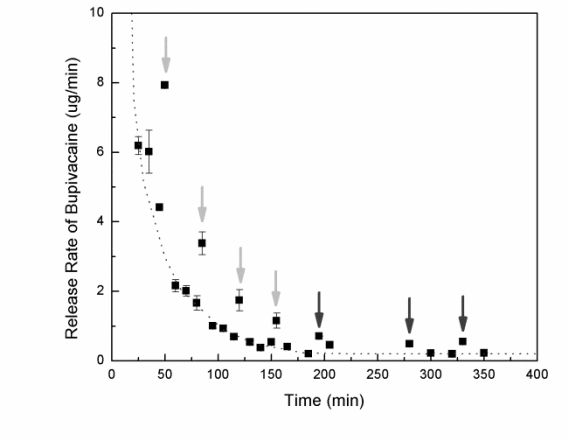

Figure 2.9: Pulsed external OMF-induced rate of release of bupivacaine with an 8 wt.% dextran-aldehyde composite. The release rates directly after pulses are indicated by the arrows, with pulses of 5 and 10 minutes in duration indicated by light grey and dark grey arrows respectively. The dashed line estimates the baseline drug release in the absence of pulses.

A significant increase in the rate of bupivacaine release from the composite was observed immediately following each pulse of the external oscillating magnetic field, with the release returning to the baseline, first-order release following the removal of the magnetic field, as shown in Figure 2.9. These pulses can also be seen in the cumulative release curve shown in Supporting Figure S2.7, with approximately 55% of bupivacaine released in the first 6 hours consistent with the burst release effect associated with hydrogel-based drug release systems. The short pulses allowed for a 163 ± 24%

increase in release relative to the baseline release rate over the full range of times tested. Thus, pulsed “on-demand” increases in drug release can be achieved upon the application of an OMF using these injectable magnetic composite materials.

The high magnetic particle content, high elasticity, and injectability of the magnetic composite material described herein offers significant advantages over other approaches reported in the literature. To date, several highly elastic hydrogel materials have been developed, particularly for bone or cartilage tissue engineering applications. Notably, Zhao *et al.*[54] fabricated hydrogels by complexing poly(ε-caprolactone)-poly(ethylene glycol)-poly(ε-caprolactone) block copolymers with α-cyclodextrin before crosslinking to form high mechanical strength hydrogels with storage moduli ranging from 2-10 (10^4) Pa, similar to what is shown in this work. When SPIONs were added within this matrix, the material exhibited a lower G’ than the material described herein; furthermore, this hydrogel is not injectable[32], a key attribute for the potential clinical translatability of these materials in either drug delivery or tissue engineering applications. Previous examples of injectable, magnetic hydrogels in the literature relied on the self-assembly of SPIONs via the sol-gel method, using fixed hydrophobic interactions to drive physical gelation[55,56], temperature-responsive polymers tethered to the SPION surface to facilitate magnetically-triggerable gelation following heating[57], or pH-triggered associations between SPION particles directly to drive gelation[58]. In contrast, the materials presented herein are covalently cross-linked, resulting in significantly more elastic hydrogel materials (at least one order of magnitude higher G’ than the strongest reported sol-gel systems[55,57]). Furthermore, the degradation of the network can be significantly better tuned using the hydrolyzable, hydrazone-cross-linked network reported herein relative to the physically-gelled networks previously reported, which are

either more subject to premature break-up via dissolution *in vivo* or cannot be degraded without a (typically infeasible) internal change in temperature or pH. As such, to the best of our knowledge, the magnetic nanocomposite material reported herein is the first injectable hydrogel-based composite system that possesses such enhanced elastic properties coupled with controllable degradation.

The demonstrated potential of this material to degrade *via* a chemical mechanism (hydrolysis) also offers significant advantages. It should be emphasized that the molecular weight of the NIPAM hydrazide polymer is maintained below the renal cutoff (~40 kDa) using chain transfer polymerization, allowing for the potential clearance of this product from the body. The dextran component can be degraded by the reticuloendothelial system (RES) until it can be cleared renally[59] or metabolized by various dextranases throughout the body[60]. The biodistribution of SPIONs is highly dependent on their surface properties. Typically SPIONs with diameters less than 100 nm and hydrophilic surfaces (such as those used herein) can avoid accumulation in the RES[46] and are instead internalized by cells and degraded by the lower local pH in lyposomes/endosomes as well as by intracellular Fe-chelating substances.[45] Therefore, the degradation products of each part of the composite material could be cleared from the body. The low demonstrated cytotoxicity of the gel components further suggests the high biological tolerability of these materials. Additionally, there is only a mild biological response to the composite itself as well as its degradation products over a chronic time frame, with no fibrous capsule formed around the material and no presence of foreign body giant cells observed. The neovascularization observed within the composite at the chronic time period suggests that this material may be applicable for wound healing or tissue engineering of stiffer tissues, facilitating the formation of new vessels and tissues

as the material degrades. The *in vivo* studies also demonstrated that the material strongly bonds the adjacent tissue, suggesting its potential application as a mechanically strong but slowly degradable tissue adhesive. In this respect, the use of SPIONs as a reinforcing phase, independent of the additional functionality SPIONs provide in terms of magnetization and the potential for induction heating, has advantages over other potential inorganic fillers (*i.e.* silica[61,62], carbon nanotubes[49], hydroxyapatite[63–65], clays[66], or other inorganic fillers) for the production of high-strength hydrogel materials.

Magnetically-stimulated drug delivery has significant potential for facilitating the pulsatile, "on-demand" release of therapeutics using a non-invasive trigger. OMF pulses applied to the composites resulted in a significantly increased rate of bupivacaine release immediately following the pulse, suggesting the utility of these materials particularly for pulsatile release of drugs whose minimal inhibitory concentration (MIC) lies between the non-pulsed and pulsed release rates. Future work will aim to combine these highly elastic scaffolds with thermoresponsive microgels that can mediate even higher gradients of on-off drug release.

2.2.5 Conclusions

Injectable magnetic composite materials with high water contents but extremely high elasticities have been fabricated by surface functionalizing SPIONs with hydrazide-functionalized poly(N-isopropylacrylamide) and using these particles as crosslinkers for aldehyde-functionalized dextran. The materials exhibit remarkably high G' values for an injectable hydrogel-based material (G' > 60 kPa), and neither the composites as a whole nor the individual components of the composite exhibit significant cytotoxicity *in vitro* or

chronic inflammation *in vivo.* Coupled with the demonstrated externally-triggerable drug delivery potential of these materials upon the application of an oscillating magnetic field, these composite materials offer significant advantages over many current SPION-containing materials for biomedical use.

2.2.6 Acknowledgements

Dennis Kinio is acknowledged for his assistance in synthesizing and purifying the pre-gel components. Diane Sivakumaran is acknowledged for the double-barrel syringe Solid-Edge image. Funding from the J.P. Bickell Foundation (Medical Research Grant) is gratefully acknowledged. S.B.C. also acknowledges the support of post-graduate scholarships from the Natural Sciences and Engineering Research Council of Canada (NSERC) and the Ontario Ministry of Research and Innovation.

2.2.7 Associated Content

Supporting Information: Thermogravimetric analysis of the modified ferrofluid, TEM images of the modified SPIONs, G'/G" data for the magnetic composites, magnetic heating curves for the modified SPIONs, a video of the elastic recovery of the composite hydrogels when dropped from a height, multi-cycle compression data, PBS-only control subcutaneous injections, and cumulative drug release kinetic profiles are provided. This material is available free of charge at http://pubs.acs.org.

2.2.8 References

1. Leach, J. B.; Schmidt, C. E. *Biomaterials* **2005**, *26*, 125–135.

2. Zhang, L.; Rakotondradany, F.; Myles, A. J.; Fenniri, H.; Webster, T. J. *Biomaterials* **2009**, *30*, 1309–20.

3. Varaprasad, K.; Mohan, Y. M.; Ravindra, S.; Reddy, N. N.; Vimala, K.; Monika, K.; Sreedhar, B.; Raju, K. M. *J. Appl. Polym. Sci.* **2010,** *115*, 1199-1207.

4. Varaprasad, K.; Mohan, Y. M.; Vimala, K.; Raju, K. M. *J. Appl. Polym. Sci.* **2011,** *121*, 784-796.

5. Lu, Y.; Spyra, P.; Mei, Y.; Ballauff, M.; Pich, A. *Macromol. Chem. Phys.* **2007,** *208*, 254-261.

6. Zhu, C.-H.; Hai, Z.-B.; Cui, C.-H.; Li, H.-H.; Chen, J.-F.; Yu, S.-H. *Small* **2012,** *8*, 930-936.

7. Endo, T.; Ikeda, R.; Yanagida, Y.; Hatsuzawa, T. *Anal. Chim. Acta* **2008,** *611*, 205-211.

8. Holtz, J. H.; Asher, S. A. *Nature* **1997**, *389*, 829–832.

9. Hoare, T. R.; Kohane, D. S. *Polymer* **2008**, *49*, 1993–2007.

10. Huang, Y.; Liu, M.; Chen, J.; Gao, C.; Gong, Q. *Euro. Polym. J.* **2012**, *48*, 1734-1744.

11. Ramanan, R. M. K.; Chellamuthu, P.; Tang, L.; Nguyen, K. T. *Biotechnol. Prog.* **2006,** *22*, 118-125.

12. Sivakumaran, D.; Maitland, D.; Hoare, T. *Biomacromolecules* **2011**, *12*, 4112–4120.

13. Tumarkin, E.; Kumacheva, E. *Chem. Soc. Rev.* **2009,** *38*, 2161-2168.

14. Pelton, R. *Adv. Colloid Interface Sci.* **2000,** *85*, 1-33.

15. Zhao, X.; Kim, J.; Cezar, C. A.; Huebsch, N.; Lee, K.; Bouhadir, K.; Mooney, D. J. *PNAS* **2011**, *108*, 67–72.

16. Seiffert, S.; Weitz, D. A. *Polymer* **2010**, *51*, 5883–5889.

17. Alarcon, C. D. H.; Pennadam, S.; Alexander, C. *Chem. Soc. Rev.* **2005,** *34*, 276-285.

18. Ramakrishna, S.; Mayer, J.; Wintermantel, E.; Leong, K. W. *Compos. Sci. Technol.* **2001,** *61*, 1189-1224.

19. Zhao, X.; Ding, X.; Deng, Z.; Zheng, Z.; Peng, Y.; Tian, C.; Long, X. *New J. Chem.* **2006,** *30*, 915-920.

20. Zhang, X.; Pint, C. L.; Lee, M. H.; Schubert, B. E.; Jamshidi, A.; Takei, K.; Ko, H.; Gillies, A.; Bardhan, R.; Urban, J. J.; Wu, M.; Fearing, R.; Javey, A. *Nano Letters* **2011,** *11*, 3239-3244.

21. Hoare, T.; Santamaria, J.; Goya, G. F.; Irusta, S.; Lin, D.; Lau, S.; Padera, R.; Langer, R.; Kohane, D. S. *Nano letters* **2009**, *9*, 3651–3657.

22. Satarkar, N. S.; Biswal, D.; Hilt, J. Z. *Soft Matter* **2010**, *6*, 2364-2371.

23. Laurent, S.; Forge, D.; Port, M.; Roch, A.; Robic, C.; Elst, L. Vander; Muller, R. N. *Chem. Rev.* **2008,** *108*, 2064-2110.

24. Rovers, S. A..; Hoogenboom, R.; Kemmere, M. F.; Keurentjes, J. T. F. *Soft Matter* **2012,** *8*, 1623-1627.

25. Laurent, S.; Dutz, S.; Häfeli, U. O.; Mahmoudi, M. *Adv. Colloid Interface Sci.* **2011,** *166*, 8-23.

26. Satarkar, N. S.; Hilt, J. Z. *J. Controlled Release* **2008,** *130*, 246-251.

27. Schmidt, A. M. *Colloid and Polym. Sci.* **2007**, *285*, 953–966.

28. Zadražil, A.; Tokárová, V.; Štěpánek, F. *Soft Matter* **2012**, *8*, 1811-1816.

29. Van Tomme, S. R.; Storm, G.; Hennink, W. E. *Int. J. Pharm.* **2008,** *355*, 1-18.

30. Hennink, W. E.; van Nostrum, C. F. *Adv. Drug Delivery Rev.* **2002,** *54*, 13-36.

31. Overstreet, D. J.; Dutta, D.; Stabenfeldt, S. E.; Vernon, B. L. *J. Polym. Sci. Part B: Polym. Phys.* **2012,** *50*, 881-903.

32. Ma, D.; Zhang, L.-M. *J. Phys. Chem. B* **2008,** *112*, 6315-6321.

33. Schexnailder, P.; Schmidt, G. *Colloid Polym. Sci.* **2009,** *287*, 1-11.

34. Oh, J. K.; Park, J. M. *Prog. Polym. Sci.* **2011,** *36*, 168-189.

35. Meid, J.; Dierkes, F.; Cui, J.; Messing, R.; Crosby, A. J.; Schmidt, A.; Richtering, W. *Soft Matter* **2012**, *8*, 4254-4263.

36. Patenaude, M.; Hoare, T. *ACS Macro Lett.* **2012,** *1*, 409-413.

37. Patenaude, M.; Hoare, T. *Biomacromolecules* **2012**, *13*, 369–378.

38. Tokárová, V.; Pittermannová, A.; Čech, J.; Ulbrich, P.; Štěpánek, F. *Soft Matter* **2012**, *8*, 1087-1095.

39. Yoon, J.; Bian, P.; Kim, J.; McCarthy, T. J.; Hayward, R. C. *Angew. Chem., Int. Ed. Engl.* **2012**, *51*, 7146–7149.

40. Zhang, F.; Wang, C.-C. *Langmuir* **2009**, *25*, 8255–8262.

41. Zhou, L.; He, B.; Zhang, F. *ACS Appl. Mater. Interfaces* **2012**, *4*, 192–199.

42. Thomason, S. C.; Kubler, D. G. *J. Chem. Educ.* **1968,** *45*, 546.

43. Mosekilde, L.; Mosekilde, L. *Bone* **1986,** *7*, 207-212.

44. Pawlikowska, P.; Gajkowska, B.; Orzechowski, A. *Cell Tissue Res.* **2007,** *327*, 571-81.

45. Gu, J.; Xu, H.; Han, Y.; Dai, W.; Hao, W.; Wang, C.; Gu, N.; Xu, H.; Cao, J. *Sci. China: Life Sci.* **2011,** *54*, 793-805.

46. Gupta, A. K.; Gupta, M. *Biomaterials* **2005,** *26*, 3995-4021.

47. Yu, Z.; Xiaoliang, W.; Xuman, W.; Hong, X.; Hongchen, G. *J. Biomed. Mater. Res. Part A* **2008,** *85A*, 582-587.

48. Lee, S.-J.; Jeong, J.-R.; Shin, S.-C.; Kim, J.-C.; Kim, J.-D. *J. Magn. Magn. Mater.* **2004,** *282*, 147-150.

49. Tong, X.; Zheng, J.; Lu, Y.; Zhang, Z.; Cheng, H. *Mater. Lett.* **2007,** *61*, 1704-1706.

50. Kristiansen, K. A; Potthast, A.; Christensen, B. E. *Carbohydr. Res.* **2010**, *345*, 1264–1271.

51. Hiemstra, C.; Aa, L. van der; Zhong, Z. *Macromolecules* **2007**, *40*, 1165–1173.

52. Qu, H.; Caruntu, D.; Liu, H.; O'Connor, C. J. *Langmuir* **2011,** *27*, 2271-2278.

53. Fu, Y.; Kao, W. J. *J. Biomed. Mater. Res. Part A* **2011,** *98*, 201-211.

54. Zhao, S.-P.; Zhang, L.-M.; Ma, D.; Yang, C.; Yan, L. *J. Phys. Chem. B* **2006,** *110*, 16503-16507.

55. Qin, J.; Asempah, I.; Laurent, S.; Fornara, A.; Muller, R. N.; Muhammed, M. *Adv. Mater.* **2009**, *21*, 1354–1357.

56. Kim, J. Il; Chun, C.; Kim, B.; Hong, J. M.; Cho, J.-K.; Lee, S. H.; Song, S.-C. *Biomaterials* **2012**, *33*, 218–224.

57. Reinicke, S.; Döhler, S.; Tea, S.; Krekhova, M.; Messing, R.; Schmidt, A. M.; Schmalz, H. *Soft Matter* **2010**, *6*, 2760-2773.

58. Woodward, R. T.; Olariu, C. I.; Hasan, E. a.; Yiu, H. H. P.; Rosseinsky, M. J.; Weaver, J. V. M. *Soft Matter* **2011**, *7*, 4335-4340.

59. Arturson, G.; Wallenius, G. *Scand. J. Clin. Lab. Invest.* **1964,** *16*, 76-80.

60. Mehvar, R. *J. Controlled Release* **2000,** *69*, 1-25.

61. Lin, W.-C.; Fan, W.; Marcellan, A.; Hourdet, D.; Creton, C. *Macromolecules* **2010,** *43*, 2554-2563.

62. Loos, W.; Du Prez, F. *Macromolecular Symp.* **2004,** *210*, 483-491.

63. Gaharwar, A. K.; Dammu, S. A.; Canter, J. M.; Wu, C.-J.; Schmidt, G. *Biomacromolecules* **2011,** *12*, 1641-1650.

64. Sinha, A.; Guha, A. *Mater. Sci. Eng. C* **2009,** *29*, 1330-1333.

65. Alves, N. M.; Leonor, I. B.; Azevedo, H. S.; Reis, R. L.; Mano, J. F. *J. Mater. Chem.* **2010,** *20*, 2911-2921.

66. Haraguchi, K.; Li, H.-J.; Matsuda, K.; Takehisa, T.; Elliott, E. *Macromolecules* **2005,** *38*, 3482-3490.

2.2.9 Supporting Information

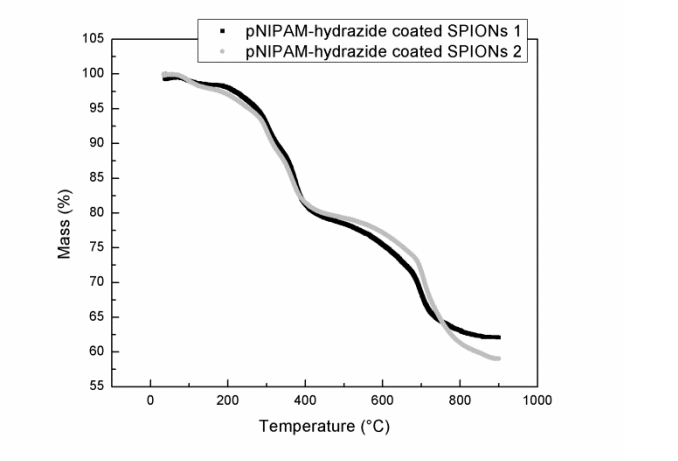

Figure S2.1: TGA of pNIPAM-hydrazide coated SPIONs.

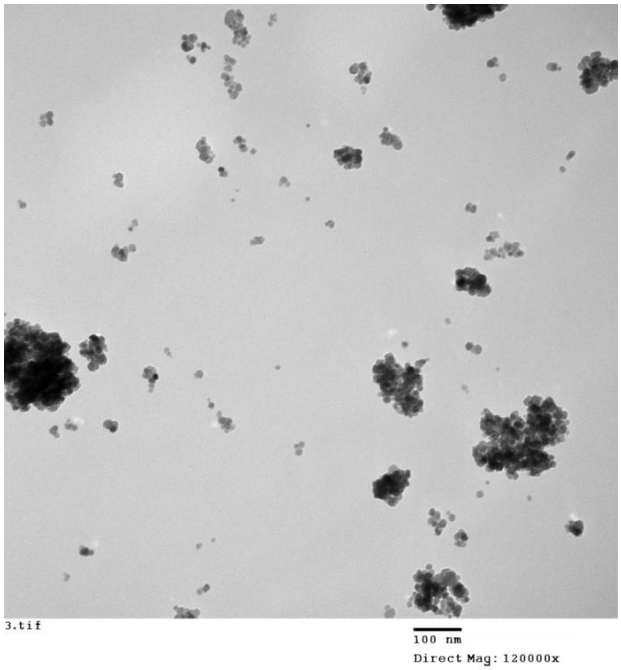

Figure S2.2: TEM of pNIPAM-hydrazide-coated SPIONs.

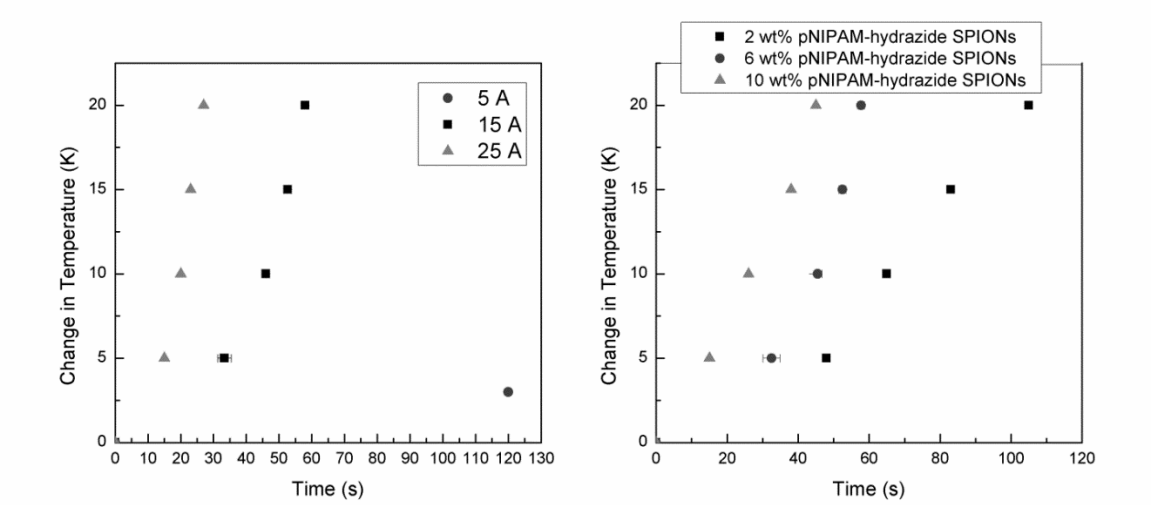

Figure S2.3: Heating characteristics of pNIPAM-hydrazide SPION solutions with varying (a) applied currents though the OMF with 6 wt% pNIPAM-hydrazide SPIONs and (b) pNIPAM-hydrazide SPION concentrations with an applied current of 15 A through the OMF.

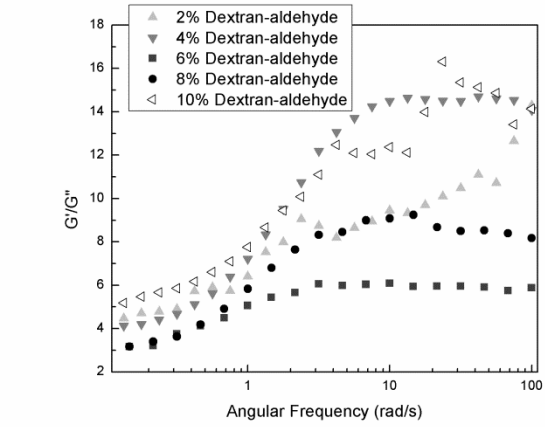

Figure S2.4: Ratio between storage and loss moduli (G/G") for composites of varying dextran-aldehyde content.

Table S2.2: Example of multiple compressive cycles at 2.5 mm/min followed by measurement 1 minute after compression is halted for 8 wt.% dextran-aldehyde composite disks.

Compression Cycle	Height (mm)	Diameter (mm)
Initial	6.36	7.66
1	6.2	7.74
2	6.3	7.63
3	6.22	7.62

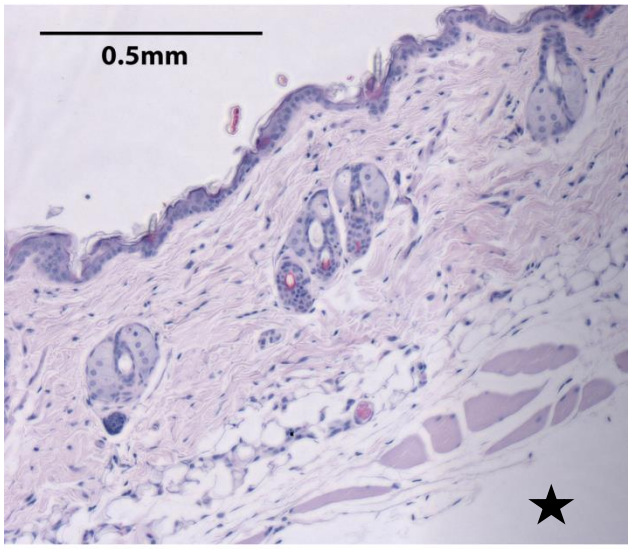

Figure S2.5: Host response toward 10 mM PBS subcutaneous injections at the acute time point (3 days). The site of subcutaneous injection is indicated by a black star.

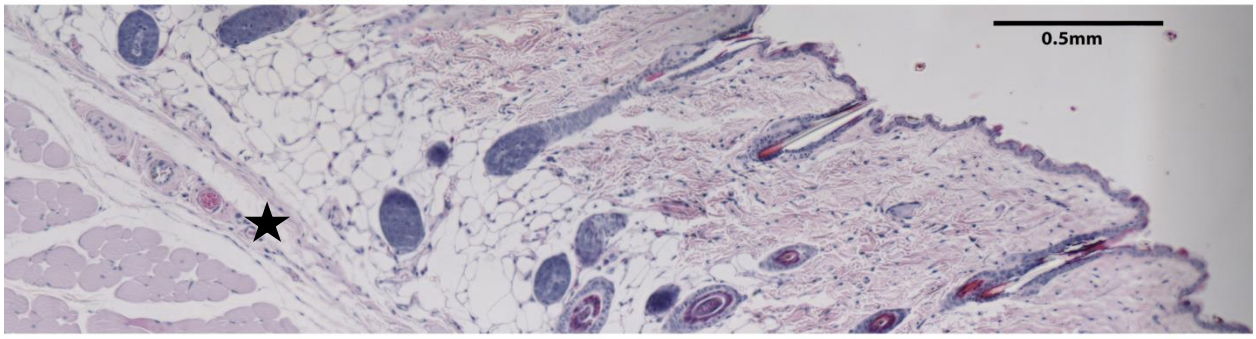

Figure S2.6: Host response toward 10 mM PBS subcutaneous injections at the chronic time point (5 weeks). The site of subcutaneous injection is indicated by a black star.

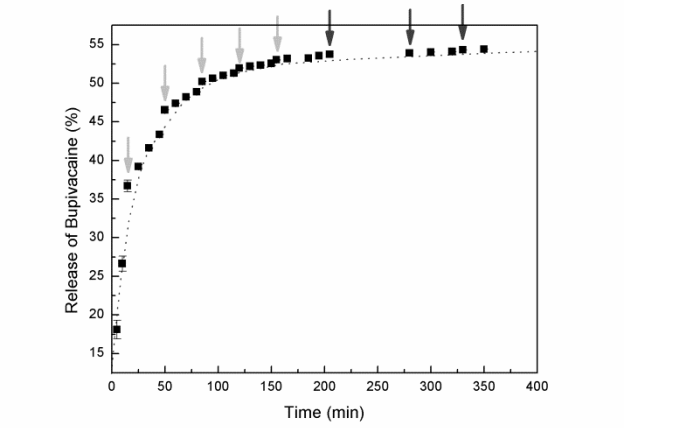

Figure S2.7: Pulsed external OMF-induced cumulative release of bupivacaine with an 8 wt.% dextran-aldehyde composite. The release rates directly after pulses are indicated by the arrows, with pulses of 5 and 10 minutes in duration indicated by light grey and dark grey arrows respectively. The dashed line estimates the baseline drug release in the absence of pulses.

Chapter 3: Microgel- and SPION-embedded hydrogel nanocomposites

3.1 Preface

This publication stemmed from the surprisingly good AMF-mediated release experiment from the previous superparamagnetic hydrogel project. The initial goal here was to try and develop a material that could exhibit a better release ratio between the on- and off-states of AMF application. The designed nanocomposite involved thermosensitive, PNIPAM-based microgels and SPIONs entrapped within an injectable hydrogel matrix. These microgel-SPION-hydrogel materials were used for two publications: a communication on the mechanism of release from these materials, described here, and a larger paper on the impact of various parameters on the AMF-mediated drug release, described in Chapter 4.

Herein, the drug release mechanism from nanocomposites was determined to be that when the AMF is applied, the SPIONs produce heat and transfer this heat to the microgel components, which causes them to shrink (or deswell) and generate pore space that encourages enhanced release from the materials. This process is completely reversible such that when the AMF is removed, the material returns to its ambient temperature and the microgels reswell and inhibit enhanced release. Pulsatile release experiments found that the ratio in release rates between the on- and off-states of AMF application were increased to a ~4:1 ratio, which is quite high for an injectable nanocomposite hydrogel AMF application. Furthermore, we showed that the application AMF pulses continued to result in an enhanced level of drug release for up to an unprecedented 4 days with these materials.

3.2 Enhanced pulsatile drug release from injectable magnetic hydrogels with embedded thermosensitive microgels

Campbell, S., Maitland, D., and Hoare, T. *ACS Macro Lett.* **2015**, *4*(3), 312-316.

3.2.1 Abstract

Nanocomposite *in situ*-gelling hydrogels containing both superparamagnetic iron oxide nanoparticles (SPIONs) and thermoresponsive microgels are demonstrated to facilitate pulsatile, high-low release of a model drug (4 kDa fluorescein-labelled dextran). The materials can be injected through a minimally-invasive route, facilitate a ~4-fold enhancement of release when pulsed on relative to the off state, and, in contrast to previous gel-based systems, can maintain pulsatile release properties over multiple cycles and multiple days instead of only hours. Optimal pulsatile release is achieved when the microgel transition temperature is engineered to lie just above the (physiological) incubation temperature. Coupled with the demonstrated degradability of the nanocomposites and the cytocompatibility of all nanocomposite components, we anticipate these nanocomposites have potential to facilitate physiologically-relevant, controlled pulsatile drug delivery.

Keywords: hydrogels, microgels, SPIONs, poly(N-isopropylacrylamide), pulsatile release, magnetic release, controlled release.

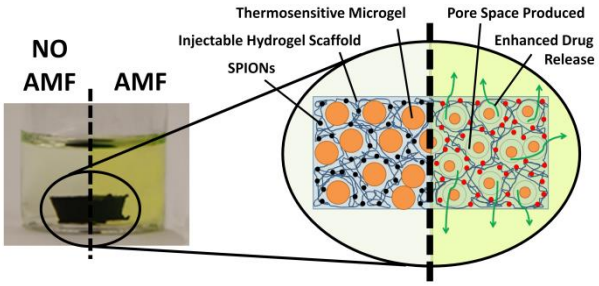

3.2.2 Triggered release from magnetic 'plum pudding' nanocomposites

Significant progress has been made in the development of "smart" polymer-based biomaterials for the purpose of drug delivery, exploiting polymers that are responsive to temperature,[1,2] pH,[3,4] light,[5,6] electric fields,[7] or specific molecule concentrations (such as glucose)[8,9] to induce on-demand or environment-specific release kinetics. Thermoresponsive hydrogels and microgels based on temperature-responsive poly(N-isopropylacrylamide) (PNIPAM)[10,11] that exhibit a volume phase transition temperature (VPTT) upon heating[14] have been used to fabricate several potential drug delivery biomaterials with temperature-dependent release kinetics.[15–17] Composite materials that combine thermosensitive hydrogels with nanomaterials that generate heat in response to specific external signals, such as carbon nanotubes (near-IR)[18,19], gold nanorods (near-IR)[20–22], or superparamagnetic iron oxide nanoparticles (SPIONs, alternating magnetic field)[23,24] have attracted particular interest since the inorganic actuating nanoparticles can be used to non-invasively induce temperature-dependent swelling/deswelling responses *in vivo* without the need for implanted electronics.[16] The design of the nanocomposite can regulate whether release occurs via bursts of drug on-demand[25] or via an up-regulation of release kinetics over an extended period of time.[26]

We have previously reported an injectable, degradable *in situ*-gelling hydrogel nanocomposite material in which SPIONs were covalently bound into the hydrogel network structure, fabricated by reacting aldehyde-functionalized dextran with hydrazide-functionalized PNIPAM-coated SPIONs[27–29]. The resulting hydrogel nanocomposite exhibited surprising mechanical strength (up to ~60 kPa shear modulus) and, notably, an ability to deliver pulsatile releases of drug upon the induction of an alternating magnetic field (AMF).[30] Relative to previous reports of materials or devices exhibiting pulsatile release kinetics, the *in situ*-gelling hydrogel approach described offers significant advantages in terms of representing an injectable, minimally-invasive method of creating a bulk implant inside the body; the hydrogel portion of the material also helps to minimize non-specific protein adsorption. However, the observed increase in drug release upon AMF application was both too small relative to the baseline release in the absence of the AMF and too short-lived (i.e. exhausted in less than one day) for practical use as an on-demand drug delivery material.

Herein, we report on the use of an injectable, degradable hydrogel-thermoresponsive microgel-SPION nanocomposite hydrogel that addresses these challenges. While microgels themselves have been investigated for therapeutic delivery, they are typically quickly sequestered by the lymphatic system.[31,32] Encapsulating microgels in a hydrogel both prevents this rapid sequestration and limits the burst release of drugs typically observed from hydrogels to permit sustained release of even small molecule drugs over several weeks.[33] Furthermore, by using SPIONs as an actuator, thermosensitive microgels can be driven to deswell via externally-mediated heating, generating free volume in the hydrogel to enhance drug release.

The *in situ*-gelling hydrogel matrix consists of thermosensitive hydrazide-functionalized PNIPAM (PNIPAM-Hzd) cross-linked with aldehyde-functionalized dextran (Dex-Ald); these materials form a hydrolytically-degradable hydrazone cross-linked network within seconds following co-extrusion from a double-barrel syringe. Two types of SPIONs were incorporated into these networks: (1) PNIPAM-Hzd functionalized SPIONs that covalently cross-link directly to the hydrogel matrix and (2) polyethylene glycol (PEG)-functionalized SPIONs that are physically entrapped within the hydrogel. The thermoresponsive microgels were prepared by copolymerizing NIPAM with N-isopropylmethacrylamide (NIPMAM) to obtain microgels that exhibit a 90% decrease in volume when heated from 37°C to 43°C (i.e. from physiological temperature to the maximum temperature before which local tissue damage is observed[34], Figure S3.1). These microgels are physically entrapped inside the hydrogel upon *in situ* gelation to form microgel-filled macropores within the bulk gel. When an AMF is applied, the heat generated by SPIONs raises the local temperature of the microgels above their VPTT, creating free volume within the composite that promotes increased drug diffusion through the hydrogel (Figure 3.1). Upon removal of the AMF, the microgels re-swell, re-filling the pores and decreasing the rate of drug release, facilitating high-low pulsatile release behavior dependent on the time over which the AMF was applied. While this mechanism has been demonstrated with bulk reservoir-based, non-degradable devices that would require surgical implantation[26,35], such behavior has not been demonstrated with a matrix that can undergo gelation *in situ* upon injection from easily injectable, low-viscosity precursor components and ultimately degrades into cytocompatible materials that would have significant advantages from a practical utilization standpoint.

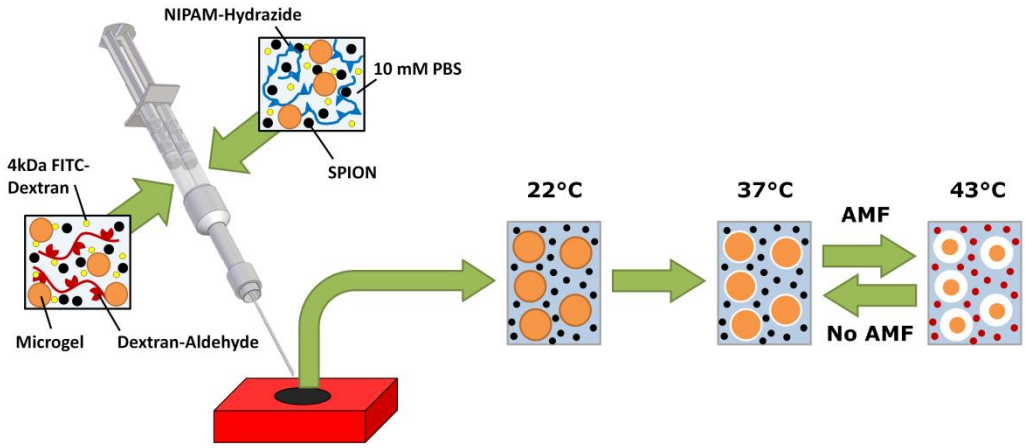

Figure 3.1: Fabrication of nanocomposites and their proposed mechanism of externally AMF-controlled enhanced drug release.

Composites were fabricated by mixing 10 mM PBS solutions of the reactive hydrogel precursors (8 wt% for each polymer, loaded into separate barrels of the double-barrel syringe) with 5 wt% SPIONs (loaded in both barrels), 1 wt% of 4 kDa FITC-dextran (used as the model therapeutic for tracking release, loaded in both barrels), and (if present) 8 wt% (by dry weight) microgels (loaded in both barrels) (Figure 3.1). Thermogravimetric analysis confirmed that all final composites contained ~5 wt% SPIONs (Figure S3.2), and SQUID analysis confirmed the nanocomposite hydrogels maintained superparamagnetic properties (Figure S3.3). In addition, the nanocomposites are confirmed to be degradable in accelerated hydrolysis conditions (~240 hour lifetime in pH 1 buffer, Figure S3.4), a similar time frame to our previously reported PNIPAM-SPION nanocomposites that degrade over ~8 months in *in vitro* physiological conditions.[30]

To examine the potential of using an AMF to control release from these injectable superparamagnetic nanocomposites, samples with 5 wt% PEG-SPIONs, 8 wt%

p(NIPAM-NIPMAM) microgels, and 1 wt% 4 kDa FITC-dextran were placed in our AMF apparatus that maintains a baseline temperature of 37°C (Figure S3.5) and exposed to a 2 hour continuous AMF application, heating the nanocomposites to an equilibrium temperature of ~43°C. Figure 3.2 shows the cumulative release of FITC-dextran from composites prepared with both microgels and PEG-SPIONs, microgels but no PEG-SPIONs, and PEG-SPIONs but no microgels.

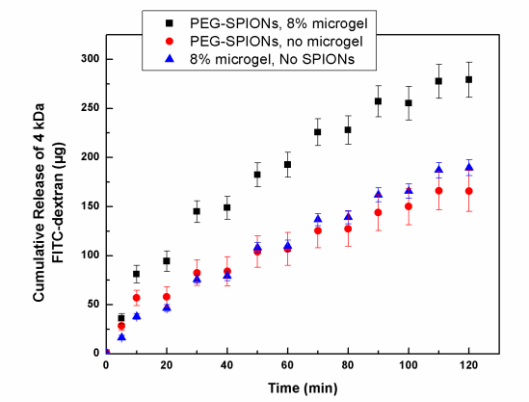

Figure 3.2: Cumulative release of 4 kDa FITC-dextran over two hours of AMF exposure from a nanocomposite with 5% PEG-SPION and 8% p(NIPAM-NIPMAM) microgel content compared to control composites prepared without SPIONs and without microgel, respectively.

Significantly more release was observed from the nanocomposite prepared with both microgels and SPIONs than composites excluding either component ($p < 0.05$). Hydrogel nanocomposites lacking SPIONs do not heat significantly in response to AMF (i.e. there is no stimulus to drive microgels deswelling), while nanocomposites without microgels do heat but have no mechanism by which to generate free volume upon heating. Of note, Figure 3.2 indicates that the longer the AMF is left on, the more differential release can be achieved, suggesting the potential for dosing of a drug as a

function of pulse time. Qualitatively similar behavior is also shown for the release of sodium fluorescein (Figure S3.6), showing that an AMF significantly enhances drug release in dual nanoparticle-based nanocomposites for drugs of significantly different molecular weights.

Pulsatile release experiments were then conducted in which the AMF was applied for a 10 minute period and then shut off; the temperature of the composites increases from their baseline temperature of 37°C to ~43°C over this time. A typical release result is shown in Figure S3.7. Significantly enhanced release of 4 kDa FITC-dextran was observed immediately after each AMF application, followed by a rapid return to a baseline release rate when AMF was shut off. While the total dose of drug decreased over time as the concentration gradient of drug was reduced, multiple AMF applications (n = 4-6) performed on days 1, 2, and 3 following composite fabrication confirm that significant pulsatile release relative to the baseline can be achieved at each time point. The AMF-induced percent increases in FITC-dextran release (relative to the non-pulsed baseline release) for composites containing cross-linked PNIPAM-SPIONs and entrapped PEG-SPIONs with and without microgels are shown in Figure 3.3a. The corresponding swelling responses of the nanocomposites during the time frame of the release experiment are shown in Figure 3.3b.

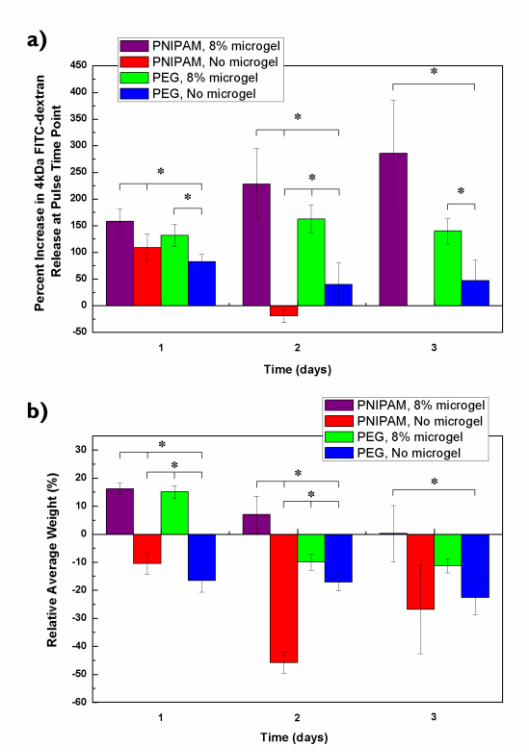

Figure 3.3: (a) Increase in release rate of FITC-dextran in response to a magnetic pulse and (b) swelling characteristics for nanocomposite hydrogels prepared with PNIPAM-SPIONs and PEG-SPIONs. * = $p < 0.05$ in a pair-wise comparison.

Both composites with entrapped PEG-SPIONs and cross-linked PNIPAM-SPIONs displayed AMF-mediated enhanced release over multiple days when microgels were incorporated. The application of short AMF pulses (<10 min) resulted in a ~4-fold increase in the release rate relative to the baseline after the first day, an enhancement that is repeatable over multiple pulsing cycles. The percentage increase in FITC-dextran release facilitated by the PEG-SPION and PNIPAM-SPION-based nanocomposites was not significantly different ($p > 0.05$, Figure 3.3a), despite the storage modulus of nanocomposites prepared with PNIPAM-SPIONs being significantly higher than that of nanocomposites based on PEG-SPIONs ($p < 0.05$, Figure S3.8); this result suggests

that it is the microgel phase rather than the properties of the bulk network that primarily drives pulsatile drug release. This hypothesis is further supported by the observation that both composite types prepared without microgels showed limited enhanced release after the first day while microgel-impregnated nanocomposites continued to facilitate pulsatile release over at least three days (Figure 3.3a), to the best of our knowledge unique for any injectable hydrogel-based system.

The macroscopic hydrogel swelling responses (Figure 3.3b) can be used to rationalize the differences in release behavior between nanocomposites with or without microgels. Microgel-embedded composites tend to initially swell (attributable to the higher solids fraction of the microgel relative to the bulk hydrogel phase that creates an enhanced osmotic gradient) followed by a period of deswelling as the gel equilibrates at 37°C (attributable to PNIPAM-Hzd collapse); in contrast, nanocomposites without microgels deswell throughout the entire release period. As such, on day 1, bulk swelling would promote higher baseline (non-AMF) FITC-dextran release from the microgel-containing nanocomposites, resulting in similar observed percentage increases in FITC-dextran release relative to nanocomposites prepared without microgel despite the higher absolute values of drug release achieved on each pulse. After one day, the microgel-containing composites have also deswelled, reducing their baseline release to the point that the microgels (and the accompanying enhancement in nanocomposite free volume upon AMF triggering) can significantly enhance the amount of FITC-dextran released upon triggering. Nanocomposites lacking SPIONs exhibit a similar swelling response to nanocomposites prepared with both SPIONs and microgels but show no discernable increase in FITC-dextran release in response to AMF pulses, confirming that the AMF is specifically driving pulsatile release in this system (Figure S3.9).

To further elucidate the proposed microgel deswelling mechanism of AMF-regulated enhanced release, further pulsatile release tests were performed using the PEG-SPION composites pre-incubated at different baseline temperatures: room temperature (22°C), physiological temperature (37°C), and the maximum temperature that magnetic composites reach during AMF application (43°C) (Figure 3.4a). The corresponding swelling results are shown in Figure 3.4b.

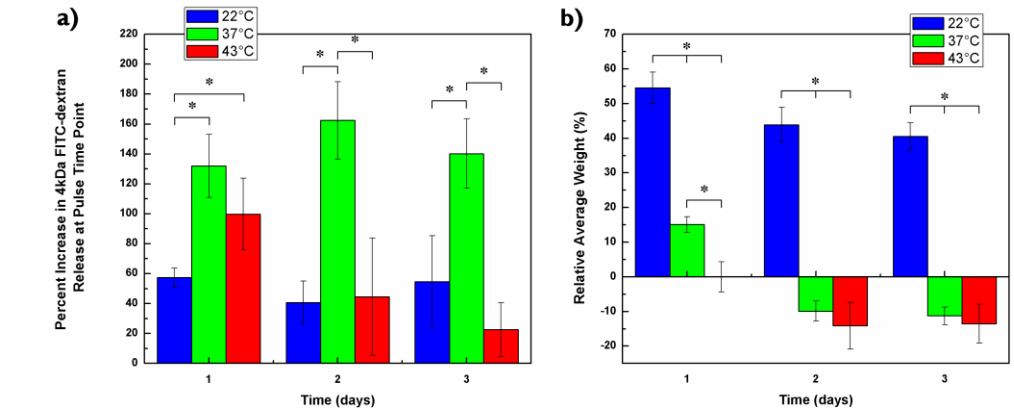

Figure 3.4: (a) Percentage increases in FITC-dextran release (relative to the baseline release in the absence of an AMF) and (b) relative swelling of the nanocomposites for PEG-SPION nanocomposites incubated at different baseline temperatures. * = $p < 0.05$ in a pair-wise comparison.

Significantly enhanced FITC-dextran release was observed for composites incubated at 37°C relative to the other two test temperatures upon AMF triggering. Given that the microgel experiences a 90% volume change from 37°C-43°C (Figure S3.1), heating via AMF application will only drive a significant phase transition in the microgel phase at a 37°C baseline temperature; nanocomposites incubated at 22°C would not heat up enough to drive microgel deswelling while nanocomposites incubated at 43°C would

contain microgels that are already largely collapsed above their VPTT, resulting in a high, “on”-state baseline release. Figure 3.4b again confirms that these release kinetics results are attributable directly to microgel swelling and not bulk gel swelling, as the 22°C and 43°C baseline tests both exhibit similar, significantly lower pulsatile release kinetics (Figure 3.4a) but highly divergent bulk swelling responses (Figure 3.4b). Note that the relatively higher percentage increase in release observed for the 43°C baseline test on day one is likely attributable to the large burst release observed for hydrogel composites incubated at higher temperatures.

In conclusion, incorporating thermoresponsive microgels inside injectable, degradable magnetic hydrogel composite materials significantly improves externally-regulated enhanced release via an AMF. In important contrast to previous hydrogel nanocomposites, these enhancements in release persist over several days instead of just hours. AMF pulses can increase the release rate of the 4 kDa FITC-dextran model drug used herein by a factor of four; based on our proposed release mechanism, a drug with a higher molecular weight may experience even further enhanced externally-modulated release. The increase in release is related to the relationship between the baseline incubation temperature and the microgel VPTT; manipulation of both these variables may be used to create pulsatile releasing hydrogel-based nanocomposites for other, non-physiological applications. All of the components of these nanocomposites also exhibit good cytocompatibility *in vitro* (Figure S3.10), suggesting that these materials may be promising candidates as externally-controlled release platforms for a variety of different drugs in applications that would benefit from repeated, pulsatile release (e.g. chronic local pain management or insulin delivery for diabetes treatment, among others).

3.2.3 Experimental Section

Synthesis of Nanocomposite Components: NIPAM-Hzd was produced via copolymerization of NIPAM and acrylic acid followed by EDC-mediated coupling of a large excess of adipic acid dihydrazide[36]. Dextran-Ald was prepared via sodium periodate-mediated oxidation of dextran[36]. Microgels were prepared by precipitation polymerization of NIPAM (36.2 mol% monomer), N-isopropylmethacrylamide (58.0 mol% monomer), and acrylamide (5.8 mol% monomer) using N,N-methylenebisacrylamide as the cross-linker and ammonium persulfate as the initiator.[35] SPIONs were prepared via redox of iron(II) chloride and iron(III) chloride salt precursor solutions using ammonium hydroxide as the base, followed by peptization of the surface with either PEG (8 kDa) or PNIPAM-Hzd at 80°C. See Supporting Information for full protocols.

Composite Formation: Entrapped SPION hydrogel nanocomposites were fabricated by first making 10 mM PBS solutions of the reactive hydrogel precursors (8 wt% PNIPAM-Hzd in barrel 1, 8 wt% Dex-Ald in barrel 2) with 5 wt% PEG-SPIONs, 1 wt% 4 kDa FITC-dextran, and 8 wt% microgels (each added in both barrels). Final composites with 1 wt% 4 kDa FITC-dextran, 5 wt% PEG-SPIONs, and either 0 wt% or 8 wt% microgel were produced by mixing the additives in both barrels of the double barrel syringes and ejecting the reactive cross-linking materials into silicone moulds (Figure 3.1). The hydrogel precursors gel *in situ* within 30s and the resulting nanocomposites take the shape of the silicon mould that they are placed in. Cross-linked PNIPAM-SPION-based nanocomposites were generated in a similar way but instead including 10 wt% PNIPAM-SPIONs in the hydrazide polymer-containing barrel only (to avoid premature cross-

linking), leading to final gels with similar polymer contents and 5 wt% overall SPION contents.[30] Control composites were made similarly but excluding one component.

Physical Characterization: SPION size and morphology was characterized by transmission electron microscopy (JEOL Ltd., Japan, Figure S3.11). The magnetic properties of both SPIONs and nanocomposites were determined using a Superconducting Quantum Interface Device (SQUID, Quantum Design MPMS SQUID Magnetometer). Storage and loss moduli of nanocomposites were measured using an ARES parallel-plate rheometer at room temperature (1 mm sample height, 8 mm diameter), using a frequency sweep from 0.1-100 rad/s at a constant strain within the linear viscoelastic region of the nanocomposite (n = 6). Nanocomposite swelling was measured by placing 6.3 mm diameter x 3.2 mm height samples in pre-weighed, perforated cell culture inserts and incubating the samples in 5 mL of 10 mM PBS at 37°C (n = 5). The composites were weighed immediately after gelation and then at pre-determined time intervals, following the removal of non-bound (surface) water via gentle wicking with a Kimwipe, to track percentage mass change over time. Nanocomposite degradation assays were performed in a similar manner, but using samples 9.5 mm in diameter x 6.3 mm in height and replacing the 10 mM PBS with a pH 1 buffer to accelerate the rate of hydrolysis.

Drug Release Experiments: A magnetic drug release apparatus was assembled to hold multiple (n = 4) composites in equivalent positions within the magnetic field while maintaining a constant temperature of 37°C (Figure S3.5). A jacketed flask, heated to 37°C via a water bath for the base experiments or 22°C or 43°C for the varying temperature experiments, was placed within a 2-coiled, 8 cm diameter solenoid operated

at 200 kHz, 30 A, and 1.3 kW to facilitate the application of an AMF. For the constant AMF experiments, nanocomposites (n = 4, 6.3 mm diameter x 3.2 mm height) were immersed in test tubes with 4 mL of 10 mM PBS and placed in the AMF for two hours. For pulsed AMF experiments, the same set-up was used but samples were collected at 10 minute intervals before and after 10 minute AMF pulsed applications, with separate pulses applied every 40 minutes and 4-6 pulses applied during each day of testing. In either case, at each sampling step, 3 x 200 µL samples were removed from each test tube and 600 µL fresh, 37°C (or, for the varying incubation temperature experiments, 22°C or 43°C) 10 mM PBS was added. The concentration of released 4 kDa FITC-dextran in each sample collected was then measured using a fluorescence plate reader (Perkin Elmer Victor3 V multilabel plate reader, 485 nm excitation/535 nm emission wavelength). The effect of the magnetic pulse on release was calculated as the percent increase in release rate between the measured value and the baseline release rate, which was determined based on a linear interpolation of the measured release rates at the two time points immediately prior to and the two points immediately after the pulse. Control gels (n = 4) were run concurrently with the pulsatile release tests using the same protocol and sampling times but without exposing the samples to the AMF.

Error and Statistical Significance: All error bars represent standard deviations ($n \geq 4$). Statistically significant differences between any pair of samples were determined using a two-tailed t-test with $p < 0.05$ assuming unequal variances.

3.2.4 Acknowledgements

The J.P. Bickell Foundation, the Natural Sciences and Engineering Research Council of Canada (NSERC), and the Vanier Canada Graduate Scholarships Program are gratefully acknowledged for funding.

3.2.5 References

(1) Arisaka, Y.; Kobayashi, J.; Yamato, M.; Akiyama, Y.; Okano, T. *Biomaterials*, **2013**, *34*, 4214–4222.

(2) Cheng, Y.; He, C.; Ding, J.; Xiao, C.; Zhuang, X.; Chen, X. *Biomaterials*, **2013**, *34*, 10338–10347.

(3) Urakami, H.; Hentschel, J.; Seetho, K.; Zeng, H.; Chawla, K.; Guan, Z. *Biomacromolecules*, **2013**, *14*, 3682-3688.

(4) Bhattacharya, S.; Eckert, F.; Boyko, V.; Pich, A. *Small*, **2007**, *3*, 650–657.

(5) Priimagi, A.; Cavallo, G.; Forni, A.; Gorynsztejn-Leben, M.; Kaivola, M.; Metrangolo, P.; Milani, R.; Shishido, A.; Pilati, T.; Resnati, G.; Terraneo, G. *Adv. Funct. Mater.*, **2012**, *22*, 2572–2579.

(6) Jochum, F. D.; Theato, P. *Chem. Comm.*, **2010**, *46*, 6717–6719.

(7) Ge, J.; Neofytou, E.; Cahill, T. J.; Beygui, R. E.; Zare, R. N. *ACS Nano*, **2011**, *6*, 227-233.

(8) Holtz, J. H.; Asher, S. A. *Nature*, **1997**, *389*, 829–832.

(9) Gordijo, C. R.; Koulajian, K.; Shuhendler, A. J.; Bonifacio, L. D.; Huang, H. Y.; Chiang, S.; Ozin, G. A.; Giacca, A.; Wu, X. Y. *Adv. Funct. Mater.*, **2011**, *21*, 73–82.

(10) Pelton, R. H.; Chibante, P. *Colloids and Surfaces*, **1986**, *20*, 247–256.

(11) Seo, K.; Doh, J.; Kim, D. *Langmuir*, **2013**, *29*, 15137-15141.

(12) Lutz, J.-F. *Adv. Mater.*, **2011**, *23*, 2237–2243.

(13) Smeets, N.; Bakaic, E.; Patenaude, M.; Hoare, T. *Chem. Comm.*, **2014**, *50*, 3306-3309.

(14) Pelton, R. *Adv. Colloid Interface Sci.*, **2000**, *85*, 1–33.

(15) Dvir, T.; Timko, B. P.; Kohane, D. S.; Langer, R. *Nat. Nanotechnol.*, **2011**, *6*, 13–22.

(16) Campbell, S. B.; Hoare, T. *Curr. Opin. Chem. Eng.*, **2014**, *4*, 1–10.

(17) Timko, B. P.; Dvir, T.; Kohane, D. S. *Adv. Mater.*, **2010**, *22*, 4925–4943.

(18) Chen, Y.-S.; Tsou, P.-C.; Lo, J.-M.; Tsai, H.-C.; Wang, Y.-Z.; Hsiue, G.-H. *Biomaterials*, **2013**, *34*, 7328–7334.

(19) Fujigaya, T.; Morimoto, T.; Niidome, Y.; Nakashima, N. *Adv. Mater.*, **2008**, *20*, 3610–3614.

(20) Wu, W.; Shen, J.; Banerjee, P.; Zhou, S. *Biomaterials*, **2010**, *31*, 7555–7566.

(21) Zhao, X.; Wang, T.; Liu, W.; Wang, C.; Wang, D.; Shang, T.; Shen, L.; Ren, L. *J. Mater. Chem.*, **2011**, *21*, 7240-7247.

(22) Brazel, C. S. *Pharm. Res.*, **2009**, *26*, 644–656.

(23) Chiang, W.-H.; Ho, V. T.; Chen, H.-H.; Huang, W.-C.; Huang, Y.-F.; Lin, S.-C.; Chern, C.-S.; Chiu, H.-C. *Langmuir*, **2013**, *29*, 6434–6443.

(24) Deka, S. R.; Quarta, A.; Di Corato, R.; Falqui, A.; Manna, L.; Cingolani, R.; Pellegrino, T. *Langmuir*, **2010**, *26*, 10315–10324.

(25) De Las Heras Alarcon, C.; Pennadam, S.; Alexander, C. *Chem. Soc. Rev.*, **2005**, *34*, 276–285.

(26) Hoare, T.; Santamaria, J.; Goya, G. F.; Irusta, S.; Lin, D.; Lau, S.; Padera, R.; Langer, R.; Kohane, D. S. *Nano Lett.*, **2009**, *9*, 3651–3657.

(27) Hoffman, A. S. *Adv. Drug Deliv. Rev.*, **2012**, *64*, 18–23.

(28) Patenaude, M.; Campbell, S.; Kinio, D.; Hoare, T. *Biomacromolecules*, **2014**, *15*, 781-790.

(29) Malda, J.; Visser, J.; Melchels, F. P.; Jüngst, T.; Hennink, W. E.; Dhert, W. J. A.; Groll, J.; Hutmacher, D. W. *Adv. Mater.*, **2013**, 25, 5011-5028.

(30) Campbell, S. B.; Patenaude, M.; Hoare, T. *Biomacromolecules*, **2013**, *14*, 644–653.

(31) Hendrickson, G. R.; Lyon, L. A. *Angew. Chem. Int. Ed.*, **2010**, *49*, 2193–2197.

(32) Kesselman, L. R. B.; Shinwary, S.; Selvaganapathy, P. R.; Hoare, T. *Small*, **2012**, *8*, 1092–1098.

(33) Sivakumaran, D.; Maitland, D.; Hoare, T. *Biomacromolecules*, **2011**, *12*, 4112–4120.

(34) Jordan, A.; Scholz, R.; Wust, P.; Schirra, H.; Schiestel, T.; Schmidt, H.; Felix, R. *J. Magn. Magn. Mater.*, **1999**, *194*, 185-196.

(35) Hoare, T.; Timko, B. P.; Santamaria, J.; Goya, G. F.; Irusta, S.; Lau, S.; Stefanescu, C. F.; Lin, D.; Langer, R.; Kohane, D. S. *Nano Lett.*, **2011**, *11*, 1395–1400.

(36) Patenaude, M.; Hoare, T. *Biomacromolecules*, **2012**, *13*, 369–378.

3.2.6 Supporting Information

Detailed experimental protocols

Materials: Acrylamide (AAm; ≥ 99%), acrylic acid (AA; 99%), ammonium hydroxide (28-30% NH_3 content), ammonium persulfate (APS; 98%), dextran from *Leuconstroc spp* (MW ≈ 500,000), ethylene glycol (99.8%), fluorescein isothiocyanate-labelled dextran (FITC-dextran, MW ≈ 4 kDa), iron(II) chloride tetrahydrate (98%), iron(III) chloride hexahydrate (97%), N'-ethyl-N-(3-dimethylaminopropyl)-carbodiimide (EDC; commercial grade), N-N'-methylene bisacrylamide (MBA; 99%), N-isopropylmethacrylamide (NIPMAM; 97%), poly(ethylene glycol) (PEG; 8 kDa), sodium periodate (>99.8%), and thioglycolic acid (≥ 98.1%) were all purchased from Sigma Aldrich (Oakville, Ontario). 2,2-azobisisobutyric acid dimethyl ester (AIBME; 98.5%) was purchased from Wako Chemicals. Adipic acid dihydrazide (ADH; 98%) was purchased from Alfa Aesar (Ward Hill, MA). N-isopropylacrylamide (NIPAM; 99%) was purchased from Thermo Fisher Scientific (New Jersey, NJ). Deionized water (DIW) was purified using a Barnstead Nanopure water purification system. 3T3 *Mus musculus* mouse fibroblast cells, purchased from Cedarlane Laboratories Ltd. (Burlington, ON), were cultured in proliferation media containing Dulbecco's Modified Eagle Medium-high glucose (DMEM), fetal bovine serum (FBS), and penicillin streptomycin (PS), all received from Invitrogen Canada (Burlington, ON). Trypsin-EDTA was acquired from Invitrogen Canada (Burlington, ON).

Synthesis of NIPAM-Hzd: Synthesis of NIPAM-Hzd was based on methods described by Patenaude and Hoare.[34] First, NIPAM-co-AA was prepared by dissolving purified

NIPAM (4.0 g, recrystallized with a 3:2 toluene-hexane mixture), acrylic acid (0.952 mL), AIBME (0.056 g), and thioglycolic acid (87 µL) in 20 mL of ethanol. The polymerization was continued overnight at 56°C under nitrogen. The ethanol was removed using a rotary evaporator, and the viscous product was dissolved in 200 mL of DIW. The resulting solution was dialyzed against DIW for six 6+ hour cycles and lyophilized. Subsequently, NIPAM-co-AA (3.0 g) and a five times molar excess of adipic dihydrazide (ADH, 7.25 g) were dissolved in 600 mL DIW. A 2.5 times molar excess of N'-ethyl-N-(3-dimethylaminopropyl)-carbodiimide (EDC, 3.99 g) dissolved in 5 mL of DIW was quickly added to the solution, and dropwise addition of 0.1 M hydrochloric acid was used to maintain the pH at 4.75 for 4 hours, after which the pH was neutralized. The resulting solution was dialyzed against DIW for six 6+ hour cycles and lyophilized. The degree of hydrazide functionalization of the polymer after EDC/NHS reaction was determined by potentiometric titration to be 8.3 ± 0.4 mol% (on a total monomer basis).

Synthesis of Dex-Ald: Dextran (500 kDa, 3.0 g) was dissolved in 300 mL of DIW. Sodium periodate (1.6 g) was dissolved in 15 mL of DIW and added dropwise to the polymer solution, after which the solution was left to stir for 2 hours. Ethylene glycol (0.8 mL) was then added to the solution to inhibit further oxidation of the dextran and the resulting solution was stirred for an additional hour, dialyzed against DIW for six 6+ hour cycles, and lyophilized. Potentiometric titration following silver oxidation (as described by Patenaude et al.[26]) indicated that 17.2% of dextran residues underwent oxidative cleavage after periodate oxidation.

Synthesis of Poly(NIPAM-NIPMAM) Microgel: Poly(NIPAM-NIPMAM) microgels were produced using a method described by Hoare et al.[33] AAm (0.05 g), MBA (0.08 g), and purified NIPAM (0.5g) and NIPMAM (0.9g) monomers were dissolved in 150 mL of DIW. After purging with nitrogen and heating to 70°C, APS (0.10 g) dissolved in 5 mL of DIW was added to the solution. The reaction proceeded overnight under nitrogen, after which the resulting suspension was dialyzed and lyophilized. The temperature-responsive behavior of the p(NIPAM-NIPMAM) microgels was determined by dynamic light scattering using a Brookhaven 90Plus Particle Analyser, measuring particle size at 1°C intervals.

Synthesis of PEG-SPIONs and PNIPAM-SPIONs: Surface-functionalized SPIONS were produced using a method similar to that described by Campbell and Hoare.[28] Iron(III) chloride hexahydrate (3.04 g) and iron(II) chloride tetrahydrate (1.98 g) were dissolved in a 2:1 molar ratio in 12.5 mL of DIW. Ammonium hydroxide (6.5 mL) was added drop-wise under magnetic mixing at 500 rpm over 10 minutes. After an additional 10 minutes of mixing, PEG (MW= 8 kDa, 1.0 g) dissolved in 10 mL of DIW or PNIPAM-Hzd (2.0 g) dissolved in 15mL of DIW was added to the iron mixture. The mixture was heated to 80°C for 2 hours to peptize the SPION surface with PEG or PNIPAM-Hzd, after which the ferrofluid was cooled, washed using magnetic separation against 10 mM PBS, and concentrated using a permanent magnet over five magnetic separation/purification cycles). The SPION concentration in the purified suspension was determined gravimetrically and diluted to make 5 wt% SPION composites. Transmission electron microscopy (JEOL Ltd., Japan) indicated the SPIONS had an average particle size in the range of 15-25 nm (Figure S3.11).

***In Vitro* Cytocompatibility Assay**: 3T3 *Mus musculus* mouse cells were used to assess the cytocompatibility of all of the components of the nanocomposites. 20,000 3T3 cells were cultured in each well of 24 well polystyrene plates with 1 mL of proliferation media and incubated for 12 h. The cells were then exposed to various concentrations of nanocomposite precursor materials (0.1, 0.4, 0.8, 1.2, 1.6, and 2.0 mg/mL) for 24 h. The solution covering the cells was aspirated and 250 µL of a 0.4 mg/mL MTT solution was then added to each well and the cells were incubated at 37°C for an additional 4 hours. The MTT solution was aspirated after the incubation period, and 500 µL of DMSO was added to each well to dissolve the insoluble formazan precipitate. 2 x 200 µL was removed from each well, transferred to a 96 well polystyrene plate, and read in a Biorad microplate reader (model 550) absorbance reader at 540 nm against a 749 nm baseline. The percent cell viability was calculated relative to positive, cell-only control wells using the equation:

$$Cell\ Viability\ (\%) = \frac{(absorbance_{polymer/SPION-exposed,540\ nm} - absorbance_{\frac{polymer}{SPION}exposed,749\ nm})}{(absorbance_{positive\ control,540\ nm} - absorbance_{positive\ control,749\ nm})}$$

For assays involving SPIONs, the SPIONs were separated from the formazan-DMSO solution via centrifugation at 3000 rpm for 10 minutes prior to measuring the absorbance of the solution.

Supporting Data

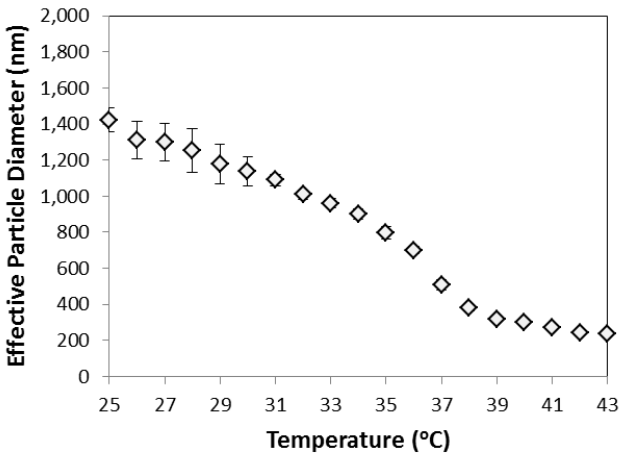

Figure S3.1: Volume phase transition behaviour of p(NIPAM-NIPMAM) microgels measured using dynamic light scattering. While the microgels deswell significantly at temperatures less than 37°C, there is a 90.0 ± 4.2 % decrease in their volume from 37°C (508 ± 31 nm diameter) to 43°C (236 ± 14 nm diameter).

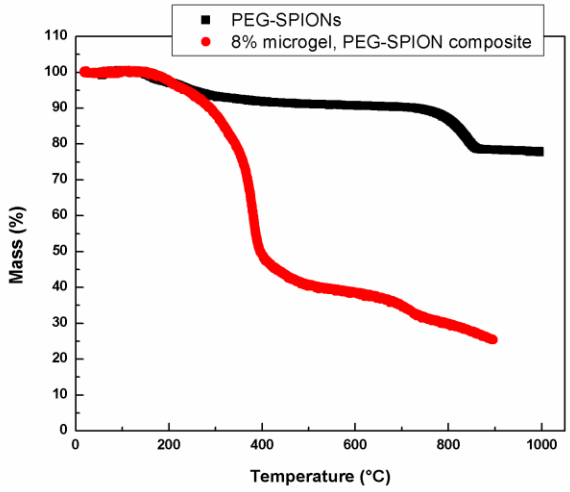

Figure S3.2: Thermogravimetric analysis of the base PEG-SPIONs and the hydrogel nanocomposites prepared with 5% PEG SPIONs and 8% microgel content. (Dry weight of the nanocomposites: ~40 wt% iron oxide; initial composites: ~86.8 ± 0.5 wt% water content.)

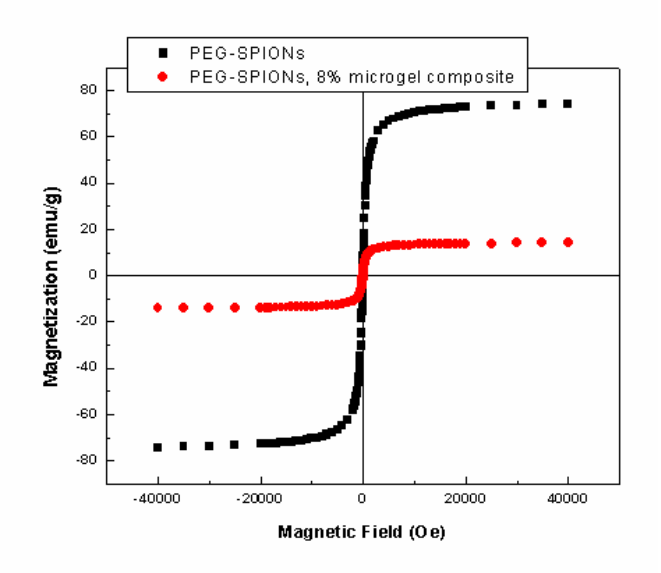

Figure S3.3: SQUID magnetization curves for the PEG-SPIONs and PEG-SPION hydrogel nanocomposites prepared with 8% microgel content, measured at 303K. The results confirm the superparamagnetism of the SPIONs as well as the nanocomposite hydrogels.

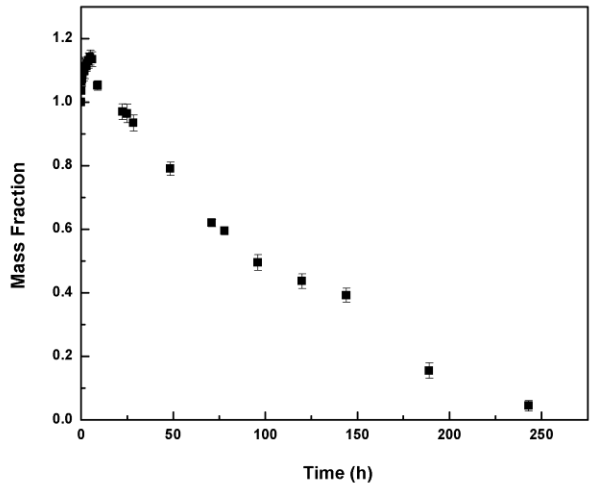

Figure S3.4: Accelerated degradation profile of PEG-SPION hydrogel nanocomposites with 8% microgel content incubated in a pH 1 buffer solution at 37°C, confirming that the nanocomposites are not only injectable, but also degradable. Note that this result at pH 1 is nearly identical to previous results reported for cross-linked PNIPAM-SPION hydrogels that degraded fully *in vitro* at physiological pH over eight months (Campbell et al.).[28]

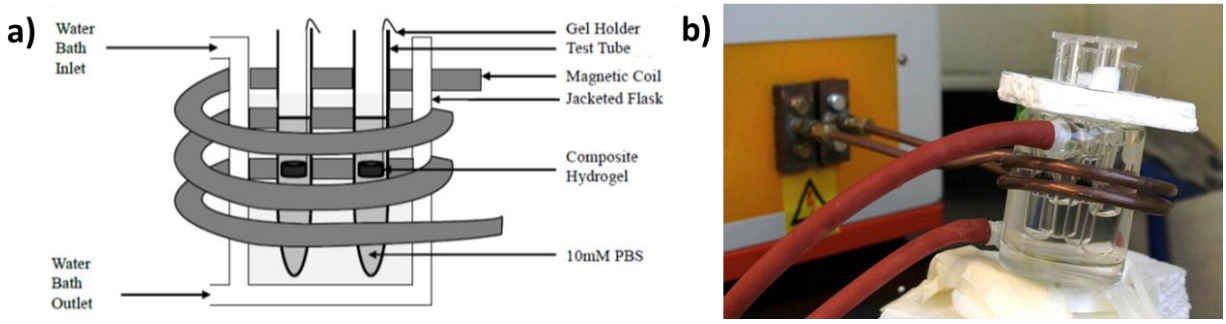

Figure S3.5: (a) Schematic and (b) photograph of experimental setup for pulsatile release experiments.

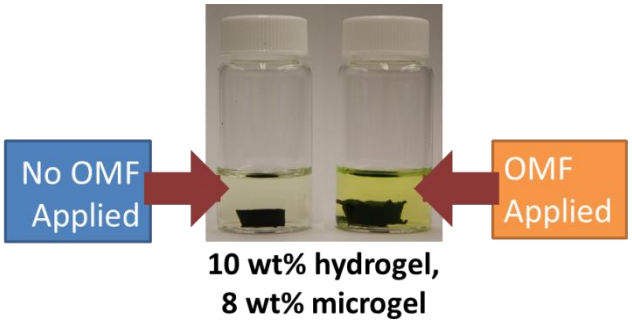

Figure S3.6: AMF-induced release of sodium fluorescein from nanocomposites prepared with 10 wt% hydrogel precursors, 5 wt% PEG-SPIONs, and 8 wt% microgel content. The clear difference in fluorescence intensity in the solution following a short 5 minute pulse indicates these nanocomposites are capable of releasing drugs with significantly different molecular weights in a pulsatile manner.

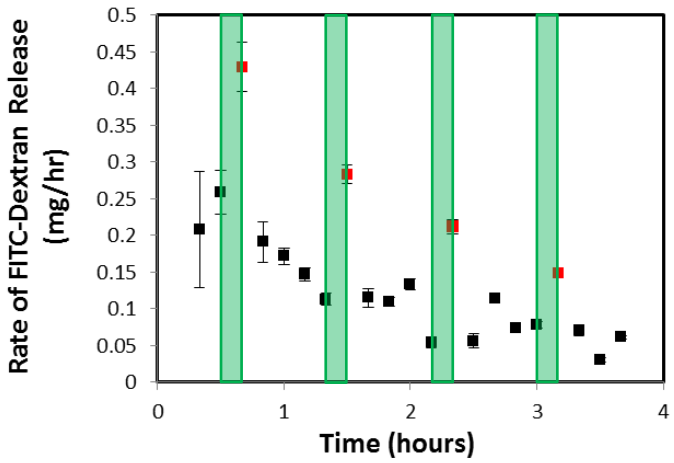

Figure S3.7: Characteristic release curve with 10 minute AMF applications. The red points represent the release rate calculated based on samples taken immediately after the application of a 10 minute AMF pulse (indicated by the green areas), while the black points represent release rates calculated after 10 minute periods without an AMF pulse.

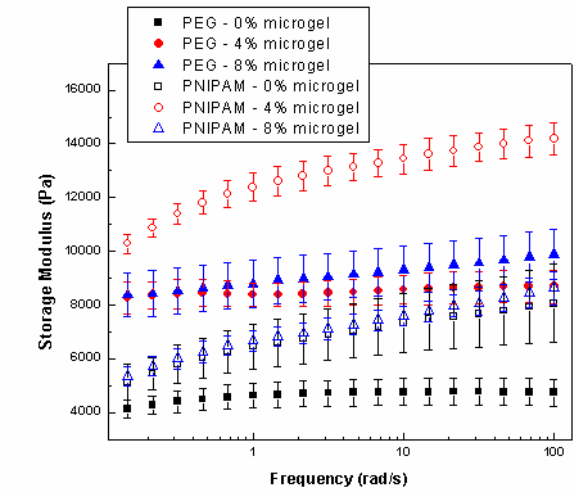

Figure S3.8: Elastic storage moduli of nanocomposites prepared using PNIPAM-SPIONs and PEG- SPIONs with varying microgel contents.

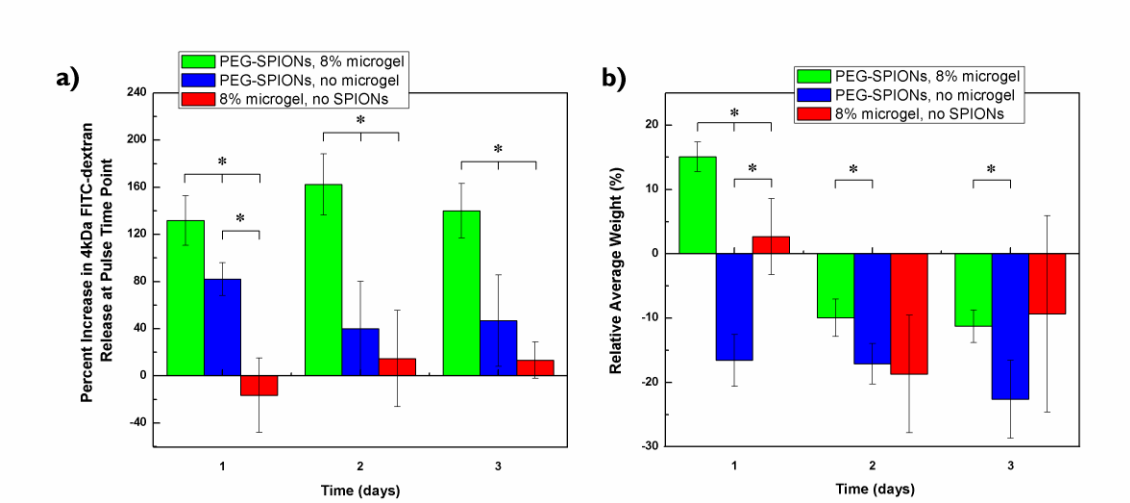

Figure S3.9: (a) Percentage increase in FITC-dextran release (relative to the baseline release in the absence of an AMF) and (b) relative swelling of nanocomposites prepared with or without PEG-SPION and microgel at 37°C * = $p < 0.05$ in a pair-wise comparison.

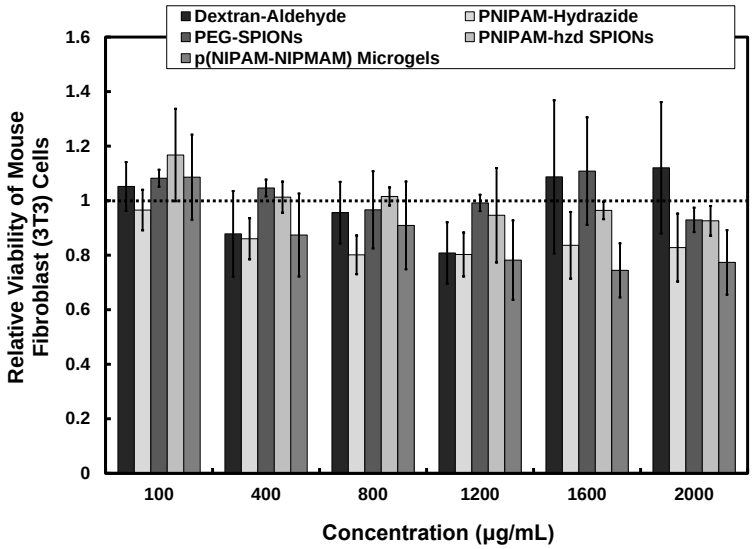

Figure S3.10: Cell viability of 3T3 mouse fibroblast cells exposed to SPION and microgel composite additives for 24 h. The dashed line represents the viability of control cells not exposed to any nanocomposite component. All components of the nanocomposite maintain high cell viabilities of >80% even at extremely high concentrations (2 mg/mL) for a contained *in vitro* assay.

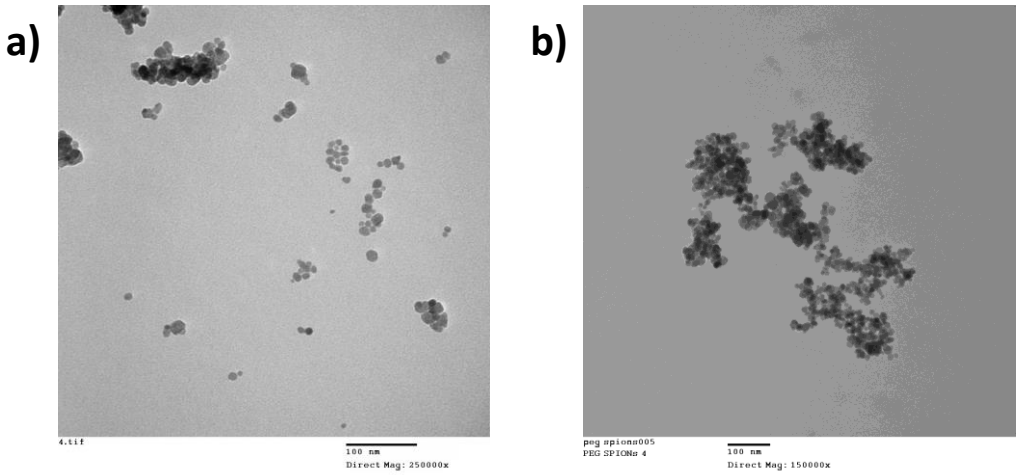

Figure S3.11: TEM images of (a) PNIPAM-coated and (b) PEG-coated SPIONs. The observed clustering on the copper grids during preparation for TEM is typical of hydrophilic nanoparticles. Sizes are consistently in the range of 15-25 nm for both types of modified SPIONs.

Chapter 4: Improving external control over release from microgel and SPION embedded hydrogel nanocomposites

4.1 Preface

This is the second part of the microgel-SPION-hydrogel nanocomposite material study. This chapter intends to improve/further understanding of the factors involving enhanced release from these nanocomposites. Various characteristics of the nanocomposites and AMF application process, such as the microgel volume phase transition temperature (VPTT), microgel content, hydrogel swelling characteristics, and the duration of the AMF pulse, were altered to observe their effect on the ratio in release rate between having the AMF in the on- versus off-state. Briefly, increasing the microgel content, operating around the VPTT of the microgels when heating/cooling via AMF, and minimizing the swelling of the hydrogel scaffold were all shown to enhance the release rate as a result of an applied AMF over the baseline release rate. Notably, the AMF pulse duration (between 10 and 20 minutes) did not affect the release rate, which could mean that the duration of application of the non-invasive AMF trigger could directly relate to the release of a specific, controlled dose of drug.

4.2 Controlling the resolution and duration of pulsatile release from injectable magnetic 'plum-pudding' nanocomposite hydrogels

Maitland, D.,[+] Campbell, S.B.,[+] Chen, J., and Hoare, T. *RSC Adv.* **2016**, *6*, 15770-15781.

[+] *These authors contributed equally to this work*

4.2.1 Abstract

Manipulation of the relative swelling and volume fractions of the microgel and bulk hydrogel phases of nanocomposite hydrogels containing superparamagnetic iron oxide nanoparticles (SPIONs) is demonstrated to enable higher on-off state resolution and enhanced total duration of pulsatile drug release potential when the nanocomposites are activated by an alternating magnetic field. Adjusting the microgel chemistry to create microgels that have less deswelling below 37°C and more proportional deswelling between 37°C and 43°C, increasing the volume fraction of microgels in the nanocomposite (while maintaining the mechanical stability of the nanocomposite), and limiting the swelling capacity of the surrounding hydrogel were all found to improve the degree of enhanced release that occurs after an externally-operated AMF pulse. Collectively, these results serve both to optimize the function of these nanocomposite materials for pulsatile drug delivery as well as confirm the proposed mechanism of pulsatile release, by which free volume is generated within the nanocomposite at the thermoresponsive microgel-bulk hydrogel interface upon internal heating of the device via SPION-driven hysteresis heating of the nanocomposite in an alternating magnetic field. Coupled with the injectability, degradability, mechanical stability, and

cytocompatibility of these nanocomposites, we anticipate potential applications as advanced 'smart' drug delivery technologies that can be operated via an external and non-invasive trigger.

Keywords: Hydrogels, microgels, SPIONs, poly(N-isopropylacrylamide), pulsatile release, magnetic release, controlled release.

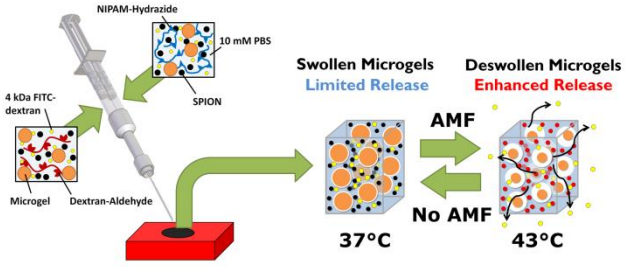

4.2.2 Introduction

In response to the understanding that spatial and temporal control over drug release has numerous advantages over conventional drug release, several "smart" biomaterials that respond to certain stimuli for therapeutic purposes have been developed in recent years.[1–5] Such materials facilitate more effective treatment options for diseases in which localizing the therapeutic agent at a particular site is critical (e.g. chemotherapy or chronic pain management[6–8]) and/or pulsatile control of release is desired (e.g. insulin delivery[9,10]). However, many of these responsive systems typically provide only a single pulse of drug release as the environment is changed, with limited potential for repeated pulsing *in vivo*. In addition, such responsive vehicles are inherently limited in terms of their adaptability to a variety of disease states in that they require differences in local biological or physical environments to target or trigger.

Instead, externally-actuated “on-demand” delivery vehicles that can be triggered by the application of a stimulus outside the body offer an alternative and more flexible option for pulsatile or on-demand drug delivery vehicle design. Such a device requires two major components: a switching material that modulates drug diffusion by altering its pore size, overall volume, or affinity for a target drug in response to a stimulus (e.g. temperature,[11–13] pH,[14–16] or solute concentrations[17,18]) and a transducing material that receives an external stimulus (e.g. ultrasound,[19] near-IR irradiation,[20] or alternating magnetic fields (AMFs)[21]) and translates that stimulus into a signal to which the switching material can respond to. Several such externally actuated systems have been developed for not only drug release, but also for tissue engineering, imaging, and hyperthermia treatments,[22–24] with each device often having multiple applications. A remarkable example of such technology is an implantable microchip device designed by Farra *et al*. that is able to deliver wirelessly-controlled pulsatile dosages of anti-osteoporosis drugs in human subjects.[25] However, these devices, and several similar systems,[26–28] require surgical implantation and would quickly develop a fibrous capsule *in vivo* due to the non-biomimetic physiochemical characteristics of the materials comprising the devices.

As a result of these limitations, an emerging research focus in pulsatile release composites involves the use of hydrogels, water-swollen cross-linked 3D networks of hydrophilic polymers, as the scaffold material given that they are physically and often-times chemically similar to soft tissues,[29,30] exhibit low protein adsorption leading to generally good biocompatibility,[30,31] can be loaded with drugs into their highly porous internal network,[32–34] and can act as a stimuli-responsive switching material to stimuli such as temperature, pH, or electric fields.[35–37] Hydrogel nanocomposites have been used to achieve temporal control over drug release with high/low release kinetics via a

variety of external mechanisms, including near-IR,[38–40] electric fields,[41,42] and AMFs[43,44]. However, few of these devices are functionally biodegradable or easily administered to a patient without requiring surgery, often requiring two invasive procedures (one for implantation and one for removal at the end of the device's functional lifetime) for practical use in the clinic.[30,41] Exceptions to this general rule include the work of Ge *et al*., who designed injectable nanocomposites composed of organic polypyrrole nanoparticles within a sol-gel forming hydrogel that exhibited exceptional dosage control over multiple days using electric fields,[41] and Wu *et al*., who fabricated an injectable hydrogel containing both physical and covalent cross-links between graphene oxide and peptides and used near-IR irradiation to break the physical cross-links to achieve pulsatile release *in vivo*.[30] However, the relatively low penetration distance of near-IR irradiation, in comparison to AMFs, and the need to create external electronics associated with these technologies require the hydrogel to be located closer to the skin for effective triggering.

An injectable system that is capable of externally and non-invasively triggering on/off or high/low dosing patterns of a therapeutic locally at a target site would significantly improve the potential translatability of these types of release vehicles to the clinic. Such a system would enable release kinetics to be tuned specifically to individual treatments, allowing for the potential to improve drug safety, reduce the risk of systemic side effects, and prolong the effective duration of action of a given drug delivery vehicle for better patient compliance.[39]

Injectable, *in situ*-gelling hydrogels that form via rapid covalent cross-linking of polymers functionalized with complementary reactive groups[45,46] offer a potential option for

creating such drug delivery vehicles. We have previously developed *in situ* gelling hydrogel networks created via the reaction of hydrazide-functionalized poly(N-isopropylacrylamide) (PNIPAM) and aldehyde-functionalized dextran to form hydrolytically degradable hydrazone cross-links.[47] By incorporating superparamagnetic iron oxide nanoparticles (SPIONs) directly into the network, exposure to an external alternating magnetic field (AMF) resulted in heat generation inside the hydrogel network via hysteresis heating of the SPIONs and (subsequently) a volume phase transition in the thermosensitive PNIPAM-containing bulk hydrogel. When drugs were loaded into these materials, they exhibited repeatable pulsatile release characteristics in response to AMF application. Recently, we enhanced both the duration of this pulsatile release potential as well as the resolution between the on- and off-states of drug release kinetics by incorporating thermoresponsive PNIPAM-based microgels into these SPION-hydrogel nanocomposite materials.[48] Enhanced release is achieved by externally heating these microgels above their volume phase transition temperature (VPTT), producing free volume within the nanocomposite that allows for more facile diffusional transport of therapeutic agents out of the gel (see Figure 4.1 for the proposed mechanism of release enhancement using microgels). However, further improvements are required for the use of these materials in a practical application, particularly in terms of extending the duration over which pulsatile drug delivery is possible and increasing the gap between release rates at the “off” (non-triggered) state and the “on” (triggered) states.

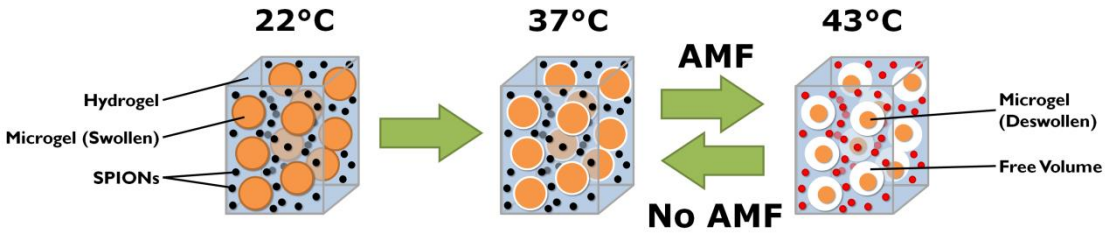

Figure 4.1: Mechanism of externally AMF-controlled enhanced drug release.

In light of the proposed mechanism for release enhancement, our aim in this work is to manipulate both the relative volume fractions as well as the relative volume changes (i.e. swelling responses) of both the bulk and microgel phases to better exploit this release mechanism for achieving prolonged and higher resolution pulsatile drug delivery. In particular, we demonstrate that increasing the microgel volume fraction, optimizing the phase transition temperature of the microgel to achieve the maximum possible volume change upon relevant triggering temperature changes, and minimizing the swelling response of the bulk gel can all improve the properties of these nanocomposite hydrogels for pulsatile drug delivery applications.

4.2.3 Experimental

Materials: Adipic acid dihydrazide (ADH; 98%) was purchased from Alfa Aesar (Ward Hill, MA). Dimethyl sulfoxide (DMSO) was purchased from Caledon Laboratory Chemicals (Georgetown, ON). Acrylamide (AAm; ≥ 99%), acrylic acid (AA; 99%), ammonium hydroxide, ammonium persulfate (APS; 98%), dextran from *Leuconostoc spp.* (MW ≈500,000), ethylene glycol (99.8%), fluorescein isothiocyanate-labelled

dextran (FITC-Dex; MW≈ 4 kDa), iron (II) chloride tetrahydrate (98%), iron (III) chloride hexahydrate (97%), N'-ethyl-N-(3-dimethylaminopropyl)-carbodiimide (EDC; commercial grade), N-N'-methylene bisacrylamide (MBA; 99%), N-isopropylmethacrylamide (NIPMAM; 97%), poly(ethylene glycol) (PEG; 8 kDa), sodium carboxymethyl cellulose (CMC, MW ≈ 700,000), sodium periodate (>99.8%), thiazolyl blue tetrazolium bromide (MTT), and thioglycolic acid (≥ 98.1%), were all acquired from Sigma Aldrich (Oakville, ON) and used without further purification. 2,2-azobisisobutyric acid dimethyl ester (AIBME; 98.5%) was purchased from Wako Chemicals. N-isopropylacrylamide (NIPAM; 99%) was purchased from J&K Scientific. 3T3 *Mus musculus* mouse fibroblast cells were obtained from Cedarlane Laboratories Ltd. (Burlington, ON) and were cultured in media containing Dulbecco's Modified Eagle Medium-high glucose (DMEM), fetal bovine serum (FBS), and penicillin streptomycin (PS) acquired from Invitrogen Canada (Burlington, ON). Trypsin-EDTA was also purchased from Invitrogen Canada (Burlington, ON). Deionized water (DIW) was purified using a Barnstead Nanopure water purification system.

Hydrazide-Functionalized PNIPAM (PNIPAM-Hzd) Hydrogel Precursor: Poly(NIPAM-co-AA) was synthesized using the method of Patenaude and Hoare.[49] Briefly, 4.0 g of purified NIPAM (recrystallized using a 3:2 toluene-hexane mixture), 1.0 g AA, 0.056 g AIBME, and thioglycolic acid (87 µL) were dissolved in 20 mL of ethanol, purged with nitrogen, heated to 56°C, and polymerized overnight. A rotary evaporator was used to remove the solvent, and the viscous product was dissolved in 200 mL of DIW and dialyzed against DIW for six 6h cycles. Following, 3.0 g of NIPAM-co-AA and a five-fold molar excess of ADH (7.25 g) were dissolved in 600 mL DIW. A 2.5 times molar excess of EDC (3.99 g) dissolved in 5 mL of DIW was added to the solution and the pH

was maintained at 4.75 manually via the addition of 0.1M HCl for 4 hours. The hydrazide-functionalized product was dialyzed against DIW for six 6h cycles and lyophilized. The degree of hydrazide functionalization was determined by potentiometric titration to be 8.2 ± 0.6 mol%.

Aldehyde Functionalization of Dextran/CMC (Dex-Ald, CMC-Ald) Hydrogel Precursor: Aldehyde-functionalized dextran (Dex-Ald) or aldehyde-functionalized carboxymethyl cellulose (CMC-Ald) was synthesized according to the method of Campbell *et al*.[47] 3.0 g of 500 kDa dextran or 700 kDa CMC was dissolved in 300 mL of DIW, following which 1.6 g of sodium periodate was dissolved in 15 mL of DIW, added dropwise to the polymer solution, and left to stir for 2 hours. The oxidation process was halted via the addition of 0.8 mL of ethylene glycol; after one hour of mixing, the product was dialyzed against DIW for six 6h cycles and lyophilized. Silver ion titration[50] indicated that 17.4% of dextran and 12.4% of CMC residues underwent oxidative cleavage after periodate oxidation.

Synthesis of Poly (NIPAM-NIPMAM) Microgels: Poly(NIPAM-NIPMAM) microgels were produced using methods described by Hoare *et al*.[43] Acrylamide (0.05 g), methylene bisacrylamide (0.08 g), and purified NIPAM and NIPMAM monomers (totaling 1.4 g) were dissolved in 150 mL of DIW, purged with nitrogen, and heated to 70°C. Ammonium persulfate (0.10 g) dissolved in 5 mL of DIW was then added to the solution, after which the reaction was allowed to proceed overnight. The microgels were then dialyzed against DIW for six 6h cycles and lyophilized. Microgels with differing NIPMAM:NIPAM ratios (and thus volume phase transition temperatures) were produced

by varying the relative amounts of NIPAM and NIPMAM used to prepare the microgels (Table 4.1).

Table 4.1: Microgel VPTTs (temperature at which different p(NIPAM-NIPMAM) microgels' effective diameters have decreased by 50% from their size at 26°C) and diameter changes between 25°C, 37°C, and 43°C for each microgel tested, all measured via dynamic light scattering.

Test Name	NIPMAM: NIPAM Ratio	NIPMAM Monomer (g)	NIPAM Monomer (g)	Microgel VPTT	% Change in Microgel Volume	
					From 25°C to 37°C	From 37°C to 43°C
$M_{1.8}$	1.8 : 1	0.9	0.5	38.6°C	-80 ± 7	-96 ± 6
M_1	1 : 1	0.7	0.7	37.9°C	-81 ± 5	-82 ± 3^
$M_{0.56}$	0.56 : 1	0.5	0.9	36.2°C	-96 ± 8	-90 ± 9
$M_{0.27}$	0.27 : 1	0.3	1.1	35.6°C	-98 ± 4	-75 ± 6

^ This size difference is based on the size of M_1 at 40°C instead of 43°C because the microgels aggregated before 43°C. The difference in size experienced by the microgels in the composite (where aggregation would not occur) is likely higher than this reported value.

The temperature-dependent size of the p(NIPAM-NIPMAM) microgels was determined by dynamic light scattering using a Brookhaven 90Plus Particle Analyzer. Lyophilized microgels were reconstituted in 0.15 M NaCl (saline) at a concentration of 1.5 mg/mL. Reading times for each measurement were 2 minutes per sample, with 4 repeat measurements taken at each temperature; the error bars represent the standard deviation of these repeated measurements (n = 4). Particle sizes were measured at 1°C intervals from 25°C to 50°C, allowing 5 minutes for temperature stabilization at each temperature point.

Synthesis of PEG-functionalized SPIONs: Iron (III) chloride hexahydrate (3.04 g) and iron (II) chloride tetrahydrate (1.98 g) were dissolved in a 2:1 molar ratio in 12.5 mL of DIW. Ammonium hydroxide (6.5 mL) was added dropwise under magnetic mixing at 500 rpm over 10 minutes with a nitrogen purge. After an additional 10 minutes of mixing, PEG (MW= 8 kDa, 1.0 g) was dissolved in 10 mL of DIW and the solution was added to the iron mixture. The mixture was heated to 80°C for 2 hours to peptize the SPION surface with PEG. After two hours, the SPION solution was cooled and washed using magnetic separation against 0.15 M saline and concentrated using a permanent magnet five times. The SPION concentration was determined gravimetrically, and the final concentrations were diluted in 0.15 M saline to make 5 wt% SPION solutions, a concentration that enables sufficient AMF-induced heating for activation without disrupting cross-linking of the bulk hydrogel. From transmission electron microscopy (JEOL Ltd., Japan) images analyzed using ImageJ software, the PEG-coated SPIONs were determined to form clusters of between 30 and 200nm, with individual particle diameters of 14 ± 5 nm (n = 258, Figure S4.1). We have previously demonstrated that SPIONs are quantitatively incorporated into the nanocomposite hydrogels and maintain their superparamagnetic properties.[48]

Composite Formation: Hydrogel nanocomposites were prepared by dissolving the reactive hydrogel precursors (6 or 8 wt%) in 0.15M saline solution along with 5 wt% PEG-SPIONs, 1 wt% 4 kDa FITC-Dex (the model drug used for this work), and varying weight percentages of microgel. After mixing overnight, the viscous solutions were pushed through a 22G needle three times to ensure complete mixing within each individual solution. The hydrazide- and aldehyde-functionalized polymer solutions were then loaded into separate barrels of a double barrel syringe (Figure 4.2) and co-extruded

through a static mixer into pre-fabricated moulds to produce composites containing 1 wt% 4 kDa FITC-Dex, 5 wt% PEG-SPIONs, 6 or 8 wt% hydrogel, and varying weight percentages and types of microgels. Gelation occurs rapidly (< 10s), which would allow for these materials to form immediately after an *in vivo* injection and effectively fill the free space of the tissue into which they are injected.[47,49]

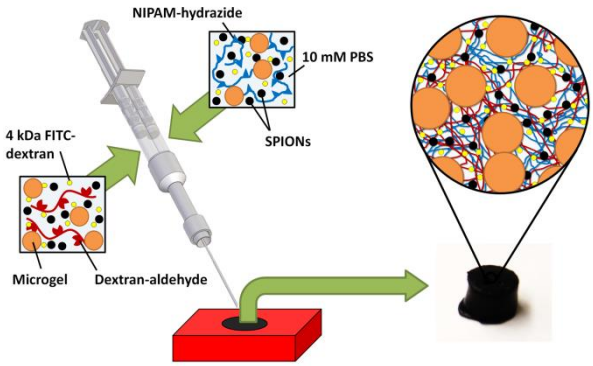

Figure 4.2: Fabrication of microgel-hydrogel-SPION composites.

Composite Swelling: Composites (*n* = 5) were placed in pre-weighed, perforated cell culture inserts and incubated in 5 mL of 10mM PBS at 37°C. The composites were weighed immediately after gelation and then at pre-determined time intervals. At each time interval, the mass of each composite plus insert was recorded. Percent mass change (associated with the swelling of the hydrogel) was calculated based on Equation 1:

$$Percent\ Weight\ Change = \frac{Mass_{time} - Mass_{initial}}{Mass_{initial}}\ x\ 100\% \quad (1)$$

Composite Degradation: Composites (*n* = 6) were placed in the same cell inserts used for swelling tests with 5 mL of 10 mM PBS (pH=7.4) or pH= 3 or pH = 1 hydrochloric

acid aqueous buffer solutions. Composite weight was recorded over time until the bulk material had completely degraded.

Pulsed-Induction Drug Release Experiments: An alternating magnetic field assembly was set up such that multiple composites (*n* = 4, 6.3 mm diameter x 3.2 mm height) could be placed in equivalent positions within the magnetic field while maintaining a constant baseline temperature of 37°C around the composites (see Supporting Information, Figure S4.2). The apparatus consisted of a jacketed flask, heated to 37°C using an attached water bath, placed within a 2-coiled, water-cooled, 8 cm diameter solenoid operated at 200 kHz, 30 A, and 1.3 kW to facilitate the exposure of the composites to AMF pulses of a given time interval. Styrofoam was placed in between the jacketed flask and the water-cooled coils to keep it in place and insulate it from and potential radiant heat from the coils. The continual water cooling was used to ensure the coil temperatures would not impact the temperature of the samples throughout each experiment. The composites were placed on specially-fabricated holders to keep them at equivalent positions within the magnetic field. Note that we have previously demonstrated no significant solution heating nor pulsatile release is observed in samples prepared without SPIONs, suggesting negligible RF-induced heating in the absence of the SPION transducers.[48]

For drug release studies, each composite was immersed in 4 mL of 10 mM PBS. Samples were collected at 10 minute intervals before and after repeated 10 minute AMF pulsatile applications (applied every 50 minutes). Concurrent with the pulsatile release tests, a set of control gels (*n* = 4) was kept in identical test tubes in a water bath at 37°C and were sampled at the same time intervals (but never exposed to the AMF). 3 x 200

µL samples were removed from each test-tube at each time point into 96-well plates. 600 µL of fresh, pre-heated PBS was added back into the test-tube to ensure the composites remained fully immersed and to maintain infinite sink conditions during the release process. This process was repeated on days one, two, three, and five to evaluate the composites' ability to facilitate repeated magnetically induced pulsatile release. The composites were exposed to 4-6 pulses on each day. The concentration of released 4 kDa FITC-Dex was measured using a fluorescence plate reader (PerkinElmer Victor3 multilabel plate reader, 485 nm excitation/535 nm emission wavelength) and converted to a mass release rate by dividing the calculated absolute mass released in each interval (from fluorimetry) by the duration of that interval (either 10 or 20 minutes).

The effect of the magnetic pulse on release was determined according to the percentage increase in release rate as a result of the AMF exposure, calculated based on comparing the experimental release rate following a pulse to the expected release rate estimated by interpolating between the rates observed at the two (non-pulsed) time points prior to and two time points after pulsatile induction (represented in the Supporting Information, Figure S4.3). This use of a weighted average to calculate the expected release rate (R) at a given time point (R_n) is described in Equation 2:

$$R_n = \frac{R_{n-2} \cdot |t_{n-2} - t_n| + R_{n-1} \cdot |t_{n-1} - t_n| + R_{n+1} \cdot |t_{n+1} - t_n| + R_{n+2} \cdot |t_{n+2} - t_n|}{|t_{n-2} - t_n| + |t_{n-1} - t_n| + |t_{n+1} - t_n| + |t_{n+2} - t_n|} \quad (2)$$

The percentage increase in the release rate directly after an applied pulse is then calculated by simply dividing the experimental release rate by this calculated estimate of the expected release rate (the likely release rate value had no AMF been applied),

converting this ratio into a percentage, and subtracting 100% to result in a percent increase in release.

This calculation was performed for both the pulsed and non-pulsed (control) nanocomposites, with the percent increase in release rate values reported in the results section representing the difference between the pulsed and control nanocomposite results. The rationale behind this calculation is that any environmental factors (i.e. a change in room temperature or a fluctuation of water bath temperature) that resulted in 'pulse' behaviour of the control composite at that time point would be filtered out, isolating the effect of the AMF only on facilitating pulsatile release. Error bars represent the standard deviation in the readings for independently-extruded composites (n = 4).

***In Vitro* Cytocompatibility Assay:** 3T3 *Mus musculus* mouse fibroblast cells were used to evaluate the cytocompatibility of the nanocomposites. The cells were grown using a proliferation media composed of 10% FBS and 1% PS in DMEM. The materials used to fabricate the nanocomposites were sterilized prior to cell viability testing by exposure to UV radiation (2 hours) inside a laminar flow cabinet and filtering with 0.45 µm syringe filters. 25,000 3T3 cells in 1 mL of media were added to each well of a 24 well polystyrene plate (n = 4 for each sample tested). After the cells were incubated at 37°C and 5% CO_2 for 24 hours, the media was aspirated, 1 mL of fresh media was added, and nanocomposites the same size as the well were added on top of the cells and incubated for an additional 24 hours. A positive control containing cells and no nanocomposites and a negative control containing no cells and no nanocomposites were also tested. After 24 hours of exposure, the solution covering the cells was aspirated and each well was rinsed with 0.5 mL of media. 150 µL of a 0.4 mg/mL MTT solution

was then added to each well, and the cells were incubated in the MTT solution for 4 hours. After the incubation period, 250 µL of DMSO was added to each well to dissolve the insoluble formazan precipitate. Plates were placed on a shaker for 20 minutes or until the purple formazan was completely dissolved. 2 x 200 µL was removed from each well, transferred to a 96 well polystyrene plate, and read in an absorbance reader at 540 nm (PerkinElmer Victor3 multilabel plate reader). The percent cell viability was calculated as the ratio of the average absorbance values of cells exposed to the nanocomposite and the average absorbance values of cells incubated only in media (positive control). Error bars represent the standard deviation of the four replicate measurements.

Mechanical Characterization: An ARES parallel-plate rheometer (TA Instruments) was used to determine the shear storage and loss moduli (*G'* and *G"*, respectively) of the nanocomposites using a parallel plate geometry (7 mm in diameter, 1 mm gap). A strain sweep test was first used to determine a strain value that lies within the viscoelastic region, followed by a frequency sweep test (0.1-100 rad/s, 25°C) at the chosen strain rate.

Error and Statistical Significance: Error bars represent the standard deviation in measurements based on multiple samples ($n \geq 4$). Statistically significant differences between any pair of samples were determined using a two-tailed t-test with $p < 0.05$ assuming unequal variances.

4.2.4 Results

Microgel temperature-responsiveness: The microgels generated via precipitation polymerization were sized at 25°C (their gelation temperature), 37°C (physiological temperature), and 43°C (the maximum temperature targeted using AMF to avoid local tissue damage during short-term exposure).[24] The thermosensitivity of each type of microgel between these critical temperatures is shown in Table 4.1, and the overall temperature-responsive nature of the different microgels is shown in Figure 4.3.

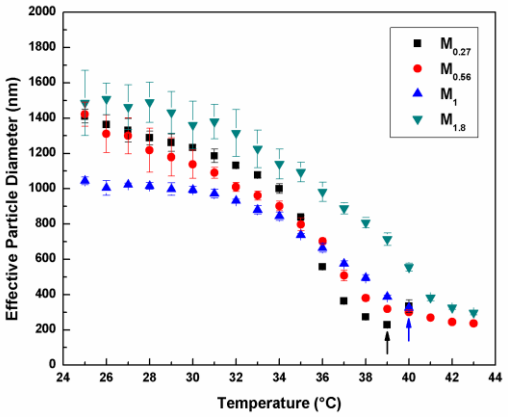

Figure 4.3: Temperature-responsive behaviour of microgels made with different NIPMAM:NIPAM ratios. Arrows indicate aggregation points of $M_{0.27}$ and M_1 microgels.

While incorporation of the more hydrophilic NIPMAM comonomer results in a phase transition over a much broader temperature range than observed for PNIPAM microgels, suggesting that these materials may possess rather heterogeneous crosslinks, increasing the NIPMAM content increases the VPTT of the microgel within the triggering temperature range (37-43°C) for the compositions studied. Of particular note, the $M_{1.8}$ microgel (containing the most NIPMAM comonomer) collapses the least between 25-37°C but exhibits the largest volume change between 37-43°C, a property which

(assuming the free volume mechanism of release to be correct) would suggest this microgel has particular utility for regulating pulsatile release (i.e. minimum free volume generation <37°C, maximum free volume change in triggering range). However, all microgels tested do exhibit significant deswelling in the triggering range and should thus have capacity to regulate on-demand release. Note that the aggregation observed in free solution for $M_{0.27}$ and M_1 would not likely be observed in the nanocomposite hydrogels given that microgels are dispersed throughout and entrapped within the hydrogel network, eliminating or sharply reducing the microgel mobility required for aggregation to occur.

Composite Rheology: The mechanical properties of nanocomposites prepared with different microgel contents were next measured to assess the range over which the microgel:hydrogel ratio could be varied without compromising the mechanical integrity of the hydrogel. As shown in Figure 4.4a, the plateau storage modulus of the nanocomposites increases until it reaches a critical microgel content of ~12 wt% (corresponding to 8.4 vol% microgel phase). This result can be ascribed to the competition of multiple factors governing nanocomposite mechanics related to the role of microgels in the structure. Microgels are more highly cross-linked in comparison to the external hydrogel, imparting higher mechanical strength to nanocomposites with greater amounts of microgel; however, above a certain microgel content (12 wt% microgel), the microgel sterically inhibits cross-linking in the bulk hydrogel phase, leading to a reduction in modulus at higher microgel contents and, eventually, the complete lack of gelation observed at concentrations >16 wt%. It should also be noted that as microgel content is increased, the storage modulus of the nanocomposite becomes more frequency dependent, an effect we attribute to the higher potential for viscous dissipation upon

shearing when more phase boundaries are introduced in the nanocomposite between the (softer) bulk hydrogel and the (harder) microgel phases. Note that while $M_{0.56}$ was used as the microgel in Figure 4.4, there is no significant difference in nanocomposite mechanics as a function of microgel composition (Supporting Information Figure S4.4), such that analogous results can be anticipated for each microgel tested.

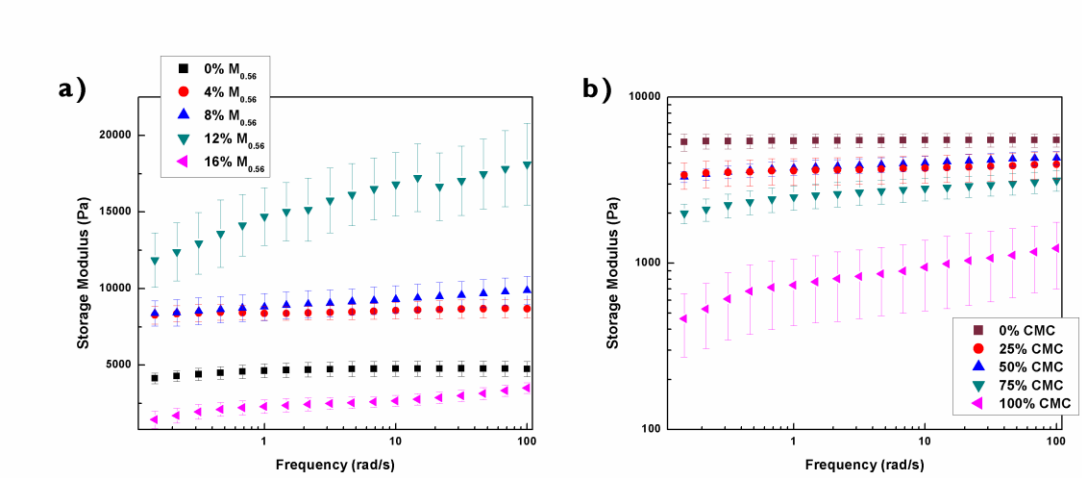

Figure 4.4: Storage modulus of magnetic nanocomposites with differing: (a) microgel ($M_{0.56}$) contents with 8 wt% hydrogel precursors, and (b) amounts of CMC-Ald replacing the Dex-Ald component in composites with 6 wt% $M_{1.8}$ microgels and 6 wt% hydrogel precursors.

Figure 4.4b shows that as more CMC-Ald is used to replace Dex-Ald in the magnetic nanocomposites, the storage modulus of the gel decreases. This can be attributed to the DEX-Ald having a greater aldehyde content (17.4% of repeat units) than the CMC-Ald polymer (12.4% of repeat units), allowing for a greater cross-link density and improved mechanical strength. Thus, the lower cross-link density coupled with the higher hydrophilicity (and limited residual charge) of CMC-rich hydrogels is expected to

lead to significantly more swelling in these hydrogels than the dextran-rich hydrogels, which are more densely cross-linked and do not contain any residual charge.

Degradability: The hydrazone cross-links forming the bulk hydrogel are hydrolytically degradable. The degradability of the hydrogels was observed at various pHs to confirm that the composites with differing microgel ($M_{0.56}$) contents do degrade hydrolytically (Table 4.2).

Table 4.2: Half-lives of composites with different microgel ($M_{0.56}$) compositions at pH= 7.4, 3, and 1. * indicates statistical significance between composites with different microgel contents at a given pH via pair-wise comparisons with all other microgels at the same pH ($p < 0.05$).

	pH=7.4 (PBS)	pH= 3	pH=1
0 wt% $M_{0.56}$	24 ± 9 days	9 ± 2 days*	5.0 ± 0.9 hrs
4 wt% $M_{0.56}$	21 ± 5 days	19 ± 2 days*	5.6 ± 1.5 hrs
8 wt% $M_{0.56}$	100 ± 10 days*	30 ± 5 days *	9.8 ± 0.5 hrs*
12 wt % $M_{0.56}$	23 ± 4 days	4 ± 2 days*	4.1 ± 1.3 hrs

Table 4.2 confirms that the nanocomposites degrade via an acid-catalyzed process, as lower pH buffers accelerated the degradation process for every nanocomposite tested. As the microgel content was increased, the nanocomposites generally take longer to degrade. We hypothesize this trend is a result of the increased content of the higher polymer fraction microgels limiting the diffusion of water through the nanocomposite. However, the 12 wt% microgel composites degraded much more rapidly than the 8 wt% nanocomposites. We attribute this result likely to the presence of the microgels significantly limiting the number of cross-links that can form upon *in situ*-gelation (resulting in fewer hydrolytic events being more effective at functionally degrading the bulk gel network). Of note, the 12 wt% microgel nanocomposites were observed to be the strongest from a mechanical perspective (Figure 4.4) but degrade significantly faster

than the 8 wt% microgel nanocomposites (Table 4.2). This result suggests that the 12 wt% microgel concentration is high enough to disrupt the formation of cross-links (sufficient to significantly influence the degradation time) but not high enough to negate the positive effects of adding additional microgel on the storage modulus of the composite as a whole.

As we observed for nanocomposite mechanics, properties that are highly dependent on the properties of the external hydrogel, as degradation is, are negligibly affected by microgel composition. However, replacing the Dex-Ald component certainly influences the degradation rate of the magnetic composites, as shown in the accelerated degradation study in Figure 4.5.

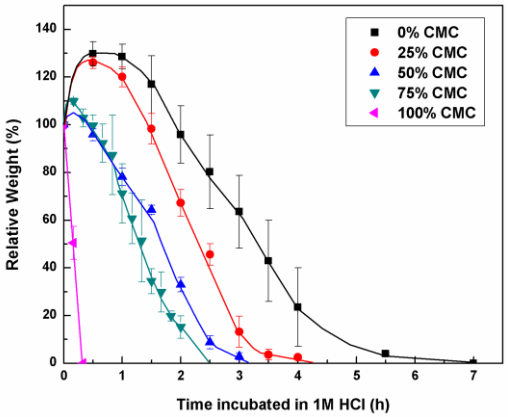

Figure 4.5: Accelerated degradation of the hydrolyzable magnetic nanocomposites with 6 wt% hydrogel precursors and 6 wt% microgel incubated in 1M HCl at 37°C.

As Dex-Ald is replaced by the CMC-Ald, the composites degrade more rapidly. This result concurs with the CMC-Ald/Dex-Ald mechanics result, in which CMC-rich gels were shown to exhibit lower elastic moduli (Figure 4.4) and likely have fewer cross-links to

undergo hydrolysis. A lower crosslink density also leads to higher swelling and thus higher water (and proton) penetration into the hydrogel to further accelerate hydrolysis.

Externally-Mediated Pulsatile Release: Nanocomposites with varying microgel contents, microgel compositions, and bulk gel compositions were evaluated in terms of their capacity to facilitate longer-term and higher-resolution pulsatile release. For each comparative set evaluated, 10 minute AMF pulses were applied such that 1) the therapy is relatively short and thus amenable to possible translation and 2) the nanocomposites would only increase in temperature up to 43°C, a temperature that is not harmful to the surrounding cell population on repeated, short-term exposures, as healthy mammalian cells are known to develop thermotolerance.[22,24] Samples were taken every 10 minutes, with 10 minute AMF pulses conducted every 50 minutes. The release rate after an AMF pulse typically increases significantly immediately following the pulse and then rapidly returns to the baseline rate of release the sample point immediately after the pulse is turned off (for a representative kinetics plot, see Supporting Information, Figure S4.5), enabling facile and unambiguous determination of the increase in release rate relative to the baseline release upon AMF signaling. This percentage increase in release was averaged throughout 3-4 applied pulses on each given day for each given composite to yield the reported results (for a representative result of release rate data over multiple days, see Supporting Information, Figure S4.6). Hydrogel swelling results collected under the same conditions are simultaneously reported to enable correlation between pulsatile release and bulk swelling properties of the nanocomposites.

Effect of Microgel Composition: Figure 4.6a shows the effect of changing the microgel composition (and thus the microgel volume phase transition temperature) on

the magnitude and duration of pulsatile FITC-dextran release observed, while Figure 4.6b shows the net swelling/deswelling of each of those nanocomposites as a function of time. Table S4.1 shows the magnitude of drug release measured at each time point for comparison.

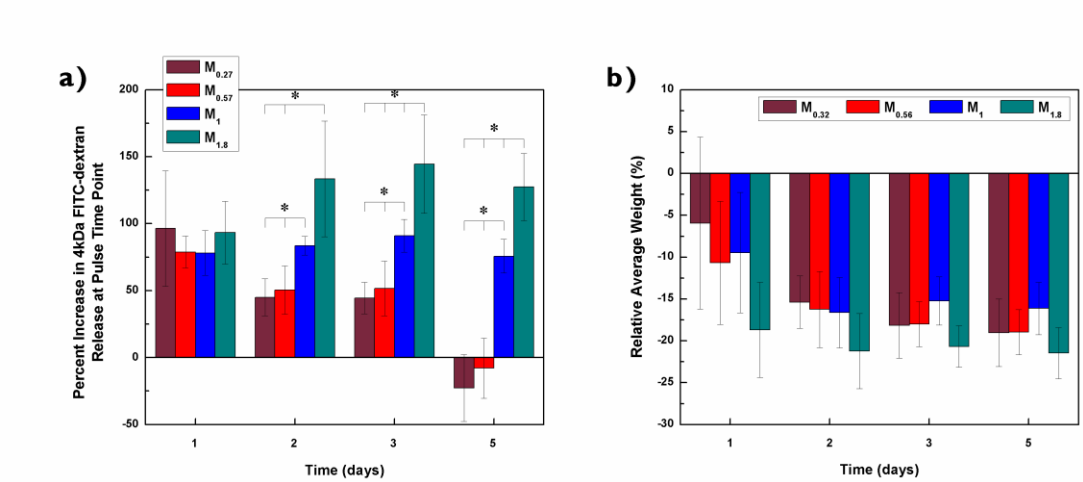

Figure 4.6: Effect of microgel phase transition temperature properties of nanocomposite hydrogels: (a) Percent increase in 4 kDa FITC-Dex release rate observed from composites made with microgels exhibiting different phase transition temperatures due to a 10 minute exposure to an alternating magnetic field; (b) weight changes associated with swelling responses of the bulk nanocomposites over the 5-day period of the release test. *indicates statistical significance, determined using a student's t-test assuming unequal variances ($p < 0.05$).

No significant difference in drug release rate was observed between nanocomposites prepared with different microgels on the first day of release ($p > 0.05$ for any pair-wise comparison). We attribute this effect to the significant background diffusional-based release that occurs from the nanocomposites on day one, in which drug loaded into the bulk hydrogel phase is convectively released from the (thermoresponsive) bulk hydrogel phase upon AMF triggering in a manner relatively independent of the microgel phase by

the collapse of the bulk hydrogel (demonstrated in Figure 4.6b). However, a clear pattern does emerge after the first day, with significantly higher degrees of enhanced release achieved as the proportion of NIPMAM in the microgels (and thus the microgel VPTT) is increased. This result is attributed to the majority of the microgel deswelling of these NIPMAM-rich microgels occurring at higher temperatures compared to the other microgels (Table 4.1), leading to the creation of more free volume upon triggering and thus enhanced pulsatile release. Figure 4.6a also indicates that higher transition temperature microgels can also prolong the lifetime of the device in terms of providing the potential for pulsatile release; pulsed releases on the same order of relative magnitude are achieved on day 5 using the $M_{1.8}$ microgel composites, while the lower transition temperature composites lose their capacity for pulsatile release by this time. Notably, these results are also independent of swelling, as Figure 4.6b indicates that the differences in swelling between any composite on any day is statistically insignificant ($p > 0.05$ for any pair-wise comparison). Collectively, these results show that increasing the phase transition temperature of the microgel (within the triggering temperature range) leads to both prolonged release as well as higher resolution between the on/off states of the drug release due to an AMF pulse (Table S4.1).

Effect of Microgel Content: Given the importance of the microgel phase for regulating the nature of the pulsatile release, the relative volume fractions of the microgel and bulk hydrogel phases in the nanocomposites were next adjusted to investigate the potential for further enhancing pulsatile release. Figure 4.7a shows the pulsatile release achieved as a function of microgel content, using $M_{1.8}$ microgels as the microgel phase due to the improved pulsatile release performance observed for this microgel over the other microgels (Figure 4.6a). Concurrent swelling properties of the bulk nanocomposite as a

whole tracked throughout the release experiment are shown in Figure 4.7b. Table S4.2 shows the overall volume fractions of microgel in the resulting nanocomposites as well as the estimated changes in microgel volume fraction observed upon triggering, as calculated based on the DLS data (Table 4.1) and the initial volume fraction of microgels present under the room temperature preparation conditions.

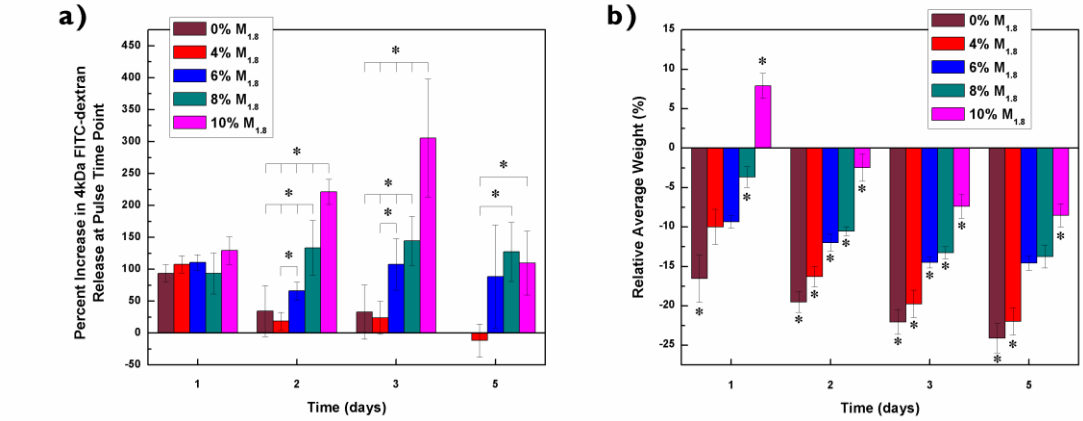

Figure 4.7: Effect of microgel ($M_{1.8}$) content on properties of nanocomposite hydrogels: (a) Percent increase in 4 kDa FITC-Dex release rate observed from composites made with different microgel contents due to a 10 minute exposure to an alternating magnetic field; (b) weight changes associated with swelling responses of the bulk nanocomposites over the 5-day period of the release test. The volume percentages of the microgels that correspond to each microgel content from 0-10 wt% are 0 vol%, 2.8 vol%, 4.2 vol%, 5.6 vol%, and 7.0 vol%, respectively (Table S4.2). *indicates statistical significance, determined using a student's t-test assuming unequal variances ($p < 0.05$).

Figure 4.7a shows that, again, the impact of the degree of AMF-enhanced release is not dependent on nanocomposite composition during the first day of release. This result was somewhat surprising, in that changing the total volume fraction of the higher polymer mass fraction microgel phase was expected to significantly reduce even the

baseline diffusion rate of drug release from the nanocomposites. However, this result can be rationalized based on the swelling results (Figure 4.7b), which show that nanocomposites prepared with higher microgel contents remained swollen on day 1 while nanocomposites with lower microgel contents deswelled significantly. This observed deswelling will decrease the pore size of the composites with lower microgel contents such that their rate of diffusional release is reduced, compensating for the higher concentration of denser microgels present.

However, after day 1, all the nanocomposites macroscopically deswell (Figure 4.7b, negating the competing convection effects observed on day 1), and nanocomposites with higher microgel contents are observed to facilitate greater degrees of enhanced release of FITC-dextran over longer time scales. These differences in enhanced drug release can be attributed to the enhanced free volume fraction of the nanocomposites generated upon AMF heating from 37°C to 43°C as the microgel fraction in the nanocomposite is increased, leading to both enhanced resolution between the on/off states (Figure 4.7a) and enhanced drug doses delivered in each pulse; for example nanocomposites containing 10 wt% microgel demonstrate up to 4-fold higher rates of release due to a pulse in comparison to the baseline release. This enhanced release rate is directly correlated with the magnitude of free volume changes in the microgel phase upon triggering (Table S4.2), supporting our proposed mechanism of externally-mediated release. Note that by day 5, the effect of microgel content is suppressed, an effect we attribute to the higher release of drug in the 10 wt% $M_{1.8}$ nanocomposite over the first four days (Table S4.3) that reduces the reservoir concentration of drug inside the nanocomposite and thus makes any pulse less effective at promoting additional drug release.

Effect of Bulk Hydrogel Swelling: While the data suggests that volume changes in the microgel phase can create free volume, concurrent changes in the swelling of the bulk gel phase may counteract this effect, either by the bulk gel swelling to fill the newly vacated space or the bulk gel deswelling and thus effectively collapsing around the created free volume. As such, the effect of bulk hydrogel swelling on the release characteristics of the nanocomposites was also investigated. Changes in bulk gel swelling responses were achieved by combining PNIPAM-Hzd polymer with a mixture of Dex-Ald (which alone induces the entire nanocomposite to deswell at 37°C) and CMC-Ald (which alone induces significant swelling in the nanocomposite at 37°C), as per previously reported work.[49] Mixtures of these two aldehyde-functionalized hydrogel precursors can lead to bulk gels with intermediate swelling responses largely predicted by the simple rule of mixtures. Each nanocomposite in this series contained 6 wt% $M_{1.8}$ microgels and 6 wt% of both PNIPAM-Hzd and total carbohydrate-aldehyde precursor polymer, with the aldehyde polymer fraction distributed according to the ratio *x* CMC (where *x* is the mass percentage of CMC-Ald in the aldehyde polymer barrel, the remainder being Dex-Ald). The pulsatile release properties (Figure 4.8a) and bulk nanocomposite swelling characteristics (Figure 4.8b) of the nanocomposite hydrogels as a function of CMC-Ald:Dex-Ald ratio in the bulk hydrogel are shown in Figure 4.8.

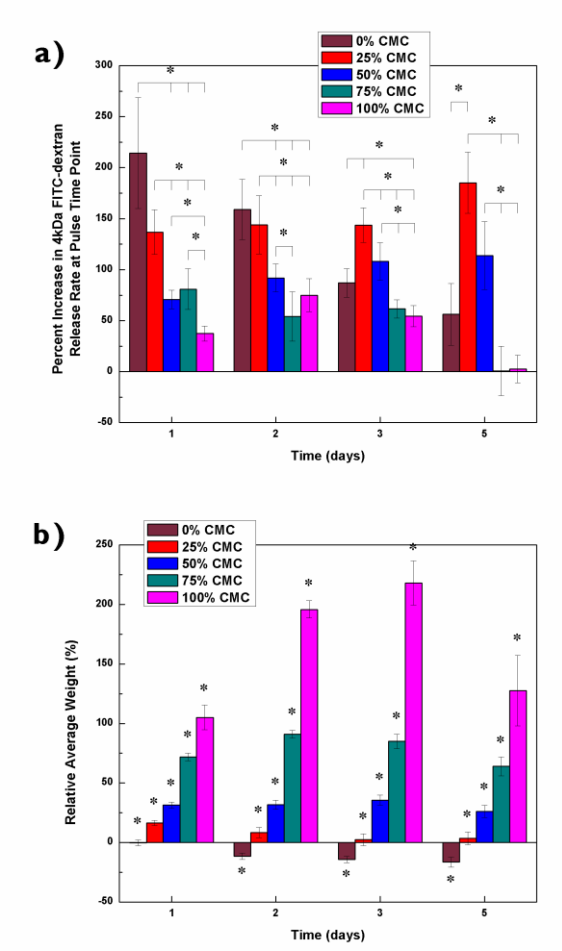

Figure 4.8: Effect of bulk gel swelling on nanocomposite properties with 6 wt% $M_{1.8}$ microgel contents: (a) Percent increase in 4kDa FITC-Dex release rate observed from composites due to exposure to an alternating magnetic field (10 minute pulses); (b) weight changes associated with swelling responses of the bulk nanocomposites over the 5-day period of the release test. *indicates statistical significance, determined using a student's t-test assuming unequal variances ($p < 0.05$).

Figure 4.8b shows that the bulk hydrogel swelling characteristics are highly dependent on the ratio of CMC-Ald:Dex-Ald used as the aldehyde-functionalized component; the greater the percentage of CMC-Ald, the more the nanocomposites swell. These swelling differences, consistent with the higher hydrophilicity and lower cross-link density in CMC-

rich gels indicated by rheology (Figure 4.4b), persist throughout the entire five day testing period. The impacts of these swelling responses on the AMF-based release profiles depend on the timescale of the release process. At all times, bulk gels that significantly swell (100% CMC and 75% CMC) facilitate the lowest pulsing, an effect we attribute to the rapid diffusion-based release from these materials and, at longer times, exhaustion of the drug reservoir in the hydrogel which leads to minimal release in the presence or absence of a magnetic field (Table S4.4). At short times (1-2 days), nanocomposites containing high Dex-Ald contents exhibit significantly higher resolution pulsatile release (Figure 4.8a); concurrently, both these nanocomposites exhibit no significant bulk swelling responses over these two days (Figure 4.8b). At longer times (3-5 days), the 25% CMC and 50% CMC nanocomposites demonstrate the highest pulsatile release properties (Figure 4.8a); again, this is directly correlated with the swelling result, in that these two nanocomposites exhibit the smallest swelling responses over these two days relative to the baseline (Figure 4.8b). Thus, the lower the swelling response of the bulk hydrogel phase (either positive or negative) from the baseline preparation condition, the higher the pulsatile release achieved upon AMF application. This result again supports the free volume mechanism of pulsatile release in that hydrogels that swell or deswell will effectively consume the free volume created by the microgel deswelling observed under the AMF, resulting in lower net free volume generation and thus reduced pulsatile release potential.

Effect of Pulse Duration: Our previous work[48] concurred with that of Satarkar and Hilt[51] in that longer AMF exposures promote greater enhancements in release over controls in continuous release experiments. Reproducing this result in the context of a pulsatile release experiment would thus provide another mechanism to easily tune the

degree of release of drug from any given nanocomposite formulation. Consequently, we performed an analogous pulsatile release experiment using 20 minute (instead of 10 minute) pulses and sampling intervals for Dex-Ald composites with 8 wt% hydrogel precursors and 8 wt% $M_{1.8}$ microgel content, the results of which are shown in Figure 4.9.

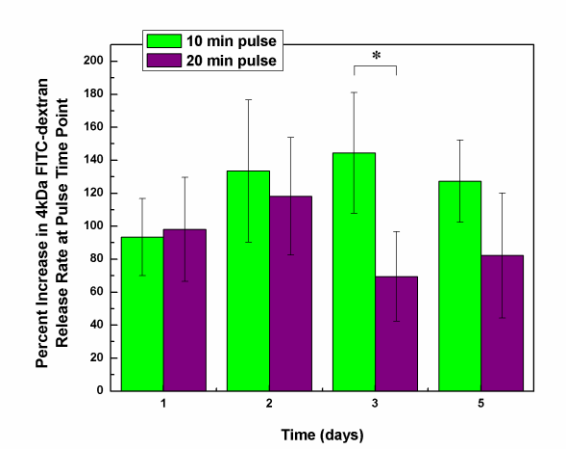

Figure 4.9: Effect of pulse duration on the AMF-induced release rate from magnetic composites with 8 wt% hydrogel precursors and 8 wt% $M_{1.8}$ microgel content. *indicates statistical significance, determined using a student's t-test assuming unequal variances ($p < 0.05$).

There was no significant difference in the relative amounts of drug released *per sampling period* before or after the pulse as a result of increasing the pulse duration from 10 minutes to 20 minutes over the first two days of release ($p > 0.05$). The only significantly higher release rate facilitated by the shorter pulses was at day 3 ($p = 0.004$), whereas while the day 5 differences are not statistically significant ($p = 0.071$) they include large error bars consistent with the small total release achieved at the longer time periods tested. Given that the baseline release data was collected at the same

intervals as the pulsing data in each experiment, this result suggests that linearly-predictable drug doses can be achieved as a function of increasing the pulse time, at least over the first two days of composite pulsing. This result simplifies the use of these nanocomposites in terms enabling delivery of a controlled dose of drug in a repeatable manner by simply changing the pulse time.

Composite Cytotoxicity: Our previous work showed that all of the components of the nanocomposites displayed no to minimal cytotoxic effects when the cells were exposed to 0.1 – 2 mg/mL of each component for 24 hours.[48] Here, the cytotoxicity of the nanocomposites as a whole was determined by placing nanocomposite discs on top of 3T3 mouse fibroblast cells and comparing the viability of these cells to controls that were not exposed to the nanocomposites. Since the microgels displayed the greatest (albeit still limited) cytotoxicity in previous studies[48] and the hydrogels with SPIONS[47] and hydrogels without SPIONs/microgels have also previously shown minimal cytotoxic responses[49], only nanocomposites with higher microgel ($M_{0.56}$) contents were tested. It should be noted that none of the microgels studied here exhibited significant cytotoxicity (Figure S4.7), rationalizing the use of the $M_{0.56}$ microgels as representative microgels for nanocomposite toxicity testing. Table 4.3 shows the cell viability (measured via MTT assay relative to a cell-only control) of nanocomposites with various microgel contents.

Table 4.3: Cell viability (via MTT assay) of 3T3 mouse fibroblast cells exposed to SPION and microgel composites. 100% viability refers to the signal from cells not exposed to nanocomposite.

Composition (with 8 wt% Hydrogel)	Cell Viability (%)
8 wt% Microgels	93 ± 2
12 wt% Microgels	92 ± 2
16 wt% Microgels	77 ± 12

Cells exposed to the nanocomposites experience only very limited cytotoxicity, with viabilities > 77% measured in all cases and a only minimal change in cytotoxicity observed as the amount of microgels in the nanocomposites is increased even at the high microgel concentrations (p = 0.048 comparing 8 wt% and 16 wt% microgels). As such, the low overall cytotoxicity of both the composites and individual components suggests that these nanocomposites have potential to be utilized *in vivo* and, ultimately, in biomedical applications.

Taken together, the results of this work demonstrate that these nanocomposites have a variety of controllable characteristics that make it possible to tune the level of release that takes place as a result of an externally-mediated AMF exposure. Further tuning of the properties of the microgel and/or hydrogel phase to change the affinity of one or both phases for the drug could also be pursued to tune the release properties as desired, as we have previously demonstrated for other microgel-hydrogel soft nanocomposites.[52] In addition, drugs of a different size or with different chemical properties (i.e. anionic, cationic, hydrophobic, hydrophilic) would diffuse out at differing rates, with larger drugs potentially experiencing even greater increases in release in response to AMF pulses due to the their lower baseline diffusion rate. The nanocomposites also have a variety of other properties amenable to their proposed biomedical application, as they are mechanically strong, can be directly injected to the site of interest (providing control over the site of localized drug release), can be degraded over time, and do not induce significant cytotoxicity.

4.2.5 Conclusion

Nanocomposite materials intended for use as externally-activated drug delivery devices were fabricated by entrapping thermosensitive microgels and SPIONs in an *in situ*-gelling hydrogel network. The nanocomposites are entirely injectable and degradable, possess good mechanical strength and cytocompatibility, and are able to deliver pulses of drug upon exposure to an AMF. Adjusting the microgel chemistry to create microgels that have less deswelling below 37°C and more proportional deswelling between 37°C and 43°C, adding higher microgel volume fractions (while maintaining the mechanical stability of the nanocomposite), and minimizing the equilibrium swelling responses of the surrounding bulk hydrogel were all found to enhance the degree of pulsatile release following an externally-operated AMF pulse. We anticipate these findings represent an additional step toward the generation of translatable 'smart' drug delivery technologies that can be operated via an external source, potentially leading to improved therapies for conditions in which pulsed and site-specific drug delivery is beneficial.

4.2.6 Acknowledgements

Funding from the J.P. Bickell Foundation (Medical Research Grants), the Natural Sciences and Engineering Research Council of Canada (Discovery Grant program and Vanier Scholarship program for SBC), and the Ontario Graduate Scholarship program (for DM) is gratefully acknowledged.

4.2.7 Electronic Supporting Information (ESI) available

TEM images, a schematic of the AMF-pulse release setup, rheological tests of magnetic nanocomposites with differing microgels, a representative pulse-induced drug release result, cumulative release results, a table of pore volume created upon heating with different microgel contents, and cell viability results for differing microgels can be found in the supporting information. This material is available free of charge via www.rsc.org.

4.2.8 References

1 S. B. Campbell and T. Hoare, *Curr. Opin. Chem. Eng.*, 2014, **4**, 1–10.

2 C. L. Weaver, J. M. Larosa, X. Luo, and X. T. Cui, *ACS Nano* 2014, **8(2)**, 1834–1843.

3 T. Endo, R. Ikeda, Y. Yanagida and T. Hatsuzawa, *Anal. Chim. Acta*, 2008, **611**, 205–211.

4 N. S. Satarkar and J. Zach Hilt, *Acta Biomater.*, 2008, **4**, 11–16.

5 J. Kost and R. Langer, *Adv. Drug Deliv. Rev.*, 2012, **64**, 327–341.

6 J. Kolosnjaj-Tabi, R. Di Corato, L. Lartigue, I. Marangon, P. Guardia, A. K. Silva, N. Luciani, P. Flaud, O. Clément, J. V Singh, P. Decuzzi, T. Pellegrino, C. Wilhelm and F. Gazeau, *ACS Nano*, 2014, **8(5)**, 4268-4283.

7 W.-H. Chiang, V. T. Ho, H.-H. Chen, W.-C. Huang, Y.-F. Huang, S.-C. Lin, C.-S. Chern and H.-C. Chiu, *Langmuir*, 2013, **29**, 6434–6443.

8 T. J. Smith, P. J. Coyne, W. R. Smith, J. D. Roberts and V. Smith, *Am. J. Hematol.*, 2005, **78**, 153–154.

9 C. M. Nolan, M. J. Serpe and L. A. Lyon, *Biomacromolecules*, 2004, **5**, 1940–1946.

10 C. R. Gordijo, K. Koulajian, A. J. Shuhendler, L. D. Bonifacio, H. Y. Huang, S. Chiang, G. A. Ozin, A. Giacca and X. Y. Wu, *Adv. Funct. Mater.*, 2011, **21**, 73–82.

11 Y. N. Dou, J. Zheng, W. D. Foltz, R. Weersink, N. Chaudary, D. Jaffray and C. Allen, *J. Control. Release*, 2014, **178**, 69–78.

12 S. Heilmann, S. Küchler, C. Wischke, A. Lendlein, C. Stein and M. Schäfer-Korting, *Int. J. Pharm.*, 2013, **444**, 96–102.

13 R. Pelton, *Adv. Colloid Interface Sci.*, 2000, **85**, 1–33.

14 C. Ju, R. Mo, J. Xue, L. Zhang, Z. Zhao, L. Xue, Q. Ping and C. Zhang, *Angew. Chem. Int. Ed.*, 2014, **53**, 6253–6258.

15 C. L. Lay, J. N. Kumar, C. K. Liu, X. Lu and Y. Liu, *Macromol. Rapid Commun.*, 2013, **34**, 1563-1568.

16 X. Yao, L. Chen, X. Chen, C. He, J. Zhang and X. Chen, *Macromol. Rapid Commun.*, 2014, **35**, 1697-1705.

17 T. Hoare and R. Pelton, *Biomacromolecules*, 2008, **9**, 733–740.

18 A. Matsumoto, K. Yamamoto, R. Yoshida, K. Kataoka, T. Aoyagi and Y. Miyahara, *Chem. Commun.*, 2010, **46**, 2203–2205.

19 H.-Y. Huang, S.-H. Hu, S.-Y. Hung, C.-S. Chiang, H.-L. Liu, T.-L. Chiou, H.-Y. Lai, Y.-Y. Chen and S.-Y. Chen, *J. Control. Release*, 2013, **172**, 118–127.

20 M. S. Yavuz, Y. Cheng, J. Chen, C. M. Cobley, Q. Zhang, M. Rycenga, J. Xie, C. Kim, K. H. Song, A. G. Schwartz, L. V Wang and Y. Xia, *Nat. Mater.*, 2009, **8**, 935–939.

21 S. Giri, B. G. Trewyn, M. P. Stellmaker and V. S.-Y. Lin, *Angew. Chem. Int. Ed.*, 2005, **44**, 5038–5044.

22 P. Wust, B. Hildebrandt, G. Sreenivasa, B. Rau, J. Gellermann, H. Riess, R. Felix and P. M. Schlag, *Lancet Oncol*., 2002, **3**,487–497.

23 Y. Niitsu, N. Watanabe, H. Umeno, H. Sonã, H. Neda, N. Yamauchi and M. Maeda, *Cancer Res.*, 1988, **48**, 654–657.

24 R. D. Issels, *Eur. J. Cancer*, 2008, **44**, 2546–2554.

25 R. Farra, N. F. Sheppard Jr., L. McCabe, R. M. Neer, J. M. Anderson, J. T. Santini Jr., M. J. Cima and R. Langer, *Sci. Transl. Med.*, 2012, **4**, 122.

26 B. C. Masi, B. M. Tyler, H. Bow, R. T. Wicks, Y. Xue, H. Brem, R. Langer and M. J. Cima, *Biomaterials*, 2012, **33**, 5768–5775.

27 S. Rahimi, E. H. Sarraf, G. K. Wong and K. Takahata, *Biomed. Microdevices*, 2011, **13**, 267–277.

28 S. A. Rovers, R. Hoogenboom, M. F. Kemmere and J. T. F. Keurentjes, *Soft Matter*, 2012, **8**, 1623–1627.

29 D. Seliktar, *Science*, 2012, **336**, 1124–1128.

30 J. Wu, A. Chen, M. Qin, R. Huang, G. Zhang, B. Xue, J. Wei, Y. Li, Y. Cao and W. Wang, *Nanoscale*, 2015, **7**, 1655-1660.

31 S. Merino, C. Martin, K. Kostarelos, M. Prato and E. Vázquez, *ACS Nano*, 2015, ***9(5)***, 4686-4697.

32 P. I. Lee, *J. Control. Release*, 1985, **2**, 277–288.

33 N. B. Graham and M. E. McNeill, *Biomaterials*, 1984, **5**, 27–36.

34 L. Brannon-Peppas and N. A. Peppas, *J. Control. Release*, 1989, **8**, 267–274.

35 H. R. Culver, A. M. Daily, A. Khademhosseini and N. A. Peppas, *Curr. Opin. Chem. Eng.*, 2014, **4**, 105–113.

36 T. R. Hoare and D. S. Kohane, *Polymer*, 2008, **49**, 1993–2007.

37 Y. Qiu and K. Park, *Adv. Drug Deliv. Rev.*, 2012, **64**, 49–60.

38 M. Bikram, A. M. Gobin, R. E. Whitmire and J. L. West, *J. Control. Release*, 2007, **123**, 219–227.

39 B. P. Timko, M. Arruebo, S. Shankarappa, J. B. McAlvin, O. S. Okonkwo, B. Mizrahi, C. F. Stefanescu, L. Gomez, J. Zhu, A. Zhu, J. Santamaria, R. Langer and D. S. Kohane, *Proc. Natl. Acad. Sci. U. S. A.*, 2014, **111**, 1349–1354.

40 L. E. Strong, S. N. Dahotre and J. L. West, *J. Control. Release*, 2014, **178**, 63–68.

41 J. Ge, E. Neofytou, T. J. Cahill, R. E. Beygui and R. N. Zare, *ACS Nano*, 2012, **6**, 227-233.

42 A. Servant, V. Leon, D. Jasim, L. Methven, P. Limousin, E. V. Fernandez-Pacheco, M. Prato and K. Kostarelos, *Adv. Healthc. Mater.*, 2014, **3**, 1334–1343.

43 T. Hoare, B. P. Timko, J. Santamaria, G. F. Goya, S. Irusta, S. Lau, C. F. Stefanescu, D. Lin, R. Langer and D. S. Kohane, *Nano Lett.*, 2011, **11**, 1395–1400.

44 X. Zhao, J. Kim, C. A. Cezar, N. Huebsch, K. Lee, K. Bouhadir and D. J. Mooney, *Proc. Natl. Acad. Sci. U. S. A.*, 2011, **108**, 67–72.

45 M. C. Giano, Z. Ibrahim, S. H. Medina, K. A. Sarhane, J. M. Christensen, Y. Yamada, G. Brandacher and J. P. Schneider, *Nat. Commun.*, 2014, **5**, 4095-4104.

46 M. Patenaude, N. M. B. Smeets and T. Hoare, *Macromol. Rapid Commun.*, 2014, **35**, 598-617.

47 S. B. Campbell, M. Patenaude and T. Hoare, *Biomacromolecules*, 2013, **14**, 644–653.

48 S. Campbell, D. Maitland and T. Hoare, *ACS Macro Lett.*, 2015, **4**, 312–316.

49 M. Patenaude and T. Hoare, *Biomacromolecules*, 2012, **13**, 369–378.

50 M. Patenaude, S. Campbell, D. Kinio and T. Hoare, *Biomacromolecules*, 2014, **15**, 781-790.

51 N. S. Satarkar and J. Z. Hilt, *J. Control. release*, 2008, **130**, 246–251.

52 D. Sivakumaran, D. Maitland and T. Hoare, *Biomacromolecules*, 2011, **12**, 4112–4120.

4.2.9 Supporting Information

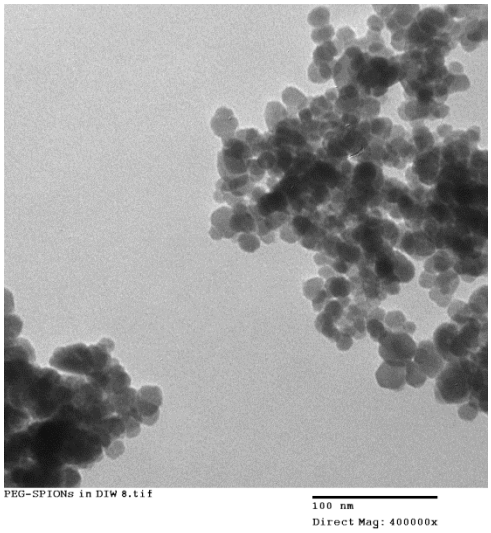

Figure S4.1: TEM image of PEG-functionalized SPIONS. The particle clustering on the copper grids, occurring during sample preparation for TEM, is typical of hydrophilic nanoparticles.

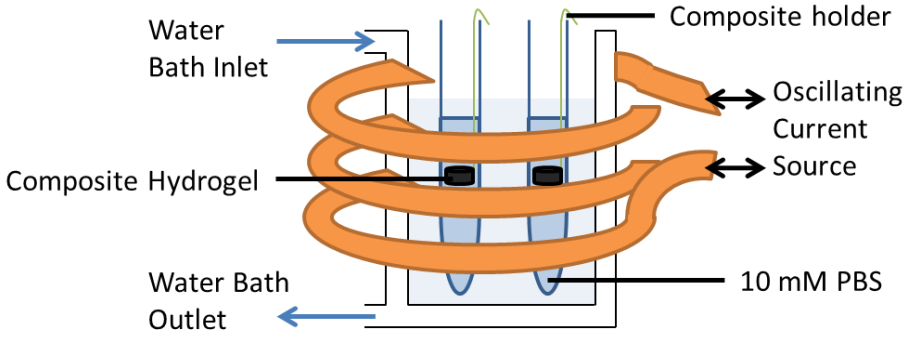

Figure S4.2: Schematic of the set up for AMF-mediated pulsatile release from nanocomposites capable of keeping the nanocomposites at a 37°C baseline temperature.

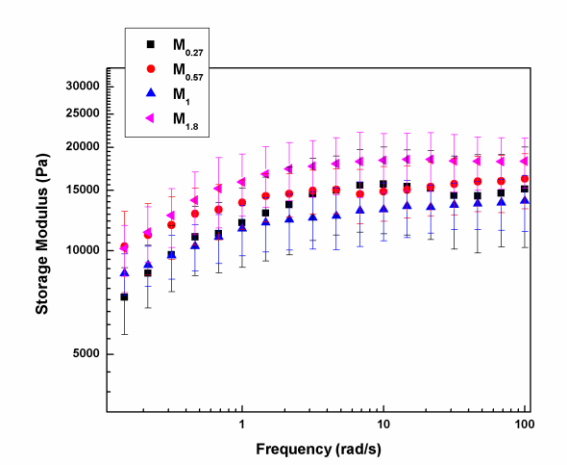

Figure S4.3: Storage modulus of nanocomposites prepared with differing PNIPMAM:PNIPAM contents with 8 wt% PNIPAM-Hzd/Dex-Ald precursor polymers.

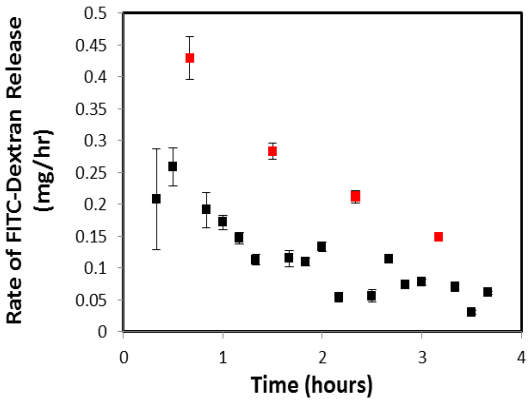

Figure S4.4: Representative release profile (expressed as rate of drug release) of 4 kDa FITC-Dex during the first day of a pulsatile release test: 8 wt% hydrogel, 8 wt% microgel, 5 wt% PEG-SPIONs, and 1 wt% 4 kDa FITC-Dex. The composite was incubated at 37°C. The red dots indicate the measured time point immediately after applying the AMF on the sample, showing the increase in the rate of release due to an AMF pulse, and the release rates that were compared to the points around them to determine the increase in the rate of release.

Table S4.1: Excess 4 kDa FITC-Dex released over the duration of the magnetic pulse for composites made with microgels with different formulations.

	Extra Drug Released During Pulses (μg)			
Test Name	Day 1	Day 2	Day 3	Day 5
$M_{1.8}$	21 ± 5	0.42 ± 0.07	0.13 ± 0.04	0.02 ± 0.01
M_{1}	18 ± 2	0.35 ± 0.02	0.10 ± 0.01	0.02 ± 0.01
$M_{0.56}$	20 ± 2	0.10 ± 0.02	0.02 ± 0.01	-0.03 ± 0.03
$M_{0.27}$	14 ± 5	0.07 ± 0.04	0.00 ± 0.01	-0.04 ± 0.05

Table S4.2: The volume fraction of the nanocomposite corresponding to microgel, the volume fraction of the gel that becomes free volume at 37°C and 43°C due to heating, and the resulting increase in free volume fraction due to AMF activation (i.e. magnetic heating to 43°C from a 37°C baseline temperature).

Wt% Microgel	$10M_{1.8}$	$8M_{1.8}$	$6M_{1.8}$	$4M_{1.8}$	$0M_{1.8}$
Vol % Microgel	7.02	5.62	4.21	2.81	0
Vol% Pore Network at 37°C (change between 25°C and 37°C)	5.61	4.49	3.37	2.24	0
Vol% Pore Network at 43°C (change between 25°C and 43°C)	6.95	5.56	4.17	2.78	0
Change in Vol% Pore Network Between 37°C and 43°C	1.34	1.07	0.80	0.54	0

Table S4.3: Average excess 4kDa FITC-Dex released over the duration of an AMF pulse for composites made with different microgel contents.

	Extra Drug Released During Pulses (μg)			
Microgel Content	Day 1	Day 2	Day 3	Day 5
10 $M_{1.8}$	25 ± 6	0.71 ± 0.07	0.12 ± 0.03	0.02 ± 0.01
8 $M_{1.8}$	21 ± 5	0.42 ± 0.07	0.13 ± 0.05	0.02 ± 0.03
6 $M_{1.8}$	27 ± 3	0.28 ± 0.04	0.12 ± 0.04	0.03 ± 0.01
4 $M_{1.8}$	21 ± 3	0.22 ± 0.08	0.01 ± 0.04	-0.01 ± 0.02
0 $M_{1.8}$	16 ± 3	0.01 ± 0.09	0.01 ± 0.08	NA

Table S4.4: Average excess 4 kDa FITC-Dex released over the duration of an AMF pulse for composites with different swelling behaviours.

% CMC (remainder Dex)	Extra Drug Released During Pulses (µg)			
	Day 1	Day 2	Day 3	Day 5
100 CMC	15 ± 1	0.29 ± 0.08	0.05 ± 0.01	-0.04 ± 0.07
75 CMC	15 ± 4	0.28 ± 0.11	0.03 ±0.01	-0.02 ± 0.05
50 CMC	15 ± 2	0.58 ± 0.09	0.16 ±0.02	0.07 ± 0.02
25 CMC	41 ± 5	0.57 ± 0.12	0.19 ±0.02	0.10± 0.02
0 CMC	36 ± 9	0.38 ± 0.10	0.04 ±0.01	0.03 ± 0.01

Table S4.5: Average excess 4 kDa FITC-Dex released over the duration of an AMF pulse for 8wt% $M_{1.8}$ composites exposed to different durations of applied AMF pulses.

Pulse Time	Extra Drug Released During Pulses (µg)			
	Day 1	Day 2	Day 3	Day 5
10 min	21 ± 5	0.42 ± 0.07	0.13 ± 0.05	0.02 ± 0.03
20 min	23 ± 2	0.47 ± 0.03	0.12 ± 0.06	0.02 ± 0.02

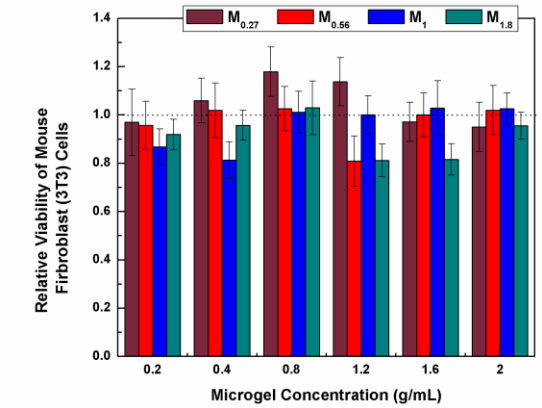

Figure S4.5: Relative viability of 3T3 mouse fibroblast cells after a 24 hour exposure to various microgel compositions in an MTT assay.

Chapter 5: Microinjector

5.1 Preface

This work represents the transition from micro- to nano-scale materials in this thesis, as the microinjector developed here produces hydrogel droplets in the millimeter size range. This chapter focusses on the development of the microinjection device for ophthalmic delivery of our *in-situ* gelling MITCH-type hydrogel materials, as no device existed that would be able to inject small amounts of MITCH-type hydrogels for animal experiments. This microinjector was shown to inject precise, low amounts (1 – 20 µL) of our injectable hydrogels for use that were shown to exhibit good tissue compatibility in *in vivo* ocular experiments with Sprague-Dawley rats. This was the first time these types of injections have ever been performed and these microinjectors (or slight variations of them) could ultimately be used to deliver magnetic, SPION-containing gels to the eye or other regions of the body for magnetic targeting or magnetically-actuated release.

5.2 Microinjector-based delivery and compatibility assessment of in-situ, reactively-gelling hydrogels to the posterior eye

Scott Campbell,[+] Jun Yang,[□] Ben Muirhead,[▶] Heather Sheardown,[+] P. Ravi Selvaganapathy,[□] and Todd Hoare[+,] [Manuscript in Preparation]*

5.2.1 Abstract

Diseases associated with the back of the eye are one of the primary causes of vision loss, particularly in more developed nations, and are often only treatable via direct intraocular injection. Recently, several injectable *in situ*-crosslinking mixing induced two-component hydrogels (MITCH) have been engineered to exhibit properties highly amenable to improving existing therapies to the back of the eye by extending the duration of efficacious drug release while maintaining the desired transparency, refractive index, and potential for clearance. However, there is currently no device capable of injecting MITCH-type hydrogels at the extremely small volumes required for intraocular injection. Herein, we describe the design of a microfluidics-based microinjection device capable of controllably injecting small volumes of *in situ*-gelling MITCH-type hydrogels and then apply the device for the first *in vivo* injection of these types of hydrogels into the vitreous humor of Sprague-Dawley rats. The devices can controllably eject gels with volumes in the 1-10 µL range with low tolerances, and hydrazone crosslinked poly(oligoethylene glycol) methacrylate (POEGMA) hydrogels delivered using the device displayed no significant tissue toxicity in comparison to saline controls. We anticipate such hydrogels, coupled with the delivery device, have potential

for minimally-invasive intraocular delivery of therapeutics while minimizing the number of required injections.

Keywords: hydrogels, drug delivery, controlled release, injectable, posterior eye treatment.

5.2.2 Introduction

The primary causes of vision loss in developed nations are diseases associated with the posterior eye, such as age-related macular degeneration, diabetic retinopathy, posterior uveitis, and retinitis due to glaucoma, etc.[1–3] Unfortunately, the posterior region of the eye is an exceptionally difficult target tissue due to a variety of anatomic and physiologic limitations.[3] Current conventional treatments involving intraocular injections to the back of the eye have proven quite successful from a therapeutic perspective, but the frequent injections that are required by many of these treatments markedly increases the risk of complications over time and, at minimum, is both incovenient for the patient and highly demanding of an ophthalmologist's time.[3–6] Thus, the development of drug delivery materials that can be delivered minimally-invasively (ideally via injections analogous to current practice) but can also prolong release of therapeutic agents (and thus limit the number of required injections for effective treatment) would be highly beneficial.

Hydrogels are particularly attractive materials in this context as they can facilitate

prolonged delivery of therapeutics, mimic the physicochemical and mechanical properties of native soft tissues *in vivo*, and can be designed to be transparent.[7–9] However, the elasticity of pre-formed bulk hydrogels makes their direct injection difficult, particularly through the narrow-gauge needles typically used for intraocular injections. As such, increasing attention has been focused on injectable, *in situ*-gelling mixing-induced two-component hydrogels (MITCH) that exploit the rapid chemical reaction of complementary groups grafted to two polymers (such as aldehyde-mediated crosslinking of alcohol-,[10] amine-,[11] or hydrazide-functionalized polymers[12–15] or thiol-mediated crosslinking with acryloyl,[16] maleimide,[17] or vinylsulfone groups[16,18]).[19–22] By judicious selection and strategic functionalization of the polymers used in MITCH-type hydrogels, such hydrogels can be designed to be transparent (effectively matching the refractive index of the vitreous humour), degradable, possess hydrophobic domains for optimizing drug binding, and facilitate tunable release kinetics.[23–25] Such hydrogels may also find ophthalmic applications as vitreous replacement materials for patients suffering from opacification of the vitreous, commonly observed upon aging.

We have recently reported on several *in situ*-gelling injectable MITCH hydrogels based on aldehyde-hydrazide chemistry, resulting in the generation of hydrolytically degradable hydrazone crosslinks upon mixing that slowly degrade at physiological conditions.[26–29] Such hydrogels are typically prepared on the bulk scale by loading hydrazide- an aldehyde-functionalized polymers into separate barrels of a double barrel syringe and then co-extruding the polymers through a static mixer to facilitate mixing and thus initiate crosslinking to form a gel (Figure 5.1). The double barrel syringe systems typically used can be applied to form hydrogels with volumes

ranging from 0.2 mL to >5 mL, with tolerances of ~ ±100 µL. However, to assess the *in vivo* capabilities of these hydrogels in mouse/rat, rabbit, and ultimately human eyes, very small amounts of each reactive material (1 – 20 µL) must be injected and effectively mixed, with tolerances of only ± 1-2 µL (and perhaps even stricter depending on the drug to be delivered) permissible to inject a controlled quantity of the given therapeutic and avoid significant changes in ocular pressure.[30] While injections on this volume scale are routinely done with single component systems, the additional requirement of mixing the two reactive polymers upon injection (while also preventing premature gelation in the injector) poses a significant additional challenge with administering MITCH-type hydrogels. Indeed, to this point, no suitable injection system exists for this application.

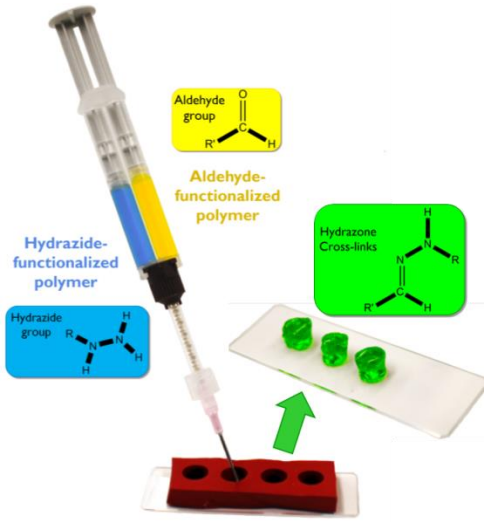

Figure 5.1: Typical hydrogel fabrication process using a double barrel syringe. Solutions of each respective reactive polymer are loaded into separate barrels of a double barrel syringe. Upon injection, these materials mix and interact rapidly in a mixing channel before being ejected out of a needle into a pre-defined mould or, for *in vivo* purposes, the tissue of interest.

In response, this work aims to design a microfluidics-based microinjector that can be used to inject MITCH hydrogels into the back of the eye with significantly better volume control and subsequently apply the microinjector to test the tissue compatibility of such hydrogels in the back of the eye for the first time. Specifically, we assess the tissue response to hydrazone crosslinked poly(oligoethylene glycol methacrylate) (POEGMA)-based hydrogels that we have extensively investigated both *in vitro* (where they demonstrate transparency, protein-repellent properties, as well as prolonged release of macromolecular therapeutics) and via subcutaneous injections *in vivo* (in which mild acute and minimal chronic inflammation was observed).[23] FITC-tagged POEGMA polymer precursors injected into one eye of Sprague-Dawley rats using our microinjector design are shown to effectively form a hydrogel *in vivo* with low volume tolerances while not inducing any significant local tissue toxicity.

5.2.3 Experimental

Materials: Acrylic acid (AA, 99%), aluminum oxide (98%), ammonium persulfate (98%), 1,4-dioxane (99%), dimethyl sulfoxide (DMSO, >99%), fluorescein isothiocyanate (FITC, >97.5%), paraffin oil (light), poly(oligoethylene glycol methacrylate) (M_n 500, $OEGMA_{500}$, >99%), and thioglycolic acid (TGA, >98%) were all purchased from Sigma Aldrich (Oakville, ON). All monomers were purified prior to their polymerization by passing them through an aluminum oxide column. *N*-(2,2-dimethylaminoethyl)methacrylamide (DMAEMAm) was synthesized in-house following the procedure of Patenaude et al.[13] N-3-dimethylaminopropyl-N-ethyl carbodiimide hydrochloride (EDC, commercial grade) was purchased from Carbosyth (Compton, CA). Adipic acid dihydrazide (ADH, 97%)

was purchased from Alfa Aesar. 1 M HCl was purchased from LabChem Inc. Dimethyl 2,2'-azobis(2-methylpropionate) (AIBMe, 98.5%) was purchased from Waterstone Technologies. The poly(dimethylsiloxane) (PDMS) elastomer used was made from Dow Corning Sylgard 184 Elastomer kit purchased from Ellsworth Adhesives. Bovine vitreous humour was obtained from fresh bovine eyes received from a local farm. Deionized water (DIW) was purified using a Barnstead Nanopure purification system.

Synthesis of hydrazide-functionalized POEGMA (POEGMA-Hzd): Hydrazide-functionalized POEGMA was synthesized by copolymerizing 4.0 g of $OEGMA_{500}$ with 286 µL of acrylic acid (AA), 1 µL of TGA, and 0.037 g of AIBMe in 20 mL of DMSO in a 100 mL Schlenk flask. The solution was purged for 30 minutes under nitrogen, and the polymerization was initiated by submerging the solution in an oil bath preheated to 75°C under a nitrogen atmosphere with magnetic stirring. The polymerization was allowed to proceed for 4 hours. The dioxane was evaporated off, and the polymer was dissolved in deionized water (DIW) and dialysed over 6 (6+ hour) cycles before lyophilization to dryness. The carboxyl groups (from the AA residues) were subsequently functionalized with hydrazide groups by dissolving 3.0 g of the resulting polymer and 3.6 g of ADH in 150 mL DIW. The pH was adjusted to pH = 4.75 with 0.1 M HCl. A solution of EDC (1.6 g of EDC in 5 mL DIW) was then added to the flask, and a pH of 4.75 was maintained for 4 hours via the dropwise addition of 0.1 M HCl. The resulting hydrazide-functionalized POEGMA polymer was then dialysed over 6 (6+ hour) cycles, lyophilized, and then stored as 20 w/w% solutions in PBS at 4°C.

To fluorescently tag this polymer with FITC, 0.5 g of the polymer was dissolved in 500 mL of 0.1M Na_2CO_3 buffer, 10 mg of FITC was added to the solution, and the solution

was allowed to stir overnight. The polymer solution was then dialysed, lyophilized, and stored in the same manner as the non-FITC tagged polymer.

Synthesis of aldehyde-functionalized POEGMA (POEGMA-Ald): POEGMA with aldehyde functionality was prepared by copolymerizing 4.0 g $OEGMA_{500}$ with 0.60 g DMAEMAm, 1 µL of TGA, and 0.050 g of AIBMe in 20 mL of DMSO in a 100 mL Schlenk flask. The solution was purged with nitrogen for 30 minutes, and the polymerization was initiated by submerging the solution in an oil bath preheated to 75°C with magnetic stirring. The polymerization was allowed to proceed for 4 hours, after which the dioxane was evaporated off and the poly(OEGMA-co-DMAEMAm) polymer was dialyzed against deionized water (DIW) for 6 (6+ hour) cycles before lyophilizing to dryness. The acetal groups of the poly(OEGMA-co-DMAEMAm) polymer were then converted to aldehydes by dissolving the copolymer in a 100 mL, 50:50 mixture of DIW and 1 M HCl and leaving the solution to stir for 24 hours. Following, the aldehyde-functionalized POEGMA polymer was dialyzed against DIW for 6 (6+ hour) cycles, lyophilized, and then stored as a 20 w/w% solution in PBS at 4°C.

Microinjector device design: A simplified schematic of the designed microinjection device is shown in Figure 5.2. The hydrazide- and aldehyde-polymer solutions were loaded within separate barrels of a double syringe (as per bulk injections). The double barrel syringe was then connected to the device with silicone tubing. Upon injection, the pressure forces the polymer solutions through a serpentine microfluidic channel structured with staggered herringbone mixers, originally described by Stroock et al.[31], which apply transverse flows to induce microvortexes and promote mixing. After navigating through the mixing channel, the mixed polymer solutions enter and fill the

volume control reservoir. The device is fully primed when these polymer solutions first exit from the microinjector via the outlet needle/capillary. After the device is primed, the material within the volume control reservoir can then be ejected by pushing the plunger of an air- or buffer-loaded (20 µL) syringe attached to the ejection syringe inlet, forcing a controlled amount material (equivalent to the designed volume of the volume control reservoir) out of the needle/capillary of the injector. A one-way valve included at the outlet of the mixing channel ensures that the contents of the volume control reservoir are ejected out of the device and not back into the mixing channel; this one-way valve was also found to be essential in the practical application of the device to avoid complications with intraocular pressure when using the device to inject gel inside the eye.

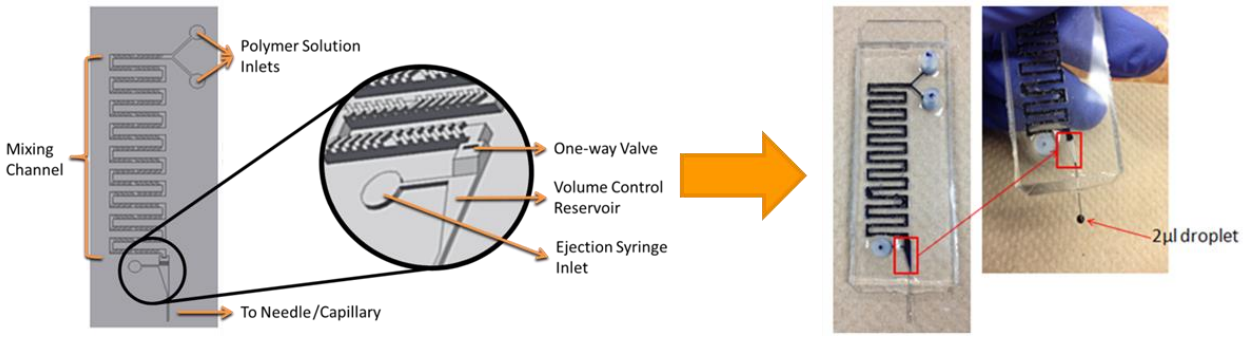

Figure 5.2: Schematic of the microinjector design. A manual pressure source propels the polymer solutions from their reservoirs into a herringbone mixing microfluidic channel before their emission from a needle. The volume contained within the volume control reservoir (designed to be 2 µL for this particular device) is the controlled volume that is released when pressure is applied to the ejection syringe inlet.

Microinjector fabrication: Two approaches were used to design the microfluidic devices: (1) Conventional soft photolithography was performed based on a master mould patterned on a 3” silicon wafer using SU-8 100 photoresist (MicroChem, MA,

USA). The inlets, pieces of Masterflex silicone tubing (L/S 13, 0.8 mm I.D., Cole Parmer, ON), were placed on the mould before casting the PDMS on the mould, after which the devices were heated on a hot plate at 75°C for 2 h to cure the PDMS. After curing, the PDMS was peeled off and bonded to a glass slide by exposing both materials to oxygen plasma at 40 W for 30 s at 0.3 mTorr and then placing the materials together to allow them to bond overnight. (2) A ProJet HD 3000 3D printer was used to create the master mould based on ProJet's VisiJet EX200 plastic, offering the benefit of cheaper and more rapid master mould fabrication better suited the need to generate moulds with varying designs and volumes while still maintaining a suitable resolution for developing a handheld microinjector.

To minimize the cost of the devices, capillaries with an outer diameter equivalent to a 33G needle were used instead of 33G blunt needles. These capillaries were added to PDMS moulds already bound to a glass slide by placing the capillary in the correct position (i.e. the exit from the volume control chamber) and sealing them to the device with PDMS before curing them once again at 75°C for 2 h. Following, the devices were sterilized in an autoclave, and the double barrel and ejection syringes were attached to the inlets using polystyrene Luer lock adapters (with 1/16" hose barbs) attached to the 0.8 mm I.D. L/S 13 silicone tubing (both obtained from McMaster-Carr).

Microinjector operation and in vitro validation: The device, with the double barrel syringe (loaded with 11.25 wt% solutions of POEGMA-Hzd and POEGMA-Ald polymer solutions) and the ejection syringe (air-loaded) attached, was first primed by applying pressure to the double barrel syringe until the mixed polymer solution exits the capillary.

The capillary was then inserted into the target delivery site, and the ejection syringe was used to push out the pre-gel solution from the volume control reservoir.

In vitro validation of the device was performed by observing (1) the efficacy of mixing of the two polymer precursors, (2) the capacity to form hydrogels in multiple different solutions, (3) the consistency with which hydrogel droplets were manufactured and (4) whether all the material within the volume is ejected when desired.

(1) The efficiency of mixing, with and without the herringbone structure, was studied by flowing polymer solutions were flowed through a slightly modified three inlet chip (still using the two precursor polymers at 3 mL/min, as controlled with a Legato 2000 syringe pump). Methylene blue was added to the POEGMA-Hzd polymer solution, enabling monitoring of mixing of the two precursor polymer solutions at various points within the chip via a microscope and a camera taking grayscale pictures. The degree of mixing was determined by using ImageJ to observe the gray value across the width of the channel in a grayscale image taken at each predetermined position in the mixing channel. In particular, the point at 17.5 mm after the solutions first interact (corresponding to 15% of the length of the entire mixing channel) was found to be most indicative of how useful herringbone grooves are at improving the mixing of the polymer solutions within the channels and is emphasized in the results section.

(2) To test the gelation of the polymer solutions and their capacity to form hydrogels on/in an array of materials, 2 µL POEGMA hydrogels were extruded onto glass surfaces (into air) as well as into solutions of 10 mM PBS and bovine vitreous humour at 37°C.

(3) To assess the reproducibility of the injected volumes delivered by the device, replicate injections into paraffin oil were performed. The surface tension between the hydrophobic oil and the hydrophilic gel resulted in the formation of near-perfect spheres, enabling facile measurements of total droplet volume by simply measuring the droplet diameter. Images of the droplets were then taken immediately post-injection via a 30½G needle (in frame), with the diameter of the droplets recorded using ImageJ using the 30½G needle diameter as the reference dimension. The volume of microgel beads from 5 µL 3D printer-bourne microinjector were estimated using a microbalance, assuming a density of the microgel of ~1.026 g/mL (determined using a newly calibrated micropipette).

(4) To determine whether the control volume can be completely emptied when the ejection syringe is depressed, POEGMA-Hzd was fluorescently labelled by conjugating FITC to a small portion (~2 mol %) of the hydrazide groups on the polymer, using a method previously described by Deng et al.[32] Fluorescence microscopy (Etaluma Lumascope 500, 493 nm excitation/512 nm emission wavelengths) was subsequently used to observe the volume control region before and after using the ejection syringe to push the material in this region out the capillary.

In vivo* assessment of microinjector device performance and hydrogel tissue compatibility in the eye*: Intraocular *in vivo* injections of POEGMA hydrogels were performed on Sprague Dawley rats (Charles River, strain code 400). All animals were handled according to the principles of the ARVO Statement for the Use of Animals in Vision Research as well as the guidelines set out by McMaster AREB and the Canadian Council of Animal Care. Streamlining the timing of this injection process is essential to

reliably inject MITCH-type hydrogels effectively. The rats were induced with isofluorane and anaesthetized with a ketamine xylazine mixture, after which they were positioned on a holder to allow for the Phoenix Micron IV Retinal Microscope System (equipped with a camera and linked to a computer) to be positioned to image the eye in real-time (Figure S5.1). A lancing incision was first made in the temporal side of the sclera-corneal limbus using 30 gauge needle coated in Nile Blue A to easily visualize the location of the hole. Following, the microinjector was primed as described previously with 11.25 wt% solutions of POEGMA-Hzd and POEGMA-Ald, with any excess solution wiped away at the capillary tip. The capillary of the microinjector was then inserted into the vitreous humour through the pre-punctured hole. Once the microinjector was in position, the injection syringe (filled with air) was depressed to eject the pre-gel solution out the volume control chamber. The microinjector was then removed from the eye and the fluorescent gel was monitored with the Micron IV microscope system. Each injection was only performed on one eye of the rats, with their other eye used as a positive control.

The intraocular pressure (IOP) was tracked with an Icare Tonolab tonometer in both the injected and control eyes. The eyes were visually observed periodically over the next two weeks using the camera system. Animals were sacrificed after 15 days and eyes were enucleated. The eye samples were fixed in 4% neutral buffered formalin (NBF) for 24 hours, followed by standard histological processing and embedding into paraffin wax. Whole eyes were processed into 5 μm sections along the sagittal plane. Tissue samples were stained using haematoxylin and eosin (H&E) following standard protocols, with the resulting cross-sections examined using a conventional light microscope (Olympus, BX51).

5.2.4 Results and discussion

Several design goals had to be met to design an effective intraocular microinjection device. In terms of the functionality of the device, the microinjector must be capable of: (1) effectively mixing the two precursor polymers from separate microchannels upon injection; (2) controllably and precisely injecting volumes in the 1 - 20 µL range through a narrow gauge needle suitable for ophthalmic applications (30G or higher) with high reproducibility; (3) rapidly injecting these materials to prevent gelation and blockage within the needle; and (4) being produced inexpensively, as the devices will be only used one time due to gelation of the precursor polymers in the mixing channel. In terms of the practical ergonomics of the device, its method of use should be as close as possible to current clinical protocol. Current vitreal injections (particularly in small animal models) are typically performed by first perforating a hole in the sclera (generally with a 27-30G needle) and inserting the blunt 33G needle of a syringe through this hole, with one person holding the syringe in place and another pushing the plunger to eject the payload.[33] In the device design pursued, one person similarly holds the device following priming and the second person depresses the ejection syringe to empty the volume control reservoir into the target position. In addition, as administration times can vary from 1 to 5 minutes to successfully insert and position the needle through the hole, the device should be not unduly complicated to use while at the same time providing some operational flexiblity for different procedure times. In this context, the relatively fast gelation of the POEGMA-hydrazone gels (1-5 minute gelation times for the formulations used herein) further requires a device design that facilitates rapid administration while retaining some degree of flexibility for the practitioner.

The ultimate device design was intended to meet all of the aforementioned requirements while operating analogously to the macroscale double-barrel system, but using a microfluidic method with an added component to control the volume released. Two methods (soft lithography and 3D printing) were used to design the devices, with the low tolerances and smaller feature sizes facilitated by microfluidics offset by the higher flexibility in terms of rapid re-design and lower per unit cost of 3D printing. For the lithography-based design, the microinjector had channels with a width of 200 μm and a height of 100 μm and alternating herringbone grooves having a height of 23 μm spaced 50 μm apart within the mixing channel. These herringbone grooves were added to the devices to enhance the mixing of the two polymer solutions, as the microfluidic nature of these devices encourages laminar flow regimes. The impact of the addition of herringbone patterns to the devices is immediately apparent in Figure 5.3, in which methylene blue dye was added to the POEGMA-Hzd polymer solution and the distribution of the methylene blue was analyzed at various positions in the serpentine mixing channel. Figure 5.3 shows a mixing comparison of devices with and without the herringbone structure at the first position studied, only 17.5 mm after the solutions first interact as the polymer solutions.

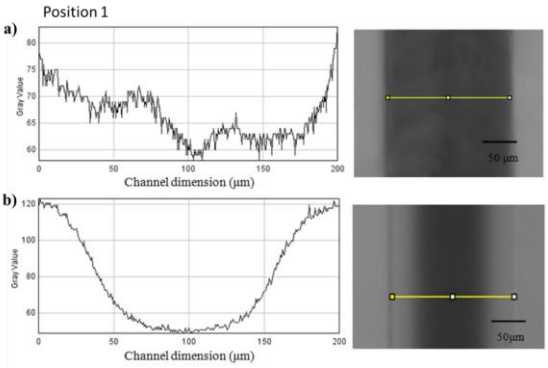

Figure 5.3: Grayscale mixing distribution over the channel width for designs (a) with and (b) without herringbone structures at 17.5 mm from the mixing junction.

With the herringbone mixers included, nearly complete mixing occurs at the first observed position, only 17.5 mm into the mixing channel (15% of the total length of the channel used). Conversely, in a microchannel of the same dimensions prepared without herringbone structures, the two streams are still clearly delineated from each other at this position, as any mixing is only due to diffusional effects based on the laminar flow regime in the channel.

To confirm both gelation of the polymers delivered through the device as well as the effective separation of the small droplets from the outlet capillary of the microinjector, gels were extruded onto glass surfaces and into solutions of PBS and (most relevant to the proposed application) bovine vitreous humour at 37°C. Figure 5.4 shows a representative sample of a small, ~2 μL hydrogel droplet containing methylene blue (for more facile visualization) ejected from the microinjector into bovine vitreous humour at 37°C. The hydrogel droplets consistently separated from the microinjector and formed small hydrogel beads directly at the site of administration. In addition, the hydrogel

droplet could be carefully removed from the solution minutes after injection, indicating that the polymer solutions do ultimately result in the formation of crosslinked hydrogels.

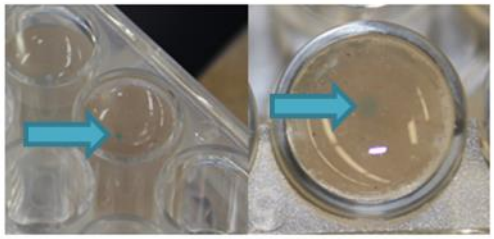

Figure 5.4: A ~2 µL gelled hydrogel droplet (dyed with methylene blue) injected into bovine vitreous humour at 37°C.

The extent of volume control provided by these initial prototypes was then assessed by injecting hydrogels into paraffin oil, which based on surface tension gradients results in very spherical hydrogel droplets that can be imaged and measured. Figure 5.5 shows the greatest variation in droplet sizes observed over ~15 repeat injections from a device intended to deliver 2 µL hydrogel droplets observed thus far with volumes of 1.92 ± 0.06 µL; even the extreme volume results obtained still lie within a ~±10% range. As such, the combination of the volume control chamber and the one-way flow valve on the device enables repeatable ejection and separation of droplets with controlled volumes (~±10%) in the range of interest for intraocular injections (1–10 µL) via an entirely handheld operation, requiring no additional equipment.

Figure 5.5: Example of small variation in droplet size from a 2 µL microinjection system developed from a mould generated using photolithography.

The reproducibility of this device, while attractive, requires a trade-off in terms of the cost of each device (problematic given the requirement to use a new device for each injection) and the flexibility of the volume to be delivered (i.e. changing the volume would require fabricating a new silicon-based master mould, which is both time-consuming and expensive). As an alternative, a mould with the same basic geometry but prepared via 3D printing was fabricated. Due to the significantly lower resolution of 3D printing versus soft lithography, the dimensions of this device are much larger than the previous device (channels with a width of 900 μm and a height of 600 μm and alternating herringbone grooves having a height of 250 μm spaced 350 μm apart); the result is slightly lower reproducibility associated with repeat injections. Indeed, for a device designed with a 5.2 μL control volume, POEGMA droplets with a volume of 4.3 ± 0.8 μL (*n=24*), as measured using a microbalance, were injected (corresponding to ~15-20% variability versus ~10% with the microfluidic injectors). However, this variability is still more than acceptable for attempting to assess the tissue responses of our hydrogels *in vivo*; furthermore, given that effective controlled release of drug would eliminate bolus dosing and thus the potential toxicity challenges with using injection volumes that are too high, even this 3D printed device may offer improvements over current clinical practice. Furthermore, relative to the lithographic injectors, the use of these larger dimensions and 3D printing for preparing the devices offers several compelling advantages: (1) microinjectors could be slightly modified and manufactured to have different control volumes in a much more rapid manner via this process, significantly lowering the costs of device development; (2) increasing the channel dimensions increases the Reynolds number in the channels, improving mixing (although the herringbone structures were still retained in this design to ensure effective mixing); (3) the same volume control reservoir

sizes that we desire (>1 µL) can be accurately 3D printed, enabling injection of the same control volumes to the eye.

Due to larger size of the devices fabricated from 3D printed moulds, the resulting reduced probability of laminar flow could result in the not all of the material in the control volume being ejected from this reservoir when pressure is applied to the ejection syringe. This possibility was examined by using fluorescently labelled polymers and observing the fluorescence intensity within the volume control reservoir before and after the ejection of a 5 µL sample of gel with an water-filled ejection syringe. As shown in Figure 5.6, the entire volume of the material in the control reservoir can indeed be ejected from the device. Note that the fluorescence intensity is not fully uniform in the volume control reservoir prior to ejection, related to the formation of pre-gel structures after the components have been mixed but prior to the formation of bulk gel monoliths.

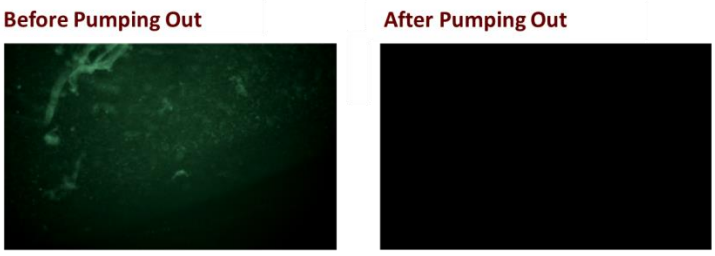

Figure 5.6: The volume control region of a microinjector primed with aldehyde-functionalized POEGMA and FITC-labelled hydrazide-functionalized POEGMA before and after using the ejection syringe to pump out the material initially inhabiting the volume control region.

The POGEMA hydrogels used in this work have previously been shown to have little to no cytotoxicity *in vitro* with NIH 3T3 mouse fibroblast cells and, notably, retinal pigment epithelium cells.[23] As such, these hydrogels were ideal candidates for intraocular

injection. The protein repellent and fluorescent (but otherwise transparent) POEGMA hydrogels were injected into one eye of Sprague Dawley rats using a 3D printed microinjector (5 µL volume reservoir) while the other eye was used as a control, with both eyes observed with a Micron IV microscope system immediately post-injection and over the next 14 days. The images for the choroidal injection and representative images for the five vitreal injections performed are shown in Figure 5.7.

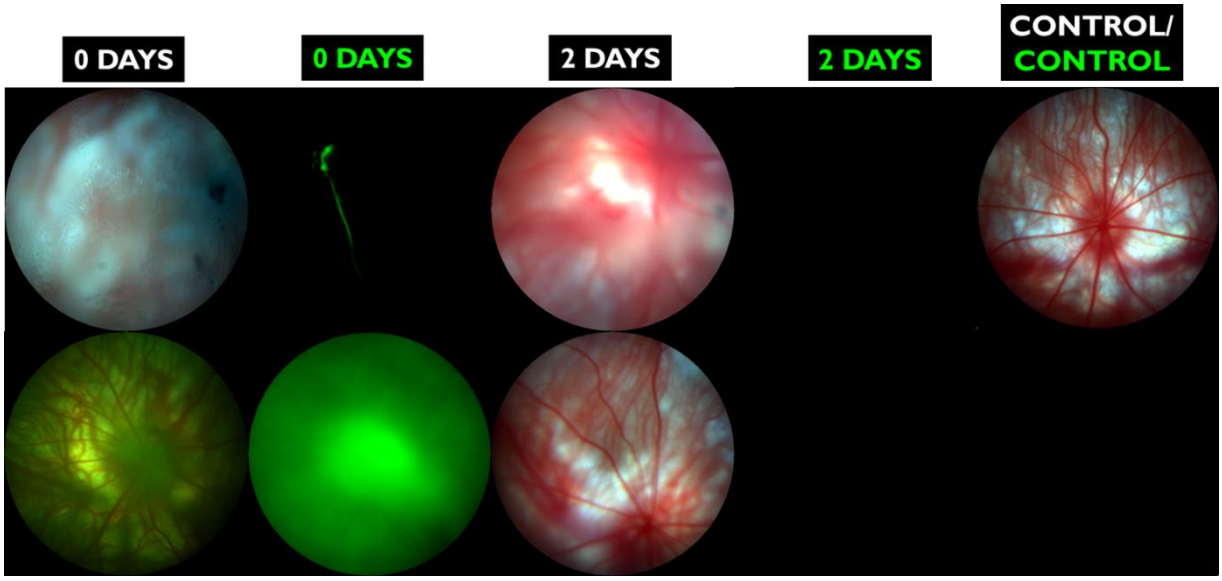

Figure 5.7: Injection of FITC-labeled POEGMA-Hzd/POEGMA-Ald hydrogels delivered via a microfluidic microinjection device into the choroid (top) and the vitreous (bottom). Fluorescent (green) and brightfield (white) images were taken immediately after the injection and two days post-injection. There was no fluorescence detected on day 2 or in the control fluorescent image.

While it was not intended to inject these materials into the choroidal region of the eye (between the retina and the sclera), the increased flexibility of the capillary over traditional needles made this form of injection much easier to perform than with conventional stiff metallic needles, with which such injections are highly challenging

even on larger (human) eyes. Given the significant interest in using the choroid itself as a drug depot for drug delivery to the back of the eye,[34,35] this apparent benefit of microinjector delivery offers the potential to more easily exploit the possible dual regulation of drug release from the injected hydrogel (i.e. diffusion through the gel) and diffusion through the choroid. The resulting hydrogel formed in the needle track and exhibits a high fluorescence intensity from a well-defined geometry, suggesting the formation of a well-defined gel (i.e. no significant diffusion of precursor polymers away from the injection site). However, no fluorescence persisted at day 2, presumably due to photobleaching of the fluorescein-based probes in the pigment-free albino rats used for the studies. Note that the transparency of the hydrogels also means that they cannot be observed under the brightfield wavelengths. In contrast, pre-gel mixtures injected into the vitreous appear to disperse significantly more than they do in the choroid, still leading to the apparent formation of a hydrogel but one that likely possesses a lower crosslink density than injections into small, well-defined choroidal space. Again, no fluorescence whatsoever was observed at day 2, presumably due to the same issues with photobleaching as noted for the choroidal injection. However, following sacrifice of rats two weeks post-injection, semi-opaque hydrogels were found to persist in each of the injected eyes but not the control eyes; this result suggests that the loss of fluorescence at day 2 is due to photobleaching and not clearance of the hydrogels and/or the hydrogel precursor polymers from the eye. Note that the conversion of the gel optical properties from fully transparent to semi-opaque is consistent with hydrogel behavior in long-term swelling experiments, presumably due to the degradation of the polymers shifting the phase transition temperature of the hydrogel or protein deposition on/within the hydrogel.

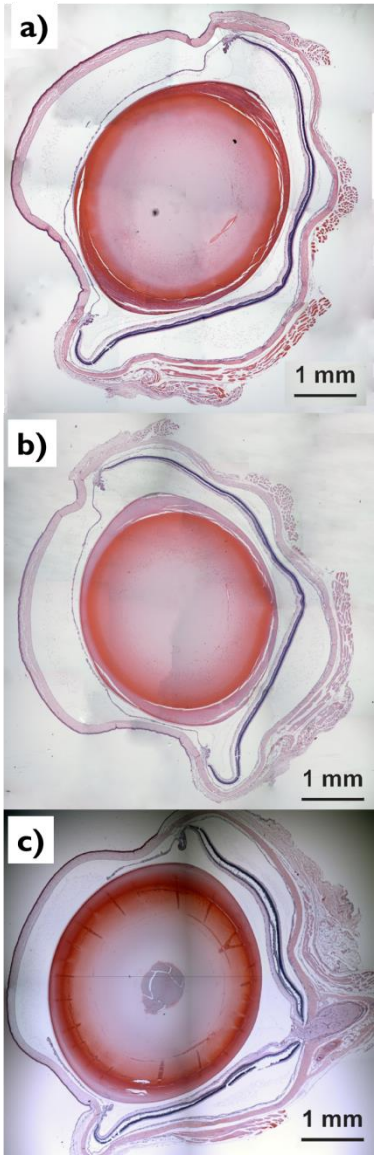

Figure 5.8: Histology of (a) eye that underwent choroidal injection, (b) eye that underwent vitreal injection, and (c) representative control eye that received a lancing injection but was not injected with the microinjector.

Images of histological sections from the eyes injected with POEGMA hydrogels (both targeting the choroid and the vitreous) and the control eyes are shown in Figure 5.8. Comparing histology of the eyes that underwent the choroidal injection (a), the

intravitreal injection (b), and the control (c) shows no retinal toxicity based on the lack of retinal necrosis, infiltration of inflammatory cells or morphological changes. There is no indication that retinal cells were affected in any way, so neither the use of the microinjection device nor the gel chemistry is inducing undesirable tissue responses in the back of the eye. POEGMA gels can therefore be injected into the vitreous, can form gels in this environment, and seem to be extremely well tolerated. This suggests the potential of MITCH-type hydrogels delivered via this microinjection system as intraocular drug delivery devices for treating posterior eye diseases (with particular potential interest in wet acute macular degeneration given the noted capacity of similar POEGMA hydrogels to facilitate long-term protein delivery)[36] and/or potential materials for intravitreal replacement.

5.2.5 Conclusions

A new microfluidics-based microinjection device was developed and demonstrated to effectively mix and subsequently deliver precise small volumes of *in situ* gelling hydrogel precursors to the back of the eye, allowing *in vivo* assessment of injectable MITCH-type hydrogels as ocular drug delivery materials for the first time. The devices are capable of delivering 1-20 µL volumes of hydrogel precursor polymers with relatively low tolerances (~10% for the photolithography injectors and ~15-20% for the 3D printed injectors) through 33G blunt needles or glass capillaries, enabling the formation of hydrogels *in situ* that can effectively separate from the needle upon injection. Injection of hydrazone crosslinked POEGMA hydrogels into the back of the eye using these devices was demonstrated to result in effective gel formation *in vivo* without inducing any significant

tissue toxicity or inflammation relative to an untreated control eye. Furthermore, choroidal injections (highly challenging with conventional needles) appear to be significantly easier with the microinjection devices given the flexibility of the glass capillaries used at the device outlets. We anticipate such devices, coupled with these or other MITCH-type hydrogels, have significant potential to deliver hydrogel-based drug delivery depots to the intraocular space to address current challenges with drug delivery for posterior eye diseases.

5.2.6 Acknowledgements

The authors thank the J.P. Bickell Foundation (Medical Research Grant Program), the Vanier Scholarship program, and the Natural Sciences and Engineering Research Council of Canada (NSERC) for funding.

5.2.7 References

1 M. E. Myles, D. M. Neumann and J. M. Hill, *Adv. Drug Deliv. Rev.*, 2005, **57**, 2063–2079.

2 S. D. Fitzpatrick, M. Jafar Mazumder, F. Lasowski, L. E. Fitzpatrick and H. Sheardown, *Biomacromolecules*, 2010, **11**, 2261–2267.

3 H. Sheardown, *Future Med. Chem.*, 2012, **4**, 2123–2125.

4 U. B. Kompella, A. C. Amrite, R. Pacha and S. A. Durazo, *Prog. Retin. Eye Res.*, 2013, **36**, 172–198.

5 M. N. Yasin, D. Svirskis, A. Seyfoddin and I. D. Rupenthal, *J. Control. Release*, 2014, **196**, 208–221.

6 V. Delplace, S. Payne and M. Shoichet, *J. Control. Release*, 2015, **219**, 652–668.

7 T. R. Hoare and D. S. Kohane, *Polymer*, 2008, **49**, 1993–2007.

8 S. Merino, C. Martin, K. Kostarelos, M. Prato and E. Vázquez, *ACS Nano*, 2015, **9**, 4686–4697.

9 S. B. Campbell and T. Hoare, *Curr. Opin. Chem. Eng.*, 2014, **4**, 1–10.

10 C. Yeom and K. Lee, *J. Memb. Sci.*, 1996, **109**, 257–265.

11 H. Tan, C. R. Chu, K. A. Payne and K. G. Marra, *Biomaterials*, 2009, **30**, 2499–2506.

12 T. Ito, I. P. Fraser, Y. Yeo, C. B. Highley, E. Bellas and D. S. Kohane, *Biomaterials*, 2007, **28**, 1778–1786.

13 M. Patenaude, S. Campbell, D. Kinio and T. Hoare, *Biomacromolecules*, 2014, **15**, 781–790.

14 D. D. McKinnon, D. W. Domaille, J. N. Cha and K. S. Anseth, *Adv. Mater.*, 2013, 865–872.

15 D. D. McKinnon, D. W. Domaille, T. E. Brown, K. A. Kyburz, E. Kiyotake, J. N. Cha and K. S. Anseth, *Soft Matter*, 2014, **10**, 9230–9236.

16 C. Hiemstra, L. van der Aa and Z. Zhong, *Macromolecules*, 2007, **40**, 1165–1173.

17 E. A. Phelps, N. O. Enemchukwu, V. F. Fiore, J. C. Sy, N. Murthy, T. A. Sulchek, T. H. Barker and A. J. García, *Adv. Mater.*, 2012, **24**, 64–70.

18 B. Qiu, S. Stefanos, J. Ma, A. Lalloo, B. A. Perry, M. J. Leibowitz, P. J. Sinko and S. Stein, *Biomaterials*, 2003, **24**, 11–18.

19 S. R. Van Tomme, G. Storm and W. E. Hennink, *Int. J. Pharm.*, 2008, **355**, 1–18.

20 D. J. Overstreet, D. Dutta, S. E. Stabenfeldt and B. L. Vernon, *J. Polym. Sci. Part B Polym. Phys.*, 2012, **50**, 881–903.

21 W. E. Hennink and C. F. van Nostrum, *Adv. Drug Deliv. Rev.*, 2002, **54**, 13–36.

22 C. T. S. Wong, P. Foo, J. Seok, W. Mulyasasmita, A. Parisi-Amon and S. C. Heilshorn, *Proc. Natl. Acad. Sci. U. S. A.*, 2009, **106**, 22067–22072.

23 N. Smeets, E. Bakaic, M. Patenaude and T. Hoare, *Chem. Commun.*, 2014, **50**, 3306–3309.

24 M. Patenaude and T. Hoare, *Biomacromolecules*, 2012, **13**, 369–378.

25 W. Mulyasasmita, L. Cai, R. E. Dewi, A. Jha, S. D. Ullmann, R. H. Luong, N. F. Huang and S. C. Heilshorn, *J. Control. Release*, 2014, **191**, 71–81.

26 M. Patenaude and T. Hoare, *ACS Macro Lett.*, 2012, **1**, 409–413.

27 S. B. Campbell, M. Patenaude and T. Hoare, *Biomacromolecules*, 2013, **14**, 644–653.

28 D. Maitland, S. B. Campbell, J. Chen and T. Hoare, *RSC Adv.*, 2016, **6**, 15770–15781.

29 S. Campbell, D. Maitland and T. Hoare, *ACS Macro Lett.*, 2015, **4**, 312–316.

30 B. Xie, L. Jin, Z. Luo, J. Yu, S. Shi, Z. Zhang, M. Shen, H. Chen, X. Li and Z. Song, *Int. J. Pharm.*, 2015, **490**, 375–383.

31 A. D. Stroock, S. K. W. Dertinger, A. Ajdari, I. Mezic, H. Stone and G. M. Whitesides, *Science*, 2002, **295**, 647–651.

32 X. Deng, N. M. B. Smeets, J. Wang, J. D. Brennan, C. D. M. Filipe and T. Hoare, *J. Am. Chem. Soc.*, 2014, **136**, 12852–12855.

33 P. Sheikholeslami, B. Muirhead, D. Sung, H. Baek, H. Wang, X. Zhao, D. Sivakumaran, S. Boyd, H. Sheardown and T. Hoare, *Exp. Eye Res.*, 2015, **137**, 18–31.

34 T. Yasukawa, Y. Ogura, Y. Tabata, H. Kimura, P. Wiedemann and Y. Honda, *Prog. Retin. Eye Res.*, 2004, **23**, 253–281.

35 N. Kuno and S. Fujii, *Polymers*, 2011, **3**, 193–221.

36 E. Bakaic, N. M. B. Smeets, H. Dorrington and T. Hoare, *RSC Adv.*, 2015, **5**, 33364–33376.

5.2.8 Supporting Information

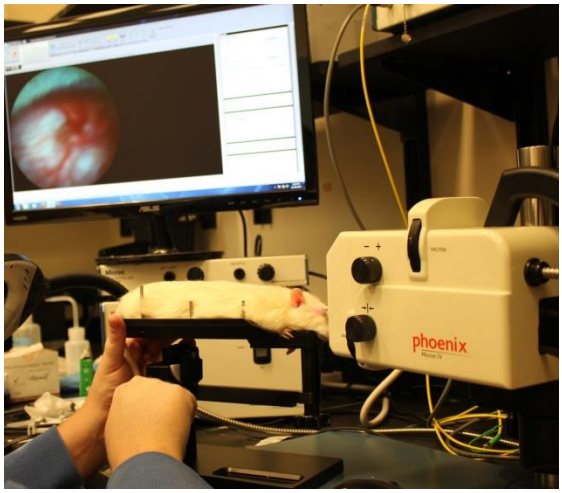

Figure S5.1: Phoenix IV camera setup for monitoring *in vivo* injections and injected materials.

Chapter 6: Magnetic microgel nanocomposites

6.1 Preface

This work investigates the use of cationic magnetic thermosensitive poly(N-isopropyl methacrylamide (PNIPMAM)-co-acetoacetoxyethyl methacrylate (AAEM)) microgels for AMF-actuated drug release, which had not been demonstrated previously. The microgels are prepared using precipitation polymerization and large fractions of SPIONs incorporated into their structure (up to 40 wt.%) as the SPIONs coordinate with the AAEM within the microgels upon synthesis. The cationic, thermosensitive microgels with 15 wt.% SPION content were loaded with fluorescein and from a simple continuous AMF study for a 6 hour period, it was shown that ~4.6 times more fluorescein was released when the AMF was applied compared to controls without any AMF application. This is the first time enhanced release has been shown from microgel-based nanocomposites in response to an AMF, opening the door to several potential applications for these, or similar, materials.

6.2 Thermosensitive magnetic microgels for remotely triggered, on-demand therapeutic delivery

Scott Campbell, Angus Lam, Jenny Chen, and Todd Hoare [Manuscript in preparation]*

6.2.1 *Abstract*

Nanoscale delivery vehicles that can be remotely steered and/or activated offer potential for patient- or practitioner-controlled drug delivery at the location and timing desired.

Herein, remote controlled release from microgel-based nanocomposites is demonstrated for the first time using an alternating magnetic field (AMF). In a simple, two-stage fabrication process, superparamagnetic iron oxide nanoparticles (SPIONs) were seeded within cationic thermosensitive gel nanoparticles that contain defined quantities of charged functional groups that enable drug loading via ionic interactions. The microgels can entrap large amounts of SPIONs in their matrix (> 25 wt/wt%) while remaining stable in aqueous suspension and maintaining superparamagnetic properties while exhibiting low cytotoxicity *in vitro*. Upon application of an AMF, the SPIONs generate heat that is transferred to the thermosensitive microgels, causing them to deswell and release drug; cationic SPION-microgels were shown release enhanced amounts of fluorescein in response to AMF exposure via this mechanism. Such magnetic microgels could potentially be used to target deliver drugs via magnetic remote activation alone or potentially be entrapped and concentrated in a larger construct to localize activatable drug delivery vehicles at a specific location.

Keywords: microgels, iron oxide nanoparticles, on-demand, drug delivery, controlled release, injectable.

6.2.2 Introduction

Inspiration for a significant portion of the recent advances in materials science is drawn from nature.[1–4] In the field of drug delivery, we can observe how the body naturally regulates its own biochemistry. A perfect example of this is how healthy beta cells

regulate insulin by monitoring glucose levels in the body and respond by delivering the appropriate amount of insulin to sustain normoglycemia. These cells are so optimized for this purpose that some of the most promising research regarding the regulation of insulin release for diabetes centers around delivering and prolonging the lifetime and efficacy of healthy allogeneic or xenogeneic beta islet cells to produce and deliver insulin to effectively regulate glucose over extended lengths of time.[5–7]

Despite this, much of the non-cell based controlled drug delivery systems intended to achieve prolonged drug release deliver the therapeutic in a passive manner, unlike their natural cellular counterparts that regulate the release of cytokines, growth factors, etc. based on signals from their *in vivo* environment.[8] These passive drug delivery systems have predetermined release rates that are independent of changing physiological circumstances or patient needs, meaning once they are implanted/injected into the body they are beyond the control of health professionals and the patient.[9] The capability instead to control release on-demand from implanted devices would thus be highly beneficial for many scenarios, such as insulin delivery, chronic pain treatments, and endocrine disorders. Even chemotherapeutic treatments have also shown improved efficacy in response to the periodic delivery of therapeutics, otherwise termed as chronopharmaceutical drug delivery.[10,11]

Recently, complex drug release profiles have been achieved by remotely triggerable systems that respond to external stimuli such as light, ultrasound, and electromagnetic fields.[12–14] A wide range of engineered biomaterials have been developed to enable control over the dose and timing of drug release, from liposomes[15] and nanoparticles[16,17] to hydrogels[18] and microchips[19]. Gold nanomaterials (activated via near-infrared

irradiation),[9,20,21] carbon nanomaterials (nanotubes and graphene, activated via alternating magnetic fields and near-infrared irradiation),[22–24] and superparamagnetic iron oxide nanoparticles (SPIONs, activated by alternating magnetic fields)[25–28] can be used to regulate drug release in thermoresponsive materials by generating heat in response to alternating magnetic fields (AMFs) that induces some change in the material that encourages drug release.[12] SPIONs are widely considered to be the more potentially biocompatible of these nanomaterials, with some reports indicating that they can be converted into nontoxic iron species within acidic intracellular lysosomes after they are internalized by cells.[29–31] The use of electromagnetic fields is particularly interesting due to the potential depth of penetration provided (with minimal energy adsorption by native tissues) relative to light and even ultrasound-controlled delivery, meaning that delivery systems could be implanted into nearly any location in the body and still be remotely accessible for on-demand drug delivery.[32,33]

Thermoresponsive polymeric materials are often based on the thermoresponsive polymer poly(N-isopropylacrylamide) (PNIPAM) or its derivatives. PNIPAM-based hydrogels have sparked considerable interest as biomaterials due to their physiochemical similarity to soft tissues, high void fractions, highly tunable properties, and thermosensitive nature.[34] Hydrogels and microgels composed of PNIPAM exhibit a volume phase transition temperature (VPTT) at which the gel reversibly swells/deswells as its temperature is switched below/above this threshold. It is this temperature-based swelling/deswelling mechanism that can be leveraged in order to control drug release, particularly if SPIONs are incorporated within the gel to manipulate the temperature around the VPTT via remote actuation.

Our lab first performed remote activated release by incorporating SPIONs into injectable PNIPAM-based hydrogel nanocomposites and activating pulsatile drug release using short 5-10 minute pulses of an AMF.[18] Further improvements in the ratio between the on- and off-state release kinetics were achieved by co-entrapping thermosensitive microgels and SPIONs in a hydrogel structure; herein, the heat produced by SPIONs is transferred to the thermosensitive microgels, prompting them to deswell and generate free volume to enhance release.[35] By changing various parameters of the nanocomposite (microgel content, microgel VPTT, hydrogel swelling ratio, AMF pulse duration, etc.), the ratio between the on- and off-states of release was vastly improved.[36] However, it remains difficult to determine the 3D distribution of microgels, SPIONs and drug within in these systems. Heterogeneities in these distributions within the hydrogel matrix could lead to differing degrees of pore generation between nanocomposites that would affect the sample-to-sample reproducibility of pulsatile release that is essential for ultimate clinical application. In addition, these bulk systems are immobilized at the injection site and are thus inherently more useful for local rather than systemic drug delivery.

A plethora of micro- or nano-scale systems that combine SPIONs (or alternative inorganic nanoparticles) with thermosensitive polymers have been reported in which individual or small clusters of SPIONs have been coated with the thermosensitive polymer.[37–39] While this fabrication method could be considered ideal for some applications, particularly MRI imaging in which the magnetic relaxation properties of individual particles is crucial,[38,40] this method also limits the overall volume (and related drug loading capacity) as well as the heating capacity of the nanocomposite particles. Microgels offer a potential compromise solution to these challenges, maintaining a clear

nanoscale size while also facilitating tunable SPION contents and significant internal free volume enabling more effective drug loading. Microgels themselves have been widely studied as drug delivery vehicles.[41–44] While liposomes, polymeric micelles, and nanoparticles incorporating SPIONs have all been widely studied,[45–47] remote drug release from microgels via an AMF has, to the best of our knowledge, never been reported. The closest work involving microgels describes gold nanoparticle-based core-shell microgels fabricated in a much different, more complex way that exhibited enhanced release upon near-IR application.[39,48,49] However, unlike AMF-activated release, near-IR mediated release is limited in terms of how deep near-IR irradiation can penetrate into tissues,[33] negating many of the benefits of making particles on this scale that could travel throughout the body. The incorporation of SPIONs also provides the potential additional benefit of being able to target the microgels to specific locations with an external permanent magnet before regulating release from such microgels with an AMF.

Herein, we report the proof-of-concept development of SPION- and drug-loaded microgel nanocomposites for remote controlled AMF mediated release. The method of SPION entrapment selected was adapted from Shen et al. (2008),[50] using an acetoacetoxyethyl methacrylate (AAEM) comonomer; SPIONs can be anchored at the β-ketoester group during coprecipitation of the constituent salts, analogous to reported methods for immobilizing quantum dots (Figure 6.1).[50–52] Cationic poly(N-isopropyl methacrylamide) (PNIPMAM) nanocomposite microgels containing AAEM monomer units are thus prepared by precipitation copolymerization, aiming to possess a VPTT ~40°C (i.e. above normal body temperature but below a temperature that is unsafe for local tissues). Upon AMF exposure, the SPIONs generate heat that is transferred to the

microgels to raise their local temperature above their VPTT, causing them to deswell and inducing burst convective transport of drug from the microgel. This release kinetic is consistent with previous temperature-stimulated reports of on-demand drug release from microgels[53–55], but by incorporating the magnetic component this burst release can now be remotely triggered at a time/location desired for effective therapy.

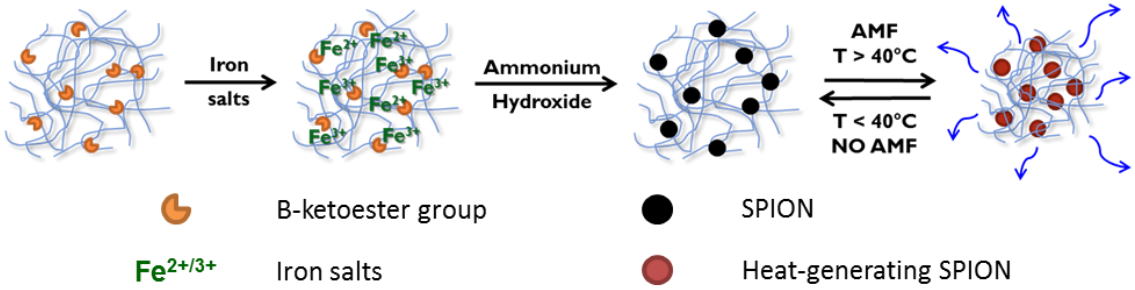

Figure 6.1: Synthesis and AMF-mediated release of SPION-laden PNIPMAM microgel nanocomposites. The iron salt precursors to SPIONs coordinate with the β-ketoester groups (in gold) and coprecipitate into SPIONs under basic conditions. Under the application of an AMF, the heat from the SPIONs is transferred to the thermosensitive microgel, inducing microgel deswelling as the temperature exceeds the VPTT and inducing convective drug release. The process is reversible such that when the AMF is turned off, the microgel temperature returns to ambient body temperature and the microgel reswells to its original state.

6.2.3 Experimental

Materials: Acetoacetoxyethyl methacrylate (AAEM, 95%), acrylamide (Am, ≥99%), acrylic acid (AA, 99%), aluminum oxide (98%), ammonium hydroxide (reagent grade), ammonium persulfate (98%), 2-2'-azobis(2-methylpropionamidine) dihydrochloride (V50, 97%), ciprofloxacin hydrochloride monohydrate (pharmaceutical secondary standard), 2-(dimethylamino)ethyl methacrylate (DMAEMA, 98%), iron(II) chloride tetrahydrate (98%), iron(III) chloride hexahydrate (97%), methylene bisacrylamide (MBA, 99%), N-isopropyl

methacrylamide (NIPMAM, 97%), hexadecyltrimethyl ammonium bromide (CTAB, ≥98%), sodium fluorescein, and thiazolyl blue tetrazolium bromide (MTT, 98%) were all purchased from Sigma Aldrich (Oakville, ON). Dimethyl sulfoxide was obtained from Caledon Laboratory Chemicals (Georgetown, ON). 1 M HCl and 1 M NaOH was purchased from LabChem Inc. N-isopropyl acrylamide (NIPAM, 99%) was purchased from J&K Scientific via Cedarlane Laboratories (Burlington, ON). NIPAM and NIPMAM monomers were further purified via recrystallization with 60:40 toluene/hexane. The AAEM and DMAEMA monomers were purified prior to their polymerization by flowing them through an aluminum oxide column. The 3T3 *Mus musculus* cell line was acquired from ATCC: Cedarlane Laboratories (Burlington, ON). The cell proliferation media (including Dulbecco's modified Eagle's medium-high glucose (DMEM), fetal bovine serum (FBS), and penicillin streptomycin (PS)), recovery media, and trypsin-EDTA were all obtained from Invitrogen (Burlington, ON). Deionized water (DIW) was purified using a Barnstead Nanopure purification system and was used for all experiments.

Synthesis of cationic microgels: Cationic microgels were made via a semi-batch precipitation polymerization process. NIPMAM (0.9178 g), Am (0.0603 g), AAEM (0.1076 g), MBA (0.08 g), CTAB (50 mg) and DMAEMA (0.1076 g, 7.0 mol% total monomer) were placed in a 250 mL 3-necked flask and dissolved in 145 g of DIW. The pH of the solution was adjusted to 3.5 via the addition of a 1 M HCl. The solution was then heated to 75°C and purged with nitrogen for 30 minutes with a condenser attached to the flask. A solution of 0.05 g V50 in 5 g DIW was then added to initiate the polymerization. After 30 minutes post-initiation, a syringe pump (KD Scientific Legato 200) was used to add the DMAEMA fraction at a rate of 0.076 mL/h (0.072 g/h) over 3 hours, increasing the total DMAEMA monomer concentration to 18.4 mol%. After an

additional 30 minutes (4 hours post-initiation), the microgels were dialyzed against DIW for six 6+ hour cycles before being centrifuged down at 26,000 rpm at 40°C with a Beckman Coulter Allegra X-22R Centrifuge. The resulting particles were analyzed for size and zeta potential via dynamic light scattering (DLS) using a Brookhaven 90Plus Particle Analyzer.

Incorporating SPIONs into the microgel matrix: On a 100 mg microgel basis, 100 mg of microgel was dissolved in 4 mL of DIW within a 20 mL scintillation vial under magnetic stirring. 10 wt% SPION microgels were produced via the addition of 100 µL of a 27.5 mg/mL DIW solution of iron(II) chloride tetrahydrate and 100 µL of a 67.5 mg/mL DIW solution of iron(III) chloride hexahydrate. The resulting solution was magnetically stirred and purged with nitrogen for 20 minutes before the injection of 1.5 mL ammonium hydroxide into the vial to cause the iron salt to coprecipitate to form SPIONs. 5 wt%, 15 wt%, 20 wt%, 25 wt%, etc. SPION-microgels can be made analogously by adding 50, 150, 200, and 250 µL respectively of each iron salt solution into the vial. The mixture was allowed to continue to stir under a nitrogen atmosphere for 30 minutes. The resulting magnetic microgels were centrifuged down at 20,000 rpm at room temperature for multiple cycles to separate the microgels from the solvent and unincorporated SPIONs, which tended to adhere to the centrifuge tube above the microgel-SPION pellet. Transmission electron microscopy (TEM; JEOL Ltd., Japan) and thermogravimetric analysis (TGA; Luxx Netzsch STA-409 thermogravimetric analyzer) was used to show the incorporation of SPIONs within the microgels. The TGA involved heating the composite microgels from room temperature to 1000°C at 5°C/min under an argon atmosphere.

In vitro cytotoxicity assay: The cytotoxicity associated with the nanocomposite microgels was assessed with 3T3 *Mus musculus* mouse fibroblast cells. The cells were grown with a proliferation media of 10 vol% FBS and 1 vol% PS in DMEM. The magnetic microgels were sterilized prior to cell viability testing by exposure to UV radiation (2 hours). Each well of a 24 well polystyrene plate was incubated with 25,000 3T3 cells in 1 mL of media (n = 4 for each microgel concentration tested) and incubated at 37°C and 5% CO_2 for 24 hours. Following, the media was aspirated, 1 mL of fresh media with various concentrations of magnetic microgels was added, and the cells were incubated for an additional 24 hours. A negative control with no cells and a positive control with cells not exposed to the nanocomposite microgels were included in the study. After this 24 hour microgel exposure time, the media/microgel solution was aspirated, and each well was rinsed with 0.5 mL of media. To assess residual cell viability, 150 µL of a 0.4 mg/mL MTT solution was added to each well, and the cells were incubated for 4 additional hours. 500 µL of DMSO was then added to each well to dissolve the insoluble formazan precipitate, and each plate was placed on a shaker until the purple formazan was completely dissolved (typically ~20 minutes). 2 x 200 µL aliquots were removed from each well, transferred to a 96 well polystyrene plate, and read in an absorbance reader at 540 nm (PerkinElmer Victor3 multilabel plate reader). The percent cell viability was determined as the normalized ratio between the average absorbance values of cells exposed to the magnetic microgels and the average absorbance values of cells incubated only in media (positive control). Error bars represent the standard deviation of the four replicate measurements.

Fluorescein release experiments: Fluorescein loading into the cationic SPION microgels was performed by dispersing 100 mg of SPION microgels in 20 mL of a 10

μg/mL solution of sodium fluorescein and allowing the mixture to stir overnight. The SPION-microgels were then centrifuged down at room temperature and 20,000 rpm, with the supernatant subsequently removed and the non-loaded concentration of fluorescein quantified with a fluorescence reader (Tecan Infinite M1000).

To track release of loaded fluorescein from the SPION-microgel nanocomposites, the loaded microgels were dispersed in 1 mL of 10 mM PBS (n = 4). The suspension was then placed in a Float-A-Lyzer dialysis system (Spectrum Labs, 3.5-5 kDa molecular weight cut-off) and placed within a 5 mL container containing 4 mL of 10mM PBS that acts as the drug sink. The Float-A-Lyzer was then placed within an AMF assembly that maintains an ambient temperature of 37°C in the absence of magnetic activation (see Figure S6.1). These Float-A-Lyzer units containing the samples were placed at roughly equivalent positions with respect to the solenoid coils so that each sample would be exposed to similar magnetic field strengths. For the same reasoning, as with the previous hydrogel nanocomposite work, the material in the Float-A-Lyzers was also centered vertically between the two coils. Regardless of their position each sample should experience the direction of the magnetic field reversing at a rate of 200 kHz; however, the exact magnetic strength that each sample is exposed to is unknown, so care is taken to make sure these samples are at equivalent positions within the magnetic field.

The samples were exposed to a constant AMF application with using a 2-coiled, 8 cm diameter solenoid operating at 30 A and 200 kHz throughout the 6 hour release experiment. Controls were performed using the same experimental assembly and conditions but keeping the AMF off throughout the experiment. Every 30 minutes,

400 µL samples were removed from the PBS sink for analysis, with 400 µL of fresh 10 mM PBS subsequently added to maintain the 4 mL total sink volume throughout the experiment. The samples were then placed in black 96 well plates, and a fluorescent plate reader (Tecan Infinite M1000) operating at 494 nm excitation/512 nm emission wavelengths was used to determine the amount of fluorescein released at each time point.

Error and statistical significance: Error bars represent the standard deviation of repeat measurements (n = 4). A two-tailed t-test with $p < 0.05$ assuming unequal variances was used to determine statistically significant differences between any pair of samples.

6.2.4 Results

Cationic microgels were synthesized via a semi-batch coprecipitation polymerization with PNIPMAM (the thermosensitive component), AAEM (the β-ketoester containing monomer), and DMAEMA (the cationic component). The cationic DMAEMA-functionalized microgel was polymerized in an acidic environment (pH = 3.5) since the pK_b of DMAEMA (8.1) decreases upon copolymerization, leading to microgel flocculation during the synthesis procedure if the polymerization is run at pH > 6.[56] The resulting microgels possessed a size of 145 ± 3 nm and an electrophoretic mobility of ~2.08 ± 0.13 (µ/s)/(V/cm) in 10 mM KCl adjusted to pH 7 after dialysis, indicating successful incorporation of the functional monomers. Conductometric titration indicated that the microgels contain ~13.4 mol% of the cationic monomer component, which means that a

good proportion of the 18.4 mol% of DMAEMA monomer that was added was eventually incorporated into the microgels.

The microgels were concentrated post-dialysis via centrifugation at 26,000 rpm at 40°C, a method found to minimize microgel aggregation upon redispersion at room temperature in comparison to lyophilization, which led to aggregates upon redispersion.

The microgels were then dispersed in a solution of iron salts (Fe^{3+} and Fe^{2+} in a 2:1 molar ratio) and coprecipitated to form SPIONs with ammonium hydroxide. As has been demonstrated previously in the literature, the iron salts coordinate with the AAEM monomer component to provide a seeding site for the growth of SPIONs upon coprecipitation. This results in microgels that are stable in aqueous solutions with significant iron content.[50,57] These particles can be centrifuged down at room temperature and 20,000 rpm, simultaneously facilitating separation of the SPION-microgels from both the solvent and unincorporated SPIONs that are not stabilized in any way during this synthetic protocol and thus adhere to the polycarbonate centrifuge tube above the microgel-SPION pellet. The resulting SPION-microgel pellet could easily be dispersed in aqueous solvents. Notably, these materials can also be separated magnetically if desired (Figure 6.2a), with facile redispersion observed following removal of the magnet.

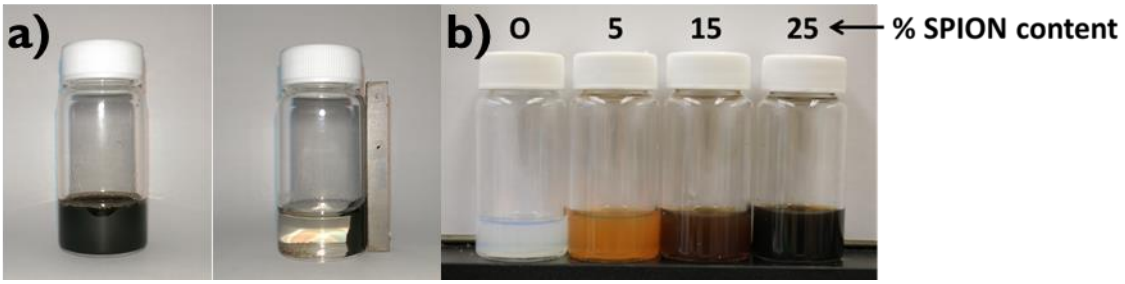

Figure 6.2: a) Magnetic separation of a concentrated solution (10 wt% magnetic microgel with respect to water) of PNIPMAM-AAEM-DMAEMA microgels with 15 wt% SPION content. b) Magnetic PNIPMAM-AAEM-DMAEMA microgels with 0, 5, 15, and 25 wt% SPION content.

Pictures of cationic microgels with SPION contents of up to 25 wt% with respect to the microgel content (in DIW) are shown in Figure 6.2b. Cationic SPION-microgels remained colloidally stable in DIW for a few days, but even upon settling were easily redispersable by simple shaking. TGA analysis revealed that the SPION content of the purified cationic magnetic microgels is ~31 wt%, slightly higher than the targeted 25 wt% SPION content (Figure S6.2). This is likely due to microgels with lesser SPION contents being separated from denser microgels containing higher SPION contents during the centrifugation/purification process.

Table 6.1 presents the size, polydispersity index (PDI), and thermoresponsiveness in the temperature range of interest (37°C to 43°C) of cationic SPION-microgels with up to 25% SPION content. Interestingly, blank microgels prepared without SPIONs aggregate at higher temperatures while all SPION-containing microgels remain colloidally stable, indicative of the relative hydrophobicity of the DMAEMA monomer used for drug complexation. Both the size and polydispersity increase with the SPION content in the microgel, indicating that the SPION seeding process can also lead to limited microgel

aggregation; such aggregation may occur via SPIONs bridging adjacent AAEM-functionalized microgels and/or hydrogen bonding between neutralized tertiary amine groups at the high pH used for SPION precipitation. However, the number of SPIONs bound to each microgel is not explicitly controlled in the fabrication process and may also promote differential swelling between different microgel sub-populations. However, unimodal particle size distributions were still observed for all SPION-containing microgels, both below and above the microgel VPTT. Similar results in terms of increasing size and polydispersity with increasing SPION content were observed for microgels also prepared with the AAEM comonomer but without any cationic comonomer, for which both colloidal stability and thermoresponsivity were maintained even at very high (in that case up to 50 wt%) SPION loadings (see Supporting Information, Figure S6.3).

Table 6.1: DLS particle sizes of PNIPMAM-AAEM-DMEAMA microgels with varying SPION contents (0 – 25 wt%) at various temperatures in 10 mM PBS, pH 7.4. The percent volume change between 37°C and 43°C (in the relevant physiological temperature range for thermally-induced triggered release) is also shown. The diameter of the microgels is the number outside the brackets (in nm) and the number within the brackets is the polydispersity (unitless). agg = aggregated under the condition noted.

	0 wt%	**5 wt%**	**15 wt%**	**25 wt%**
25°C	145 ± 21 (0.08)	165 ± 36 (0.19)	204 ± 52 (0.26)	255 ± 61 (0.23)
37°C	110 ± 13 (0.06)	139 ± 28 (0.16)	192 ± 53 (0.30)	218 ± 48 (0.20)
43°C	agg	109 ± 23 (0.18)	151 ± 42 (0.31)	193 ± 51 (0.28)
% Volume Change		52 ± 19	51 ± 26	31 ± 23

The thermosensitivity is relatively independent of SPION content until >15 wt% SPIONs are incorporated into the microgels, at which point it appears that the SPION fraction begins to suppress the temperature responsiveness of the microgels. While we have found that such suppression of thermoresponsivity is common as non-thermoresponsive components are introduced into a temperature-responsive hydrogel and interfere with the cooperative nature of the volume phase transition,[18] this difference is not statistically significant due, primarily, to the high PDIs associated with the diameters used to determine the volume change.

A TEM image of the 15 wt% SPION microgels (dried on a copper grid) prior to centrifugation is shown in Figure 6.3 and supports both possible mechanisms of particle size and polydispersity increases. Although drying results in significantly lower particle sizes than in the (swollen) DLS measurements, the TEM image shows that most of the microgels contain SPIONs but the number of SPIONs per particle varies significantly (consistent with the PDI increase observed). Furthermore, particles with higher SPION contents seem to have agglomerated together; while drying artefacts cannot be fully discounted as a potential reason for such a morphology, the independence of the majority of the microgels observed suggest that higher SPION contents can drive microgel aggregation as speculated. Note also that while some smaller, electron-dense particles are also visible that are not directly associated with microgels (likely SPIONs or SPION clusters that have not been incorporated into the microgels), on the whole a large proportion of SPIONs are incorporated within the particles.

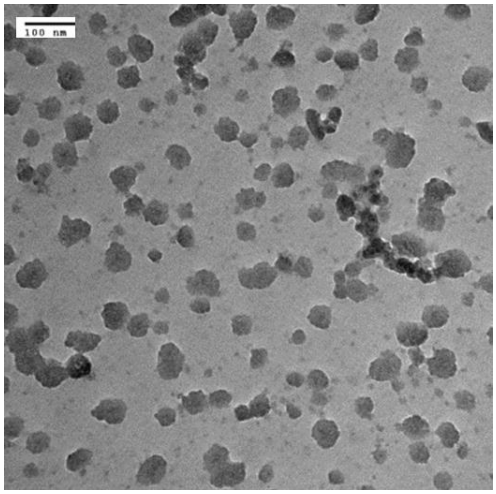

Figure 6.3: TEM image of 15 wt% SPION-containing PNIPMAM-AAEM-DMEAMA microgels (120,000x magnification).

Based on these results, cationic microgels with 15 wt% SPIONs are used in the remainder of this work as such microgels have a substantially high SPION content, remain stable in aqueous suspension over extended periods, and exhibit a large volume change in the 37°C to 43°C temperature range. These magnetic microgels also have an electrophoretic mobility value of ~1.76 ± 0.28 (μ/s)/(V/cm), similar to that of the cationic microgels prior to SPION incorporation.

The magnetization properties of the 15% SPION-microgels were assessed with Superconducting Quantum Interference Device (SQUID, Quantum Design MPMS SQUID Magnetometer) measurements (Figure 6.4a). While SPION-microgels have a reduced magnetic saturation when compared to SPIONs alone (as expected since the microgel content lowers the effective SPION concentration), the microgels still exhibit low coercivity and overall superparamagnetic characteristics. As a result, these particles can effectively increase the temperature of their aqueous suspension solution by over 5°C under the application of an AMF with a 2-coiled, 8 cm diameter solenoid at 30 A and

200 kHz for 10 minutes (Figure 6.4b), providing an ideal temperature gradient for inducing physiologically-relevant switchable drug release.

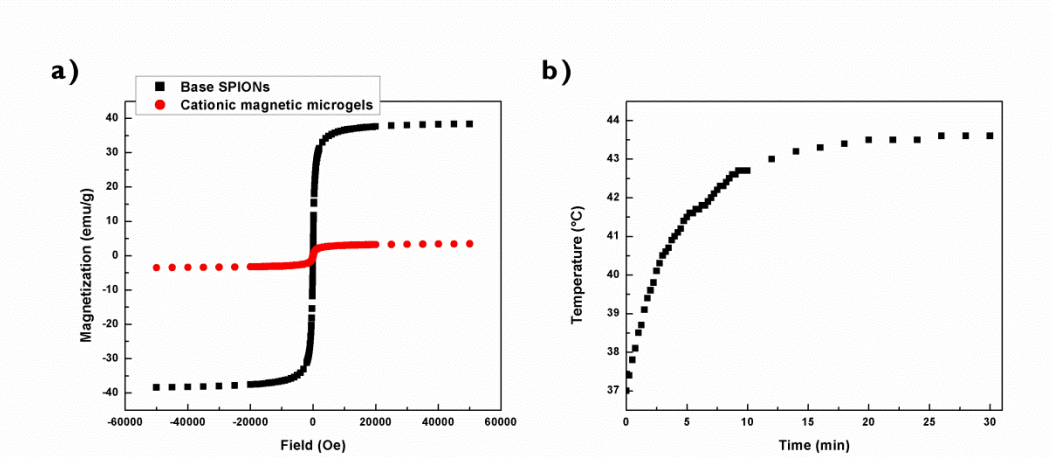

Figure 6.4: a) SQUID results for SPIONs alone (black line) and 15 wt% SPION cationic magnetic microgels (red line), with both displaying superparamagnetic characteristics. b) Heating profile of magnetic microgel suspensions (15 wt%) exposed to an AMF operating at 30 A and 200 kHz (2-coiled 8 cm solenoid).

The *in vitro* cytotoxicity of the 15 wt% SPION microgels was screened with an MTT assay using 3T3 mouse fibroblasts. Figure 6.5 indicates that the microgels exhibit negligible cytotoxicities, with all viabilities statistically ≥80% (noted to represent a non-toxicity threshold in prior studies).[58] Coupling this result with the ideal size of the SPION-microgels (Table 6.1) in terms of avoiding the reticuloendothelial system (RES) and extending the half-life of particles in systemic circulation (~10 – 200 nm),[59] these particles may be useful *in vivo* as components that can facilitate long-term circulation for localized or systemically activated drug delivery.

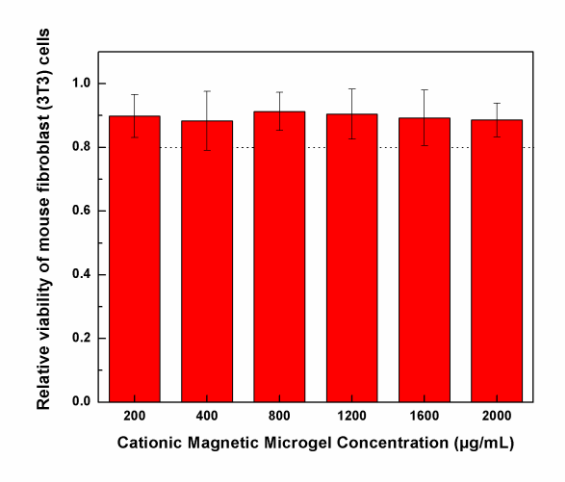

Figure 6.5: Relative 3T3 mouse fibroblast cell viability (in comparison to cell-only controls) for a range of concentrations of cationic 15 wt% SPION-microgels.

While triggered release from microgels has been demonstrated with near-IR sources, it has, to the best of our knowledge, yet to be performed via the use of magnetic fields. Our primary goal associated with this work was to assess the potential for magnetic-triggered drug release using our cationic 15 wt% SPION-microgels by releasing a model anionic therapeutic, chosen herein to be sodium fluorescein. Fluorescein is a relatively small (MW ~332 g/mol), hydrophilic, and anionic model compound for which release can be easily quantified (via fluorescence); however, triggered release of other small molecule anionic water-soluble compounds is anticipated based on these model results. The amount of fluorescein loaded was determined from the concentration of the supernatant following drug loading and isolation of the microgels via centrifugation and was determined as 0.18 ± 0.02 g/g sodium fluorescein with respect to microgel mass, corresponding to 116 ± 10% of the charged groups per microgel being bound with drug. This overestimate can likely be attributed to non-specific absorption of the drug into the microgels.

Release experiments were performed immediately upon redispersion of the fluorescein-loaded microgels with and without presence of an AMF to demonstrate the potential for magnetic field-enhanced drug delivery (Figure 6.6). The presence of an AMF significantly enhanced the rate of release of fluorescein throughout the course of the experiment, with the exception of the first half-hour time point in which burst release of non-bound (absorbed) fluorescein is likely occurring rapidly in both the triggered and non-triggered systems. The difference in the release between the two remained fairly constant throughout the experiment time, with 4.6 ± 0.3 times more fluorescein release observed from the sample triggered with the AMF versus the sample where no AMF was applied. This result indicates that these magnetic microgel nanoconstructs may have the potential for remotely activated triggered release in applied scenarios.

Note that only 3.8 ± 1.3% of the loaded drug was released through the membrane into the 10 mM PBS sink solution even in the presence of AMF after 6 hours. This is much lower than what would be expected for the release of the small, hydrophilic fluorescein compound from microgels, likely attributable to partial inhibition of the transport of fluorescein into the sink solution by the membrane. Even so, the fluorescence in the solution inside the membrane was stronger in the sample exposed to the AMF than the one that was not, and based on membrane partitioning higher concentrations of fluorescein in the sink solution would necessarily correspond to higher free fluorescein concentrations inside the membrane; as such, it is clear that magnetically-responsive fluorescein release occurs in these microgels.

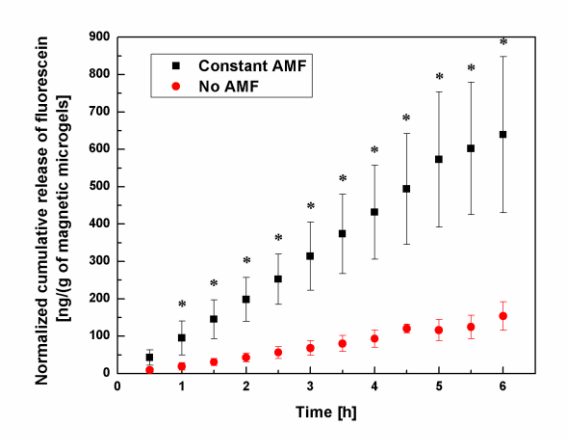

Figure 6.6: The release of fluorescein normalized against the initial weight of cationic 15 wt% SPION microgels in each sample over 6 hours with the AMF applied to the magnetic microgels throughout the course of the experiment (black points) or no AMF applied (red points). * indicates statistically significant differences in the cumulative release between the two incubation temperatures at a given time point ($p < 0.05$).

The AMF-controlled release from SPION-microgel nanocomposites shown in Figure 6.6 represents the first demonstration of such release in microgels controlled by a magnetic field, opening the door for using SPION-microgels for simultaneous targeting and controlled release applications. Alternately, these particles could be incorporated into injectable hydrogels to perform an analogous triggered-release function at a specific location in the body, providing potentially faster and higher-resolution on-off release relative to current physical mixtures of SPIONs and microgels within such constructs due to the explicit localization of the heating within the thermoresponsive microgel phase.[35,36]

6.2.5 Conclusions

SPION-loaded microgels prepared with comonomers specifically to immobilize iron salts for efficient SPION loading as well as cationic comonomers that facilitate higher loadings of anionic model drugs can facilitate triggered release in the presence of an alternating magnetic field. Indeed, these materials experienced nearly 4 times more fluorescein release with an AMF application compared to controls. The SPION-loaded microgels are furthermore easy to fabricate, can contain large proportions of SPIONs while maintaining stability in aqueous solutions, retain desirable superparamagnetic characteristics, are non-cytotoxic. As such, these materials have significant potential to improve our capacity for remote regulation of drug release that is more adaptive to changing physiological circumstances and patient needs, critical for improving the efficacies of a wide range of therapies.

6.2.6 Acknowledgements

The authors thank the J.P. Bickell Foundation (Medical Research Grant Program), the Vanier Scholarship program, and the Natural Sciences and Engineering Research Council of Canada (NSERC) for funding.

6.2.7 References

(1) Boesel, B. L. F.; Greiner, C.; Arzt, E.; del Campo, A. Gecko-Inspired Surfaces: A Path to Strong and Reversible Dry Adhesives. *Adv. Mater.* **2010**, *22*, 2125–2137.

(2) Wegst, U. G. K.; Bai, H.; Saiz, E.; Tomsia, A. P.; Ritchie, R. O. Bioinspired Structural Materials. *Nat. Mater.* **2015**, *14*, 23–36.

(3) Leslie, D. C.; Waterhouse, A.; Berthet, J. B.; Valentin, T. M.; Watters, A. L.; Jain, A.; Kim, P.; Hatton, B. D.; Nedder, A.; Donovan, K.; *et al.* A Bioinspired Omniphobic Surface Coating on Medical Devices Prevents Thrombosis and Biofouling. *Nat. Biotechnol.* **2014**, *32*, 1134–1140.

(4) Fan, Z.; Sun, L.; Huang, Y.; Wang, Y.; Zhang, M. Bioinspired Fluorescent Dipeptide Nanoparticles for Targeted Cancer Cell Imaging and Real-Time Monitoring of Drug Release. *Nat. Nanotechnol.* **2016**, *11*, 388–394.

(5) Veiseh, O.; Tang, B. C.; Whitehead, K. A.; Anderson, D. G.; Langer, R. Managing Diabetes with Nanomedicine: Challenges and Opportunities. *Nat. Rev. Drug Discov.* **2014**, *14*, 45–57.

(6) Vegas, A. J.; Veiseh, O.; Gürtler, M.; Millman, J. R.; Pagliuca, F. W.; Bader, A. R.; Doloff, J. C.; Li, J.; Chen, M.; Olejnik, K.; *et al.* Long-Term Glycemic Control Using Polymer-Encapsulated Human Stem Cell-Derived Beta Cells in Immune-Competent Mice. *Nat. Med.* **2016**, *22*, 306–311.

(7) Vegas, A. J.; Veiseh, O.; Doloff, J. C.; Ma, M.; Tam, H. H.; Bratlie, K.; Li, J.; Bader, A. R.; Langan, E.; Olejnik, K.; *et al.* Combinatorial Hydrogel Library Enables Identification of Materials That Mitigate the Foreign Body Response in Primates. *Nat. Biotechnol.* **2016**, *34*, 345–352.

(8) Timko, B. P.; Dvir, T.; Kohane, D. S. Remotely Triggerable Drug Delivery Systems. *Adv. Mater.* **2010**, *22*, 4925–4943.

(9) Timko, B. P.; Arruebo, M.; Shankarappa, S.; McAlvin, J. B.; Okonkwo, O. S.; Mizrahi, B.; Stefanescu, C. F.; Gomez, L.; Zhu, J.; Zhu, A.; *et al.* Near-Infrared-Actuated Devices for Remotely Controlled Drug Delivery. *Proc. Natl. Acad. Sci.* **2014**, *111*, 1349–1354.

(10) Youan, B. C. Chronopharmaceutical Drug Delivery Systems: Hurdles, Hype or Hope? *Adv. Drug Deliv. Rev.* **2010**, *62*, 898–903.

(11) Tong, R.; Hemmati, H. D.; Langer, R.; Kohane, D. S. Photoswitchable Nanoparticles for Triggered Tissue Penetration and Drug Delivery. *J. Am. Chem. Soc.* **2012**, *134*, 8848–8855.

(12) Campbell, S. B.; Hoare, T. Externally Addressable Hydrogel Nanocomposites for Biomedical Applications. *Curr. Opin. Chem. Eng.* **2014**, *4*, 1–10.

(13) Merino, S.; Martin, C.; Kostarelos, K.; Prato, M.; Vázquez, E. Nanocomposite Hydrogels: 3D Polymer-Nanoparticle Synergies for On-Demand Drug Delivery. *ACS Nano* **2015**, *9*, 4686–4697.

(14) Mura, S.; Nicolas, J.; Couvreur, P. Stimuli-Responsive Nanocarriers for Drug Delivery. *Nat. Mater.* **2013**, *12*, 991–1003.

(15) An, X.; Zhan, F.; Zhu, Y. Smart Photothermal-Triggered Bilayer Phase Transition in AuNPs − Liposomes to Release Drug. *Langmuir* **2013**, *29*, 1061–1068.

(16) Viger, M. L.; Sheng, W.; Doré, K.; Alhasan, A. H.; Carling, C.-J.; Lux, J.; de Gracia Lux, C.; Grossman, M.; Malinow, R.; Almutairi, A. Near-Infrared-Induced Heating of Confined Water in Polymeric Particles for Efficient Payload Release. *ACS Nano* **2014**, *8*, 4815–4826.

(17) Wang, C.; Xu, H.; Liang, C.; Liu, Y.; Li, Z.; Yang, G.; Cheng, L.; Li, Y.; Liu, Z. Iron Oxide @ Polypyrrole Nanoparticles as a Multifunctional Drug Carrier for Remotely Controlled Cancer Therapy with Synergistic Antitumor Effect. *ACS Nano* **2013**, 6782–6795.

(18) Campbell, S. B.; Patenaude, M.; Hoare, T. Injectable Superparamagnets: Highly Elastic and Degradable Poly(N-Isopropylacrylamide)-Superparamagnetic Iron Oxide Nanoparticle (SPION) Composite Hydrogels. *Biomacromolecules* **2013**, *14*, 644–653.

(19) Farra, R.; Sheppard, N. F.; McCabe, L.; Neer, R. M.; Anderson, J. M.; Santini, J. T.; Cima, M. J.; Langer, R. First-in-Human Testing of a Wirelessly Controlled Drug Delivery Microchip. *Sci. Transl. Med.* **2012**, *4*, 122ra121, doi:10.1126/ scitranslmed.3003276.

(20) Liu, J.; Detrembleur, C.; De Pauw-Gillet, M.; Mornet, S.; Jerome, C.; Duguet, E. Gold Nanorods Coated with Mesoporous Silica Shell as Drug Delivery System for Remote Near Infrared Light-Activated Release and Potential Phototherapy. *Small* **2015**, *11*, 2323–2332.

(21) Strong, L. E.; Dahotre, S. N.; West, J. L. Hydrogel-Nanoparticle Composites for Optically Modulated Cancer Therapeutic Delivery. *J. Control. Release* **2014**, *178*, 63–68.

(22) Yang, K.; Feng, L.; Liu, Z. Stimuli Responsive Drug Delivery Systems Based on Nano-Graphene for Cancer Therapy. *Adv. Drug Deliv. Rev.* **2016**, *105*, 228–241.

(23) Zhou, M.; Liu, S.; Jiang, Y.; Ma, H.; Shi, M.; Wang, Q.; Zhong, W.; Liao, W.; Xing, M. M. Q. Doxorubicin-Loaded Single Wall Nanotube Thermo- Sensitive Hydrogel for Gastric Cancer Chemo-Photothermal Therapy. *Adv. Funct. Mater.* **2015**, *25*, 4730–4739.

(24) Cheng, Z.; Chai, R.; Ma, P.; Dai, Y.; Kang, X.; Lian, H.; Hou, Z.; Li, C.; Lin, J. Multiwalled Carbon Nanotubes and NaYF4:Yb 3+/Er3+ Nanoparticle- Doped Bilayer Hydrogel for Concurrent NIR-Triggered Drug Release and Up-Conversion Luminescence Tagging. *Langmuir* **2013**, *29*, 9573–9580.

(25) Rose, L. C.; Bear, J. C.; Mcnaughter, P. D.; Southern, P.; Piggott, R. Ben; Parkin, I. P.; Qi, S.; Mayes, A. G. A SPION-Eicosane Protective Coating for Water Soluble Capsules : Evidence for on-Demand Drug Release Triggered by Magnetic Hyperthermia. *Sci. Rep.* **2016**, 1–5.

(26) Oliveira, H.; Pérez-andrés, E.; Thevenot, J.; Sandre, O.; Berra, E.; Lecommandoux, S. Magnetic Field Triggered Drug Release from Polymersomes for Cancer Therapeutics. *J. Control. Release* **2013**, *169*, 165–170.

(27) Chiang, W.-H.; Ho, V. T.; Chen, H.-H.; Huang, W.-C.; Huang, Y.-F.; Lin, S.-C.; Chern, C.-S.; Chiu, H.-C. Superparamagnetic Hollow Hybrid Nanogels as a Potential Guidable Vehicle System of Stimuli-Mediated MR Imaging and Multiple Cancer Therapeutics. *Langmuir* **2013**, *29*, 6434–6443.

(28) Yassine, O.; Zah, A.; Li, E. Q.; Alfadhel, A.; Perez, J. E. Highly Efficient Thermoresponsive Nanocomposite for Controlled Release Applications. *Sci. Rep.* **2016**, *6:28539*, doi:10.1038/srep28539.

(29) Mok, H.; Zhang, M. Superparamagnetic Iron Oxide Nanoparticle-Based Delivery Systems for Biotherapeutics. *Expert Opin. Drug Deliv.* **2013**, *10*, 73–87.

(30) Levy, M.; Luciani, N.; Alloyeau, D.; Elgrabli, D.; Deveaux, V.; Pechoux, C.; Chat, S.; Wang, G.; Vats, N.; Gendron, F.; *et al.* Long Term in Vivo Biotransformation of Iron Oxide Nanoparticles. *Biomaterials* **2011**, *32*, 3988–3999.

(31) Gu, J.; Xu, H.; Han, Y.; Dai, W.; Hao, W.; Wang, C.; Gu, N.; Xu, H.; Cao, J. The Internalization Pathway, Metabolic Fate and Biological Effect of Superparamagnetic Iron Oxide Nanoparticles in the Macrophage-like RAW264.7 Cell. *Sci. China. Life Sci.* **2011**, *54*, 793–805.

(32) Satarkar, N. S.; Hilt, J. Z. Magnetic Hydrogel Nanocomposites for Remote Controlled Pulsatile Drug Release. *J. Control. Release* **2008**, *130*, 246–251.

(33) Tong, R.; Kohane, D. S. Shedding Light on Nanomedicine. *WIREs Nanomed. Nanobiotechnol.* **2012**, *4*, 638–662.

(34) Hoare, T. R.; Kohane, D. S. Hydrogels in Drug Delivery: Progress and Challenges. *Polymer* **2008**, *49*, 1993–2007.

(35) Campbell, S.; Maitland, D.; Hoare, T. Enhanced Pulsatile Drug Release from Injectable Magnetic Hydrogels with Embedded Thermosensitive Microgels. *ACS Macro Lett.* **2015**, *4*, 312–316.

(36) Maitland, D.; Campbell, S. B.; Chen, J.; Hoare, T. Controlling the Resolution and Duration of Pulsatile Release from Injectable Magnetic “Plum Pudding” Nanocomposite Hydrogels. *RSC Adv.* **2016**, *6*, 15770–15781.

(37) Gupta, A. K.; Gupta, M. Synthesis and Surface Engineering of Iron Oxide Nanoparticles for Biomedical Applications. *Biomaterials* **2005**, *26*, 3995–4021.

(38) Hannecart, A.; Stanicki, D.; Vander Elst, L.; Muller, R. N.; Lecommandoux, S.; Thévenot, J.; Bonduelle, C.; Trotier, A.; Massot, P.; Miraux, S.; *et al.* Nano-Thermometers with Thermo-Sensitive Polymer Grafted USPIOs Behaving as Positive Contrast Agents in Low- Field MRI. *Nanoscale* **2015**, *7*, 3754–3767.

(39) Wu, W.; Shen, J.; Banerjee, P.; Zhou, S. Core-Shell Hybrid Nanogels for Integration of Optical Temperature-Sensing, Targeted Tumor Cell Imaging, and Combined Chemo-Photothermal Treatment. *Biomaterials* **2010**, *31*, 7555–7566.

(40) Laurent, S.; Dutz, S.; Häfeli, U. O.; Mahmoudi, M. Magnetic Fluid Hyperthermia: Focus on Superparamagnetic Iron Oxide Nanoparticles. *Adv. Colloid Interface Sci.* **2011**, *166*, 8–23.

(41) Kesselman, L. R. B.; Shinwary, S.; Selvaganapathy, P. R.; Hoare, T. Synthesis of Monodisperse, Covalently Cross-Linked, Degradable “Smart” Microgels Using Microfluidics. *Small* **2012**, *8*, 1092–1098.

(42) Schmid, A. J.; Dubbert, J.; Rudov, A. A.; Pedersen, J. S.; Lindner, P.; Karg, M.; Potemkin, I. I.; Richtering, W. Multi-Shell Hollow Nanogels with Responsive Shell Permeability. *Sci. Rep.* **2016**, 1–13.

(43) Hoare, T.; Pelton, R. Impact of Microgel Morphology on Functionalized Microgel-Drug Interactions. *Langmuir* **2008**, *24*, 1005–1012.

(44) Kwon, J.; Drumright, R.; Siegwart, D. J.; Matyjaszewski, K. The Development of Microgels / Nanogels for Drug Delivery Applications. *Prog. Polym. Sci.* **2008**, *33*, 448–477.

(45) Talelli, M.; Rijcken, C. J. F.; Lammers, T.; Seevinck, P. R.; Storm, G.; Nostrum, C. F. Van; Hennink, W. E. Superparamagnetic Iron Oxide Nanoparticles Encapsulated in Biodegradable Thermosensitive Polymeric Micelles: Toward a Targeted Nanomedicine Suitable for Image-Guided Drug Delivery. *Langmuir* **2009**, 2060–2067.

(46) Schleich, N.; Sibret, P.; Danhier, P.; Ucakar, B.; Laurent, S.; Muller, R. N.; Jérôme, C.; Gallez, B.; Préat, V.; Danhier, F. Dual Anticancer Drug/superparamagnetic Iron Oxide-Loaded PLGA-Based Nanoparticles for Cancer Therapy and Magnetic Resonance Imaging. *Int. J. Pharm.* **2013**, *447*, 94–101.

(47) Lorenzato, C.; Oerlemans, C.; Elk, M. Van; Geerts, W. J. C.; Denis, B.; Senneville, D.; Moonen, C.; Bos, C. MRI Monitoring of Nanocarrier Accumulation and Release Using Gadolinium-SPIO Co-Labelled Thermosensitive Liposomes. *Contrast Media Mol. Imaging* **2016**, *11*, 184–194.

(48) Kang, H.; Trondoli, A.; Zhu, G.; Chen, Y.; Chang, Y. Near-Infrared Light-Responsive Core-Shell Nanogels for Targeted Drug Delivery. *ACS Nano* **2011**, *5*, 5094–5099.

(49) Budhlall, B. M.; Marquez, M.; Velev, O. D. Microwave, Photo- and Thermally Responsive PNIPAm-Gold Nanoparticle Microgels. *Langmuir* **2008**, *24*, 11959–11966.

(50) Shen, L.; Pich, A.; Fava, D.; Wang, M.; Kumar, S.; Wu, C.; Scholes, G. D.; Winnik, M. a. Loading Quantum Dots into Thermo-Responsive Microgels by Reversible Transfer from Organic Solvents to Water. *J. Mater. Chem.* **2008**, *18*, 763–770.

(51) Oh, J. K.; Park, J. M. Iron Oxide-Based Superparamagnetic Polymeric Nanomaterials: Design, Preparation, and Biomedical Application. *Prog. Polym. Sci.* **2011**, *36*, 168–189.

(52) Papaphilippou, P.; Christodoulou, M.; Marinica, O.-M.; Taculescu, A.; Vekas, L.; Chrissafis, K.; Krasia-Christoforou, T. Multiresponsive Polymer Conetworks Capable of Responding to Changes in pH, Temperature, and Magnetic Field: Synthesis, Characterization, and Evaluation of Their Ability for Controlled Uptake and Release of Solutes. *ACS Appl. Mater. Interfaces* **2012**, *4*, 2139–2147.

(53) Shin, Y.; Chang, J. H.; Liu, J.; Williford, R.; Shin, Y.; Exarhos, G. J. Hybrid Nanogels for Sustainable Positive Thermosensitive Drug Release. *J. Control. Release* **2001**, *73*, 1–6.

(54) Sivakumaran, D.; Maitland, D.; Hoare, T. Injectable Microgel-Hydrogel Composites for Prolonged Small-Molecule Drug Delivery. *Biomacromolecules* **2011**, *12*, 4112–4120.

(55) Qian, J.; Wu, F. Thermosensitive PNIPAM Semi-Hollow Spheres for Controlled Drug Release. *J. Mater. Chem. B* **2013**, *1*, 3464–3469.

(56) Zha, L.; Hu, J.; Wang, C.; Fu, S.; Elaissari, A. Preparation and Characterization of Poly (N-Isopropylacrylamide-Co-Dimethylamino-Ethyl Methacrylate) Microgel Latexes. *Colloid Polym. Sci.* **2002**, *280*, 1–6.

(57) Bhattacharya, S.; Eckert, F.; Boyko, V.; Pich, A. Temperature-, pH-, and Magnetic-Field-Sensitive Hybrid Microgels. *Small* **2007**, *3*, 650–657.

(58) Fu, Y.; Kao, W. J. In Situ Forming Poly(ethylene Glycol)-Based Hydrogels via Thiol-Maleimide Michael-Type Addition. *J. Biomed. Mater. Res. A* **2011**, *98*, 201–211.

(59) Mahmoudi, M.; Sant, S.; Wang, B.; Laurent, S.; Sen, T. Superparamagnetic Iron Oxide Nanoparticles (SPIONs): Development, Surface Modification and Applications in Chemotherapy. *Adv. Drug Deliv. Rev.* **2011**, *63*, 24–46.

6.2.8 Supporting Information

Figure S6.1: Photos of experimental AMF-activation assembly (left), with a close-up view of the Float-A-Lyzer devices in the jacked flask within the device (right). The size of jacketed flask limited the number of Float-A-Lyzer membrane devices that could be used in a single experiment to three, so two separate experiments with two samples each had to be performed to achieve n = 4 replicates.

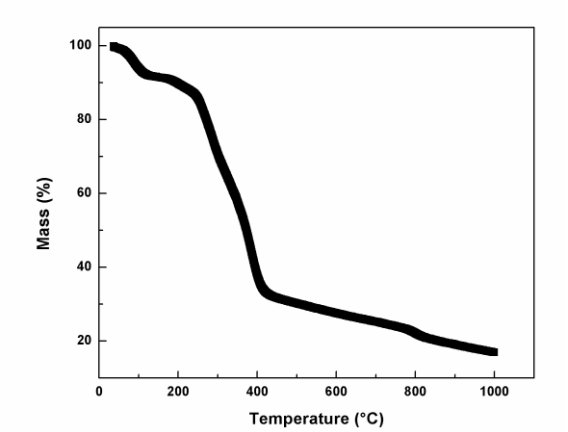

Figure S6.2: Thermal gravimetric analysis of cationic magnetic microgels designed to have 25 wt% SPION content. This result indicates that the microgels are ~31 wt% SPION content, slightly higher than expected.

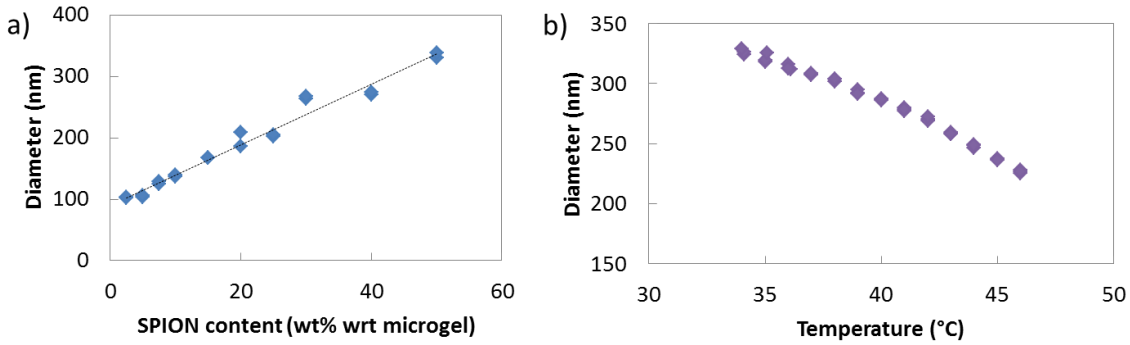

Figure S6.3: (a) Effect of SPION content on the diameter of neutral microgels (prepared without any ionic monomer component). These microgels could remain stable with up to 50 wt% SPION content (with respect to the microgel content), but the duration stability becomes more limited above 30 wt%. (b) Effect of temperature on the diameter of 50 wt% SPION nanocomposite microgels showing maintenance of thermoresponsive behaviour even at the highest SPION content tested.

Chapter 7: T_g nanocomposites

7.1 Preface

A T_g-controlled release mechanism was investigated to see if we could further improve the ratio of release between the on- and off-states of AMF application. Previously demonstrated T_g systems had not been demonstrated on the nanoscale, so p(MMA-co-BMA) latexes were fabricated using miniemulsification for the purpose of AMF-triggered drug release. The latex particles were entrapped, along with SPIONs, within our MITCH-type hydrazone-crosslinked hydrogel systems and the resulting systems were shown to exhibit enhanced release in response to both constant and pulsed AMF applications compared to controls. However, the ratio of release rates between the on- and off-state was less than expected, at ~2:1. Nonetheless, this is still the first example of nanoscale latex particles being used for T_g-mediated release.

7.2 Latex nanoparticles for AMF-mediated remote controlled release: Using the glass transition temperature to regulate the release of hydrophobic drugs

Scott Campbell, Angus Lam, Jared Gour, Niels Smeets, and Todd Hoare [Manuscript in preparation]*

7.2.1 Abstract

Remote controlled release has significant potential in a wide range of treatments that could benefit from complex therapeutic release profiles but is hindered by the low resolution between the on- and off-states of drug release and/or the need for surgical

implantation of larger controlled release devices. Herein, we describe a method based on a combination of injectable hydrogels, superparamagnetic iron oxide nanoparticles (SPIONs) that heat using an alternating magnetic field (AMF), and polymeric nanoparticles with a glass transition temperature (T_g) just above physiological temperature that addresses these challenges. Miniemulsion polymerization was used to fabricate p(MMA-co-BMA) nanoparticles with a specific T_g (~40°C) that also incorporates model hydrophobic drug in a simple, industrially utilized process. These latex nanoparticles, along with SPIONs, were then entrapped in an injectable hydrogel matrix that could be injected to a target site. Application of AMF causes the SPIONs to generate heat that is then transferred to the p(MMA-co-BMA) nanoparticles, increasing their temperature above their T_g and thus inducing faster release of the model drug due its markedly enhanced diffusivity through the nanoparticle at $T > T_g$. Temperature-based drug release experiments indicated a 2.5-6:1 rhodamine release ratio between on- and off-states when the nanocomposites were maintained at 45°C and 37°C, respectively; release was similarly enhanced by exposing the magnetic nanocomposite latex nanoparticle-laden microgels to an AMF. Coupled with the apparent cytocompatibility of all the nanocomposite components, these injectable materials appear to be promising systems as minimally-invasive but remotely-actuated release systems that could prove capable of complex release kinetics with high on-off resolutions.

Keywords: methyl methacrylate, latex, iron oxide nanoparticles, glass transition temperature, on-demand, drug delivery, controlled release, injectable.

7.2.2 Introduction

Nearly all treatments that would benefit from active release kinetics, such as insulin delivery,[1–3] chronic pain treatments,[4,5] endocrine disorders,[6] and several cancer treatments,[6,7] are currently treated with passive release systems. Even the vast majority of controlled release systems being researched and developed attempt to prolong the duration of passive release of therapeutics rather than controlling their release kinetics on-demand.[8] Thus, substantial research and market opportunities exist in the development of drug release systems that are capable of remote-controlled, on-demand, triggered release. Such release systems would be highly adaptable to changing physiological circumstances or patient needs, unlike passive release systems that are beyond the control of health professionals and/or the patient once they are implanted/injected into the body.[8,9]

Research in remote controlled delivery devices has recently intensified, with various systems such as liposomes[10], nanoparticles[11,12], hydrogels[5], and microchips[13] all having their dosage and timing of drug release remotely triggered via external stimuli such as ultrasound, light, and electromagnetic fields.[14–16] These advances take promising new steps towards the commercialization of remote controlled release that can achieve complex release kinetics. However, these systems are not without their disadvantages; indeed, the all of these triggerable systems only can be remotely triggered for release a single time, or lack reproducibility between multiple release cycles, have an inadequate ratio between on- and off-state release kinetics, and/or must be surgically implanted for effective use.[8]

Many of these remotely triggerable systems operate via combining nanoparticles that can be heated by a remote external stimulus to generate heat with thermosensitive lipids that can be melted upon heating or polymers that possess a lower critical solution temperature (LCST) or, for gel-based systems, a volume phase transition temperature (VPTT).[14–16] When such nanocomposite systems are remotely heated, the solubility/insolubility or swelling/deswelling transitions induced in the polymer phase can be used to actuate drug release. While these systems can theoretically be triggered over multiple release cycles, reproducibility and achieving useful ratios between the on- and off-state release kinetics (enabling both low off state leakage and high on state doses) remain difficult to achieve.[14,15] Hydrogel- and microgel-based systems also inherently have a high basal release rate in the off-state due to their highly hydrated natures that intrinsically makes achieving a high on-/off-state release ratio challenging, although this same property makes hydrogels highly attractive for *in vivo* applications in terms of their generally good tissue compatibility and physiochemical similarity to soft tissues.[17]

An alternative approach to designing such materials is to utilize thermosensitive polymers with a glass transition temperature (T_g) instead of an LCST or VPTT. While this area of drug delivery research remains relatively unexplored, Rovers et al. have reported on macroscale drug delivery devices capable of delivering therapeutic agents remotely using an alternating magnetic field (AMF) by combining a magnetic core comprised of superparamagnetic iron oxide nanoparticles (SPIONs), which generate heat in response to AMFs, surrounded by a poly(methyl methacrylate) (MMA)-co-(butyl methacrylate) (BMA) shell with a T_g that is slightly higher than physiological temperatures.[4,18] The benefit of this approach is the release associated with such

systems when in the glassy state (below the T_g) is significantly lower than that achieved in a gel-based system. When the temperature exceeds the T_g, the diffusivity coefficient increases by 1-2 orders of magnitude, resulting in an excellent differential in the release rate between the on- and off-state (of the AMF in this case).[18] This release mechanism both minimizes unwanted drug release (key in particular for delivering drugs with significant side-effects or with biological tolerance issues) as well as increases the duration over which this controlled release system could be used, as the diffusion-based baseline release would be fairly minimal in many cases. Tuning the T_g of a polymer via copolymerization is also a relatively simple process that is well established for multiple copolymers.[4]

While these devices are very promising, smaller injectable materials that could be injected and targeted to specific sites to remotely release therapeutics via this T_g-based mechanism could prove more advantageous. To this end, we have developed p(MMA-co-BMA) nanoparticles with a T_g of ~40°C, fabricated by miniemulsion polymerization for the purpose of T_g-enhanced drug delivery with magnetic particles and latex nanoparticles within a hydrogel scaffold. Miniemulsion polymerization involves stable nanodroplets of monomer dispersed in a continuous phase.[19–21] During polymerization, each droplet acts as its own individual bioreactor, allowing for the direct incorporation of various moieties in the resulting latex nanoparticles.[19,20] The miniemulsification method of fabricating such particles is versatile, allowing for the incorporation of SPIONs and/or hydrophobic drug directly in the polymerization process; however, this method does require the drugs to be heat stable and would not be effective with hydrophilic therapeutics.[21] The ability to incorporate hydrophobic drugs is of particular interest, as many chemotherapeutics are rather hydrophobic in nature, and several chemotherapies

have also shown improved efficacy in response to the periodic delivery of therapeutics that can be achieved with remote delivery (i.e. chronopharmaceutical drug delivery).[6,7]

Herein, we demonstrate effective AMF-mediated on-demand release triggered by T_g transitions in an injectable nanocomposite drug delivery system. Rhodamine B, a model small molecule hydrophobic drug, was encapsulated in p(MMA-co-BMA) nanoparticles that are subsequently physically entrapped together with SPIONs inside an injectable hydrogel. This approach allows for a well-defined amount of both SPIONs and p(MMA-co-BMA) latex particles to be incorporated within the hydrogel matrix, facilitating more well-defined and direct control over local heating, drug loading, and release kinetics once these materials are injected into a specific area of interest. The injectable hydrogels, previously developed in our lab, and are mixing-induced two component hydrogels (MITCH) involving hydrazide-functionalized carboxymethyl cellulose (CMC) and aldehyde-functionalized dextran that rapidly condense to form hydrolytically-degradable hydrazone crosslinks (Figure 7.1).[22,23] If the latex nanoparticles are designed with a T_g of ~40°C, applying the AMF will cause the SPIONs to generate heat within the hydrogel that will be transferred to the nanoparticles to trigger a glass transition. The transition from a glassy to an amorphous state results significantly faster diffusion of rhodamine B from the nanoparticles and out of the nanocomposite (Figure 7.1). When the AMF is removed, the material cools down to ambient temperature and the nanoparticles will return to their glassy, low-diffusion state. All the injectable hydrogel components and SPIONs have been shown to display little to no cytotoxicity[5,24] while pMMA and pBMA are both well-established biomaterials, suggesting the potential translatability of this approach to the clinic.

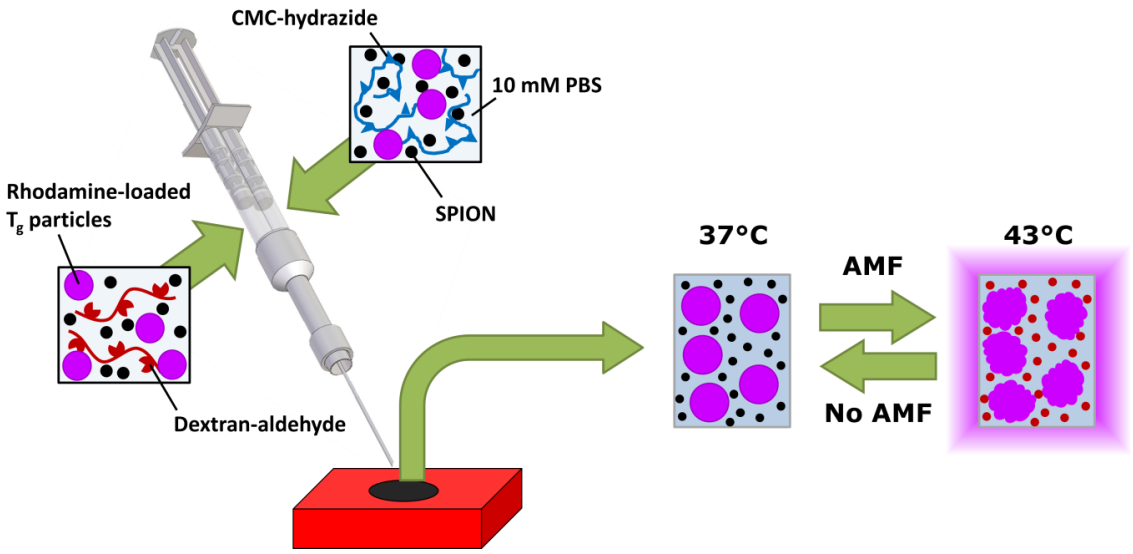

Figure 7.1: Development of hydrogel nanocomposites with embedded rhodamine B-loaded T_g p(MMA-co-BMA) latex nanoparticles and SPIONs. PBS suspensions of CMC-hydrazide in one barrel, dextran-aldehyde in the other barrel, and the rhodamine B-loaded T_g p(MMA-co-BMA) nanoparticles and SPIONs loaded with their desired final concentrations in both barrels are extruded through a double-barrel syringe. The material rapidly gels upon injection, and little release is observed at 37°C when the AMF is not applied. Upon AMF application, the SPIONs produce heat that raises the temperature of the nanoparticles above their T_g to significantly enhance the diffusion and release of rhodamine B from the nanoparticles and thus the hydrogel composite.

7.2.3 Experimental

Materials: Aluminum oxide (98%), ammonium hydroxide (reagent grade), ammonium persulfate (98%), benzoyl peroxide (BPO, ≥98%), benzyl ether (98%), butyl methacrylate (BMA, 99%), dimethyl sulfoxide (DMSO, reagent grade), hexadecane (99%), 1-hexadecanol (99%), iron(II) chloride tetrahydrate (98%), iron(III) acetylacetonate (97%), iron(III) chloride hexahydrate (97%), methylene bisacrylamide (MBA, 99%), methyl methacrylate (MMA, 99%), *N*-hydroxysuccinimide (NHS, 97%), oleic acid (90%), oleylamine (70%), poly(ethylene glycol) (PEG, MW: 8 kDa), rhodamine B (≥95%), sodium carboxymethyl cellulose (CMC, MW 250,000), sodium dodecyl sulfate (SDS,

≥99%), sodium periodate (>99.8%), and thiazolyl blue tetrazolium bromide (MTT, 98%) were all purchased from Sigma Aldrich (Oakville, ON). 1 M HCl and 1 M NaOH was purchased from LabChem Inc. Adipic acid dihydrazide (ADH, 97%) and 1-ethyl-3-(3-dimethylaminopropyl)carbodiimide hydrochloride (EDC, 98%) were purchased from Cedarlane Laboratories (Burlington, ON). The BMA and MMA monomers were purified with aluminum oxide. The 3T3 *Mus musculus* cell line was acquired from ATCC: Cedarlane Laboratories (Burlington, ON). The cell proliferation media, which included Dulbecco's modified Eagle's medium-high glucose (DMEM), fetal bovine serum (FBS), and penicillin streptomycin (PS), recovery media, and trypsin-EDTA, were all obtained from Invitrogen (Burlington, ON). All deionized water (DIW) was obtained following purification using a Barnstead Nanopure purification system.

Miniemulsion polymerization of p(MMA-co-BMA) latex nanoparticles: An emulsion was first made by mixing 2.01 g BMA, 1.74 g MMA, 0.30 g hexadecane, 0.23 g BPO, and 40 mg rhodamine B with a solution of 0.045 g SDS dissolved in 22.72 g of DIW. The chosen BMA:MMA ratio was shown to result in a latex T_g of ~39°C. This emulsion was mixed in a 100 mL beaker for 15 minutes under 500 rpm magnetic mixing. The emulsion was then placed in an ice bath, and a Misonix Ultrasound Liquid Processor sonicator (Model S-4000) was used to apply ~8 kJ of energy (80% amplitude) to the emulsion for 2 minutes using a QSonica CL5 probe. The resulting emulsion was taken up in a syringe and injected into a three-necked 100 mL round bottom flask that was preheated to 80°C in a nitrogen atmosphere with an attached condenser. A rotor-stator setup (with a VWR VOS 16 rotor) was also mounted in the flask to vigorously stir the miniemulsion as it was allowed to polymerize over the next 4 hours. After the polymerization was complete, the suspension was purified by centrifuging the particles

at 26,000 rpm at 4°C with a Beckman Coulter Allegra X-22R centrifuge over 4 cycles of centrifugation/redispersion in 10 mm PBS, using an ultrasonic cleaner to assist with re-suspension in each cycle. The size and polydispersity of the resulting particles were via dynamic light scattering (DLS) with a Brookhaven 90Plus Particle Analyzer.

Synthesis of oleic acid stabilized iron nanoparticles: Hydrophobic oleic acid-stabilized SPIONs were prepared based on procedures described by Sun.[25,26] Briefly, 15 nm particles were made by mixing $Fe(acac)_3$ (2 mmol), 1-hexadecanol (10 mmol), oleic acid (6 mmol), and oleylamine (6 mmol) with 10 mL of benzyl ether under nitrogen. Using a heating mantle, the mixture was heated to 200°C for 2 hours and then further heated to reflux (~300°C) for 1 more hour. The mixture was allowed to cool to room temperature, and the particles were precipitated with ~40 mL ethanol. The precipitate was collected via centrifugation at 10,000 rpm for 10 minutes with a Beckman Coulter Allegra X-22R centrifuge and subsequently redispersed in 20 mL hexane together with ~0.05 mL of each oleic acid and oleylamine. The material was again precipitated in ethanol and centrifuged in the same manner. The resulting SPIONs (7.2 ± 1.1 nm in size) were dispersed in BMA/MMA at 2 wt% relative to the total monomer mass, and magnetic latex nanoparticles were synthesized using the same miniemulsion protocol outlined above.

Synthesis of PEG-coated SPIONs: Hydrophilic SPIONs to be entrapped in the matrix of the nanocomposite were prepared via coprecipitation in a similar manner to Hoare et al.[27] Briefly, 3.04 g of iron (III) chloride hexahydrate and 1.98 g of iron (II) chloride tetrahydrate were dissolved in 12.5 g of DIW and stirred at 300 rpm under nitrogen. The iron salts were precipitated by adding 6.5 mL of ammonium hydroxide dropwise and

increasing the stirring speed, if the mixture ceased to spin. The mixture was then stirred for 10 minutes, after which 1 g of 8 kDa PEG dissolved in 5 mL DIW was added to the suspension. The mixture was then heated to 80°C for 2 hours to peptize the PEG to the SPION surface. The resulting material was separated with a permanent magnet and redispersed in 10 mM PBS over 4-6 cycles to purify the PEG-functionalized SPIONs. The final concentration was diluted to 5 wt% SPIONs. Transmission electron microscopy (TEM, JEOL Ltd., Japan) indicated that the PEG-SPIONs formed clusters of sizes between 30 and 200 nm, with individual particle diameters of 14 ± 5 nm.

Synthesis of hydrazide-functionalized CMC: In an analogous procedure to Sivakumaran et al.,[23] 1.00 g of CMC was dissolved in 200 mL of DIW in a 500 mL round bottom flask with magnetic stirring. 3.0 g of ADH was then added to the flask and allowed to dissolve, resulting in the solution of pH ~7. Subsequently, 0.07 g of NHS was dissolved in 4 mL of a 1:1 mixture of DMSO/DIW and added dropwise to the flask. 0.3 g of EDC was then dissolved in 1 mL of a 1:1 DMSO/DIW mixture and added to the mixture. The pH of the reaction was then maintained at 6.8 over the next 2 hours by dropwise addition of 0.1 M HCl/NaOH as required. The resulting aldehyde-functionalized CMC polymer was then dialyzed for six 6+ hour dialysis cycles before being lyophilized for storage. Base-into-acid conductometric titration (ManTech Inc.) comparing the number of moles of –COOH present in unmodified CMC to that present in the hydrazide-functionalized CMC (assuming that grafting of one hydrazide group consumes one carboxylic acid group) revealed that 43.9% of the –COOH groups in CMC were converted to hydrazide groups.

Synthesis of aldehyde-functionalized dextran: Following a protocol described by Patenaude and Hoare,[24] 1.50 g of dextran (MW: 500,000 Da) was dissolved in 150 mL of DIW in a 500 mL round bottom flask. 0.8 g of sodium periodate (dissolved in 5mL of DIW) was added to this solution dropwise under magnetic stirring, and the solution was left to stir for 2 hours. At this point, 0.4 mL of ethylene glycol was added to the solution and stirred for one more hour to consume residual oxidation agent. The product was dialyzed over six 6+ hour cycles against DIW before being lyophilized for storage. The aldehyde content of periodate-oxidized dextran was determined by using silver(I) oxide to selectively oxidize the polysaccharide-bound aldehyde groups to carboxylic acid groups and quantifying the acid groups using conductometric titration.[5,28] Here, 0.0002 mmol of oxidized dextran was dissolved in 10 mL of DIW with 6.2 mmol NaOH. Once the dextran was completely dissolved, 1.6 mmol of silver (I) oxide was added to the solution and the mixture was stirred overnight. 5 mL of reaction solution was then diluted with 45 mL of DIW and was titrated with 0.1M NaOH. Based on this assay, 17.4% of dextran residues underwent oxidative cleavage, resulting in ~2400 aldehyde groups per chain of 500 kDa oxidized dextran.

Nanocomposite fabrication: The use of a double barrel syringe to generate the nanocomposites is shown in Figure 7.1. Each barrel contains 5 wt% SPIONs (as we have previously shown that this concentration is sufficient for maintaining superparamagnetic properties within the composites and for their controlled heating via AMF)[29], 10 wt% rhodamine-loaded p(MMA-co-BMA) nanoparticles, and 4 wt% of either hydrazide-functionalized CMC or aldehyde-functionalized dextran (all weight percentages are with respect to the 10 mM PBS solvent). Precursor suspensions are prepared by diluting the SPION suspension to 5 wt% and dispersing the appropriate

weight of centrifuged nanoparticles into the SPION suspension using a sonication cleaner. The resulting mixed suspension was then split into two, with the CMC-hydrazide added to one suspension and dextran-aldehyde added to the other suspension; both were allowed to dissolve overnight and then loaded into opposite barrels of the double barrel syringe. Co-extrusion of the suspensions through a static mixer into cylindrical silicone moulds (diameter 3/8″ and height 1/ 8″) facilitates mixing of the reactive hydrogel precursors, followed by gelation over 15 minutes to form magnetic hydrogel nanocomposites with embedded p(MMA-co-BMA) nanoparticles.

Thermally-triggered drug release: Thermally-initiated drug release experiments were conducted by placing the nanocomposite disks (*n* = 4, 6.3 mm diameter x 3.2 mm height) in cell culture inserts (2.5 cm, 8 µm pore size) within the wells of a 12 well plate, submerged in 4 mL of 10 mM PBS per well. One set of samples was incubated at 37°C and another at 45°C in separate incubating orbital shakers (VWR Model 3500I). At predetermined time intervals over 6 days, 500 µL of the PBS was removed from each well and replaced with fresh 10 mM PBS. 2 x 200 µL aliquots of each release sample were transferred into a black-backed 96 well plate, with the quantity of rhodamine B in the sample determined with a fluorescent plate reader (Tecan Infinite M1000, 540 nm excitation/625 nm emission wavelengths).

AMF-triggered drug release: Drug release experiments using both a pulsed and constant application of an AMF were performed analogously to methods described by Maitland et al.[30] Briefly, rhodamine B-loaded nanocomposite disks (*n* = 4, 6.3 mm diameter x 3.2 mm height) were placed in test tube vials with prefabricated holders that hold the nanocomposite disks the center of the 10 mM PBS solution when 4 mL of this

PBS solution are placed in a given test tube. The test tubes themselves are positioned within a jacketed flask at equivalent positions within an alternating magnetic field generated using a Superior Induction induction heater (HF-series, Model SI-7KWHF) fitted with a 2-coiled, 8 cm diameter solenoid (Figure S7.1). A water bath was attached to the jacketed flask to maintain a constant temperature of 37°C in the nanocomposites in the absence of AMF. When desired, the AMF device was operated at 200 kHz, 30 A, and 1.3 kW to expose the nanocomposites to short AMF pulses or a constant exposure to the AMF. Each test tube was filled with 4 mL of 10 mM PBS to fully immerse the nanocomposite disks, with 0.5 mL samples collected from each test tube at 15 minute time intervals over a time period of 6 hours and immediately replaced with 0.5 mL of fresh pre-heated 10 mM PBS. For pulsed release experiments, a 30 minute pulse of AMF was applied 1, 3, and 5 hours into the experiment. For continuous activated release experiments, nanocomposite disks were loaded in the same AMF setup as the pulsed experiments but the AMF was applied throughout the 6 h duration of the experiment. A set of control gels (not exposed to AMF) was kept in identical test tubes in an incubator at 37°C, with drug release kinetics assessed by sampling at the same volumes and time intervals as used for the AMF experiment. In each experiment, 2 x 200 µL from each sample was placed in black 96-well plates and the amount of rhodamine B in each sample was analyzed using a fluorescent plate reader (Tecan Infinite M1000, 540 nm excitation/625 nm emission wavelength).

In vitro cytotoxicity assay: The cytotoxicities of the p(MMA-co-BMA) nanoparticles were assayed with 3T3 *Mus musculus* mouse fibroblast cells. A proliferation media of 10 vol% FBS and 1 vol% PS in DMEM was used to grow the 3T3 cells. All materials were sterilized prior to cell viability testing by exposure to UV radiation (2 hours) or (when

possible) filtration through 0.45 µm filters. Each well of a 24-well polystyrene plate (n = 4 for each latex concentration/hydrogel tested) was incubated with 25,000 3T3 cells with 1 mL of media at 37°C and 5% CO_2 for 24 hours. The media was then aspirated, and 1 mL of fresh media with the appropriate concentrations of magnetic microgels was added. A negative control (no cells) and a positive control (cells not exposed to any synthetic materials) were included in the study. After 24 hours of incubation, the media and microgel solution was aspirated and each well was rinsed with 0.5 mL of media. 150 mL of a 0.4 mg/mL MTT solution was then added to each well, and the cells were incubated for 4 additional hours. Following, the MTT solution was aspirated and 500 µL of DMSO was added to each well to dissolve the insoluble formazan precipitate; each plate was placed on a shaker until the formazan was completely dissolved (typically ~20 minutes). 2 x 200 µL were sampled from each well, transferred to a 96 well polystyrene plate, and read in an absorbance reader at 540 nm (PerkinElmer Victor3 multilabel plate reader). The percent cell viability was determined as the ratio the average absorbance values of cells exposed to the p(MMA-co-BMA) nanoparticles and the average absorbance values of the positive control (cells incubated only in media, with no synthetic materials).

Error and statistical significance: Error bars represent the standard deviation of a given measurement based on multiple samples (n = 4). A two-tailed t-test with $p < 0.05$ assuming unequal variances was used to detect statistically significant differences between any given pair of samples.

7.2.4 Results

Multiple miniemulsion polymerization experiments in which the BMA:MMA monomer ratio was adjusted were first performed to identify the BMA:MMA ratio that yielded a T_g within the range of interest (38-42°C). This temperature range was chosen because it is above normal physiological temperatures (i.e. release would remain slow in the "off", non-triggered state) but below temperatures that could harm healthy local tissues under moderate exposure times (>45°C).[15]

A T_g of ~39°C was achieved with a 0.81:1 molar ratio of BMA:MMA, resulting in monodisperse and stable polymer particles with a hydrodynamic diameter of ~97 ± 1 nm in size with a polydispersity of 0.054, and were quite stable in suspension.

Magnetic drug-loaded nanoparticles were subsequently prepared by adding oleic acid-functionalized SPIONs and/or the rhodamine B model drug to the same 0.81:1 BMA:MMA miniemulsion recipe. DSC results of the p(MMA-co-BMA) nanocomposites and rhodamine incorporated into the structure indicated that the nanocomposites maintain a glass transition temperature of ~39°C (Figure 7.2).

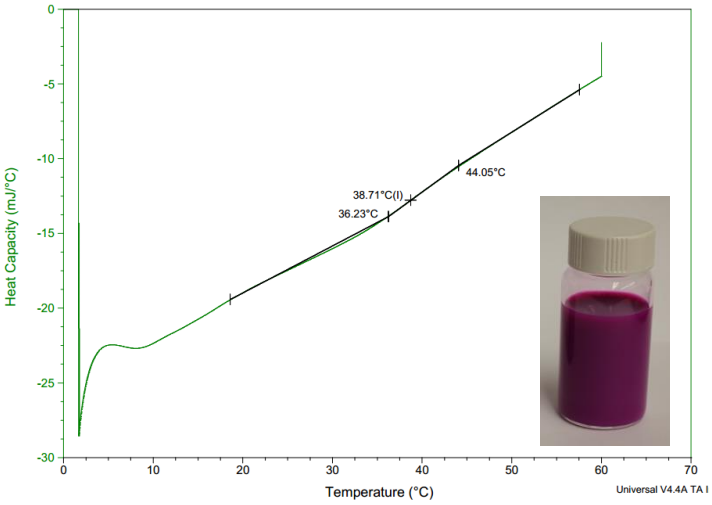

Figure 7.2: DSC of p(MMA-co-BMA) nanocomposites with 1 wt% rhodamine B content (with respect to the initial monomer content). (inset) Suspension of rhodamine B-loaded p(MMA-co-BMA) nanoparticles.

Analogously, magnetic nanoparticles fabricated by incorporating hydrophobic, oleic-acid stabilized SPIONs into the pre-polymerization emulsion resulted in slightly larger size (~161 nm diameter) and higher polydispersity (0.125) nanoparticles but still maintained a T_g of ~39°C. Based on these results, the T_g is not significantly affected when additional components that do not specifically interact with the polymer structure/function are added to the miniemulsion polymerization, confirming the versatility of this approach to facilely incorporate multiple hydrophobic moieties into the particles. Here, each miniemulsion droplet acts as its own batch reactor, allowing multiple hydrophobic moieties incorporated into the hydrophobic droplet prior to polymerization will be incorporated into polymer nanoparticles upon polymerization of the droplet.

TGA indicated that ~15 wt% of SPIONs were incorporated into a latex nanoparticle formed from a prepolymerization emulsion containing 20 wt% SPIONs (Figure S7.2). This slightly less than stoichiometric incorporation can be attributed to some aggregation

of the SPIONs that is observed upon sonication. Indeed, TEM images indicate that SPIONs appeared to be clustered in a small section of each particle rather than dispersed throughout it, although the number of SPIONs per particle was relatively consistent (2-4 particles/particle as shown in Figure S7.2). Superconducting quantum interference device (SQUID) measurements indicated that the magnetic nanoparticles possessed superparamagnetic characteristics, with the magnetic saturation much lower than the hydrophobic SPIONs alone due to the high polymer content of the nanoparticles (Figure S7.3). However, this magnetic saturation is too low for these particles and we are not capable of heating these materials magnetically with our rather lower magnetic strength AMF setup (a 1.3 kW, 200 kHz, 30 A, with a 2-coiled, 8 cm solenoid).

It should be noted that the versatility of the miniemulsion polymerization method extends to after these particles are made. For example, magnetic cores of SPIONs and MMA were made via a similar miniemulsion polymerization approach and then used as seeds to form a shell with a specific T_g by adding BMA and MMA monomers (at a rate of 0.77 mL/h) using a semi-batch polymerization method. The shell thickness and PDI are dependent on the duration of the semi-batch addition (Figure S7.4), with the shell size gradually increasing and the PDI decreasing until ~5 hours addition time, after which point both the PDI and shell thickness increase dramatically, potentially due to the formation of dimer/trimer particles. These particles could then be used as seeds to form either a thermosensitive or highly protein-repellent poly(oligoethylene glycol methacrylate) (POEGMA)-based gel shell using a similar approach (Table S7.1), creating multi-shell nanocomposites with desirable interfacial properties as well as potential for T_g-mediated release.

Based on the low magnetic saturation of the SPION-nanoparticle composites, nanocomposite hydrogels in which the rhodamine-loaded latex nanoparticles is physically mixed and co-encapsulated with SPIONs inside an injectable hydrogel were selected to proceed with drug release kinetics measurements. This structure offers several advantages over the SPION-nanoparticle composite approach: (1) a known SPION concentration (independent of the drug loading) can be added to precisely tune the temperature increase and resulting drug release from nanocomposite systems for a given AMF application; (2) entrapping the latex nanoparticles in a hydrogel that can be injected into the specific therapeutic region of interest would also allow for a known drug particle concentration at the desired location, in contrast to circulating nanoscale systems in which the majority of delivered drug is delivered to off-target tissues.[31]

Thermoresponsive release behavior of an injectable nanocomposite hydrogel comprised of 5 wt% PEG-stabilized SPIONs, 10 wt% rhodamine B-containing p(MMA-co-BMA) nanoparticles (prepared with 10 wt% rhodamine B loading), 4 wt% of hydrazide-functionalized CMC and 4 wt % of aldehyde-functionalized dextran is shown in Figure 7.3. All release rates were normalized against the initial weight of the nanocomposite.

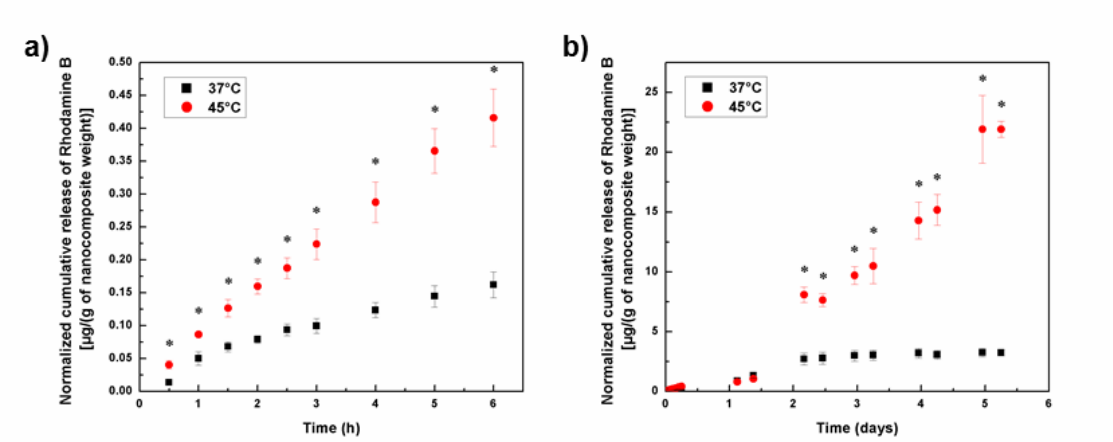

Figure 7.3: Release of rhodamine B from the p(MMA-BMA) nanoparticles with T_g ~40°C entrapped in an injectable MITCH-type hydrogel with 5 wt% SPION content made from the natural polymers CMC and dextran: (a) short term release over 6 hours; (b) longer term release over ~6 days. * indicates statistically significant differences in the cumulative release between the two incubation temperatures at a given time point (p < 0.05).

Significantly more rhodamine B was released from nanocomposites at 45°C than the same composites at 37°C throughout the course of the experiment, with the exception of two samples taken just after 24 hours; this lack of difference at early release times is likely attributable to the early diffusion of rhodamine B encapsulated at or near the p(MMA-BMA) nanoparticle surface that is not significantly retarded by the glassy nature of the latex nanoparticles. Otherwise, 2.5-3 times more rhodamine B was consistently released at the higher temperature of 45°C over the first three days of sampling until this difference expanded to a ~7 times enhancement of rhodamine B release at 45°C over 37°C after 5 days. Indeed, following the hypothesized non-specific release of near-surface rhodamine B in the 37°C sample, no significant change in cumulative release at $T<T_g$ was observed between days 2-5 (in all statistical comparisons p > 0.12), in sharp contrast to various hydrogel/VPTT-based systems (including those reported elsewhere

in this thesis) in which "off" state basal release is significant. These results together demonstrate that the T_g of these materials can meter temperature-responsive release above 37°C, affording the potential for these materials to be capable of remote-controlled release via AMF.

Notably, Figure 7.3 also shows that this injectable hydrogel nanocomposite system is capable of releasing hydrophobic moieties with little-to-no burst release; indeed, there is a slight lag in release at early times which we attribute to the required diffusion of the drug (initially localized in the p(MMA-BMA) nanoparticles) from the nanoparticle surface through the hydrogel and then out into the release medium. To the best of our knowledge, this is a rare example of near zero-order and zero burst release from an injectable hydrogel system, a kinetic profile of significant interest for hydrophobic drugs that are effective at low concentrations for long term therapies. The hydrazone chemistry of the MITCH-type hydrogels also is ideal for long term delivery, as we have previously demonstrated degradation times over a period of 3-6 months in physiological conditions for these hydrogels.[5]

The capacity of nanocomposites comprised of 10 wt% rhodamine B-loaded latex nanoparticles and 5 wt% PEG-coated SPIONs entrapped in a CMC-dextran injectable MITCH-type hydrogel to deliver hydrophobic drug at enhanced rates upon exposure to an AMF was then assessed. The release rates of samples exposed to short, 30 minute pulses of AMF compared to samples not exposed to the AMF are shown in Figure 7.4, with release again normalized against the initial weight of the nanocomposite.

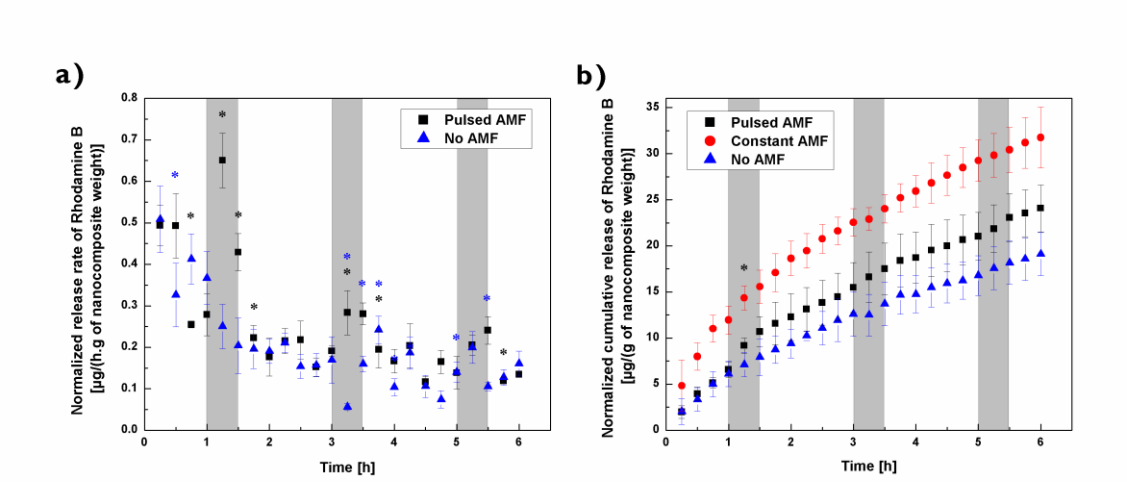

Figure 7.4: (a) Release rate of rhodamine B with and without 30 minute pulsatile AMF applications at 1, 3, and 5 hours (indicated by the grey boxes). (b) Cumulative release of rhodamine B with the 30 minute AMF pulses, with the AMF constantly applied to the nanocomposites, and without an applied AMF. All of the results are normalized against the weight of the nanocomposites and * of each colour indicates each point that is statistically significantly different from the previous point ($p < 0.05$).

Figure 7.4a shows that the release rate generally significantly increases in response to the AMF pulse and shifts back down to the baseline release level immediately after the AMF is removed. The pulsed samples tend to have a release rate that is 1.5-2 times the release rate of the non-pulsed sample during the pulse. This lower resolution between the on- and off-states may be attributed to the AMF only heating the nanocomposite disks up to ~43°C in this system compared to the temperature-based release and/or the T_g of the nanocomposites being so close to physiological temperatures that a portion of them are not in the glassy state at the baseline 37°C temperature (which would also raise the baseline, off-state rhodamine B release rate). This resolution could thus potentially be improved through the use of latex nanoparticles with a slightly higher targeted T_g value and/or including more SPIONs in the nanocomposite to facilitate higher

local heating within the gel. Samples that are not exposed to the AMF pulses do still experience significant differences in the release rates between time points, but these fluctuations are random throughout the 6 hour timeframe, indicative of noise within the sampling protocol used instead of pulsatile release potential.

Figure 7.4b shows the cumulative release results from these nanocomposite materials. At each time point there is significantly more release from the nanocomposites constantly exposed to the AMF versus the control composites that were kept at 37°C. The samples that underwent AMF pulses are understandably in between these two, with the differences entirely due to the increase in release as a result of the 30 minute AMF pulses. Furthermore, only a small proportion of the small, hydrophobic model drug was released over the 6 hour duration of these experiments, with 1.2 ± 0.2%, 1.6 ± 0.2%, and 1.0 ± 0.2% released constant AMF exposure, with pulsed AMF applications, and with no AMF exposure respectively (assuming the rhodamine B was completely retained in the particles throughout synthesis and purification). This desirable low basal release rate in the off-state is difficult to achieve with hydrogel systems and can be entirely attributed to loading of the drug exclusively within the latex nanoparticles entrapped within the hydrogel. Consequently, this system could potentially be used for long term delivery of small, hydrophobic therapeutics capable of being repeated pulsatile release as activated externally with an AMF.

All of the components of the nanocomposites tested for drug release, and similar nanocomposites as a whole, have previously been shown to be cytocompatible in *in vitro* (Figure 7.5) and *in vivo* studies, with the exception of the rhodamine B-loaded p(MMA-BMA) nanoparticles.[5,30] Consequently, the cytocompatibility of these nanoparticles was

analyzed with an MTT metabolic assay using 3T3 mouse fibroblast cells, the results of which are shown in Figure 7.5.

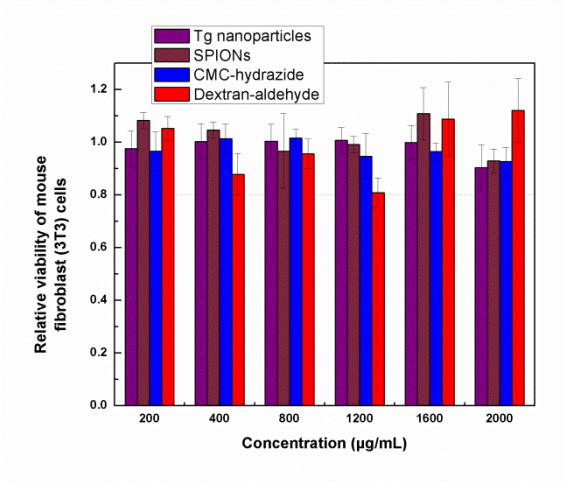

Figure 7.5: Relative viability (to cell-only control) of 3T3 mouse fibroblast cells for various concentrations of rhodamine B-loaded p(MMA-BMA) T_g nanoparticles, SPIONs, hydrazide-functionalized CMC, and aldehyde-functionalized dextran.

No significant cytotoxicity was exhibited over the full range of tested nanoparticle concentrations, with all concentrations showing cell viabilities significantly greater than 80%. Note that the higher concentrations tested here are expected to be greatly in excess of the potential exposure concentrations in the body after *in vivo* injection given the rapid gelation and slow degradation characteristics of the hydrazone MITCH-type hydrogels used. This result is not unexpected, as pMMA and pBMA were some of the earliest traditional biomaterials reported. This *in vitro* result, along with our previous *in vivo* results with similar composite hydrogels,[5] suggests that these materials would be suitable candidates for *in vivo* applications.

7.2.5 Conclusions

A wide range of treatments could benefit from complex therapeutic release profiles that could be achieved by remotely controlled drug delivery systems. Here, p(MMA-co-BMA) nanoparticles with a T_g ~40°C loaded with rhodamine B and entrapped in an injectable hydrogel matrix with SPIONs are shown to enable AMF-actuated hydrophobic small molecule release. The resulting nanocomposites displayed desirable compatibilities *in vitro* and had a significantly improved release ratio between the on- and off-states of 2.5-7:1 in temperature-based studies. While this resolution decreased slightly (1.5-2:1) when AMF-mediated release was attempted, the lack of a burst release, low release rate, and low amount of total release after 6 hours is unique for an injectable hydrogel-based release system and could prove useful for a wide range of treatments requiring low doses hydrophobic therapeutics over extended periods of time.

7.2.6 Acknowledgements

The authors thank the J.P. Bickell Foundation (Medical Research Grant Program), the Vanier Scholarship program, and the Natural Sciences and Engineering Research Council of Canada (NSERC) for funding.

7.2.7 References

(1) Veiseh, O.; Tang, B. C.; Whitehead, K. A.; Anderson, D. G.; Langer, R. Managing Diabetes with Nanomedicine: Challenges and Opportunities. *Nat. Rev. Drug Discov.* **2014**, *14*, 45–57.

(2) Vegas, A. J.; Veiseh, O.; Gürtler, M.; Millman, J. R.; Pagliuca, F. W.; Bader, A. R.; Doloff, J. C.; Li, J.; Chen, M.; Olejnik, K.; *et al.* Long-Term Glycemic Control Using Polymer-Encapsulated Human Stem Cell-Derived Beta Cells in Immune-Competent Mice. *Nat. Med.* **2016**, *22*, 306–311.

(3) Vegas, A. J.; Veiseh, O.; Doloff, J. C.; Ma, M.; Tam, H. H.; Bratlie, K.; Li, J.; Bader, A. R.; Langan, E.; Olejnik, K.; *et al.* Combinatorial Hydrogel Library Enables Identification of Materials That Mitigate the Foreign Body Response in Primates. *Nat. Biotechnol.* **2016**, *34*, 345–352.

(4) Keurentjes, J. T. F.; Kemmere, M. F.; Bruinewoud, H.; Vertommen, M. M. E.; Rovers, S.; Hoogenboom, R.; Stemkens, L. F. S.; Péters, F. L. M.; Tielen, N. J. C.; van Asseldonk, D. T.; *et al.* Externally Triggered Glass Transition Switch for Localized on-Demand Drug Delivery. *Angew. Chem. Int. Ed.* **2009**, *48*, 9867–9870.

(5) Campbell, S. B.; Patenaude, M.; Hoare, T. Injectable Superparamagnets: Highly Elastic and Degradable Poly(N-Isopropylacrylamide)-Superparamagnetic Iron Oxide Nanoparticle (SPION) Composite Hydrogels. *Biomacromolecules* **2013**, *14*, 644–653.

(6) Tong, R.; Hemmati, H. D.; Langer, R.; Kohane, D. S. Photoswitchable Nanoparticles for Triggered Tissue Penetration and Drug Delivery. *J. Am. Chem. Soc.* **2012**, *134*, 8848–8855.

(7) Youan, B. C. Chronopharmaceutical Drug Delivery Systems: Hurdles, Hype or Hope? *Adv. Drug Deliv. Rev.* **2010**, *62*, 898–903.

(8) Timko, B. P.; Dvir, T.; Kohane, D. S. Remotely Triggerable Drug Delivery Systems. *Adv. Mater.* **2010**, *22*, 4925–4943.

(9) Timko, B. P.; Arruebo, M.; Shankarappa, S.; McAlvin, J. B.; Okonkwo, O. S.; Mizrahi, B.; Stefanescu, C. F.; Gomez, L.; Zhu, J.; Zhu, A.; *et al.* Near-Infrared-Actuated Devices for Remotely Controlled Drug Delivery. *Proc. Natl. Acad. Sci.* **2014**, *111*, 1349–1354.

(10) An, X.; Zhan, F.; Zhu, Y. Smart Photothermal-Triggered Bilayer Phase Transition in AuNPs − Liposomes to Release Drug. *Langmuir* **2013**, *29*, 1061–1068.

(11) Viger, M. L.; Sheng, W.; Doré, K.; Alhasan, A. H.; Carling, C.-J.; Lux, J.; de Gracia Lux, C.; Grossman, M.; Malinow, R.; Almutairi, A. Near-Infrared-Induced Heating of Confined Water in Polymeric Particles for Efficient Payload Release. *ACS Nano* **2014**, *8*, 4815–4826.

(12) Wang, C.; Xu, H.; Liang, C.; Liu, Y.; Li, Z.; Yang, G.; Cheng, L.; Li, Y.; Liu, Z. Iron Oxide @ Polypyrrole Nanoparticles as a Multifunctional Drug Carrier for Remotely Controlled Cancer Therapy with Synergistic Antitumor Effect. *ACS Nano* **2013**, 6782–6795.

(13) Farra, R.; Sheppard, N. F.; McCabe, L.; Neer, R. M.; Anderson, J. M.; Santini, J. T.; Cima, M. J.; Langer, R. First-in-Human Testing of a Wirelessly Controlled Drug Delivery Microchip. *Sci. Transl. Med.* **2012**, *4*, 122ra121, doi:10.1126/ scitranslmed.3003276.

(14) Campbell, S. B.; Hoare, T. Externally Addressable Hydrogel Nanocomposites for Biomedical Applications. *Curr. Opin. Chem. Eng.* **2014**, *4*, 1–10.

(15) Merino, S.; Martin, C.; Kostarelos, K.; Prato, M.; Vázquez, E. Nanocomposite Hydrogels: 3D Polymer-Nanoparticle Synergies for On-Demand Drug Delivery. *ACS Nano* **2015**, *9*, 4686–4697.

(16) Mura, S.; Nicolas, J.; Couvreur, P. Stimuli-Responsive Nanocarriers for Drug Delivery. *Nat. Mater.* **2013**, *12*, 991–1003.

(17) Hoare, T. R.; Kohane, D. S. Hydrogels in Drug Delivery: Progress and Challenges. *Polymer.* **2008**, *49*, 1993–2007.

(18) Rovers, S. A.; Hoogenboom, R.; Kemmere, M. F.; Keurentjes, J. T. F. Repetitive on-Demand Drug Release by Magnetic Heating of Iron Oxide Containing Polymeric Implants. *Soft Matter* **2012**, *8*, 1623–1627.

(19) Antonietti, M.; Landfester, K. Polyreactions in Miniemulsions. *Science.* **2002**, *27*, 689–757.

(20) Campbell, S. B.; Larson, T.; Smeets, N. M. B.; El-Jaby, U.; McKenna, T. F. L. Miniemulsification by Catastrophic Phase Inversion. *Chem. Eng. J.* **2012**, *183*, 534–541.

(21) Ramírez, L. P.; Landfester, K. Magnetic Polystyrene Nanoparticles with a High Magnetite Content Obtained by Miniemulsion Processes. *Macromol. Chem. Phys.* **2003**, *204*, 22–31.

(22) Patenaude, M.; Campbell, S.; Kinio, D.; Hoare, T. Tuning Gelation Time and Morphology of Injectable Hydrogels Using Ketone-Hydrazide Cross-Linking. *Biomacromolecules* **2014**, *15*, 781–790.

(23) Sivakumaran, D.; Maitland, D.; Hoare, T. Injectable Microgel-Hydrogel Composites for Prolonged Small-Molecule Drug Delivery. *Biomacromolecules* **2011**, *12*, 4112–4120.

(24) Patenaude, M.; Hoare, T. Injectable, Mixed Natural-Synthetic Polymer Hydrogels with Modular Properties. *Biomacromolecules* **2012**, *13*, 369–378.

(25) Sun, S.; Zeng, H.; Robinson, D. B.; Raoux, S.; Rice, P. M.; Wang, S. X.; Li, G. Monodisperse MFe2O4 (M = Fe, Co, Mn) Nanoparticles. *J. Am. Chem. Soc.* **2004**, *126*, 273–279.

(26) Xie, J.; Peng, S.; Brower, N.; Pourmand, N.; Wang, S. X.; Sun, S. One-Pot Synthesis of Monodisperse Iron Oxide Nanoparticles for Potential Biomedical Applications. *Pure Appl. Chem.* **2006**, *78*, 1003–1014.

(27) Hoare, T.; Timko, B. P.; Santamaria, J.; Goya, G. F.; Irusta, S.; Lau, S.; Stefanescu, C. F.; Lin, D.; Langer, R.; Kohane, D. S. Magnetically Triggered Nanocomposite Membranes: A Versatile Platform for Triggered Drug Release. *Nano Lett.* **2011**, *11*, 1395–1400.

(28) Thomason, S. C.; Kubler, D. G. Acids as Derivatives of Aldehydes Prepared with Silver Oxides. *J. Chem. Educ.* **1968**, *45*, 546.

(29) Campbell, S.; Maitland, D.; Hoare, T. Enhanced Pulsatile Drug Release from Injectable Magnetic Hydrogels with Embedded Thermosensitive Microgels. *ACS Macro Lett.* **2015**, *4*, 312–316.

(30) Maitland, D.; Campbell, S. B.; Chen, J.; Hoare, T. Controlling the Resolution and Duration of Pulsatile Release from Injectable Magnetic “Plum Pudding” Nanocomposite Hydrogels. *RSC Adv.* **2016**, *6*, 15770–15781.

(31) Bae, Y. H.; Park, K. Targeted Drug Delivery to Tumors: Myths, Reality and Possibility. *J. Control. Release* **2012**, *153*, 198–205.

7.2.8 Supporting Information

Figure S7.1: Picture of the AMF triggering apparatus. The nanocomposites are held in the test tubes by custom polyethylene holders and positioned at equivalent locations with the coils of the solenoid.

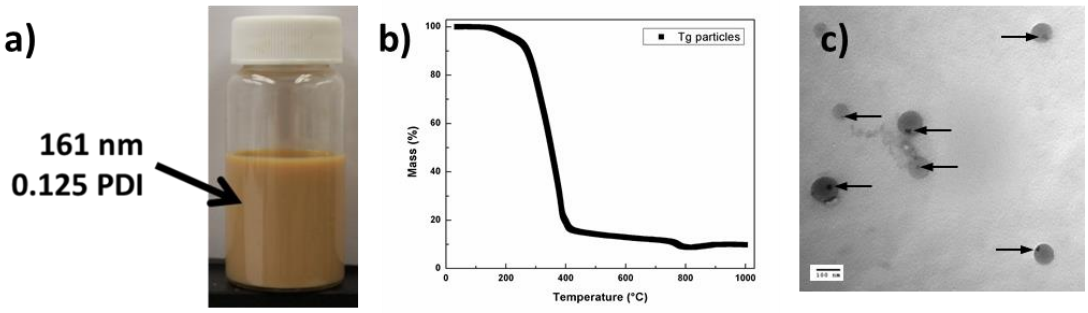

Figure S7.2: a) Dispersion of SPION-laden p(MMA-co-BMA) nanoparticles in DIW. b) TGA of magnetic p(MMA-co-BMA) nanoparticles, confirming that the particles contain ~15% SPIONs. c) TEM of the magnetic latex nanoparticles, in which 2-4 SPION particles

can be seen clustered together per latex particle, as indicated by arrows (120,000x magnification).

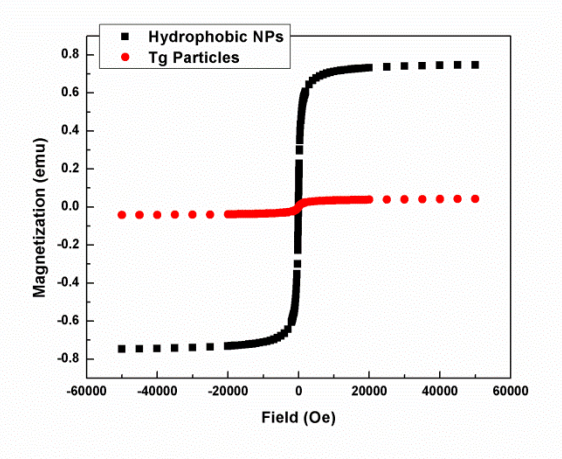

Figure S7.3: SQUID measurements of superparamagnetic hydrophobic SPIONs and magnetic p(MMA-co-BMA) nanoparticles with such SPIONs entrapped in the latex particles.

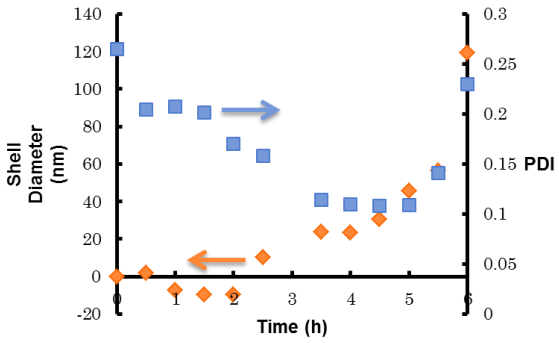

Figure S7.4: Shell diameter and PDI, analyzed via DLS, during MMA/BMA shell growth on SPION-MMA core seed particles over time (monomer feed rate 0.77 mL/h).

Table S7.1: DLS results of particles with a SPION/MMA core, these cores with a BMA/MMA shell, and the core-shell particles with an additional POEGMA gel on the outside of the particles.

Particle	Size (nm)
Core	99 ± 5
Core-Shell	136 ± 2
Core-Shell-Gel (25˚C)	194 ± 7
Core-Shell-Gel (60˚C)	169 ± 3

Chapter 8: Conclusions

8.1 Significance and concluding discussion

The overall body of work presented here explores the use of injectable "smart" thermosensitive hydrogels for biomedical applications and drug delivery, transitioning from large, macroscale systems to nanoscale devices. The general focus of this work lies in the development of materials that can be manipulated remotely to control drug release, specifically via alternating magnetic fields (AMFs). The combination of SPIONs and thermosensitive hydrogels and/or microgels is integral to this release, as the SPIONs produce heat in response to AMF that can be transferred to the thermosensitive hydrogels or microgels to raise their local temperature above their VPTT to cause them to deswell. This mechanism is fully reversible such that when the AMF is removed the temperature of the gel components will return to their ambient temperature (~37°C both *in vivo* and in all experiments presented herein) and re-swell back to their original size as their temperature decreases below their VPTT. This swelling/deswelling mechanism, which is ultimately regulated by the applied AMF, is the mechanism applied to control drug release for a wide range of drug moieties. This type of regulation of drug release post-implantation/injection could have marked benefits over traditional passive release systems, potentially putting control back into the hands of healthcare professionals and/or patients by providing them capacity to react to changing physiologic conditions and patient needs. This type of control could be tremendously useful for a wide range of treatments including, but not limited to, insulin/hormone delivery, chronic pain treatments, vaccine delivery, and cancer therapies (some of which respond more favourably to cyclical therapeutic delivery).

My PhD work in this area began by using SPIONs as the crosslinking component of our two-component hydrazone-crosslinked hydrogels (Chapter 2). Here, the SPIONs were functionalized with hydrazide-functionalized PNIPAM which can be used to form magnetic macroscale hydrogels when co-injected through a double barrel syringe with aldehyde-functionalized dextran loaded in the second barrel. The resulting hydrogels had very unique properties, including impressively high mechanical strength for a hydrogel, "bouncy ball"-like mechanical properties, and high tissue adhesion *in vivo*. These hydrogels were also able to release drug in response to pulses from an AMF, with 2.5-fold enhancements in the release rate achievable upon application of a given pulse.

Subsequent projects (Chapters 3 and 4) focused on improving control over drug release from macroscale hydrogel-based systems. To achieve this, nanocomposite hydrogels containing both SPIONs and thermosensitive PNIPAM-based microgels entrapped within the hydrogel scaffold were fabricated. The proposed mechanism of drug release from these systems involves SPIONs transferring the heat they produce in response to an AMF application to the microgels, which deswell and in the process generate free volume to encourage enhanced drug release. When the AMF is removed, the microgels refill the pore space that was created as they reswell to their original state and the rate of drug release is returned back to its lower baseline level. The first of these two chapters confirmed that mechanism and demonstrated a 4:1 ratio in terms of the rate of release with the applied AMF versus the baseline release rate. The second chapter observes the influence of various parameters associated with these nanocomposites on drug release. In short, increasing the microgel content (at least up to a certain point prior to gel destabilization), operating around the VPTT of the microgels when heating/cooling via AMF, and limiting the swelling of the hydrogel scaffold were all shown to enhance the

release rate as a result of an applied AMF over the baseline release rate. Notably, the release rate was not affected by the AMF pulse duration between 10 and 20 minutes, which could significantly simplify the relation between how long an AMF should be applied to release a specific, controlled dose.

Chapter 5 involves micro-scale systems for controlled release, describing the development of a microinjector to inject precise, low amounts (1 – 20 µL) of our injectable hydrogels for use in *in vivo* ocular experiments. The microinjector was capable of injecting ~5 µL droplets of our hydrazone-crosslinked mixing induced two component hydrogels (MITCH) into the eyes of rats *in vivo*. The injected hydrogels showed good tissue compatibility when delivered to the eye with the designed microinjector. While these systems were not capable of remote controlled drug release (or even assessed for their drug release *in vivo*), analogous MITCH-type hydrogel systems could be injected with these devices that are capable of remotely actuated release. For example, the previously discussed macroscale magnetic nanocomposites or the nano-scale systems entrapped within hydrazone MITCH-type hydrogel scaffolds (Chapters 6 and 7) could be delivered with these microinjection devices. Furthermore, it is now becoming known that hydrogels and other particulate-based vehicles with sizes in this micron-to-millimetre size range are markedly more favourable in terms of avoiding the immune response in vivo.[1] Thus, such a microinjection device could prove useful for delivering nanocomposite hydrogel droplets of this size that can avoid immune responses.

The last chapters (Chapters 6 and 7) describe nanoscale systems that also have the potential for AMF-mediated remote release. Chapter 6 describes cationic microgels

containing large fractions of SPIONs incorporated into their structure (up to 40 wt.%), prepared via a simple, two-stage fabrication process. The resulting magnetic microgels can be used to deliver anionic drugs, undergo magnetic targeting, and have the potential for AMF-mediated release. Chapter 7 describes nanoscale MMA/BMA latex particles manufactured via miniemulsion polymerization have also been developed that release upon heating via a glass transition (T_g) rather than a volume phase transition. The ratio of MMA:BMA was designed such that the T_g of the polymer is ~40°C. As a result, these materials were shown to release greater amounts of Rhodamine B, a model hydrophobic drug, when activated above its T_g, with drug loaded into the particles directly during synthesis at temperatures exceeding this T_g. These particles can also be developed to contain hydrophobic SPIONs without affecting their T_g or can be encased within an injectable, MITCH-type hydrogel that entraps SPIONs that can drive magnetically-activated glass transitions in the latex particles. This latter method was used to show the capacity of these T_g materials to release significantly greater amounts of Rhodamine B in response to both pulsed and continuous AMF applications.

Collectively, this work presents as clear evidence of what a powerful tool the combination of SPIONs and thermosensitive hydrogels and/or microgels could be for the purposes controlled release. These systems seem to be effective from the macro- to the nano-scale, leading to their potential use in a wide range of therapies. Notably, the sufficient ratio of on- versus off-state release from the systems developed here all involved small model drugs and could likely be improved upon when using larger therapeutics. While there would be numerous alterations required to all of these devices before they are commercialized, this work provides a basis for the optimization of remote release from hydrogel-based systems, from localized magnetic hydrogels to hydrogel

droplet nanocomposites injected into a specific location *in vivo* to nano-scale systems that could be introduced to the circulatory system and be magnetically targeted to a specific location before remotely actuated release takes place.

An issue specific to AMF-mediated release is that while small-scale devices (large enough to activate a material implanted in an arm, for example) are relatively common, large scale devices that can fit an entire individual and activate these vehicles in deeper tissues are currently few and far between, especially in North America. Most full-body AMF machines are located in Europe, specifically Germany, where AMFs are routinely in clinical use for the hyperthermia treatments in cancer patients. Even harder to come by are full body systems capable of both AMF-controlled heating and magnetic targeting. To the best of my knowledge, there are only two such devices in the world, one in Montréal and the other in Germany, and both are modified MRI machines for research purposes. Consequently, the clinical practicality of using our nanoscale materials as systems that will circulate and then be magnetically targeted to a specific location before remote controlled release with an AMF is at this time quite limited. Instead, at least in the short term, it is probably more beneficial to take advantage of our injectable hydrogel systems to concentrate and orient our systems at a specific location in the body. These injectable MITCH-type hydrogel systems could entrap a known concentration of SPIONs and drug-loaded nanomaterials at a specific site in the body, allowing for more predictable heating and release *in vivo* from a given AMF application. This method would thus improve the effectiveness and consistency using an AMF *in vivo,* and, as such, it would be much more sensible to focus on to treating our injectable nanosystems in this way as this research moves forward.

The use of magnetic fields to remotely activate release of drug payloads remains a relatively new field, a field whose very existence is owed to recent advancements in polymer and materials science. Several complex elements are inherently involved in these remotely-responsive systems, and this complexity means that there is still a lot of work in this field before a great deal of commercialization occurs (particularly for injectable, biocompatible systems that would ultimately be superior in terms of patient compliance). Indeed, the only system enabling remote-controlled release that is currently undergoing FDA trials toward eventual commercialization is the MicroCHIPS device, a microchip device with degradable seals over micro-scale drug reservoirs that can remotely deliver drug doses upon electrical stimulation.[2] While this device is incredibly promising, it is large and metallic and undergoes fibrosis after it is implanted in the body via an invasive surgical procedure. Consequently, the success of this device (or the lessons learned from this attempt at clinical translation) could open the door to more biocompatible, injectable systems that perform similar functions.

The field of remote-controlled delivery has a great deal of potential for advancement, and this advancement could be remarkably useful for a wide range of medical therapies. Indeed, nearly every therapy could benefit from improved control over the release kinetics of their therapeutic. Thus, the main contribution to the field of this work, due to its novelty, would be as a stepping stone or a basis for future research in the area of remotely-actuated delivery systems using “smart” polymers as this field continues to mature. Hopefully future attempts at achieving systems capable of chronopharmaceutical delivery will take note from this work and realize the potential importance developing localized, remotely actuated release systems that are injectable and biocompatible. These would avoid surgical procedures and improve patient

compliance and well-being in the process. These systems will also require a large ratio between the on- and off-states of drug release, as that is the primary limitation of the systems developed here from being clinically translatable. This may be able to be done by tweaking some of the systems developed in this work. However, this work could be valuable even if it simply encourages others to go against the grain of typical present drug delivery research, which is currently generally focussing on targeting circulating nanoparticles to a specific point in the body or the development of localized delivery systems that undergo passive release, and come up with novel delivery strategies that could lead to a game changer in the field of drug delivery. Ultimately, if this work helps, in any way, to lead to future commercialized systems that can benefit hundreds to thousands of individuals requiring pulsatile or user/physician-controlled remote actuation of drug release, it will undoubtedly be worthwhile.

8.1.1 References

(1) Veiseh, O.; Dolo, J. C.; Ma, M.; Vegas, A. J.; Tam, H. H.; Bader, A. R.; Li, J.; Langan, E.; Wycko, J.; Loo, W. S.; *et al. Nat. Mater.* **2015**, *14*, 643–652.

(2) Farra, R.; Sheppard, N. F.; McCabe, L.; Neer, R. M.; Anderson, J. M.; Santini, J. T.; Cima, M. J.; Langer, R. *Sci. Transl. Med.* **2012**, *4*, 122ra121, doi:10.1126/ scitranslmed.3003276.